Graduate School for Cellular and Biomedical Sciences

University of Bern

Intracoronary electrocardiogram as a direct measure of myocardial ischemia

PhD Thesis submitted by

Marius Reto Bigler

from **Worb BE**

for the degree of

Doctor of Medicine and Philosophy (MD,PhD)

Supervisor
Prof. Dr. Christian Seiler
Department of Cardiology
Faculty of Medicine of the University of Bern

Co-advisor
Prof. Dr. Josef Götte
Bern University of Applied Sciences
Faculty of Science of the University of Bern

Accepted by the Faculty of Medicine, the Faculty of Science and the Vetsuisse Faculty of the University of Bern at the request of the Graduate School for Cellular and Biomedical Sciences

Bern, Dean of the Faculty of Medicine

Bern, Dean of the Faculty of Science

Bern, Dean of the Vetsuisse Faculty Bern

Copyright Notice

Table of Contents

Abstract

The electrocardiogram is a valuable diagnostic method providing insight into pathologies of the heart, especially rhythm disorders or insufficient myocardial blood supply (myocardial ischemia). The commonly used surface ECG is, however, limited in detecting short-lasting myocardial ischemia, in particular in the territory of the left circumflex coronary artery supplying the postero-lateral wall of the left ventricle. Conversely, an ECG recorded in close vicinity to the myocardium, i.e., within a coronary artery (intracoronary ECG, icECG) has been thought to overcome these limitations. Since its first implementation during cardiac catheterization in 1985, icECG has shown ample evidence for its diagnostic value given the higher sensitivity for myocardial ischemia detection when compared to the surface ECG. In addition, icECG has been demonstrated to be a direct measure of myocardial ischemia in real-time, thus, providing valuable information during percutaneous coronary diagnostics and interventions. However, a lack of analysing systems to obtain and quantify icECG in real-time discourages routine use.

The goals of this MD-PhD thesis are two-fold: First, to determine the diagnostic accuracy of icECG ST-segment shift during pharmacologic inotropic stress in comparison to established indices for coronary lesion severity assessment using quantitative angiographic percent diameter stenosis as reference (Project I). Second, to determine the optimal icECG parameter for myocardial ischemia detection and quantification (Project II and III).

In essence, this thesis demonstrates that the icECG is an easy available diagnostic method providing highly accurate information on the amount of myocardial ischemia in real-time. Quantitative assessment of acute, transmural myocardial ischemia by icECG is most accurately performed by measuring ST-segment shift at the J-point, while the quantitative assessment during physical exercise, respectively its pharmacologic simulation, is most accurately performed by measuring ST-segment shift 60ms after the J-point.

Abbreviations

ATP	Adenosine triphosphate
AUC	Area under the (ROC) curve
CAD	Coronary artery disease
CFI	Collateral flow index
CFR	Coronary flow reserve
CMD	Coronary microvascular dysfunction
CNN	Convolutional neural networks
CVP	Central venous pressure
ECG	Electrocardiogram
FFR	Fractional flow reserve
icECG	Intracoronary electrocardiogram
iFR	Instantaneous wave-free ratio
LAD	Left anterior descending coronary artery
LCX	Left circumflex coronary artery
LV	Left ventricle
P_{ao}	Aortic pressure
PCI	Percutaneous coronary intervention
P_{dist}	Distal coronary pressure (measured downstream of a stenosis)
P_{occl}	Coronary occlusive pressure
PTCA	Percutaneous transluminal coronary angioplasty
%S	Percent diameter stenosis
QCA	Quantitative coronary angiography
QTc	Corrected QT-time
RCA	Right coronary artery
TPE	T-peak-to-end time
ROC	Receiver-operating characteristic (analysis)

Please note: Figures of the thesis are numbered by Roman numerals, while figures of the published papers/ the manuscripts are numbered by Arabic numerals starting at “1” for each manuscript.

1. Introduction

The heart is responsible for the maintenance of adequate blood supply to all organs. In order to achieve this purpose, an electrical signal (via depolarization of myocardial cells) originating from the sinoatrial node propagates across the atrial myocardium, the atrioventricular node and the ventricular conduction system induces a temporally and spatially organized contraction of the myocardium. This results in the subsequent ejection of blood in the pulmonary, respectively the systemic circulation.

Because of the electrical conductivity of the human tissue, it is possible to record this electrical activity of the heart by simple methods, i.e., using electrodes attached directly on the body surface, resulting in an electrocardiogram (ECG). The ECG represents the vectored sum of the electrical processes in myocardial cells as a function of time and of the position of the recording electrodes. Hence, analysis of strategically placed electrodes allows assessment of the cardiac electrical activity in different planes, and thus, the diagnosis of various cardiac pathologies.

1.1 Electrocardiogram

At the end of the 19th century, electrical impulses as the trigger for muscle contractions were well recognized[1]. This led to the investigations of the physiologist Augustus Desiré Waller who connected a pair of chest electrodes to a Lippmann's capillary electrometer (device for detecting electric current using mercury solutions), the experimental setup of which resulted in the movement of the mercury "slightly but sharply at each beat of the heart" (i.e., the first human electrocardiogram)[2]. In this study, Waller described not only the temporal dependence of the electrical activity preceding the heartbeat, but also the relationship between the electrical signal and the placement of the electrodes[2].

In 1889, Waller presented his findings at the First International Congress of Physiology in Basel, Switzerland[3]. There, Willem Einthoven witnessed the recording of a human ECG and pursued this concept. However, further development of the Waller approach did not lead to appropriate results. Hence, Einthoven replaced the capillary electrometer by a string galvanometer. This device comprises a thin filament passing between two electromagnets. The filament then moves accordingly to the applied electrical voltage[3-6]. This device allowed the recording of cardiac electrical activity in a quality comparable to current days. Besides the improvement in recording, Einthoven further introduced the use of three leads (i.e., Einthoven I,II and III, see figure I) to calculate the axis of the heart[3].

Several years later, the ECG was expanded by six chest leads (V_1-V_6 as introduced by Frank Norman Wilson), and three additional extremity leads called augmented voltage leads (avR, avL, aVF in the context of a 50% voltage augmentation introduced by Emanuel Goldberger)[7].

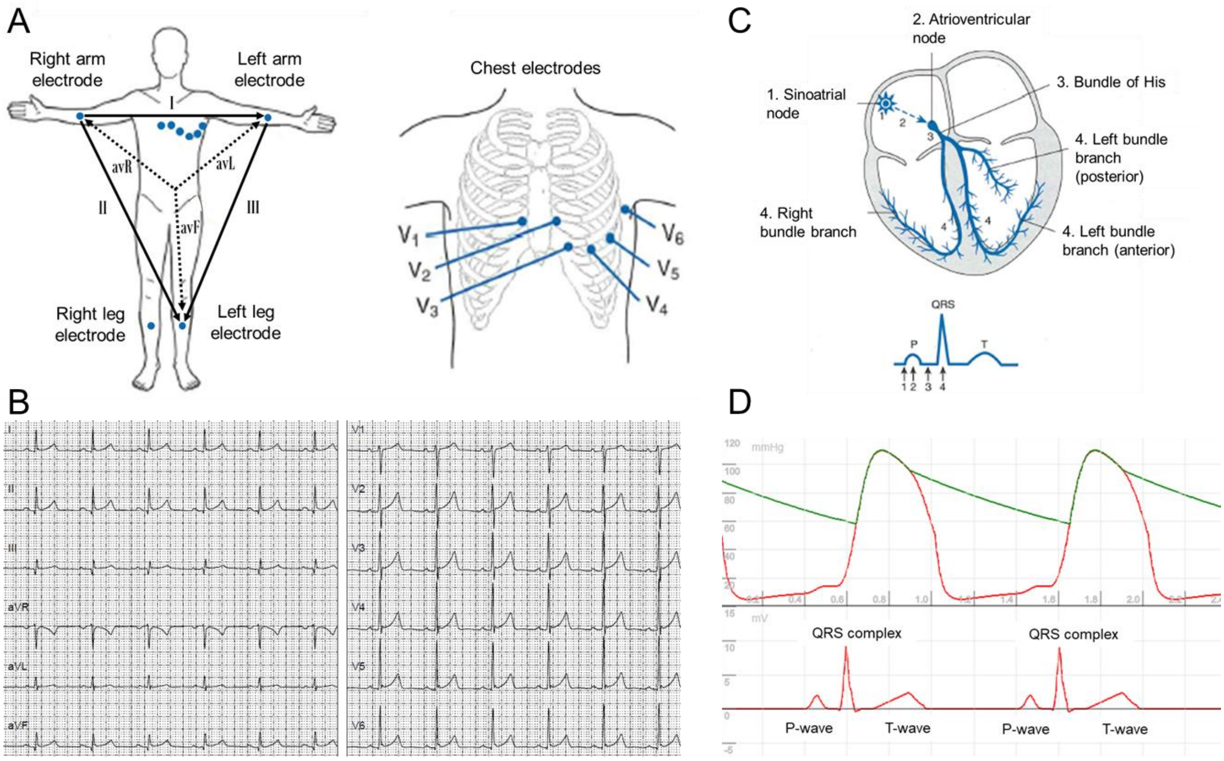

Figure I: Overview of the electrocardiogram (ECG). A) *Placement of the ten electrodes necessary to record a standard 12-lead ECG, as shown in* ***B)****. Three out of the 12 leads are bipolar (i.e., they record the difference between two electrodes), while the rest is pseudo-unipolar (i.e., they record against a reference point with close to zero potential.* ***C)*** *Illustration of the different structures of the cardiac conductive system and their representation in the ECG.* ***D)*** *Electromechanical coupling: Depolarization of the myocardium (i.e., the QRS-complex) causes contraction of the ventricle, resulting in pressure generation and blood ejection, once the circulation pressure is exceeded.*

A and C were taken from Leonard S. Lilly – Pathophysiology of Heart Disease, Fifth Edition and further adapted, D was generated using www.harvi.online.

In comparison to the bipolar leads of Einthoven, the additional leads are historically called unipolar leads (even if this term is not correct). Hence, they do not record the difference in the electrical potential between two electrodes, but rather between one electrode and a reference value with close to zero potential. For the chest leads according to Wilson, the reference point is called Wilson Central Terminal, defined as the arithmetic mean of the three extremity leads, i.e., left and right arm plus left leg divided by three. For the Goldberger-leads, this reference value is constructed by connecting two electrodes through a central point with high resistance (5000 Ohm), resulting in a neutral point, i.e., for avR, the reference value for the right arm electrode is the neutral point constructed as described between the left arm and left leg electrode.

As outlined above, the electrical activity of the heart usually originates from the sinoatrial node and is coupled to myocardial contraction. This electric propagation is reflected in the ECG with distinctive patterns. Atrial depolarization is represented by the P-wave (figure I) followed by a return to baseline (isoelectric line = full cardiac de- or repolarisation). This return, i.e., the PQ-interval represents the conduction delay at the atrioventricular node. The next deflection of the ECG is the QRS-complex, representing depolarization of the ventricular myocardium, which is, once again, followed by return to the baseline (ST-segment). The last deflection of the ECG is called T-wave, which represents the repolarization of ventricular myocardium. On surface ECG, atrial repolarization is masked by the large amplitude QRS-signal.

The twelve standard ECG leads reflect the cardiac electric activity in two planes, i.e., the frontal plane (Einthoven and Goldberger) and the transverse (or horizontal) plane (Wilson). This electrode placement enables three-dimensional imaging of the electrical activity of the heart, thus, providing information about spatially localized electrical activity based on the occurrence in different (grouped) leads:

- Lead II, III and aVF represent the inferior wall of the left ventricle
- Lead V_1-V_2 the anteroseptal region of the left ventricle
- Lead V_3-V_4 the anteroapical region of the left ventricle
- Lead I, aVL, V_5 and V_6 the anterolateral region of the left ventricle

In conclusion, the ECG is an easy to acquire diagnostic tool providing information about cardiac electrical activity in real-time. In this context, the ECG is a valuable diagnostic method in the daily clinical practice, especially in the timely diagnosis of heart rhythm disorders or acute myocardial ischemia.

1.1.1 Myocardial ischemia detected by ECG

Inadequate coronary blood flow to myocardial cells, i.e., myocardial ischemia, causes a depletion of adenosine triphosphate (ATP), which is often referred to as the "molecular unit of currency of intracellular energy transfer”[8]. Shortage of ATP directly affects all energy-dependent cellular processes in the myocardium, in particular ion channels and transporters. These membrane proteins are responsible for the maintenance of ion gradients between the intra- and extracellular space, which are necessary for rapid in- and efflux of ions during de- and repolarisation. The resting membrane potential is roughly -90 mV[9] (and increases during depolarization within milliseconds to +50 mV because of massive sodium inflow[9]). During myocardial ischemia, however, the resting potential is reduced causing a pathologic ion current across the “injured” cell membrane with subsequent distortion of the normally isoelectric ECG ST-segment[10,11]. Simultaneously, opening of ATP-potassium channels[12] distorts myocardial repolarization and thus, directly affects the morphology and duration of the T-wave[10].

On surface ECG, myocardial ischemia affecting a large territory causes ST-segment elevation in the leads representing this region (figure II). This electrical pattern representing myocardial ischemia was first described by Harold Pardee[13] one hundred years ago. Since then, ECG ST-segment shift assessment in suspected acute coronary syndrome has become crucial for the subsequent management[14], and the extent of ST-segment elevation (number of leads, amplitude of the shift) reflects the size of myocardial ischemia at risk for infarction, and as such, cardiovascular outcome[15].

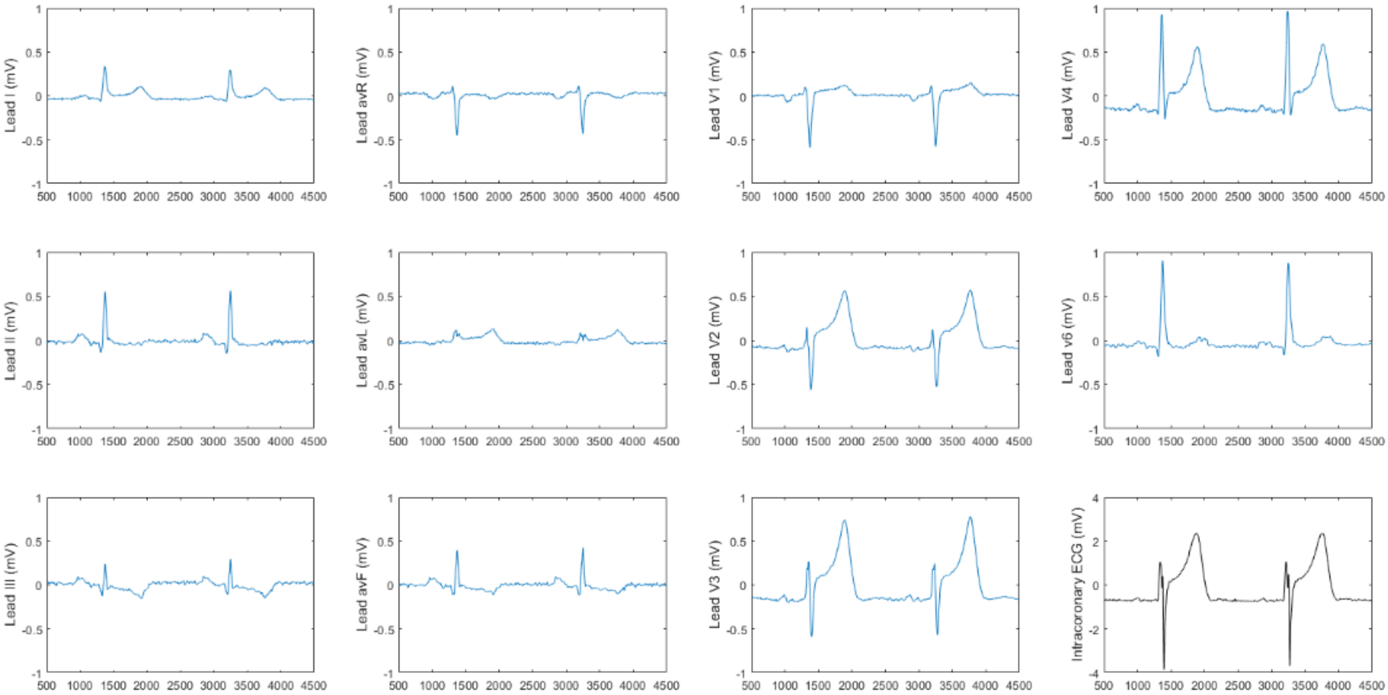

Figure II: 11-lead surface electrocardiogram (ECG) during coronary balloon occlusion of the left anterior descending artery (LAD). *In this patient, proximal coronary balloon occlusion of the LAD caused myocardial ischemia in the anteroseptal, -apical and –lateral region as reflected by ST-segment elevation in* V_2*-*V_4*, I and avL. The chest lead* V_5 *was replaced by the intracoronary ECG (black) within the course of a clinical trial. Please note the different scales for the surface and the intracoronary ECG.*

Myocardial ischemia affecting a smaller territory, i.e., not the entire ventricular wall but rather the innermost part (subendocardial myocardium), is represented by ST-segment depression. This is often the case in coronary artery disease (CAD, see chapter 1.4.1), whereby obstructed, but not completely occluded coronary arteries result in a perfusion supply/ demand mismatch, to which the subendocardial region is more exposed than the epicardial area due to the transmission of LV diastolic filling pressure.

In clinical practice, ECG ST-segment shifts (i.e., elevation and depression) in the acute setting are measured directly at the J-point[14] (i.e., the transition of the QRS-complex to the ST-segment), while ST-segment shifts assessed during physical exercise for diagnostic evaluation of CAD are measured 60 ms after the J-point[16,17] (figure III).

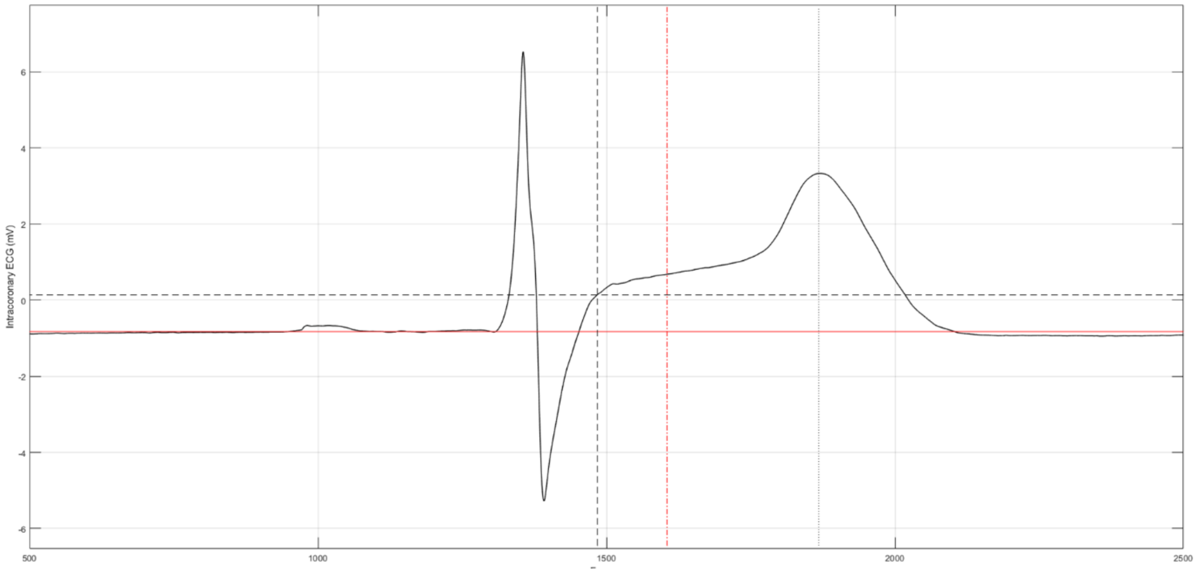

Figure III: Assessment of the ECG ST-segment shift *In acute coronary syndrome: ST-segment shift is measured directly at the J-point (crossing of black dotted lines) as the difference between the J-point and the isoelectric line (solid red line). During (physical) stress test to detect coronary artery disease, ST-segment shift is measured 60ms after the J-point (crossing between the black and red dotted lines).*

Hence, the ECG is an indispensable tool in the diagnosis of myocardial ischemia. However, the commonly used surface ECG has several limitations. It is susceptible to other physiologic electrical activities, i.e., muscle contraction during breathing or limb movements. Further, as stated by Birnbaum and Alam[18], the amplitude of ST-segment shifts are directly affected by lead positioning, habitus and even by the posture of the patient. Finally, short-lasting or minor myocardial ischemia, especially in the territory of the left circumflex coronary artery (i.e., the posterior wall of the left ventricle) remain often undetected in the commonly used 12-lead surface ECG.

1.2 Intracoronary ECG

An ECG recorded in close vicinity to the myocardial region of interest was thought to overcome the spatial limitations of the surface ECG. In 1976, Hashimoto et al.[19] were the first to record an ECG with electrodes placed within a coronary artery, i.e., an intracoronary ECG (icECG). In this study, the authors analyzed the course of the icECG ST-segment shift during complete coronary balloon occlusion during up to 3 hours in 18 dogs. They concluded that "the intracoronary ST-segment elevations after coronary occlusion resembled those recorded from the epicardial surface but were free of artifacts"[19]. Nine years later, Meier and Rutishauser were the first to employ an icECG during percutaneous transluminal coronary angioplasty (PTCA) by attaching a reusable alligator clamp to a coronary guidewire and connecting it to an ECG electrode[20]. With the guidewire positioned in a coronary artery, the derived (pseudo-) unipolar icECG served as a local epicardial ECG. Meier and Rutishauser showed the clinical value of the icECG to monitor myocardial ischemia during coronary angioplasty. These results, which were reproduced in larger clinical trials by Friedman et al.[21], Pande et al.[22] and additionally confirmed by a meta-analysis[23], demonstrated the higher sensitivity of the icECG to detect transient myocardial ischemia during PTCA when compared to the surface ECG. In cases with no ischemic changes in the icECG, either a prior myocardial infarction in the territory undergoing balloon dilatation or angiographic collaterals were present, consistent with the fact that ischemia was not inducible in necrotic myocardium or prevented by sufficient collateral supply. ECG ST-segment shifts seen by both methods occurred sooner and more pronounced using icECG[24,25].

Currently, our research group acquires icECG signals by attaching a reusable alligator clamp to a pressure monitoring angioplasty guidewire positioned in a major coronary artery, and connecting it to a precordial lead (mainly V_5, see figure II). Use of the pressure-monitoring guidewire with non-conductive coating allows the generation of an icECG-lead between the

Wilson Central Terminal and the conductive pressure sensor of the guidewire located near the tip without the need for additional isolation (figure IV).

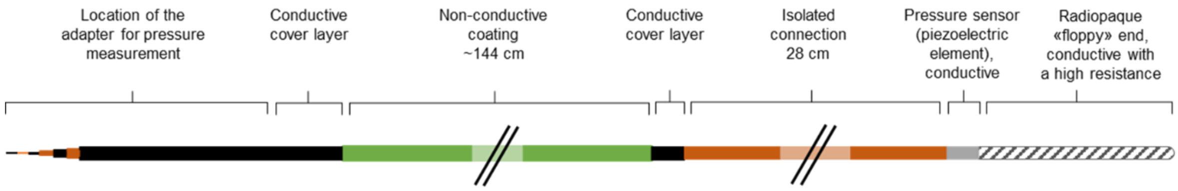

Figure IV: Structure of the pressure-monitoring angioplasty guidewire *The non-conductive coating makes an additional isolation redundant. The conductive part (black) before the isolated connection (orange) is placed within the guiding catheter, and thus, isolated by the catheter.*

Recording of an icECG-lead provides independent information on the *regional* myocardium, i.e., the particular territory supplied by the wired coronary artery. Hence, the exact position of the guidewire up- or downstream in the coronary artery directly affects the recorded signal by altering signal vectors as well as the amount of directly adjacent myocardial mass as shown by figure V.

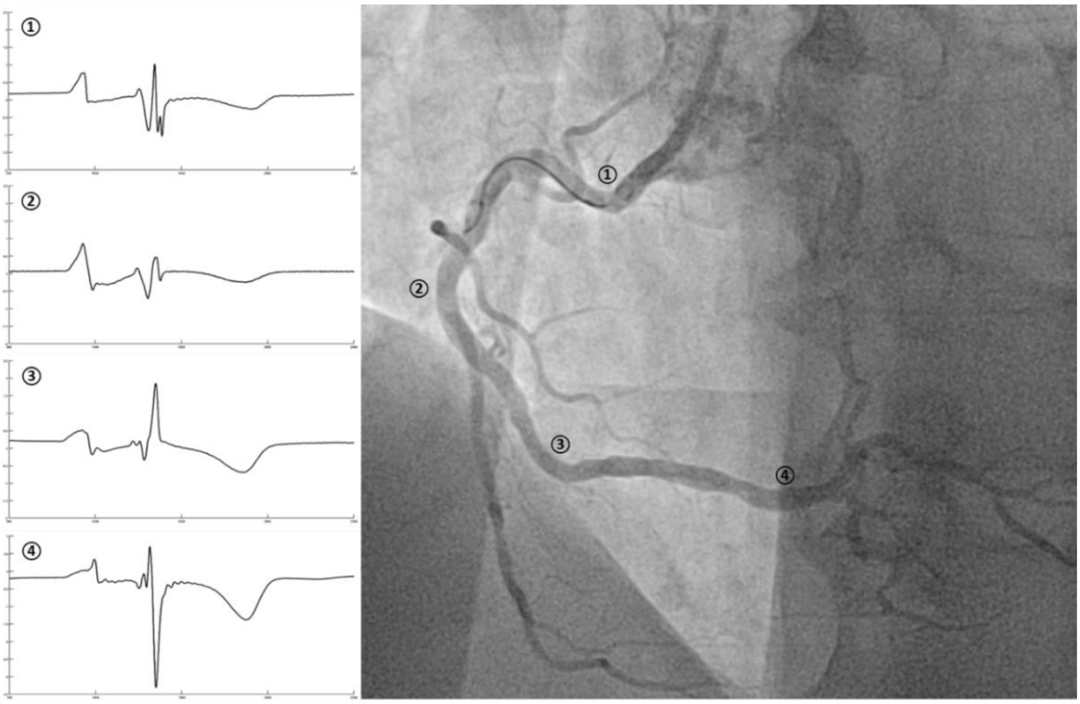

Figure V: The intracoronary ECG as a function of the guidewire position within the coronary artery *This figure shows the angiography of a right coronary artery (RCA) and the corresponding icECG recordings at different locations. In the proximal part, the RCA is close to the right atrium and ventricle, while the distal parts of the RCA are adjacent to the myocardium of the left ventricle. Hence, recording of the icECG lead (between the Wilson Central Terminal and the pressure sensor located near the tip) demonstrates a large ventricular signal (i.e., QRS-complex) in the distal RCA (④). During guidewire pullback, (④→①), the QRS-amplitude decreases, while the amplitude of the atrial signal (i.e., P-wave) increases. Guidewire pullback changes the position of the distal ECG electrode and thus, changes the morphology of the recorded icECG signal because of an altered vector.*

IcECG recording is performed at a sampling frequency of 2’000 Hz, and with standard system filtering (corresponding to a bandpassfilter 0.05-100Hz). Thus, application of this filter method does not affect the ECG signal with frequencies between 10-50 Hz[26].

1.2.1 IcECG for guidance of percutaneous coronary intervention

The higher sensitivity to detect myocardial ischemia of the icECG when compared to the surface ECG was further demonstrated by Hishikari et al.[27]. The authors assessed the occurrence of ST-segment elevation in the icECG in patients with non-ST-segment elevation myocardial infarction (NSTEMI, diagnosed with the commonly 12-lead ECG) and showed, that 27.6% of patients before percutaneous coronary intervention (PCI) had a significant ST-segment elevation in the icECG (>0.1 mV). This discrepancy between icECG and surface ECG was more common with LCX than other culprit lesions[27]. In a subsequent clinical trial, the same research group conducted a multiple regression analysis, showing that ST-segment shift in the icECG predicted greater peak values of troponin levels, consistent with greater myocardial injury[28]. Thus, they concluded that the icECG “might help to identify high-risk NSTEMI patients with greater myocardial injury”[28]. In patients undergoing elective PCI, Uetani et al.[29] as well as Balian et al.[30] showed that icECG provided a useful method to predict peri-procedural myocardial injury. In this context, Sato et al.[31] have applied the icECG to assess the relation between lipid core burden of coronary lesions (as determined by intravascular ultrasound and near-infrared spectroscopy) and peri-interventional myocardial ischemia by distal embolization of lipid contents. They could demonstrate that higher lipid burden was associated with prolonged ST-segment elevation after PCI.

Balian et al.[32] conducted a clinical trial to assess, whether icECG ST-segment shift during maximal pharmacologic vasodilation (by intravenous adenosine) could be used as an estimate of hemodynamic relevance of a coronary lesion (as defined by the fractional flow reserve (FFR), see chapter 1.4.1 and Project I). They demonstrated a modest linear correlation (r^2=0.206) between the tested icECG and the reference FFR and concluded, that icECG “during adenosine infusion may be of value in assessing the functional significance of a borderline stenosis”[32].

1.2.2 IcECG for the assessment of myocardial viability

In the context of the icECG’s sensitivity to detect changes of myocardial physiology, and due to the fact that myocardial scar remains electrically silent, icECG provides an opportunity to assess myocardial viability during PCI. First, Ferrari et al.[33] showed that icECG ST-segment shifts occurring during angioplasty indicates myocardial viability in 20 patients using thallium-201 myocardial scintigraphy as the reference for viability assessment. Subsequently and with the same reference method, Yaijma et al.[34] evaluated the clinical value of icECG for detecting myocardial viability in acute myocardial infarction among 65 patients. They demonstrated preserved myocardial viability by scintigraphy after treatment when an amplified icECG ST-segment shift of >0.2 mV occurred during emergency coronary angioplasty.

Using low-dose dobutamine echocardiography as another reference method to identify viable myocardium after myocardial infarction, Abaci et al.[35] demonstrated high diagnostic accuracy of icECG ST-segment shift assessment during coronary angioplasty. Further, a positive correlation has been shown between the number of viable segments in the low-dose dobutamine echocardiography and the magnitude of icECG ST-segment shift[35].

More recently, real-time assessment of myocardial viability during coronary catheterization using icECG was proposed by Petrucci et al.[36]. They recorded peak-to-peak voltage of the icECG using a common PCI-guidewire electrically isolated by a microcatheter, and matched their results with corresponding segments containing scar by cardiac magnetic resonance imaging as the reference standard. Using this approach, the icECG amplitude (in mV, measured between the highest and the lowest peak of the QRS-complex) distinguished viable from non-viable left ventricular segments with a sensitivity of 99% and a specificity of 69%.

1.2.3 IcECG and the assessment of the coronary collateral circulation

The coronary collateral circulation represents a pre-existing inter-arterial anastomotic network of the coronary artery circulation[37] established during embryogenesis. The peak density of this network occurs in neonates and declines subsequently by physiological regression, a process called pruning[38-41]. Nevertheless, these coronary anastomoses do not vanish completely but rather recede in calibre and present in varying functionality to prevent myocardial ischemia in the setting of an acute or chronic coronary syndrome[42]. Quantitative evaluation of the coronary collateral circulation is based on coronary occlusive pressure measurements, from which collateral flow index (CFI)[43,44] is derived. CFI is calculated as mean coronary occlusive pressure relative to mean aortic pressure, both subtracted by central venous pressure as obtained during a 1-minute proximal coronary balloon occlusion[43] (figure VI). As the coronary collateral circulation is capable to prevent myocardial ischemia, icECG as a direct measure of myocardial ischemia has been used in several clinical trials to assess functionally sufficient coronary collateral circulation.

In 2003, Wustmann et al. showed that functional collaterals exist in angiographically normal coronary arteries to the extent, that 20-25% of the subjects did not show signs of myocardial ischemia in the icECG during brief coronary occlusion[45]. The same research group demonstrated that “absence of ECG ST-segment shift during brief coronary occlusion in patients with chronic coronary artery disease conveys a decreased mortality and is directly influenced by a well-developed collateral supply to the right versus left coronary ischemic region”[46]. In this context, Seiler et al.[47] documented the prognostic value of icECG by assessing coronary collateral function and the associated icECG ST-segment shift at the end of a 1-minute angioplasty coronary balloon occlusion in 1181 patients. During a follow-up of 7.3±4.3 years, absence of icECG ST-segment shift during coronary balloon occlusion has been shown associated with reduced all-cause mortality[47].

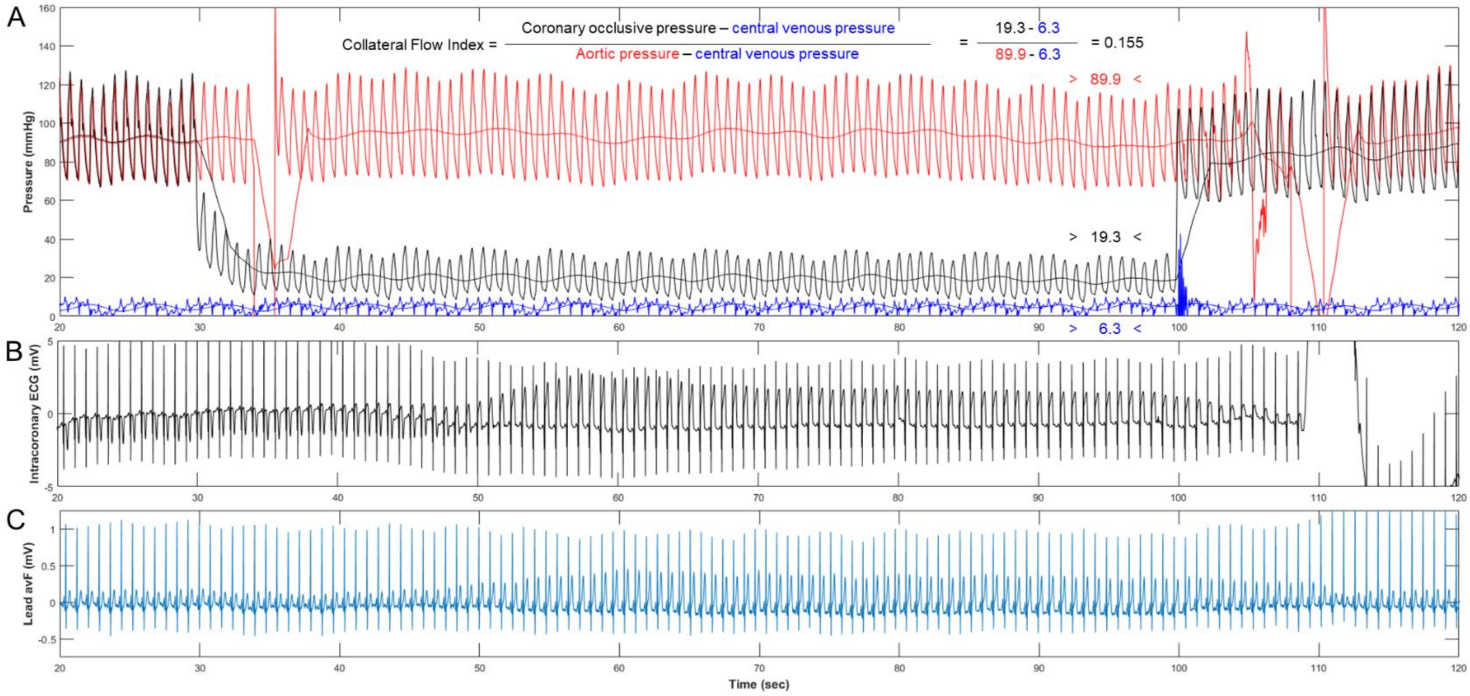

Figure VI: Collateral flow index (CFI) measurement. A) *Simultaneous recordings of mean and phasic aortic (red signals), coronary occlusive (black signals) and central venous pressure (blue signals) immediately before (left side) and during coronary artery occlusion in a patient with poor coronary collateral function.* ***B)*** *Detection of myocardial ischemia during coronary artery occlusion by intracoronary electrocardiogram (icECG). Immediately after balloon occlusion, icECG shows marked electrical alterations with inverted T-waves and ST-segment elevation (after 40sec). Generally, a CFI of >0.20–0.25 is related to absent signs of ischemia on icECG during a 1-min proximal coronary balloon occlusion.* ***C)*** *Detection of myocardial ischemia during the same coronary artery occlusion by surface ECG (lead avF). Note the difference in ischemic alterations when compared to icECG (slightly later (after 45sec) and less pronounced signal amplitude).*

IcECG was also used as an independent measure of myocardial ischemia to assess myocardial ischemic preconditioning[48-54] or the success of various therapeutic approaches to augment coronary collateral function[55-68]. In the study by Billinger et al.[48], 30 patients underwent three repetitive 2-minutes coronary artery balloon occlusions, whereby coronary collateral recruitment could be demonstrated with each occlusion, but also a simultaneous decrease in icECG ST-segment shift. In a similar study with four consecutive balloon inflations[49], a significant decrease in ST-segment shift due to collateral recruitment was shown by icECG, but not on surface ECG, hence providing additional evidence for the superior sensitivity of icECG compared to surface ECG in detecting subtle changes in myocardial pathophysiology.

1.3 Myocardial perfusion

The heart is responsible for the maintenance of adequate blood supply to all organs. Hence, it is also responsible for adequate self-sufficiency. Myocardial blood supply, however, has several specific characteristics, most importantly, cardiac cycle-dependent myocardial perfusion. During systole with contraction of the left ventricular myocardium the high intramyocardial pressure compresses and obliterates intramural coronary blood vessels, and, thus, blocks coronary arterial flow[69]. Hence, left (and less pronounced right) myocardial perfusion is restricted to diastole[70]. As opposed to other organs, e.g., skeletal muscle, the myocardium maintains a high level of oxygen extraction even at rest[71]. Because of this characteristic, exercise induced increases in myocardial oxygen demand is mainly responded to by an increase in coronary blood flow[72].

Resting myocardial perfusion is equal to 1ml/min/g. The coronary microcirculation, the key regulator of coronary resistance and thus myocardial flow, acts as resistance-to-flow regulator[73] and maintains resting blood flow over a broad range of arterial perfusion pressures between 50–150 mmHg[69,74], the physiologic feature of which is called coronary flow autoregulation. In situations of increased oxygen demand, the adequate increase in coronary blood flow is carried out by reducing coronary arteriolar resistance up to 80% as compared to resting levels[72]. This resistance reduction, in combination with a 20%–40% elevation of mean arterial pressure[72], allows a 4-5 fold blood flow increase during physical exercise[67], also called coronary flow reserve (CFR).

1.4 Myocardial ischemia

Myocardial ischemia is defined as reduction or interruption of myocardial perfusion[75] resulting in a discrepancy between myocardial oxygen demand and supply. Hence, it is reflected by inadequate myocardial oxygen supply and with consecutive impairment of all energy-dependent processes, which causes impaired diastolic and systolic ventricular function. The etiology of myocardial ischemia is diverse, but mainly due to impaired myocardial perfusion as a consequence of coronary artery atherosclerotic narrowing lesions, due to coronary vasospasm, to coronary microvascular dysfunction (CMD), and to increased transmural pressure in the context of elevated ventricular filling pressure. Additionally, there are other etiologies for myocardial ischemia as arterial hypotension or severely decreased blood oxygen content because of marked anemia or impaired oxygenation[76]. This introduction will focus on pathophysiologies of the coronary circulation, i.e., CAD and CMD.

The prognostic impact of inducible myocardial ischemia has been shown both by non-invasive and invasive stress testing[77]. The extent of myocardial ischemia depends on multiple factors, namely duration of insufficient oxygen supply, ischemic area at risk for infarction, myocardial oxygen consumption and coronary collateral blood supply[47]:

$$\text{Extent of myocardial ischemia}$$

$$\triangleq \frac{\text{Duration of insufficient oxygen supply} * \text{Area at risk} * \text{Myocardial oxygen consumption}}{\text{Coronary collateral blood supply}}$$

$$\triangleq\!: \textit{being related to}$$

In this formula, area at risk depends on the involved coronary artery and its supply territory as well as the degree of coronary stenotic lesions, varying from narrowings only relevant under strenuous physical exercise or symptomatic already at rest. Hemodynamic mild stenoses predominantly affect subendocardial regions and thus, a smaller mass of myocardium while the latter induces transmural myocardial ischemia in the whole vascular territory given absence of coronary collateral blood supply, which itself limits the area at risk. Myocardial oxygen consumption is mainly dependent on heart rate, myocardial contractility and ventricular wall stress[78]. In this context, “it is estimated that the exercise-induced increases in oxygen consumption can be explained for 50%–70% by heart rate, for 15%–25% by contractility, and for 15%–25% by stroke work[72].” Coronary collateral blood supply is the only factor preventing myocardial ischemia as outlined in chapter 1.2.3.

1.4.1 Coronary artery disease

CAD is a leading global cause of death[79], accounting for approximately 20% of deaths in developed countries[80]. The underlying pathology of CAD is atherosclerosis, a disease of the arterial wall with inflammation, lipid infiltration and smooth muscle cell proliferation[81]. Driven by cardiovascular risk factors as hereditary disposition, tobacco smoking, diabetes mellitus, arterial hypertension and abnormal circulating low-density lipoprotein cholesterol (LDL-C), endothelial cells and smooth muscle cells are stimulated to produce pro-inflammatory cytokines, which allow leukocyte infiltration into the arterial wall[82]. This disturbance of the integrity of the arterial wall causes accumulation of intracellular lipid in the subendothelial region[81,83] with local oxidation of LDL-C. Oxidized LDL-C is then metabolized by macrophages, transforming them into “foam cells” (i.e., lipid-filled macrophages)[84]. Macroscopically, an accumulation of these foam cells gives the arterial wall the appearance of a “fatty streak”[81]. Cholesterol accumulation in the arterial wall impairs endothelial function and causes abnormal vascular tone already at an early stage[76]. With progression of atherosclerosis, migration of smooth muscle cells from the arterial media into the intima[76] as well as apoptosis of foam cells leads to further accumulation of extracellular lipoproteins, which eventually forms an avascular core of lipid-rich debris[81]. In comparison to fatty streaks, which are covered by an intact layer of endothelium, these lipid-rich cores are covered by a fibrous cap of collagenous material and prone to rupture. Hence, calcification of these plaques is induced as adaptive healing response to limit the atherosclerotic diseases[85]. All these pathologic processes can directly influence coronary blood flow by progressive narrowing of the arterial lumen as well as impaired vascular tone[76] and become hemodynamically relevant coronary lesions causing myocardial ischemia.

Hemodynamically relevant coronary lesions are defined as those inducing restriction to flow beyond the compensatory autoregulation of the myocardial microcirculation under stress conditions. As outlined above, coronary blood flow can normally be increased 4-5 fold during physical exercise. With increasing coronary narrowing, this so-called coronary flow reserve (defined as the maximal coronary blood flow divided by the resting coronary blood flow[86], figure VII) allows a compensatory microcirculatory vasodilatation to maintain adequate resting perfusion at the cost of a decreased CFR. Accordingly, in situations with higher oxygen demand, for example during physical exercise, the limited microcirculatory vasodilatory reserve causes myocardial ischemia. Figure VII illustrates this interaction between extent of coronary stenosis, coronary blood flow and myocardial ischemia.

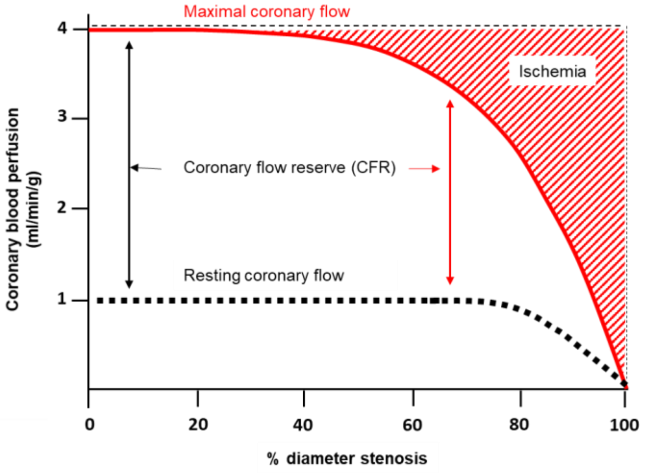

$$CFR = \frac{Maximal\ coronary\ blood\ flow}{Resting\ coronary\ blood\ flow}$$

Norm values:
Resting coronary blood flow: *1ml/min/g*
Max. coronary blood flow: *3-5ml/min/g*

Figure VII: Coronary blood perfusion and coronary flow reserve as a function of coronary stenosis *Because of compensatory coronary vasodilatation, resting coronary perfusion is not affected by narrowing of up to 80 percent in arterial diameter. However, preservation of an adequate resting perfusion occurs at the expense of a decreased coronary flow reserve (CFR) as outlined by the distance between the dotted black line (i.e., resting coronary flow) and the solid red line (i.e., maximal coronary flow). Starting from a 50% diameter stenosis, increasing narrowing causes a simultaneous decrease of the CFR. Situations that require coronary blood flow beyond the CFR result in myocardial ischemia (red striped area above the maximal coronary flow curve).*
Constructed according to a schema from Leonard S. Lilly – Pathophysiology of Heart Disease, Fifth Edition

In clinical practice, i.e., during coronary catheterization, assessment of coronary lesion severity necessary to guide coronary revascularization is mainly performed by physician-based visual assessment with its notorious tendency to overestimate lesion severity[87]. Instead, quantitative coronary angiography (QCA, figure VIII A), i.e., the measurement of coronary diameter at the narrowest point in proportion to the non-diseased reference diameter as obtained in more than one image projection has a well-documented basis for PCI[86,88].

In comparison to this angiographic, structural approach, diagnostic assessment of functional stenosis relevance by coronary pressure measurement has been suggested to affect patient outcome[89]. Unlike direct measurement of coronary blood flow reserve, coronary pressure measurements are technically more robust. Given temporary paralysis of the coronary microcirculation by, e.g., pharmacologic vasodilation, pressure is, theoretically, directly related to coronary flow[90]. Thus, the pressure drop across a coronary stenosis, i.e., fractional flow reserve (FFR[91], figure VIII B), respectively instantaneous wave-free ratio (iFR[92,93], , figure VIII C) provides an estimate of its restrictive effect on flow. Figure VIII provides an overview of these three parameters. In-detail description of the assessment of hemodynamic relevance of coronary lesions is provided in project I (Functional assessment of myocardial ischemia by intracoronary electrocardiogram).

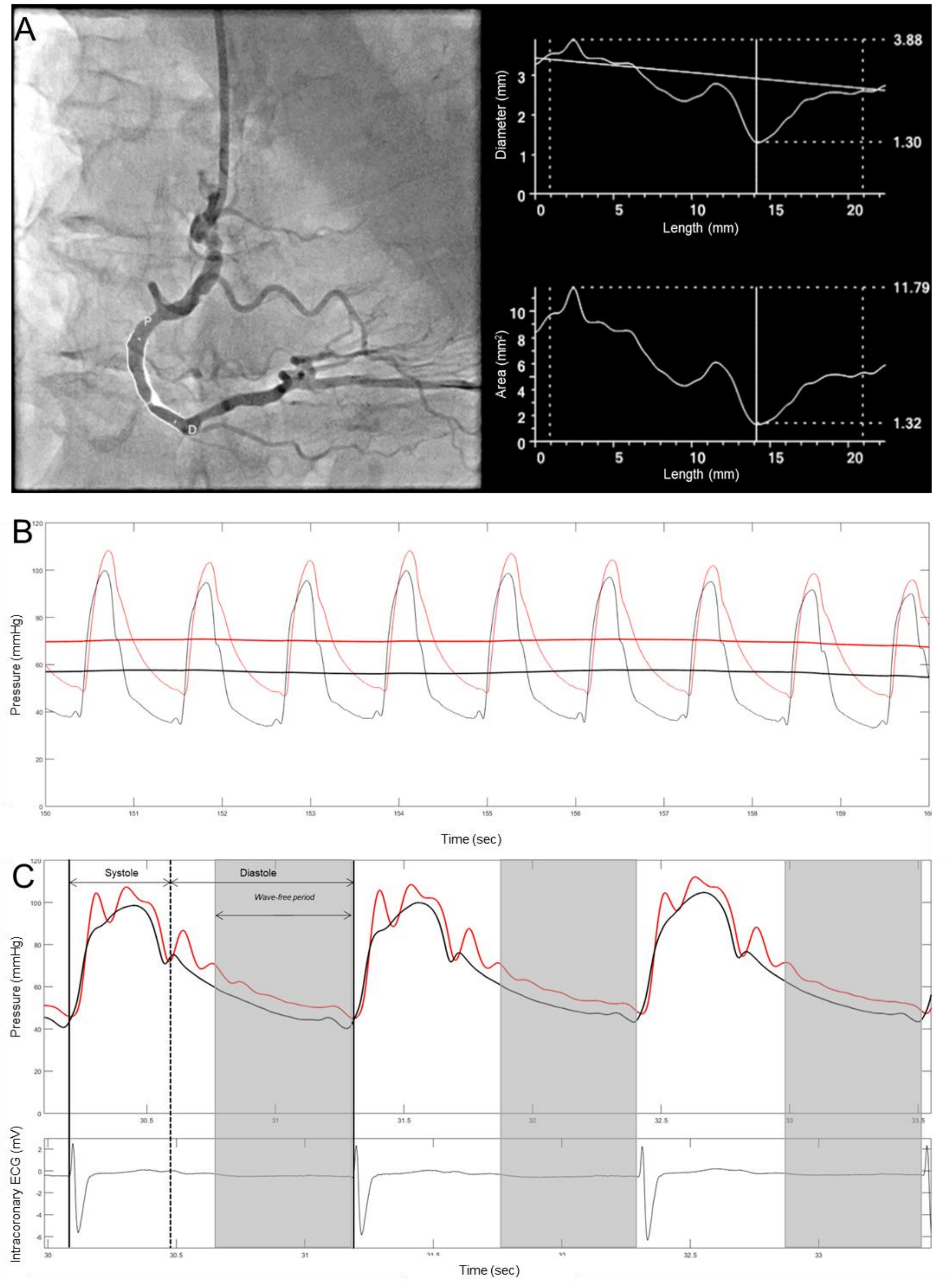

Figure VIII: Parameters for the assessment of coronary lesion severity A) *Quantitative coronary angiography with determination of percent diameter stenosis. This assessment is performed in two orthogonal planes to account for non-concentric (i.e., eccentric) coronary lesions.* ***B)*** *Determination of the pressure drop across a coronary stenosis during maximal vasodilatation, i.e., fractional flow reserve. It is calculated as mean distal coronary pressure (solid, thick black line) divided by mean aortic pressure (solid, thick red line), both measured over several heart cycles during maximal vasodilatation.* ***C)*** *Determination of pressure drop across a coronary stenosis at rest, i.e., instantaneous wave-free ratio, defined as phasic distal coronary pressure (black solid line) divided by the phasic aortic pressure (red solid line), both measured in the wave-free period of the diastolic phase (grey area).*

1.4.2 Coronary microvascular dysfunction

A large proportion of patients with angina pectoris and evidence of myocardial ischemia do not have obstructive CAD when undergoing coronary angiography[94] (i.e., ischemia with non-obstructive coronary arteries). In these patients, myocardial ischemia is caused by CMD, elevated left ventricular filling pressure (hypertensive heart disease), and/or epicardial vascular dysfunction (i.e., arterial spasm). CMD shares the cardiovascular risk factors with atherosclerotic CAD[95,96]. Hence, there is a significant overlap of these pathologies including the adverse cardiovascular outcomes compared with the general population[97]. However, as compared to CAD, CMD affects predominantly female patients[95,98,99] and women with CMD are younger than those with CAD[96].

From the pathophysiologic point of view, the underlying mechanism of CMD is structural microcirculatory remodeling and/or functional arteriolar dysregulation[100]. In the first case, inward remodeling of capillary arterioles impairs the microcirculatory conductance and oxygen delivery, resulting in a decreased vasodilatory range and thus, decreased CFR[101,102]. This remodeling is often seen in the presence of left ventricular hypertrophy[101]. The latter component of CMD affects larger arterioles, where flow-mediated vasodilation is impaired even to paradoxical vasoconstriction in situations with increased oxygen demand. Vasoconstriction can also be triggered by stimuli such as systemic blood pressure peaks, cold exposure, emotional stress or smoking[98]. Cocaine has also been recognized to provoke severe vasospastic reactions leading even to acute myocardial infarction[103,104].

Concerning the therapeutic management, all etiologies of myocardial ischemia require an adjustment of lifestyle factors. In addition, hemodynamically relevant coronary lesions are treated by revascularization (i.e., PCI or coronary-artery bypass graft), while microvascular dysfunction requires anti-ischemic treatment with beta-blockers and/or calcium channel blockers.

2. Hypotheses and aims of the thesis

2.1 Project I

Objective: To determine the diagnostic accuracy of icECG ST-segment shift during pharmacologic inotropic stress in comparison to established hemodynamic indices (FFR, iFR) for coronary lesion severity assessment using quantitative percent diameter stenosis (%S) as reference value.

Hypothesis: IcECG-ST-segment shift during pharmacologic hyperemia correlates positively with the severity of hemodynamic obstruction as defined by %S.

2.2 Project II

Objective: To determine the diagnostic accuracy of different icECG ischemia parameters in comparison to icECG ST-segment shift (reference) during a controlled, 1-minute proximal coronary balloon occlusion.

Hypothesis: Myocardial ischemia at the end of a 1-minute proximal coronary balloon occlusion is most accurately detected by icECG ST-segment shift measured at the J-point.

2.3 Project III

Objective: To determine the optimal icECG ischemia parameter using a deep learning approach with two pretrained convolutional neural networks.

Hypothesis: Using coronary patency or occlusion as reference for absent or present myocardial ischemia, convolutional neural networks distinguish more accurately between non-ischemic and ischemic icECG tracings than manually determined icECG ST-segment shift.

2.4 Project IV

Objective: To determine the diagnostic accuracy of different icECG ischemia parameters during pharmacologic inotropic stress in comparison to pretrained neural networks and to hemodynamic stenosis severity indices (FFR, iFR) using percent diameter stenosis (%S) as reference value.

Hypothesis: From the different icECG parameters and the neural networks, icECG-ST-segment shift during pharmacologic hyperemia has the highest diagnostic accuracy to distinguish between non-relevant and relevant stenotic lesions as defined by quantitative %S.

3. Results

While Project I and II have been published in peer-reviewed journals, Project III has not been accepted yet for publication. Project IV has been conducted exclusively for the course of my MD / PhD program to apply the results of Project II and III to data from Project I.

3.1 Project I

Functional assessment of myocardial ischemia by intracoronary ECG

The first project aimed to test the amount of myocardial ischemia by icECG during inotropic stress for coronary lesion severity assessment in comparison to structural quantitative stenosis severity (%S; reference), and to established hemodynamic indices for lesion severity (FFR, iFR).

My contributions were acquiring, analyzing and interpreting the data, statistical data analysis, writing the first draft including production of all figures and revision of the manuscript.

The paper has been published in *Open Heart* in January 2021. In the year of publication, *Open Heart* had an impact factor of 2.130 and was ranked Q1 according to SCImago Journal Rank in Cardiology and Cardiovascular Medicine.

openheart

Functional assessment of myocardial ischaemia by intracoronary ECG

Marius Reto Bigler, Michael Stoller, Fabien Praz, George C M Siontis, Raphael Grossenbacher, Christine Tschannen, Christian Seiler

To cite: Bigler MR, Stoller M, Praz F, *et al*. Functional assessment of myocardial ischaemia by intracoronary ECG. *Open Heart* 2021;**8**:e001447. doi:10.1136/openhrt-2020-001447

Received 14 September 2020
Revised 17 November 2020
Accepted 17 December 2020

Cardiology, Inselspital University Hospital Bern, Bern, Switzerland

Correspondence to
Professor Christian Seiler;
christian.seiler@insel.ch

ABSTRACT

Introduction In patients with chronic coronary syndrome, percutaneous coronary intervention targets haemodynamically significant stenoses, that is, those thought to cause ischaemia. Intracoronary ECG (icECG) detects ischaemia directly where it occurs. Thus, the goal of this study was to test the accuracy of icECG during pharmacological inotropic stress to determine functional coronary lesion severity in comparison to the structural parameter of quantitative angiographic per cent diameter stenosis (%S), as well as to the haemodynamic indices of fractional flow reserve (FFR) and instantaneous wave-free ratio (iFR).

Method The primary study endpoint of this prospective trial was the maximal change in icECG ST-segment shift during pharmacological inotropic stress induced by dobutamine plus atropine obtained within 1 min after reaching maximal heart rate(=220 - age). IcECG was acquired by attaching an alligator clamp to the angioplasty guidewire positioned downstream of the stenosis. For the pressure-derived stenosis severity ratios, coronary perfusion pressure and simultaneous aortic pressure were continuously recorded.

Results There was a direct linear relation between icECG ST-segment shift and %S: icECG=–0.8+0.03*%S (r^2=0.164; p<0.0001). There were inverse linear correlations between FFR and %S: FFR=1.1–6.1*10–3*%S (r^2=0.494; p<0.0001), and between iFR and %S: iFR=1.27–8.6*10–3*%S (r^2=0.461; p<0.0001). Using a %S-threshold of ≥50% as the reference for structural stenosis relevance, receiver operating characteristics-analysis of absolute icECG ST-segment shift during hyperemia showed an area under the curve (AUC) of 0.678±0.054 (p=0.002; sensitivity=85%, specificity=50% at 0.34 mV). AUC for FFR was 0.854±0.037 (p<0.0001; sensitivity=64%, specificity=96% at 0.78), and for iFR it was 0.816±0.043 (p<0.0001;sensitivity=62%, specificity=96% at 0.83).

Conclusions Hyperaemic icECG ST-segment shift detects structurally relevant coronary stenotic lesions with high sensitivity, while they are identified highly specific by FFR and iFR.

Key questions

What is already known about this subject?

- Diagnostic assessment of functional stenosis relevance by coronary pressure measurement (that is, fractional flow reserve, instantaneous wave-free ratio) has been shown to be efficacious on patient outcome.
- Intracoronary ECG provides a direct measure of myocardial ischaemia in real time, and thus, is useful to predict postprocedural myocardial injury.

What does this study add?

- The theoretical stenosis-specificity of the pressure-derived functional indices was directly corroborated for the first time in clinical practice.
- Hyperaemic intracoronary ECG ST-segment shift detects structurally relevant coronary stenotic lesions with high sensitivity

How might this impact on clinical practice?

- In a selected population, intracoronary ECG can act as a high-sensitivity rule out test for relevant stenosis severity.

INTRODUCTION

In patients with chronic coronary syndrome (CCS), percutaneous coronary intervention (PCI) targets haemodynamically relevant stenotic lesions, that is, those thought to cause ischaemia. That is, coronary lesions inducing flow restrictions beyond the compensatory autoregulation of the myocardial microcirculation under stress conditions. This key feature of coronary resistance, and thus, myocardial perfusion normally allows a fourfold to fivefold blood flow increase[1] (that is, coronary flow reserve, CFR), respectively, is responsible for maintaining constant resting myocardial perfusion of 1 mL blood per minute per gram over a broad range of arterial perfusion pressures. Hence in patients with CCS, compensatory coronary vasodilatation preserves adequate perfusion at the expense of decreased CFR. Accordingly, in situations with higher oxygen demand, for example, during physical exercise, the limited vasodilatory reserve causes ischaemia. Gould and Lipscomb[2] were the first to investigate these coronary pathophysiologic mechanisms. Based on their findings, coronary angiographic lesion severity of ≥50% diameter narrowing has been extensively used as the relevant threshold for PCI.

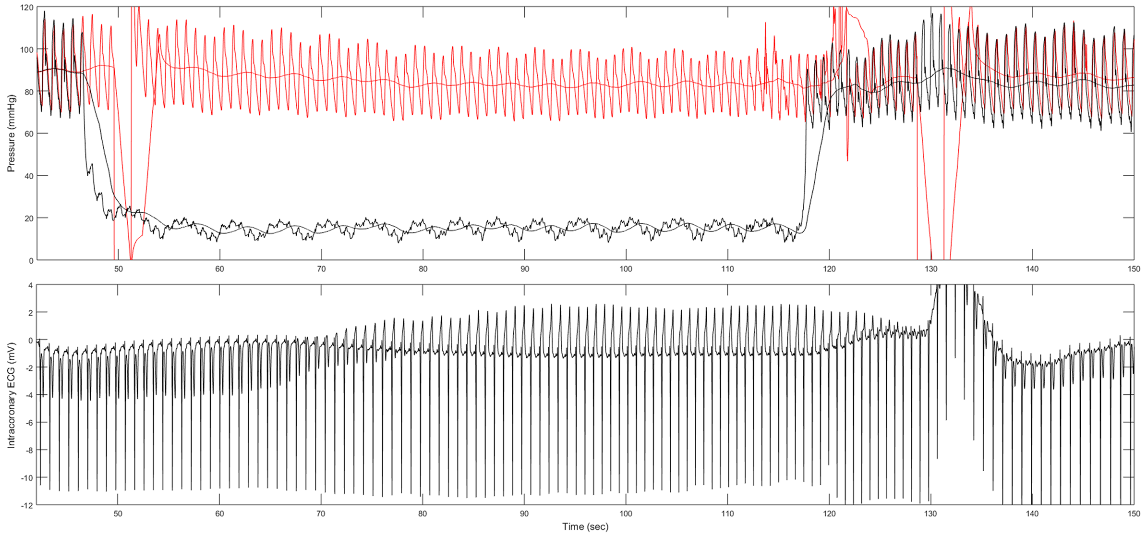

Figure 1 Collateral flow index measurement for the induction of reactive hyperaemia. Simultaneous recordings of mean and phasic aortic (upper panel, red signals), coronary occlusive pressure (upper panel, black signals) and intracoronary ECG (lower panel, icECG). Fractional flow reserve during reactive hyperaemia is calculated immediately after the 1 min occlusion, followed by angiography (marked by the outlier of the red pressure signal).

Compared with the structural, mostly visual angiographic approach, diagnostic assessment of functional stenosis relevance by coronary pressure measurement has been suggested to affect patient outcome.[3] In comparison to direct measurement of coronary blood flow reserve, coronary pressure measurements are more robust. Given temporary paralysis of the coronary microcirculation, pressure is, theoretically, directly related to coronary flow.[4] Thus, the pressure drop across a coronary stenosis, that is, fractional flow reserve (FFR[5]), respectively, instantaneous wave-free ratio (iFR[6 7]) provides an estimate of its restrictive effect on flow. However and despite their prognostic value derived from large randomised clinical trials, both FFR and iFR rely on the, so far, untested concept of their being stenosis-specific,[5] and not stenosis-plus microcirculatory-specific, the fact of which limits their usefulness in defining a true ischaemic threshold.

Conversely, intracoronary ECG (icECG) provides a direct measure of myocardial ischaemia in real time[8–11] (figure 1). Hence, the goal of this study was to test the amount of myocardial ischaemia by icECG during inotropic stress for coronary lesion severity assessment in comparison to structural quantitative stenosis severity (%S), and to established haemodynamic indices for lesion severity (FFR, iFR).

METHODS

Study design and patients

This was a prospective observational study in 100 patients with CCS undergoing diagnostic coronary angiography due to chest pain. The primary study endpoint was the maximal change in icECG ST-segment shift during pharmacological inotropic stress induced by dobutamine plus atropine obtained within 1 min after reaching maximal heart rate in beats per minute (=220 -age). Secondary study endpoints were %S using biplane quantitative coronary angiography, and the pressure-derived haemodynamic indices FFR and iFR. Criteria for study inclusion were age >18 years, and written informed consent for study participation. Exclusion criteria were acute coronary syndrome, severe aortic stenosis, prior myocardial infarction in the vascular territory undergoing study measurement, presence of left bundle branch block, presence or history of non-sinus rhythm or paced rhythm, contraindication to pharmacological inotropic stress as well as severe hepatic or renal failure (creatinine clearance <15 mL/min/1.73 m^2).

All patients gave written informed consent before the start of the study procedure.

Cardiac catheterisation and quantitative coronary angiography

Patients underwent left heart catheterisation and coronary angiography for diagnostic purposes from the right radial artery approach via a 6-in-5F introducer sheath. Biplane coronary angiography was performed followed by left ventriculography. Coronary artery stenoses were assessed quantitatively in two orthogonal planes as per cent diameter narrowing (%S) using the guiding catheter for calibration. In the situation of serial coronary lesions, %S of the most severe stenosis was calculated.

Acquisition of the icECG

IcECG was acquired by attaching an alligator clamp to the 0.014-inch pressure monitoring angioplasty guidewire (PressureWire X Guidewire, Abbott, Chicago, Illinois, USA) positioned downstream of the stenosis, and connecting it to a precordial lead generating a pseudo-unipolar lead between Wilson Central Terminal and the pressure sensor. Due to the structure of the pressure guidewire with integrated isolation, isolating the guidewire

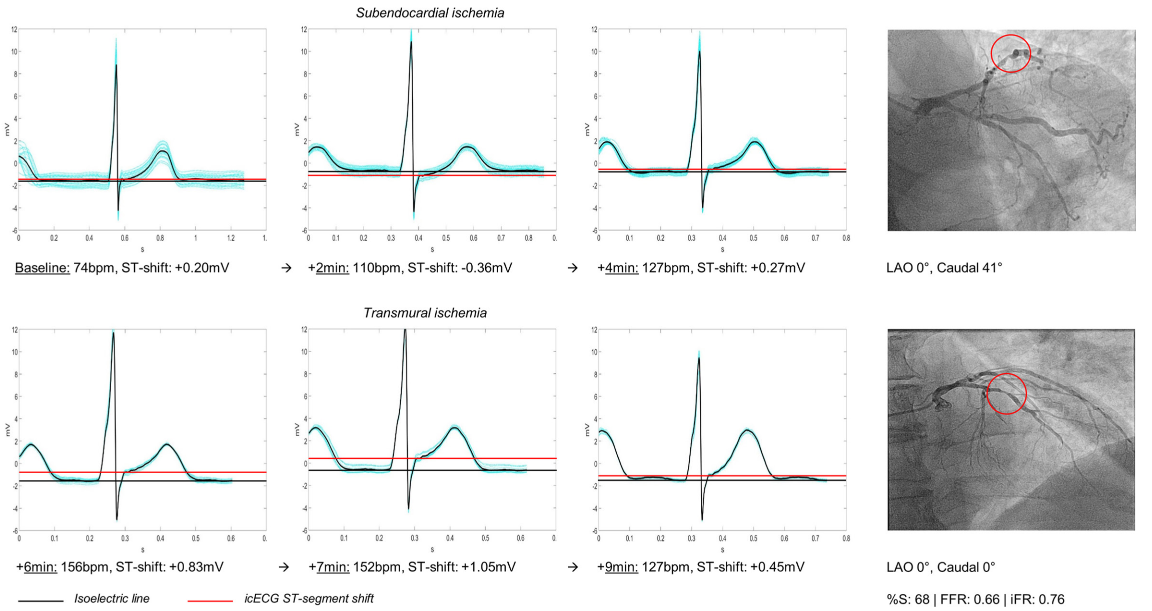

Figure 2 Pharmacological inotropic stress test with recording of intracoronary ECG (icECG). With increasing heart rate and myocardial oxygen consumption, flow impairment of the coronary lesion causes first subendocardial and later transmural myocardial ischaemia with a positive icECG ST-segment shift. Turquoise=IcECG of a single heartbeat, black=signal-averaged icECG of at least 12 consecutive QRS-complexes, %S, per cent diameter stenosis; FFR, fractional flow reserve; iFR, instantaneous wave-free ratio.

also proximally was not required.[11] IcECG recording was performed at a sampling frequency of 2000 Hz, and with standard system filtering (corresponding to a bandpassfilter 0.05–100 Hz). The primary study endpoint, maximal change in icECG ST-segment shift obtained within 1 min after reaching maximal heart rate was measured 60 ms after the J-point on 10–15 consecutive and signal-averaged QRS-complexes (figure 2).

Assessment of pressure-derived haemodynamic indices

For the pressure-derived ratios FFR and iFR, distal coronary artery pressure (P_d, mm Hg) and aortic pressure (P_{ao}, mm Hg) were continuously recorded. FFR, defined as 'the ratio of maximal blood flow downstream of a stenosis relative to unimpaired maximal blood flow (=meanP_d/meanP_{ao}) during hyperaemia'[5] was calculated continuously during pharmacologic inotropic stress. In addition, to receive an independent reference method for the assessment of stenosis severity, FFR was also determined during reactive hyperaemia. Hyperaemia was induced by a 1 min proximal coronary artery balloon occlusion in the vessel of interest (figure 1) immediately followed by angiography. This method has been previously validated against $FFR_{adenosine}$,[12] and it allowed also the determination of collateral flow index (CFI), defined as mean coronary occlusive pressure relative to mean aortic pressure, both subtracted by central venous pressure.[13 14]

IFR was calculated offline according to the proposed method of Sen *et al*[6] as the pressure ratio P_d/P_{ao} in the so called diastolic wave-free period. During this period, that is, beginning 25% of diastolic duration (ms) after the dicrotic notch of the phasic aortic pressure curve, and ending 5 ms before the start of the next ECG QRS complex, coronary resistance is thought to be stable and minimal.[6]

Study protocol

Immediately following right radial artery sheath insertion, 5'000 units of intravenous heparin plus two puffs of oral isosorbidedinitrate were given. Following diagnostic coronary angiography, the 0.014 inch pressure monitoring angioplasty guidewire was set at zero, calibrated, advanced through the guiding catheter, and positioned in the distal part of the vessel downstream of the coronary stenosis. Special care was taken to ensure the position of the guidewire in the main vessel to exclude the possibility of coronary side branch occlusion. Before start of pharmacologic inotropic stress, flushing of the catheter with 15 mL of saline allowed the recording of unsmoothed aortic and coronary pressure signals necessary for the calculation of iFR. Immediately after recording of iFR, pharmacological inotropic stress test using intravenous dobutamine at a rate of 20 µg/kg/min was started for 2 min, followed by 4 min of intravenous dobutamine at a rate of 40 µg/kg/min. To prevent cardiac preload reduction, that is, a conventional side effect of dobutamine, continuous infusion of saline was maintained throughout the study procedure. If the maximal heart rate (=220 -age) was not reached after 6 min, 0.5–1 mg of intravenous atropine was given. At maximal heart rate, infusion of dobutamine was maintained for another minute to allow for full development of ischaemia. Afterwards, dobutamine was stopped, and esmolol (10 mg stepwise) was given to slow down the heart rate. During the entire procedure, continuous recording of the icECG, P_d and P_{ao} was performed.

After normalisation of heart rate, an adequately sized angioplasty balloon catheter was positioned in the ostial part of the vessel of interest. Coronary balloon inflation for measurement of CFI and induction of reactive hyperaemia occurred at an inflation pressure of 1–2 atmospheres for exactly 1 min. Complete coronary occlusion was confirmed by angiography. Immediately after balloon deflation, reactive hyperaemia, that is, postocclusive FFR was obtained following angiography.

Treatment of the coronary lesion was independent of the study results, and at the discretion of the interventional cardiologist.

Statistical analysis

For the purpose of data presentation, two study groups were formed based on %S (<or ≥50%). Between-group comparison of continuous demographic variables and haemodynamic parameters was performed by an unpaired Student's t-test.

Linear regression analysis was performed for univariate association testing between icECG ST-segment shift and secondary study endpoints. Non-parametric receiver operating characteristics (ROC) curve analysis was used for accuracy assessment of detecting a %S of ≥50% defining coronary structural stenosis significance by icECG ST-segment shift, FFR and iFR. Comparison of the area under the ROC curve was performed using the DeLong-Test.

Statistical significance was defined at a $p<0.05$. Continuous variables are given as mean±SD. All analyses were performed using SPSS V.25 (IBM Statistics) or MedCalc for Windows, V.19.1 (MedCalc Software, Ostend, Belgium).

RESULTS

One hundred patients were included in the study. Using the %S threshold of ≥50% as definition for structural significance, 52 patients were in the group with a significant coronary stenosis.

Patient characteristics

There was no significant difference between the groups in terms of age, sex, body mass index or cardiovascular risk factors (table 1). There was a significant difference between the groups in Canadian cardiovascular society class, demonstrating a higher level of symptoms in patients with a significant coronary lesion. Regarding

Table 1 Patient characteristics

	Overall	%S<50%	%S≥50%	p-value
No of patients	100	48	52	–
Patient characteristics				
Age	66±11	67±10	66±11	0.623
Female gender, n (%)	25 (25)	15 (31)	10 (19)	0.176
Height (cm)	174±8	174±8	174±8	0.803
Weight (kg)	84±16	85±17	83±15	0.627
Body mass index (kg/m^2)	28±5	28±5	27±4	0.523
Angina pectoris before intervention (%)	53	58	48	0.324
Duration of angina pectoris (months)	9±21	6±6	13±30	0.414
Canadian cardiovascular society class of angina pectoris	2.10±1.05	1.67±0.83	2.56±1.12	0.002
Diabetes mellitus (%)	23	21	25	0.643
Arterial hypertension (%)	69	67	71	0.670
Current smoking (%)	12	8	15	0.362
Cumulative pack years of cigarettes	38±21	36±20	40±24	0.664
Dyslipidaemia (%)	73	75	71	0.822
Family history for coronary artery disease (%)	32	33	31	0.832
Prior myocardial infarction (%)	37	29	44	0.148
Medical treatment				
Aspirin (%)	87	83	90	0.377
Platelet inhibitor (%)	43	38	48	0.317
Calcium channel-blocker (%)	27	31	23	0.377
Beta-blocker (%)	51	42	60	0.109
Nitrate (%)	12	15	10	0.544
Oral anticoagulation (%)	7	6	8	1.000
Statin (%)	77	77	77	1.000
ACE-inhibitor or ARB (%)	71	63	79	0.082
Diuretics (%)	28	33	23	0.274

ACE, angiotensin-converting enzyme; ARB, angiotensin receptor blocker.

Table 2 Haemodynamic parameters

	Overall	%S<50%	%S≥50%	p-value
Heart rate (beats per minute)	77±16	76±20	78±12	0.545
Systolic blood pressure (mm Hg)	122±21	121±20	124±22	0.540
Diastolic blood pressure (mm Hg)	66±12	66±11	67±12	0.578
Left ventricular end-diastolic pressure (mm Hg)	11±6	11±6	11±6	0.898
Left ventricular ejection fraction (%)	63±8	64±7	63±8	0.552
Coronary angiographic parameters				
No of diseased vessels	1.81±0.94	1.50±0.99	2.10±0.84	0.001
No of coronary lesions (visually relevant)	1.83±1.60	1.21±1.21	2.38±1.68	<0.001
Target vessel distribution				
Left anterior descending, n	55	23	32	0.362
Left circumflex coronary artery, n	24	14	10	
Right coronary artery, n	21	11	10	
Study parameters				
Maximum heart rate achieved (beats per minute)	150±16	149±18	151±13	0.508
Maximal heart rate in % of theoretical maximal heart rate (220-age)	98±11	98±12	98±10	0.705
Quantitative coronary angiography of the lesion of interest (%)	53±17	39±6	66±12	–
Fractional flow reserve	0.798±0.143	0.887±0.073	0.716±0.143	<0.001
Instantaneous wave-free ratio	0.812±0.209	0.922±0.052	0.710±0.245	<0.001
Intracoronary ECG ST-segment shift measured @ J-Point +60 ms (mV) within 1 min after maximal heart rate	0.965±1.324	0.545±0.892	1.352±1.533	0.002
Collateral flow index	0.118±0.100	0.083±0.070	0.148±0.113	0.001

cardiovascular medication, there was no difference between the groups.

Haemodynamic and coronary angiography data

There was no significant difference between the groups in basic haemodynamic parameters, that is, heart rate at rest, left ventricular ejection fraction or arterial blood pressure. Patients with a %S ≥50% showed a higher number of structurally relevant stenoses on coronary angiogram (table 2).

Left anterior descending artery served more often as the study vessel than other coronary arteries; maximum heart rate was similar between the groups. Overall, %S, FFR and iFR were equal to 53±17, 0.789±0.143, and 0.812±0.209, respectively.

There was a direct linear relation between icECG ST-segment shift and %S: icECG = -0.8+0.03*%S (r^2=0.164; p<0.001, figure 3). There were inverse linear correlations between FFR and %S: FFR=1.1–6.1*10^{-3}*%S (r^2=0.494; p<0.001, figure 4), and between iFR and %S: iFR=1.27–8.6*10^{-3}*%S (r^2=0.461; p<0.001, figure 4).

Using a %S threshold of ≥50% as the reference for structural stenosis relevance, ROC-analysis of absolute icECG ST-segment shift showed an area under the curve (AUC) of 0.678±0.054 (p=0.002). AUC for FFR was 0.854±0.037 (p<0.0001), and for iFR it was 0.816±0.043 (p<0.0001, figure 5).

The DeLong-Test of the ROC-curves showed a significant difference for FFR and iFR as compared with icECG ST-segment shift (p=0.002, respectively p=0.024). There was no relevant difference in AUC between FFR and iFR (p=0.3151).

Regarding the optimum cut-off for icECG, an absolute ST-segment shift of 0.34 mV (taken 60 ms after the J-point) distinguished best between haemodynamically relevant and irrelevant stenotic lesions; sensitivity 85%, specificity 50%.

The best cut-off point for FFR to detect a %S≥50% was 0.78 (sensitivity 64%, specificity 96%). For iFR, the best cut-off point was 0.83 (sensitivity 62%, specificity 96%).

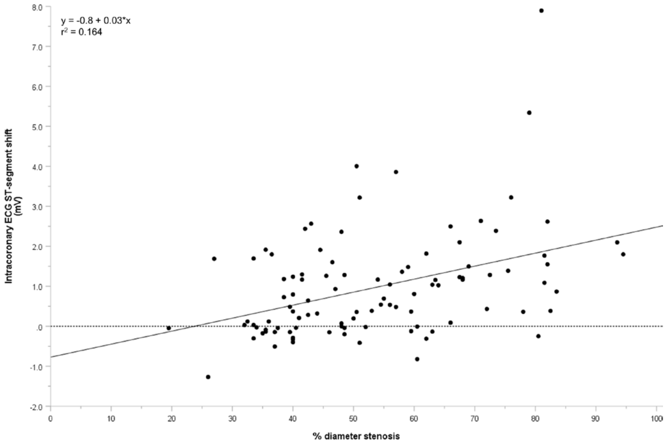

Figure 3 Linear regression between intracoronary ECG (icECG) ST-segment shift and per cent diameter coronary stenosis. solid line=regression line; dashed line=marker for 0 mV icECG ST-segment shift.

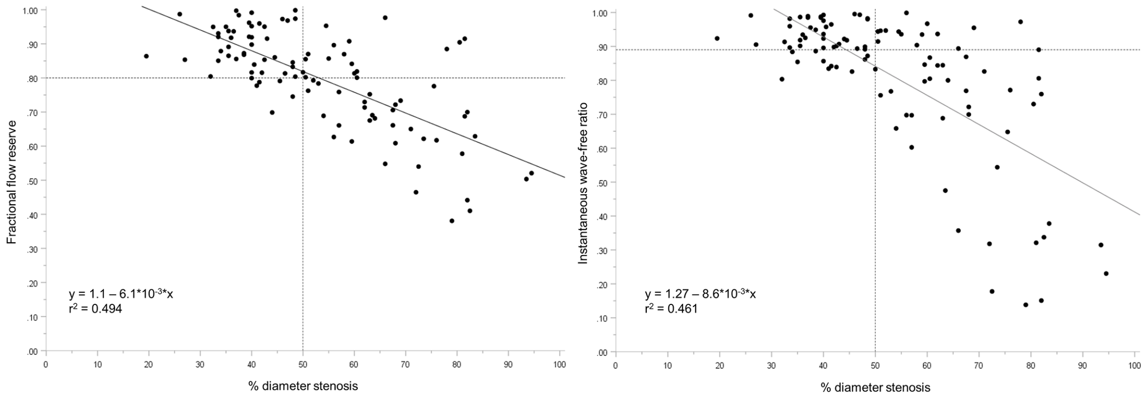

Figure 4 Linear regression between fractional flow reserve, respectively, instantaneous wave-free ratio and per cent diameter coronary stenosis. Solid lines=regression lines; dashed lines=common thresholds, that is, %S≥50%, FFR ≤0.80, iFR ≤0.89. %S, per cent diameter stenosis; FFR, fractional flow reserve; iFR, instantaneous wave-free ratio.

Adverse events associated with dobutamine/atropine infusion were the following: one ventricular fibrillation requiring defibrillation (provoked by wedge position of the guiding catheter during maximal hyperemia), and two cases of supraventricular tachycardia (terminated during esmolol infusion at the end of the study protocol).

DISCUSSION

When tested against the structural parameter of per cent diameter coronary narrowing, haemodynamically relevant stenotic lesions are -overall- detected less accurately by icECG ST-segment shift during myocardial ischaemia than by hyperaemic FFR or diastolic wave-free coronary pressure ratio. The theoretically claimed stenosis-specificity of the pressure-derived functional indices was directly corroborated for the first time in our study, while icECG during hyperaemia very sensitively detected a relevant coronary stenosis responsible for myocardial ischaemia.

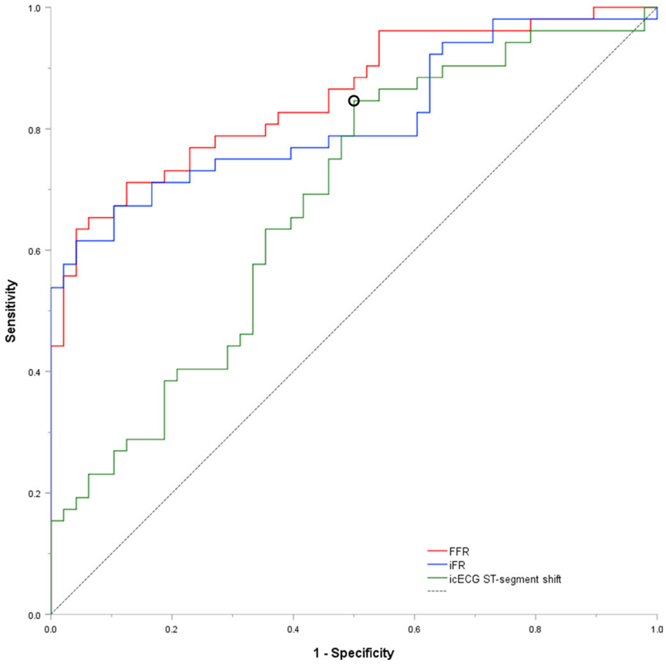

Figure 5 Non-parametric receiver-operating characteristic curve of intracoronary ECG (icECG) ST-segment shift, FFR and iFR, using a %S threshold of 50% as structural significance definition. The black circle marks the best cut-off point for icECG ST-segment shift according to the Youden-Index: 0.34 mV, sensitivity 85%, specificity 50%. %S, per cent diameter stenosis; FFR, fractional flow reserve; iFR, instantaneous wave-free ratio.

icECG as direct indicator of myocardial physiology

The ECG is essential in the diagnosis of myocardial ischaemia, the amount of which is a crucial prognostic factor.[15] The commonly used surface ECG is, however, limited in detecting short-lasting or minor myocardial ischaemia. Conversely, due to its close vicinity to the myocardium, icECG is much more sensitive than surface ECG in detecting myocardial ischaemia.[8] Thus, several clinical trials have assessed the value of icECG to guide PCI, and rated it useful to predict postprocedural myocardial injury.[9 16]

The detection of vasodilator-induced ischaemia by icECG is not unprecedented. Balian *et al*[11] compared icECG ST-segment shift during intravenous adenosine with FFR. Eighty-one per cent of the 48 patients with an FFR ≤0.80 showed a significant icECG ST-segment shift during adenosine infusion, while 14% did so despite an FFR >0.80 (false positive cases). The major limitation of the study as stated by the authors was the induction of coronary perfusion heterogeneity by adenosine, that is, coronary steal.[11] Hence, the use of dobutamine as a pharmacologic simulator of physical exercise with consecutive physiological hyperaemia might be preferable, since unmasking a haemodynamically relevant coronary stenosis does not require asymmetric stenosis distribution within the coronary tree as in the case of adenosine-induced hyperaemia.

Using dobutamine/atropine for ischaemia induction, icECG ST-segment shift showed a significant, but modest linear correlation with per cent diameter stenosis (r^2=0.164, figure 3). However, myocardial ischaemia, that is, the cause of icECG ST-segment shift, does not only depend on structural stenosis severity, but also on the area of ischaemic myocardium, and on the extent of coronary collateral blood supply. Accounting for these different determinants of ischaemia, the accuracy analysis results for icECG ST-segment shift is not surprising, showing a high sensitivity but a low specificity for structural stenosis relevance (figure 5). Hence, icECG could act as a rule out diagnostic test, that is, a functional test with high negative predictive value similar to the non-invasive coronary computed tomography angiography. Practically speaking, the presence of myocardial ischaemia on icECG with a ST-segment shift of >0.34 mV requires further structural and/or function assessment while the absence of ischaemia allows abstaining from further tests.

Aside from its high test sensitivity for detecting structurally relevant stenoses, icECG has a remarkable temporal sensitivity for dynamically changing ischaemia as illustrated by figure 2. IcECG as the vectored sum of energy dependant electrical processes in myocardial cells directly reflects the adequacy of myocardial perfusion, and is able to detect subtle voltage changes. Thus, in this patient with a haemodynamically significant coronary lesion (FFR=0.66, iFR=0.76, %S=68%), icECG recorded shortly after the start of the pharmacologic stress test showed subendocardial ischaemia. With progressive pharmacological stress, regional ischaemia extended across the myocardial wall. Transmural ischaemia, however, resolved quickly after termination of dobutamine infusion.

Taken together, for the detection of coronary structural (figure 5) as well as myocardial temporal supply (figure 2) changes, icECG is a highly sensitive instrument.

Assessment of haemodynamic significance of epicardial coronary lesions

Gould *et al* showed that epicardial coronary lesions cause diminished flow at rest once the arterial diameter reduction reaches 80%, or 50% in case of maximal coronary blood flow.[17] Thus, quantitative coronary angiography has offered a well-documented basis for revascularisation given a non-diseased reference diameter as obtained in more than one image projection. Yet, physician-based visual assessment with its notorious tendency to overestimate lesion severity remained the standard method instead of quantitative angiographic assessment for guiding revascularisation.[18]

Hence, to reduce unnecessary PCIs of coronary lesions, haemodynamic stenosis parameters have been introduced. FFR, which first has been validated against exercise stress testing to determine a cut-off value for inducible myocardial ischaemia (FFR ≤0.66[19]) has later been compared with various exercise stress tests, dobutamine stress echocardiography and myocardial perfusion imaging yielding a threshold for stenosis relevance of 0.75.[5] In the subsequent FFR versus Angiography for Multivessel Evaluation (FAME-trials), a higher cut-off value of 0.80 has been selected based on the previously demonstrated practice of interventional cardiologists to perform PCI in the grey zone of 0.75–0.80.[20] Among patients preselected for PCI by conventional visual (instead of quantitative) coronary angiographic assessment, the FAME-1 trial documented an advantage of angiography- plus FFR-guided versus angiography-guided PCI on major adverse cardiac events after 1 year.[21]

In theory, FFR has been thought to be stenosis-specific under the -uncertain- condition of adenosine-induced constant and minimal coronary arterial microcirculatory resistance.[22] This concept has been mutually adopted based on an early study claiming FFR to be ‘a lesion-specific index that reflects the effect of the epicardial stenosis on maximum myocardial perfusion’.[22] In this regard, the present study’s results corroborated for the first time the assumption of FFR’s stenosis specificity, revealing specificity values of 96% for both FFR and iFR when tested against the truly structural quantitative parameter of %S (figure 5). Of note, the optimum cut-off value for FFR to detect a structural relevant stenosis of ≥50% diameter narrowing was 0.78, thus demonstrating an almost perfect agreement with the commonly used FFR threshold of 0.80.

More recently, a drug-free and thus more practical approach for haemodynamic stenosis assessment, iFR, has been introduced and compared with FFR, yielding good agreement between the two indices.[6] In a subsequent clinical trial using a threshold of ≤0.89, iFR has been proven non-inferior to FFR in guiding PCI.[7] In regard to our study results, iFR showed an almost identical diagnostic performance to FFR with the same specificity, that is, demonstrating stenosis-specificity as well.

Nevertheless, both indices are affected by the distribution of coronary atherosclerotic disease, by asymmetrically distributed regional vascular resistances. This can only be accounted for by direct regional assessment of myocardial ischaemia as with icECG. In a broader sense and in the context of coronary blood flow as the source for the myocardium,[4] icECG reflects the adequacy of regional myocardial perfusion.

ECG and haemodynamic mismatch

It is important to reiterate, that coronary pressure indices are not a true reference for myocardial ischaemia. Accordingly, a value below the threshold does not automatically represent myocardial ischaemia, but rather indicates a higher probability to induce myocardial ischaemia. Consequently, lesions with lower vs higher values benefit more from revascularisation as shown previously.[23] The oversimplification of the relation between a coronary pressure ratio and myocardial ischaemia has been further demonstrated by the comparison of FFR and CFR, showing disagreement between the two methods in 40% of cases.[24] There, the discrepancy has been assumed to be the result of variable stenosis morphology and its effect on coronary blood flow, that is, that focal atherosclerotic disease can cause a relevant pressure drop without relevant impairment of coronary blood flow.[24]

A similar situation was also encountered in the present study using the icECG as indicator for myocardial ischaemia. Applying a binary cut-off of 0.6 mV for icECG, as derived from the surface ECG cut-off of 0.1 mV and adjusted to the sixfold higher signal amplitude of the icECG, and an iFR cut-off of 0.89, only 29% of the cases were concordant in demonstrating absent ischaemia, and 31% were concordant with ischaemia; 17% were discordant without ischaemia in the presence of focal disease, while 23% were discordant in the presence of diffuse or small-vessel disease. IcECG in combination with coronary pressure-derived indices allow comprehensive assessment of myocardial perfusion and thus, also an appraisal of the regional extent of atherosclerotic disease. Taken into account the results of the FAME-II-trial, where 80% of patients with abnormal FFR values did not experience cardiac events throughout the 2-year follow-up period,[4 25] an optimal functional assessment should be preferred.

Study limitations

The major limitation of this study is the lack of information on cardiovascular outcome as a function of the amount of myocardial ischaemia by icECG ST-segment shift. Although myocardial ischaemia was proven several times as the principal predictor of cardiovascular outcome,[15] its assessment would have increased the validity of the presented method. However, the present study was primarily designed to evaluate the interaction between structural and functional parameters of myocardial ischaemia. Thus, it would have been underpowered as an outcome trial.

Additionally, the employed stress test required an elaborated study protocol, which prolonged the assessment of coronary lesion severity. However, the observed high test sensitivity of icECG can be attributed to dobutamine/atropine for ischaemia induction. In a post hoc analysis with assessment of the icECG ST-segment shift during reactive hyperaemia (that is, simultaneous assessment with the FFR), diagnostic performance shifted towards a higher specificity while completely losing sensitivity.

Clinical implication

IcECG is an easy to acquire parameter providing insight into myocardial physiology in real time with a fraction of the costs as it does not require expensive pressure monitoring angioplasty guidewires. Clinical application is, however, for a selected population with relative contraindications to PCI (for example bleeding history), where the prolonged measurement duration is out-weighed by the importance of accurate coronary lesion assessment. There, icECG can act as a high-sensitivity rule out test for relevant stenosis severity. Consequently, absence of ischaemia in the icECG during pharmacological inotropic stress represents maintained coronary blood flow and thus, PCI can be deferred. On the other hand, icECG ST-segment shift in combination with normal iFR may reflect diffuse epicardial or microvascular disease with a hampered vasodilator reserve capacity, in which case medical treatment would be indicated.[26]

CONCLUSION

Hyperaemic icECG ST-segment shift detects structurally relevant coronary stenotic lesions with high sensitivity, while they are identified highly specific by FFR and iFR.

Twitter Marius Reto Bigler @biglermarius

Contributors MRB: data analysis, interpretation, drafting and revising of the manuscript; MS: conception and design, revising of the manuscript; FP, GCMS, RG, CT: data interpretation, revising the manuscript; CS: conception and design, data analysis, interpretation, drafting and revising of the manuscript.

Funding This study was supported by a grant from the Swiss Heart Foundation to MS.

Competing interests None declared.

Patient consent for publication Not required.

Ethics approval The study was approved by the Ethics Committee of the Canton of Bern, Switzerland (KEK-ID 2016–00726).

Provenance and peer review Not commissioned; externally peer reviewed.

Data availability statement The data, methods used in the analysis and materials used to conduct the research will be made available on reasonable request to any researcher for purposes of reproducing the results or replicating the procedure.

ORCID iD

Marius Reto Bigler http://orcid.org/0000-0002-3199-4664

REFERENCES

1. Zbinden R, Zbinden S, Meier P, *et al*. Coronary collateral flow in response to endurance exercise training. *Eur J Cardiovasc Prev Rehabil* 2007;14:250–7.
2. Gould KL, Lipscomb K. Effects of coronary stenoses on coronary flow reserve and resistance. *Am J Cardiol* 1974;34:48–55.
3. van Nunen LX, Zimmermann FM, Tonino PAL, *et al*. Fractional flow reserve versus angiography for guidance of PCI in patients with multivessel coronary artery disease (FAME): 5-year follow-up of a randomised controlled trial. *Lancet* 2015;386:1853–60.
4. Stegehuis VE, Wijntjens GW, Piek JJ, *et al*. Fractional flow reserve or coronary flow reserve for the assessment of myocardial perfusion. *Curr Cardiol Rep* 2018;20:77.
5. Pijls NH, De Bruyne B, Peels K, *et al*. Measurement of fractional flow reserve to assess the functional severity of coronary-artery stenoses. *N Engl J Med* 1996;334:1703–8.
6. Sen S, Escaned J, Malik IS, *et al*. Development and validation of a new adenosine-independent index of stenosis severity from coronary wave-intensity analysis: results of the advise (adenosine vasodilator independent stenosis evaluation) study. *J Am Coll Cardiol* 2012;59:1392–402.
7. Davies JE, Sen S, Dehbi H-M, *et al*. Use of the instantaneous Wave-free ratio or fractional flow reserve in PCI. *N Engl J Med* 2017;376:1824–34.
8. Friedman PL, Shook TL, Kirshenbaum JM, *et al*. Value of the intracoronary electrocardiogram to monitor myocardial ischemia during percutaneous transluminal coronary angioplasty. *Circulation* 1986;74:330–9.
9. Balian V, Galli M, Marcassa C, *et al*. Intracoronary ST-segment shift soon after elective percutaneous coronary intervention accurately predicts periprocedural myocardial injury. *Circulation* 2006;114:1948–54.
10. de Marchi SF, Streuli S, Haefeli P, *et al*. Determinants of prognostically relevant intracoronary electrocardiogram ST-segment shift during coronary balloon occlusion. *Am J Cardiol* 2012;110:1234–9.
11. Balian V, Marcassa C, Galli M, *et al*. Intracoronary electrocardiogram ST segment shift evaluation during intravenous adenosine infusion: a comparison with fractional flow reserve. *Cardiol J* 2011;18:662–7.

12 Stoller M, Seiler C. Reactive myocardial hyperaemia for functional assessment of coronary stenosis severity. *EuroIntervention* 2017;13:e201–9.

13 Pijls NH, van Son JA, Kirkeeide RL, *et al*. Experimental basis of determining maximum coronary, myocardial, and collateral blood flow by pressure measurements for assessing functional stenosis severity before and after percutaneous transluminal coronary angioplasty. *Circulation* 1993;87:1354–67.

14 Vogel R, Zbinden R, Indermühle A, *et al*. Collateral-flow measurements in humans by myocardial contrast echocardiography: validation of coronary pressure-derived collateral-flow assessment. *Eur Heart J* 2006;27:157–65.

15 Hachamovitch R, Rozanski A, Shaw LJ, *et al*. Impact of ischaemia and scar on the therapeutic benefit derived from myocardial revascularization vs. medical therapy among patients undergoing stress-rest myocardial perfusion scintigraphy. *Eur Heart J* 2011;32:1012–24.

16 Hishikari K, Yonetsu T, Lee T, *et al*. Intracoronary electrocardiogram ST-segment elevation in patients with non-ST-segment elevation myocardial infarction and its association with culprit lesion location and myocardial injury. *EuroIntervention* 2014;10:105–12.

17 Gould KL, Lipscomb K, Hamilton GW. Physiologic basis for assessing critical coronary stenosis. instantaneous flow response and regional distribution during coronary hyperemia as measures of coronary flow reserve. *Am J Cardiol* 1974;33:87–94.

18 Zhang H, Mu L, Hu S, *et al*. Comparison of physician visual assessment with quantitative coronary angiography in assessment of stenosis severity in China. *JAMA Intern Med* 2018;178:239–47.

19 De Bruyne B, Bartunek J, Sys SU, *et al*. Relation between myocardial fractional flow reserve calculated from coronary pressure measurements and exercise-induced myocardial ischemia. *Circulation* 1995;92:39–46.

20 Fearon WF, Tonino PAL, De Bruyne B, *et al*. Rationale and design of the fractional flow reserve versus angiography for multivessel evaluation (FAME) study. *Am Heart J* 2007;154:632–6.

21 Tonino PAL, De Bruyne B, Pijls NHJ, *et al*. Fractional flow reserve versus angiography for guiding percutaneous coronary intervention. *N Engl J Med* 2009;360:213–24.

22 Pijls NH, Van Gelder B, Van der Voort P, *et al*. Fractional flow reserve. A useful index to evaluate the influence of an epicardial coronary stenosis on myocardial blood flow. *Circulation* 1995;92:3183–93.

23 Johnson NP, Tóth GG, Lai D, *et al*. Prognostic value of fractional flow reserve: linking physiologic severity to clinical outcomes. *J Am Coll Cardiol* 2014;64:1641–54.

24 Johnson NP, Kirkeeide RL, Gould KL. Is discordance of coronary flow reserve and fractional flow reserve due to methodology or clinically relevant coronary pathophysiology? *JACC Cardiovasc Imaging* 2012;5:193–202.

25 De Bruyne B, Pijls NHJ, Kalesan B, *et al*. Fractional flow reserve-guided PCI versus medical therapy in stable coronary disease. *N Engl J Med* 2012;367:991–1001.

26 Lanza GA, Crea F. Primary coronary microvascular dysfunction: clinical presentation, pathophysiology, and management. *Circulation* 2010;121:2317–25.

3.2 Project II

Accuracy of intracoronary ECG parameters for myocardial ischemia detection

The second project aimed to assess the accuracy of different icECG ischemia parameters for myocardial ischemia assessment to determine the optimal diagnostic icECG parameter.

My contributions were the conception and design of this retrospective study as well as data analysis and interpretation, writing the first draft including production of all figures and revision of the manuscript.

The paper has been published in the *Journal of Electrocardiology* in December 2020. In the year of publication, *Journal of Electrocardiology* had an impact factor of 0.944 and was ranked Q3 according to SCImago Journal Rank in Cardiology and Cardiovascular Medicine.

Journal of Electrocardiology 64 (2021) 50–57

Contents lists available at ScienceDirect

Journal of Electrocardiology

journal homepage: www.jecgonline.com

Accuracy of intracoronary ECG parameters for myocardial ischemia detection

Marius Reto Bigler, Patrick Zimmermann, Athanasios Papadis, Christian Seiler *

Department of Cardiology, Inselspital, Bern University Hospital, University of Bern, Switzerland

A R T I C L E I N F O

Available online xxxx

Keywords:
Intracoronary electrocardiogram
Myocardial ischemia
ST-segment shift
ST-integral
T-wave-integral
T-peak
T-peak-to-end time
QTc-time

A B S T R A C T

Introduction: The electrocardiogram (ECG) is a valuable diagnostic tool for the diagnosis of myocardial ischemia during acute coronary syndrome. Aside from the commonly used ST-segment shift indicative of ischemia, several other ECG parameters are pathophysiologically reasonable. Thus, the goal of this study was to assess the accuracy of different ischemia parameters as obtained by the highly susceptible intracoronary ECG (icECG).

Method: This was a retrospective observational study in 100 patients with chronic coronary syndrome. From each patient, a non-ischemic as well as ischemic icECG at the end of a one-minute proximal coronary balloon occlusion was available, and analysed twice by three different physicians, as well as once together for consensual results. The evaluated parameters were icECG ST-segment shift (mV), ST-integral (mV**sec*), T-wave-integral (mV*sec), T-peak (mV), T-peak-to-end time (TPE; msec) and QTc-time (msec).

Results: All six icECG parameters showed significant differences between the non-ischemic and the ischemic recording. Using the icECG recording during coronary patency or occlusion as criterion for absent or present myocardial ischemia, ROC-analysis of icECG ST-segment shift showed an area under the curve (AUC) of 0.963 ± 0.029 ($p < 0.0001$). AUC for ST-integral was 0.899 ± 0.044 ($p < 0.0001$), for T-wave integral 0.791 ± 0.059 ($p < 0.0001$), for T-peak 0.811 ± 0.057 ($p < 0.0001$), for TPE 0.667 ± 0.068 (p < 0.0001), and for QTc-time 0.770 ± 0.061 (p < 0.0001). The best cut-off point for the detection of ischemia by icECG ST-segment shift was 0.365 mV (sensitivity 90%, specificity 95%).

Conclusion: When tested in a setting with artificially induced absolute myocardial ischemia, icECG ST-segment shift at a threshold of 0.365 mV most accurately distinguishes between absent and present ischemia.

Introduction

The electrocardiogram (ECG) is a valuable diagnostic tool and essential in the diagnosis of various cardiac pathologies, in particular acute myocardial ischemia. The presence or absence of ECG ST-segment elevation determines subsequent therapeutic management [1].

Historically, acute myocardial ischemia has been thought to cause sequential and stepwise development of ECG-alteration, starting with a tall and upright T-wave, followed by ST-segment elevation and finally QRS-complex alteration. However, intracoronary ECG (icECG) during invasive coronary angiography with its increased susceptibility to ischemia as compared to the standard 12-lead surface ECG [2,3] has provided evidence for a continuous transition among these steps [4], the fact of which is reasonable as myocardial ischemia affects all energy dependent cellular processes over the entire cardiac cycle involving de- and repolarization alike. Hence, ischemia can be detected and quantified by various ECG parameters. Nevertheless, assessment of the ST-segment shift has dominated in clinical practice so far. ECG ST-segment shift is based on the reduced resting potential of the ischemic myocardial cells, caused by a pathologic ion current across the “injured” cellular membrane with subsequent distortion of the normally isoelectric ST-segment [5]. Of note, not only the shift, i.e., the amplitude of the distortion but also the temporal area of the repolarization abnormality, i.e., ST-segment integral, can serve as a measure of ischemia.

Simultaneously, inadequate energy supply during ischemia causes opening of adenosine triphosphate-potassium channels [6], thus, directly affecting the morphology and duration of the T-wave as electrocardiographic representation of the ventricular repolarization [5]. Accordingly, quantification of voltage (amplitude or area under the T-wave) or temporal (T-wave peak to end interval, TPE) T-wave parameters have been evaluated in various settings [7,8]. QT interval reflecting both de- and repolarization has been shown to be affected during ischemia [6,8–10].

So far, comprehensive and side-by-side accuracy testing of these pathophysiologically reasonable ECG parameters during controlled myocardial ischemia has been lacking. Thus, the goal of this study

---

* Corresponding author at: Inselspital, Bern University Hospital, Department of Cardiology, University of Bern, Freiburgstrasse 8, Bern CH-3010, Switzerland.
E-mail address: christian.seiler@insel.ch (C. Seiler).

https://doi.org/10.1016/j.jelectrocard.2020.11.018

using icECG was to assess the diagnostic accuracy of the described myocardial ischemia parameters.

Methods

Study design and patients

This was a retrospective observational study in 100 patients with chronic coronary syndrome undergoing coronary angiography due to chest pain and participating in clinical trials [11,12] of our research group with determination of coronary collateral flow index (CFI), the quantitative measure of coronary collateral function during a brief, artificial coronary occlusion. A detailed description of CFI has been previously published [13]. In brief, CFI is a measure of coronary collateral blood supply obtained during a 1-min proximal coronary artery balloon occlusion, and is defined as mean coronary occlusive pressure relative to mean aortic pressure, both subtracted by central venous pressure [14]. Hence, in the absence of sufficient collateral blood supply, coronary balloon occlusion induces maximal myocardial ischemia at the end of the occlusion. This allows the direct comparison of icECG-parameters during non-ischemic (i.e. before the occlusion) and controlled ischemic (i.e. at the end of occlusion) conditions. Study endpoints were the six icECG parameters described below. Criteria for retrospective study inclusion were previously conducted measurement of CFI with simultaneous recording of icECG, and written informed consent for further use of the patient's data. Exclusion criteria were prior Q-wave myocardial infarction in the vascular territory undergoing icECG measurement, presence of ECG bundle branch blocks, presence of non-sinus rhythm or paced rhythm as well as sufficient coronary collateral supply (defined as CFI ≥0.217 [15]).

All original studies had been approved by the Ethics Committee of the Canton of Bern, Switzerland, and all patients gave written informed consent for further use of their data.

Acquisition of the intracoronary ECG

IcECG was acquired by attaching an alligator clamp to the 0.014-in. pressure monitoring angioplasty guidewire (PressureWire™ X Guidewire, Abbott, Chicago, Illinois, United States) positioned in the distal third of a major coronary artery, and connecting it to a precordial lead. The structure of this guidewire with non-conductive coating allows the generation of an icECG-lead between the Wilson Central Terminal and the conductive pressure sensor of the guidewire located near the tip without the need for additional isolation. IcECG recording was performed at a sampling frequency of 2′000 Hz, and with standard system filtering (corresponding to a bandpassfilter 0.05-100 Hz). Of note, the same angioplasty guidewire served as guidance for the balloon catheter used for proximal coronary balloon occlusion.

In a subsequent step, 12 to 15 consecutive cardiac cycles were manually chosen, signal averaged, and, according to the time of recording, labelled as “non-ischemic” or “ischemic”, thus, leading to 100 non-ischemic icECGs and 100 ischemic icECGs.

Assessment of the ECG parameters

Quantitative processing of icECG parameters was performed with customized software (written in Matlab, R2017b), presenting each icECG without information on the ischemic state. All icECGs were analysed twice by three different physicians (MRB, PZ and AP) as well as once together for a consensual result. Calculation of the different icECG-parameters was based on the following cornerstones (Fig. 1):

- Isoelectric line (Fig. 1, solid red line, manually determined): The reference line for the determination of any shifts. PQ-junction, which is the end of the PR segment, was used in the absence of a relevant atrial repolarization signal (occasionally visible in the icECG) as recommended [16]. In case of unstable PR-segment, TP-segment served as reference.
- Q-point (Fig. 1, solid black line, manually determined): Start of the QRS-complex
- Junction(J)-point (Fig. 1, intersection between the two dashed black lines, manually determined): Transition of the QRS-complex to the ST-segment
- Start of T-wave (Fig. 1, dashed/dotted red line, automatically determined): Point of intersection between the height of J-point (Fig. 1, vertical dashed black line) and the tangent at the steepest point of T-wave upslope (Fig. 1, dashed green line).
- Peak of T-wave (Fig. 1, solid blue line, automatically determined): Automatically determined by the algorithm as maximum between the start and end of T-wave.
- End of T-wave (Fig. 1, dashed/dotted red line, automatically determined): Point of intersection between isoelectric line (Fig. 1, solid red line) and the tangent at the steepest point of T-wave downslope (Fig. 1, dashed green line).

Alternatively, start and end of T-wave was determined manually in case of a noisy signal disturbing tangent calculation.

Using the described cornerstones, the different parameters were defined as follows:

- ST-segment shift: Difference in mV between the isoelectric line and the ST-amplitude at the J-point. In addition, ST-segment shift was assessed 40, 60 and 80 m*sec* after the J-point.
- ST-integral: Area under the ST-segment in mV*sec defined as the time integral between the isoelectric line and the entire ST-segment from the J-point to the start of the T-wave.
- T-wave integral: Area under the T-wave in mV*sec defined as the time integral between the isoelectric line and the entire T-wave between the start and the end of the T-wave.
- T-peak: Amplitude of the T-wave in mV.
- T-peak-to-end time: Time in msec between T-peak and the end of the T-wave.
- QTc-time: Defined as QT-interval between Q-point and the end of the T-wave in msec, corrected according to Framingham [17] ($QTc = QT + 0.154^*(1000\text{-}RR)$) as previously described [18].

Statistical analysis

The two study groups of non-ischemic and ischemic icECG were based on the time of icECG recording, i.e., before or at the end of the coronary balloon occlusion. Between-group comparison of continuous demographic variables and hemodynamic parameters was performed by a paired student's *t*-test.

For determining measurement variability, one way analysis of variance (ANOVA), Bland and Altman [19] analysis as well intraclass correlation coefficients (ICC) [20] were calculated. Intra-rater ICC was based on absolute-agreement, two-way mixed-effects model for all individual measurements (i.e. $n = 1200$). Inter-rater ICC was based on an absolute-agreement, two-way random-effects model for the second performance ($n = 600$). Linear regression analysis was performed for calculation of the regression line in the scatter plots for the illustrative presentation of intra-rater as well as inter-rater variability.

Nonparametric receiver operating characteristics (ROC) curve analysis was used for accuracy assessment of detecting myocardial ischemia by the icECG parameters. For reasons of readability, only the parameter with the best performance was presented in case of multiple possibilities (i.e., different time points after the J-point for the determination of ST-segment shift). Optimal cut-off points for each parameter were determined by the Youden-Index. Comparison of the area under the ROC curves was performed using the DeLong-Test.

Statistical significance was defined at a p-level of <0.05. Continuous variables are given as mean ± standard deviation. All analyses were

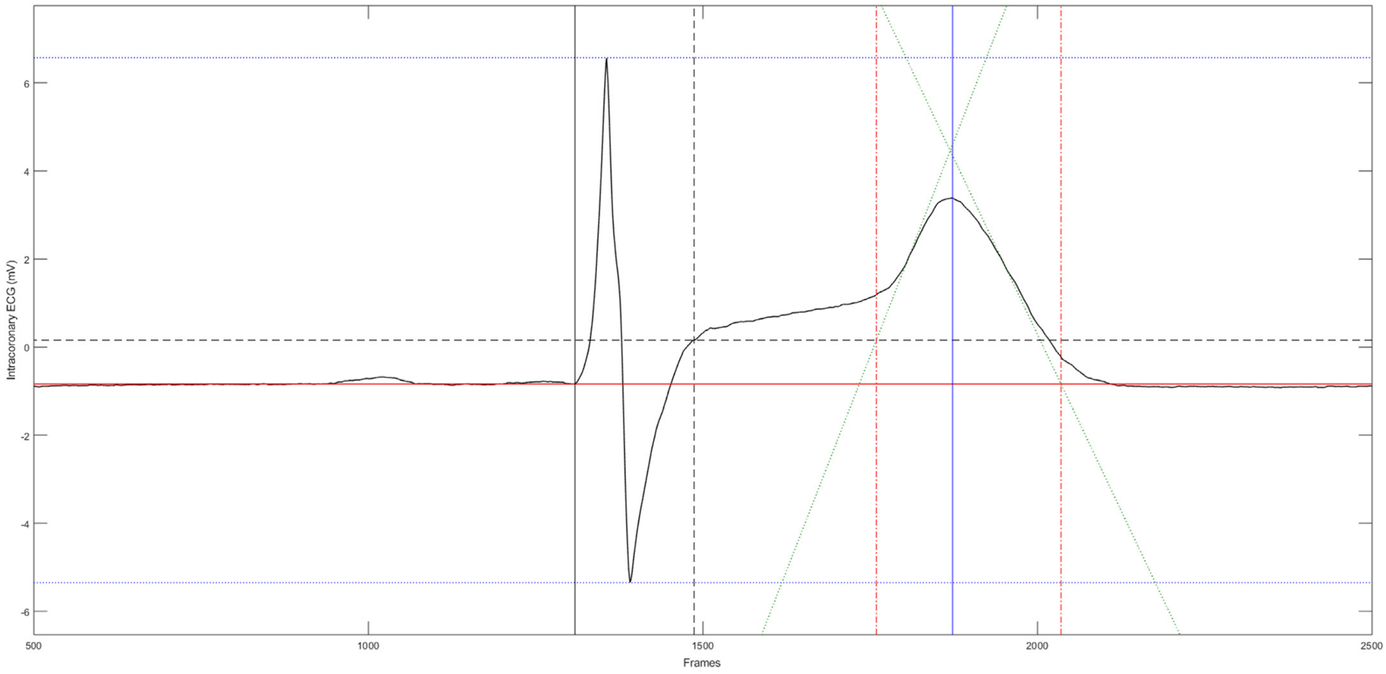

Fig. 1. Assessment of the icECG parameters. Isoelectric line = solid red line; Q-point = solid black line; J-point = dashed black lines; tangents for the determination of start and end of the T-wave = dotted green lines; start and end of the T-wave = dashed/dotted red lines; T-peak = solid blue line; R- and S-peak = dotted blue lines. (For interpretation of the references to colour in this figure legend, the reader is referred to the web version of this article.)

performed using SPSS version 25 (IBM Statistics, Armonk, New York) or MedCalc for Windows, version 19.1 (MedCalc Software, Ostend, Belgium).

Results

Two hundred icECGs from 100 patients were included in the study. From each patient, a non-ischemic as well as an ischemic icECG were analysed. Left anterior descending (LAD) artery served twice as often as the study vessel than the other coronary arteries.

Table 1
Patient characteristics.

	Overall
Number of patients	100
Patient characteristics	
Age (years)	68 ± 11
Female gender (%)	22
Body mass index (kg/m^2)	27 ± 4
Angina pectoris before intervention (%)	50
Duration of angina pectoris (months)	11 ± 22
Canadian cardiovascular society class of angina pectoris	1.98 ± 0.92
Diabetes mellitus (%)	25
Arterial hypertension (%)	68
Current smoking (%)	14
Cumulative pack years of cigarettes	42 ± 28
Dyslipidemia (%)	76
Family history for coronary artery disease, CAD (%)	29
Prior myocardial infarction in vessel of interest	10
Medical treatment	
Aspirin (%)	84
Platelet inhibitor (%)	41
Calcium channel-blocker (%)	25
Beta-blocker (%)	49
Nitrate (%)	13
Oral anticoagulation (%)	9
Statin (%)	78
ACE inhibitor or ARB (%)	66
Diuretics (%)	31

Patient characteristics

Patient characteristics are presented on Table 1.

Intra-rater and inter-rater variability

One-way ANOVA factorial analysis did not show significant differences between intra-rater or inter-rater measurements (supplemental Table 1). Determination of the ICC showed the lowest variability for T-peak (intra-rater ICC 0.996, inter-rater ICC 0.994), followed by T-wave integral (intra-rater ICC 0.990, inter-rater ICC 0.987), ST-segment shift (intra-rater ICC 0.987, inter-rater ICC 0.979) and ST-integral (intra-rater ICC 0.953, inter-rater ICC 0.949). The highest variability was observed with time measurements. Classified according to Koo et al. [21], extent of variability was excellent for ST-segment shift, ST-integral, T-wave-integral and T-peak, good for QTc-time and moderate for TPE. Please see Table 2 for a presentation of the variability analysis, Figs. 2 and 3 for graphical illustration of the intra-rater respectively inter-rater variability and supplemental Figs. 1 and 2 for Bland and Altman plots.

Descriptive statistics

Descriptive statistics are presented on Table 3 and on Fig. 4, grouped according to the non-ischemic vs. ischemic state. Overall, all six icECG parameters showed significant differences between the groups, while TPE was not different on a per vessel basis in the LAD, and in the right coronary artery (RCA, Table 3). There was a significant gender-difference in all parameters except for QTc-time during ischemia (Table 4). Of note, because of the inclusion of seventy-seven patients from a pharmacological stress study with intravenous administration of dobutamine and atropine before CFI measurement, heart rate in the absence of ischemia was significantly lower than during ischemia.

Table 2
Intraclass correlation coefficient and Bland and Altman analysis for intra-rater and inter-rater variability.

	Intraclass correlation coefficients		Bland and Altman				
	ICC coefficient	95%CI	$\text{Mean}_{\text{Diff}}$	SE of $\text{Mean}_{\text{Diff}}$	95% CI for $\text{Mean}_{\text{Diff}}$	SD_{Diff}	95% limits of agreement
ST-segment shift at J-point (mV)							
Intra-rater analysis	0.987	0.985–0.989	0.0067	0.0065	−0.006-0.019	0.1580	−0.303-0.316
Inter-rater analysis	0.978	0.971–0.983	−0.0446	0.0082	−0.061- -0.029	0.2013	−0.439-0.350
ST-segment integral (mV*sec)							
Intra-rater analysis	0.953	0.945–0.960	0.0013	0.0012	−0.001-0.004	0.0283	−0.054-0.057
Inter-rater analysis	0.949	0.936–0.960	−0.0021	0.0012	−0.004-0.000	0.0291	−0.059-0.055
T-wave integral (mV*sec)							
Intra-rater analysis	0.990	0.989–0.992	−0.0006	0.0012	−0.003-0.002	0.0304	−0.060-0.059
Inter-rater analysis	0.987	0.983–0.990	0.0045	0.0014	0.002–0.007	0.0354	−0.065-0.074
T-peak (mV)							
Intra-rater analysis	0.996	0.996–0.997	0.0058	0.0065	−0.007-0.019	0.1597	−0.307-0.319
Inter-rater analysis	0.994	0.993–0.995	0.0050	0.0084	−0.011-0.022	0.2061	−0.399-0.409
T-peak to end-time (msec)							
Intra-rater analysis	0.760	0.724–0.792	−0.2290	0.6735	−1.549-1.091	16.4974	−32.56-32.11
Inter-rater analysis	0.674	0.610–0.733	−1.4881	0.7871	−3.031-0.055	19.2800	−39.28-36.30
QTc-time (msec)							
Intra-rater analysis	0.792	0.760–0.820	−0.6521	1.0199	−2.651-1.347	24.9821	−49.62-48.31
Inter-rater analysis	0.802	0.756–0.842	−4.2105	0.9516	−6.076- -2.345	23.3094	−49.90-41.48

Receiver-operating characteristic curves

Using the time point of icECG recording as allocation reference for absent or present myocardial ischemia, ROC-analysis of icECG ST-segment shift showed an area under the curve (AUC) of 0.963 ± 0.029 ($p < 0.0001$). There was no statistically significant difference between the assessment of the ST-segment shift at vs after the J-point ($p = 0.951$, $p = 0.578$, $p = 0.226$ for 40, 60 and 80 ms after the J-point respectively). AUC for ST-integral was 0.899 ± 0.044 ($p < 0.0001$), for T-wave integral 0.791 ± 0.059 ($p < 0.0001$), for T-peak amplitude 0.811 ± 0.057 ($p < 0.0001$), for TPE 0.667 ± 0.068 ($p < 0.0001$), and for QTc-time 0.770 ± 0.061 ($p < 0.0001$, Fig. 5).

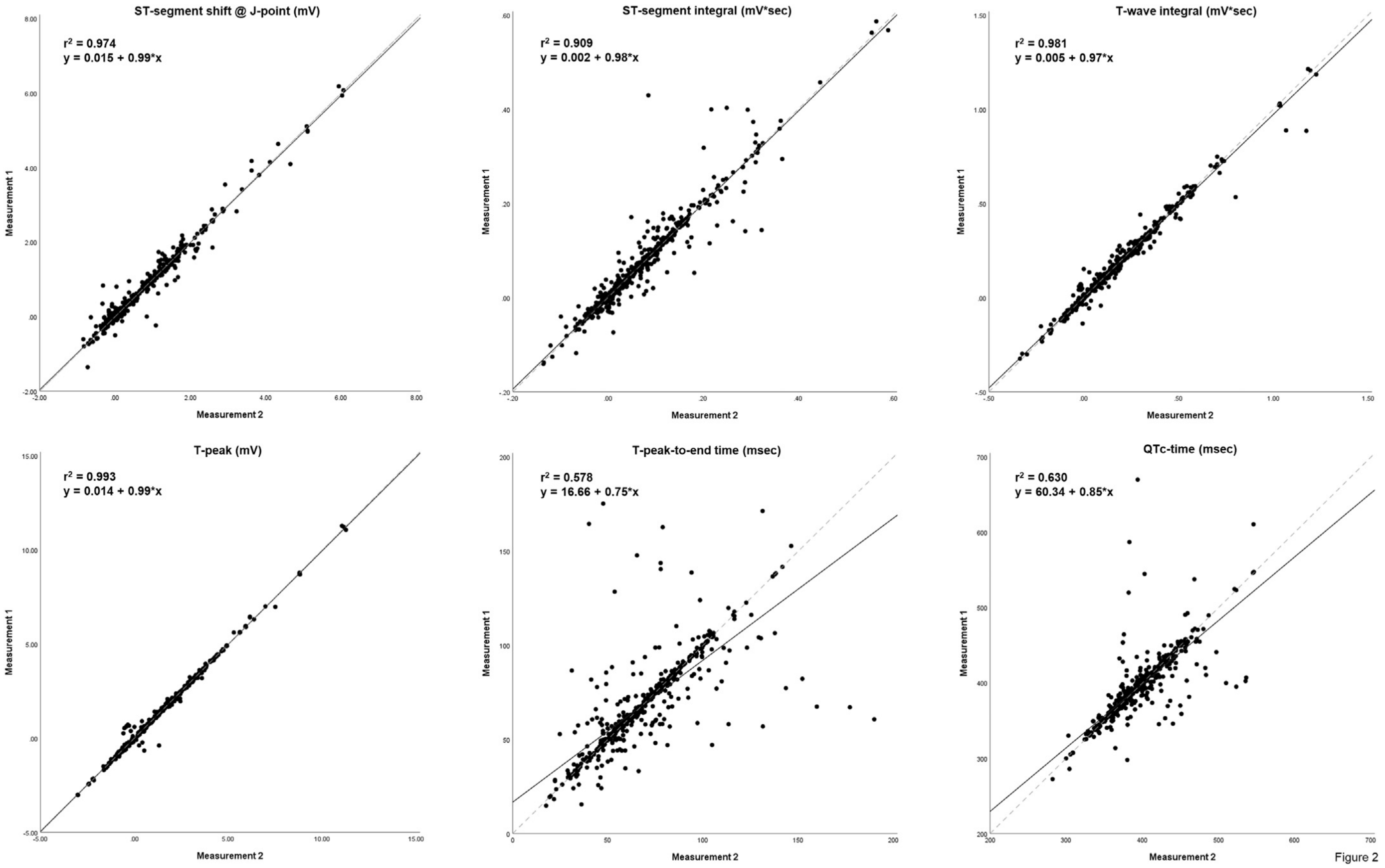

Fig. 2. Linear regression between test and retest measurements. Solid black lines = regression lines; dashed grey lines = reference lines, i.e. y = x.

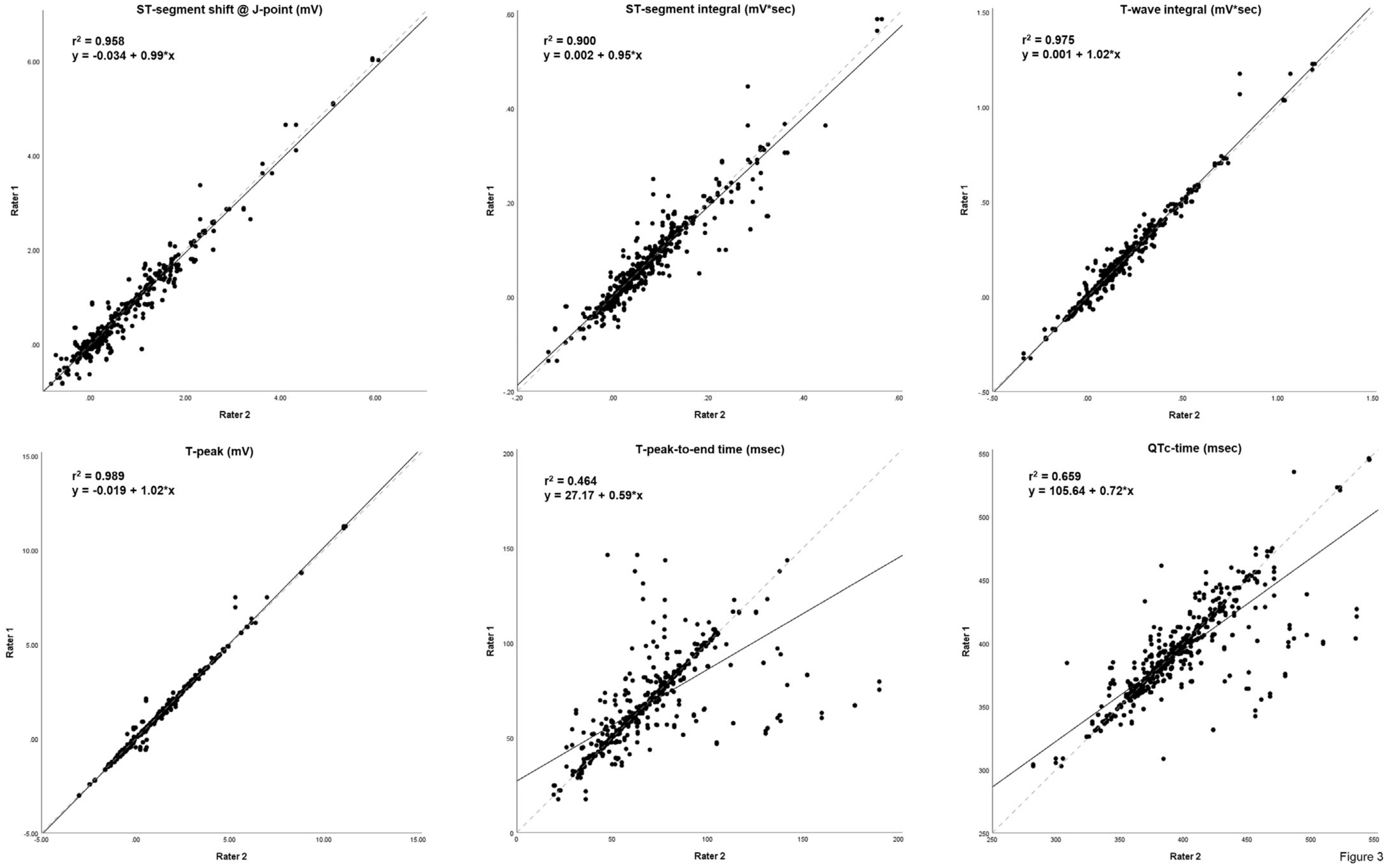

Fig. 3. Linear regression between the raters. The second performance of individual measurements were used for the illustration with the pairing MB-PZ, MB-AP and PZ-AP, resulting in $n = 600$. Solid black lines = regression lines; dashed grey lines = reference lines, i.e. y = x.

DeLong-Test of the ROC-curves showed a significant difference of AUC for ST-segment shift in comparison to all other parameters ($p \le 0.0001$), as well as a significant difference for ST-integral as compared to the remaining parameters ($p \le 0.0009$). T-wave integral and T-peak showed a significant difference between each other ($p = 0.029$) as well as vs TPE ($p \le 0.0008$ and $p \le 0.0005$, respectively), but not vs QTc-time ($p = 0.641$, respectively $p = 0.352$). There was no significant difference between the AUCs of the time measurements ($p = 0.076$).

Regarding the optimum cut-off of the parameters for ischemia detection, a ST-segment shift of 0.365 mV distinguished best between non-ischemic and ischemic ECG, sensitivity 90%, specificity 95%. The best cut-off point for ST-integral was 0.061 mV**sec* (sensitivity 77%, specificity 88%), for T-integral 0.242 mV*sec (sensitivity 53%, specificity 91%), for T-peak 1.834 mV (sensitivity 62%, specificity 87%), for TPE 60 msec (sensitivity 76%, specificity 57%) and for QTc-time 396 msec (sensitivity 84%, specificity 63%). Of note, all parameters but QTc-time increased during ischemia. Thus, the optimum cut-off point for QTc-time is inverse (i.e., ischemia below 396 msec).

Discussion

When tested in an experimental setting with systematically induced, complete coronary balloon occlusion, and thus, absolute myocardial ischemia, non-ischemic and ischemic icECG is distinguishable most accurately by icECG ST-segment shift at an ischemia threshold of 0.365 mV. Conversely, icECG time measurements are significantly less accurate for ischemia detection.

IcECG ST-segment shift

One hundred years ago, ST-segment shift as an ECG pattern during acute myocardial infarction was first described by Harold Pardee [22]. Since then, ECG ST-segment shift assessment in suspected acute coronary syndrome has become crucial for the subsequent management, and the extent of ST-segment shift (number of leads, amplitude of the shift) reflects the size of myocardial ischemia, and as such, cardiovascular outcome [23]. However as stated by Menown et al. [24], “the definition of significant ST-elevation varies considerably with respect to both the required minimum height of ST-elevation, and the number of leads with ST-elevation”. In the same study, myocardial ischemia has been defined as an ECG ST-segment shift of >0.1 mV in inferior/lateral leads, or > 0.2 mV in anteroseptal leads [24]. ECG ST-segment shift is strongly affected by age [25], gender [26] and ethnicity [27], and is highly variable even in healthy individuals without myocardial ischemia [27,28]. In the latter, elevated J-points reflect earlier onset of repolarization, which is an expression of variations in the ion channels across the myocardium [29]. This affects more often men than women, since testosterone is thought to be the common mechanism accounting for this phenomenon [30]. Additionally, the amplitude of ST-segment shift in the surface ECG is directly affected by lead positioning, habitus and even by the posture of the patient as stated by Birnbaum and Alam [28].

Conversely, icECG is located directly on the epicardium and thus, less affected by noise signals. Furthermore, its configuration with a pseudo-unipolar lead between Wilson Central Point and the pressure sensor ensures site specificity, which cannot be achieved by the 12-lead surface ECG. Consequently in our study, icECG ST-segment shift demonstrated

Table 3
Study parameters.

	Non-ischemic	Ischemic	*p*-value
Overall, n	100	100	–
ST-segment shift at J-point (mV)	−0.011 ± 0.270	1.272 ± 0.998	$p < 0.001$
ST-segment integral (mV*sec)	0.013 ± 0.047	0.124 ± 0.093	p < 0.001
T-wave integral (mV*sec)	0.060 ± 0.133	0.273 ± 0.232	p < 0.001
T-peak (mV)	0.493 ± 1.291	2.420 ± 1.929	p < 0.001
T-peak to end-time (msec)	63.64 ± 25.79	73.95 ± 19.86	p < 0.001
Heart rate	71 ± 13	95 ± 25	p < 0.001
QTc-time (msec)[a]	409.73 ± 39.66	377.74 ± 26.62	p < 0.001
Left anterior descending artery, n	50	50	–
ST-segment shift at J-point (mV)	0.006 ± 0.236	1.169 ± 0.692	p < 0.001
ST-segment integral (mV*sec)	0.037 ± 0.033	0.111 ± 0.062	p < 0.001
T-wave integral (mV*sec)	0.129 ± 0.105	0.316 ± 0.156	p < 0.001
T-peak (mV)	1.074 ± 1.004	2.802 ± 1.117	p < 0.001
T-peak to end-time (msec)	69.80 ± 31.28	77.22 ± 16.59	$p = 0.099$
Heart rate	72 ± 14	104 ± 22	p < 0.001
QTc-time (msec)[a]	407.73 ± 35.17	371.86 ± 19.76	p < 0.001
Left circumflex artery, n	25	25	–
ST-segment shift at J-point (mV)	0.041 ± 0.324	2.120 ± 1.278	p < 0.001
ST-segment integral (mV*sec)	−0.001 ± 0.056	0.205 ± 0.117	p < 0.001
T-wave integral (mV*sec)	0.053 ± 0.128	0.367 ± 0.314	p < 0.001
T-peak (mV)	0.575 ± 1.372	3.287 ± 2.689	p < 0.001
T-peak to end-time (msec)	55.79 ± 11.86	71.00 ± 18.90	p < 0.001
Heart rate	69 ± 12	92 ± 20	p < 0.001
QTc-time (msec)[a]	416.80 ± 35.42	382.80 ± 22.03	p < 0.001
Right coronary artery, n	25	25	–
ST-segment shift at J-point (mV)	−0.099 ± 0.244	0.630 ± 0.542	p < 0.001
ST-segment integral (mV*sec)	−0.021 ± 0.030	0.069 ± 0.062	p < 0.001
T-wave integral (mV*sec)	−0.073 ± 0.078	0.094 ± 0.165	p < 0.001
T-peak (mV)	−0.751 ± 0.781	0.790 ± 1.314	p < 0.001
T-peak to end-time (msec)	59.16 ± 20.99	70.35 ± 25.75	$p = 0.065$
Heart rate	70 ± 13	83 ± 28	$p = 0.030$
QTc-time (msec)[a]	406.66 ± 51.38	384.45 ± 38.67	$p = 0.041$

[a] QTc-time = QT-time corrected according to the Framingham method

a narrow distribution around zero in the non-ischemic state, and a distinctive increase during myocardial ischemia (Fig. 4). Also, the present study protocol with systematically controlled for proximal balloon occlusion, identical ischemia duration, and for exclusion of patients with sufficient collateral supply provides ideal, but clinically realistic conditions for the comprehensive analysis of electrocardiographic behavior during ischemia. Hence, icECG should serve as reference for ischemia threshold determination, followed by adjustment for the 6-fold lower signal amplitude in the surface ECG (unpublished data, comparison between icECG recordings in the LAD and lead V_3 and V_6). Thus, taken into account the optimal icECG ST-segment ischemia detection threshold of 0.365 mV measured at the J-point, the optimal cut-off point using the surface ECG should be around 0.06 mV. Interestingly, this corresponds well with the recommendation in isolated posterior myocardial infarction (≥0.05 mV in posterior chest wall leads V_7-V_9) [1], and is quite close to the abovementioned 0.1 mV registered in inferior leads.

Less accurate icECG ischemia parameters

Concerning the other parameters, icECG ST-integral as alternative measure of the same pathophysiologic process as icECG ST-segment shift performed second best (Fig. 5). The application of this parameter as a measure of myocardial ischemia has been known for decades, and has been explored for the improvement of coronary artery disease diagnosis during exercise test [31,32]. In addition, assessment of ST- and T-wave integral (ST-T-integral) as well as T-wave amplitude with body surface potential mapping has been shown as sensitive and specific markers of transient myocardial ischemia [32]. However, despite the use of the more sensitive icECG [2,3], the present study could not reproduce these findings and showed substantially less accuracy of all these parameters when compared to ST-segment shift. Also, ischemia parameters were significantly less pronounced in women than in men (Table 4). A possible explanation for this finding is the variable myocardial mass being 25% to 38% bigger in men than in women [33], thus, generating a larger-amplitude ischemic signal.

Concerning time measurements on icECG, they provide less accurate and less reliable results than the other parameters. Interestingly, both TPE and QTc-time haven been shown clinically useful in estimating arrhythmic risk [5], while their behavior during myocardial ischemia remains ambiguous. It has been shown, that TPE as an index for transmural dispersion of repolarization [5] (T-peak marks the end of epicardial repolarization while the end of the T-wave marks the end of repolarization for the entire myocardium [7]) decreases by 14 msec after successful percutaneous treatment in patients with ST-elevation myocardial infarction [7]. This finding could be indirectly confirmed in the present study, in which a prolongation of icECG TPE of 10 msec during ischemia was documented. The slight difference may be due to the shorter ischemia time in our study. IcECG TPE showed the lowest

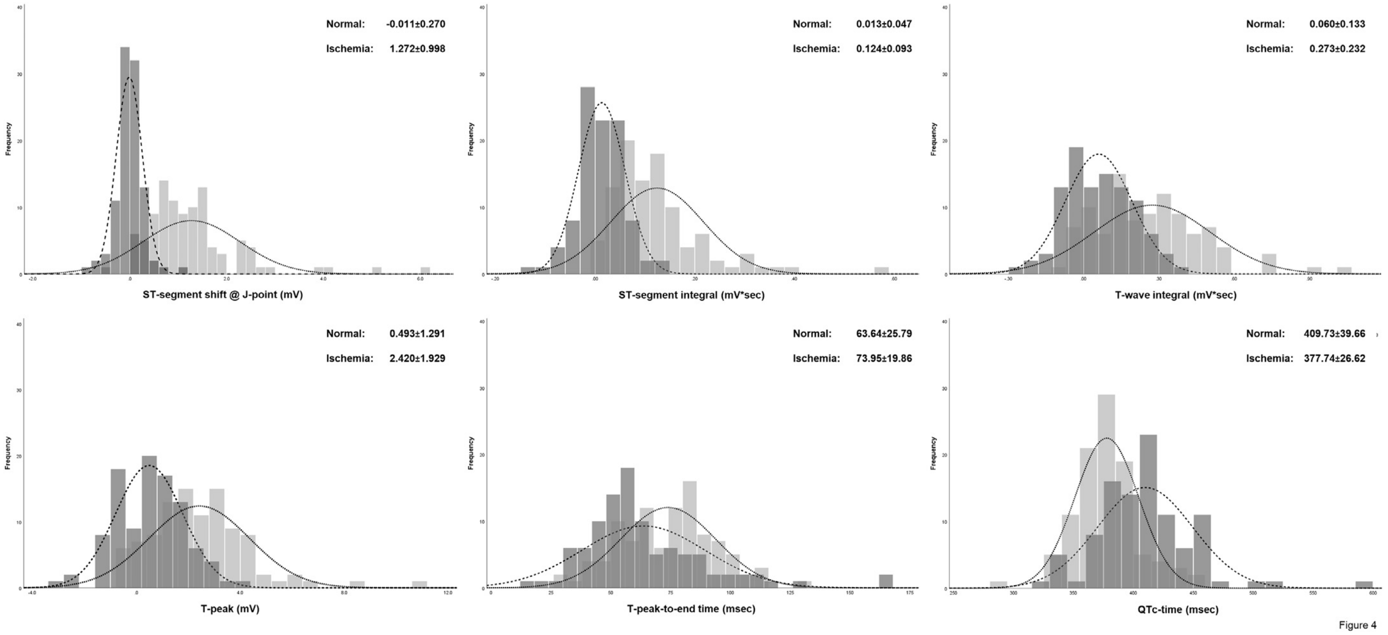

Fig. 4. Frequency distribution of the icECG parameters grouped by the physiologic state. Dark-grey: distribution of the non-ischemic group, light-grey: distribution of the ischemic group. All values are mean ± standard deviation.

Table 4
Study parameters according to gender.

	Non-ischemic			Ischemic		
	Male	Female	p-value	Male	Female	p-value
Overall, n	78	22	–	78	22	–
ST-segment shift at J-point (mV)	−0.015 ± 0.298	0.000 ± 0.133	$p = 0.732$	1.358 ± 0.110	0.967 ± 0.383	$p = 0.010$
ST-segment integral (mV*sec)	0.014 ± 0.050	0.012 ± 0.033	$p = 0.901$	0.135 ± 0.101	0.086 ± 0.037	$p = 0.001$
T-wave integral (mV*sec)	0.057 ± 0.141	0.068 ± 0.103	$p = 0.705$	0.294 ± 0.249	0.199 ± 0.138	$p = 0.022$
T-peak (mV)	0.455 ± 1.376	0.627 ± 0.941	$p = 0.503$	2.628 ± 2.072	1.682 ± 1.034	$p = 0.004$
T-peak to end-time (msec)	63.33 ± 26.04	64.73 ± 25.43	$p = 0.824$	71.56 ± 18.77	82.41 ± 21.70	$p = 0.023$
Heart rate	70 ± 13	76 ± 14	$p = 0.062$	94 ± 24	102 ± 26	$p = 0.178$
QTc-time (msec)[a]	407.80 ± 39.99	416.59 ± 38.57	$p = 0.361$	376.39 ± 27.69	382.54 ± 22.31	$p = 0.341$

[a] QTc-time = QT-time corrected according to the Framingham method

accuracy for ischemia detection in our study, and in the LAD and RCA even failed to be statistically different during ischemia as compared to the non-ischemic state (Table 3).

The effect of temporary acute ischemia on the QTc-time has been widely evaluated with ambiguous results. Meier et al. measured QTc-time from surface ECG leads II, aVL and aVF in 150 patients during a one-minute coronary balloon occlusion and showed a significant increase during occlusion of the LAD and the left circumflex artery (LCX), but not in the RCA [18]. These findings are in line with other measurements of QT-interval from surface ECG during balloon angioplasty [34,35]. On the other hand, QTc-interval during ischemia assessed by icECG quite consistently revealed a shortening [6,36] within the range of our results. In the present study, both, QTc-time as well as uncorrected QT-time decreased significantly during ischemia.

Because of the consistent difference between icECG and surface ECG, a systematic difference responsible for the diverging findings is most likely. Possibly, the higher sensitivity of the icECG associated with more frequent recording of ischemia induced U-waves than in the

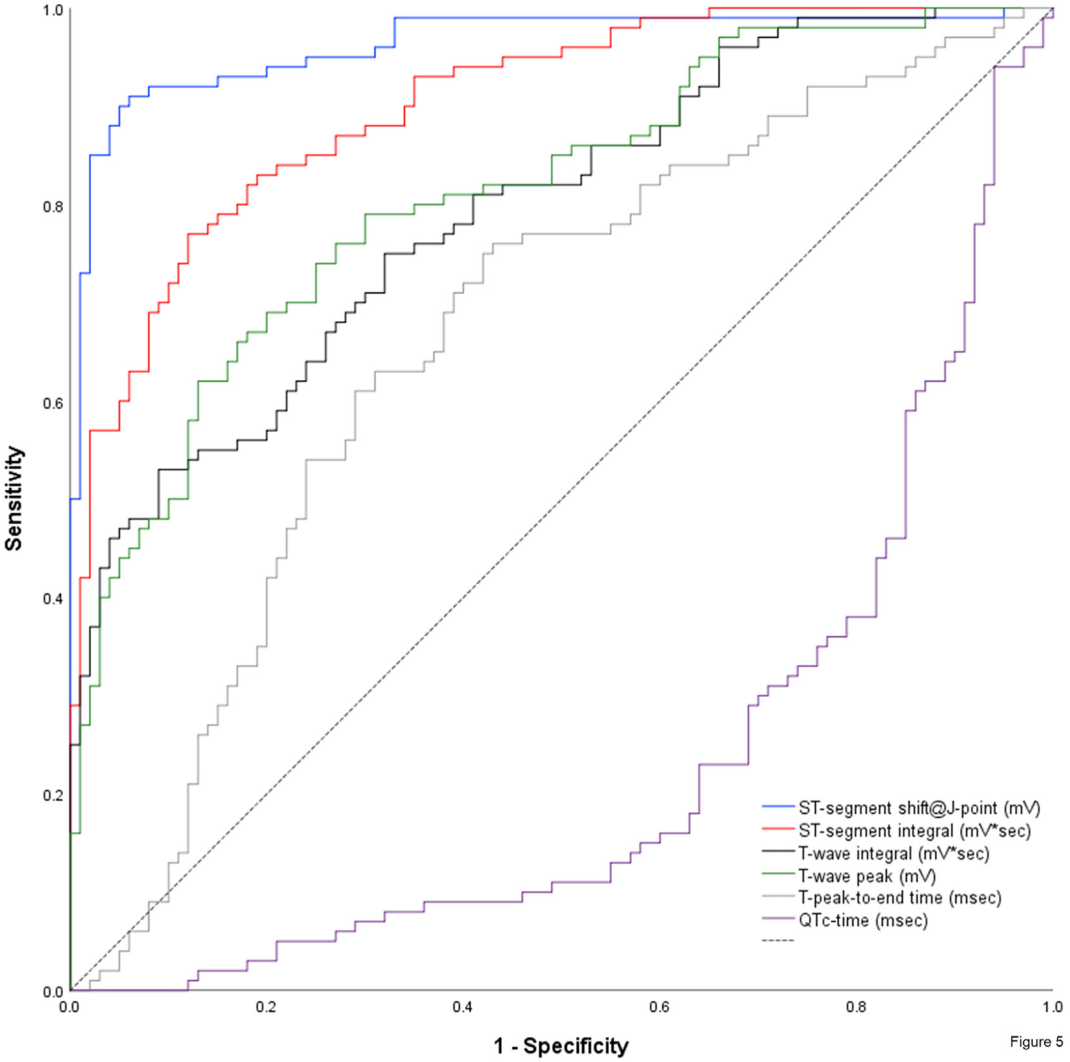

Fig. 5. Nonparametric receiver-operating characteristic curve of the icECG parameters using the time point of icECG recording as reference. Of note, all parameters but QTc-time increased during ischemia. Thus, QTc-time is below the reference line (dashed black line).

surface ECG is liable for the difference [37]. Thus, considering the recommended measurement at the nadir between T- and U-wave [38], QT-time will be systematically shorter in the presence versus the absence of an U-wave. However, since the U-wave as well as the behavior of the QT-interval in the surface ECG were not analysed in this study, the above explanation remains untested. Consequently, further prospective studies with simultaneous recording of icECG and surface ECG would be required to elucidate the actual behavior of the QT-interval during acute ischemia.

Study limitations

The present study results were obtained in a selected population (no arrhythmia or bundle branch blocks) of the same ethnicity, and may be not generally representative. Furthermore, the low percentage of female patients did not allow a separate ROC-analysis for calculation of gender-specific ischemia threshold values of icECG ST-segment shifts.

In addition, retrospective inclusion of seventy-seven patients from a pharmacological stress study with higher heart rate at the time of ischemia directly affected the time-measurements (i.e. TPE and QTc-time) as well as time integrals. However, first, QT-interval was corrected for heart rate and second, a posthoc-analysis of the remaining twenty-three patients revealed similar results.

Clinical implication

Quantitative assessment of myocardial ischemia by icECG should be performed by measuring ST-segment shift at the J-point. An ST-segment shift of 0.365 mV distinguished best between non-ischemic and transmural ischemic myocardium. Thus, cut-off values commonly used in the surface ECG (i.e. 0.1–0.2 mV) are not applicable in the icECG.

Conclusion

When tested in a setting with artificially induced absolute myocardial ischemia, icECG ST-segment shift at a threshold of 0.365 mV most accurately distinguishes between absent and present ischemia.

Supplementary data to this article can be found online at https://doi.org/10.1016/j.jelectrocard.2020.11.018.

Funding

None

Disclosures

None

Author statement

MRB: conception and design, data analysis, interpretation, visualization, drafting and revising of the manuscript; PZ and AP: data analysis and interpretation, revising of the manuscript; CS: data interpretation, drafting and revising of the manuscript.

References

[1] Ibanez B, et al. 2017 ESC Guidelines for the management of acute myocardial infarction in patients presenting with ST-segment elevation: The Task Force for the management of acute myocardial infarction in patients presenting with ST-segment elevation of the European Society of Cardiology (ESC). Eur Heart J. 2018;39:119–77.

[2] Friedman PL, et al. Value of the intracoronary electrocardiogram to monitor myocardial ischemia during percutaneous transluminal coronary angioplasty. Circulation. 1986;74:330–9.

[3] Pande AK, et al. Intracoronary electrocardiogram during coronary angioplasty. Am Heart J. 1992;124:337–41.

[4] Bigler MR, Seiler C. The human coronary collateral circulation, its Extracardiac anastomoses and their therapeutic promotion. Int J Mol Sci. 2019;20.

[5] Yan GX, et al. Ventricular repolarization components on the electrocardiogram: cellular basis and clinical significance. J Am Coll Cardiol. 2003;42:401–9.

[6] Safi AM, et al. Use of intracoronary electrocardiography for detecting ST-T, QTc, and U wave changes during coronary balloon angioplasty. Heart Dis. 2001;3:73–6.

[7] Elitok A, et al. The relationship between T-wave peak-to end interval and ST segment recovery on intracoronary ECG during primary PCI. Eur Rev Med Pharmacol Sci. 2015;19:1086–91.

[8] Eslami V, et al. Evaluation of QT, QT dispersion, and T-wave peak to end time changes after primary percutaneous coronary intervention in patients presenting with acute ST-elevation myocardial infarction. J Invasive Cardiol. 2013;25:232–4.

[9] Meier B, Rutishauser W. Coronary pacing during percutaneous transluminal coronary angioplasty. Circulation. 1985;71:557–61.

[10] Rezaian GR, et al. Earliest time of change in QT dispersion after stenting in patients with single vessel coronary artery disease. Int J Angiol. 2007;16:50–2.

[11] Bigler MR, et al. Effect of permanent right internal mammary artery occlusion on right coronary artery supply: a randomized placebo-controlled clinical trial. Am Heart J. 2020;230:1–12.

[12] Bigler MR, et al. Functional assessment of myocardial ischemia by intracoronary electrocardiogram. under review.

[13] Vogel R, et al. Collateral-flow measurements in humans by myocardial contrast echocardiography: validation of coronary pressure-derived collateral-flow assessment. Eur Heart J. 2006;27:157–65.

[14] Seiler C, et al. Coronary collateral quantitation in patients with coronary artery disease using intravascular flow velocity or pressure measurements. J Am Coll Cardiol. 1998;32:1272–9.

[15] de Marchi SF, et al. Determinants of prognostically relevant intracoronary electrocardiogram ST-segment shift during coronary balloon occlusion. Am J Cardiol. 2012; 110:1234–9.

[16] Kashou AH, et al. ST segment *StatPearls* Treasure Island (FL): StatPearls Publishing, Copyright © 2020. StatPearls Publishing LLC; 2020.

[17] Sagie A, et al. An improved method for adjusting the QT interval for heart rate (the Framingham Heart Study). Am J Cardiol. 1992;70:797–801.

[18] Meier P, et al. An indicator of sudden cardiac death during brief coronary occlusion: electrocardiogram QT time and the role of collaterals. Eur Heart J. 2010;31:1197–204.

[19] Bland JM, Altman DG. Statistical methods for assessing agreement between two methods of clinical measurement. Lancet. 1986;1:307–10.

[20] Rankin G, Stokes M. Reliability of assessment tools in rehabilitation: an illustration of appropriate statistical analyses. Clin Rehabil. 1998;12:187–99.

[21] Koo TK, Li MY. A guideline of selecting and reporting intraclass correlation coefficients for reliability research. J Chiropr Med. 2016;15:155–63.

[22] Pardee HEB. An electrocardiographic sign of coronary artery obstruction. Arch Intern Med. 1920;26:244–57.

[23] Antman EM, et al. ACC/AHA guidelines for the management of patients with ST-elevation myocardial infarction–executive summary: a report of the American College of Cardiology/American Heart Association Task Force on Practice Guidelines (Writing Committee to Revise the 1999 Guidelines for the Management of Patients With Acute Myocardial Infarction). Circulation. 2004;110:588–636.

[24] Menown IB, et al. Optimizing the initial 12-lead electrocardiographic diagnosis of acute myocardial infarction. Eur Heart J. 2000;21:275–83.

[25] Macfarlane PW. Age, sex, and the ST amplitude in health and disease. J Electrocardiol. 2001;34(Suppl):235–41.

[26] Dellborg M, et al. ECG changes during myocardial ischemia. Differences between men and women. J Electrocardiol. 1994;27(Suppl):42–5.

[27] Ter Haar CC, et al. Prevalence of ECGs exceeding thresholds for ST-segment-elevation myocardial infarction in apparently healthy individuals: the role of ethnicity. J Am Heart Assoc. 2020;9:e015477.

[28] Birnbaum Y, Alam M. LVH and the diagnosis of STEMI - how should we apply the current guidelines? J Electrocardiol. 2014;47:655–60.

[29] Reddy VK, et al. Ethnic differences in ST height in the multiethnic study of atherosclerosis. Ann Noninvasive Electrocardiol. 2008;13:341–51.

[30] Rautaharju PM, et al. Race- and sex-associated differences in rate-adjusted QT, QTpeak, ST elevation and other regional measures of repolarization: the Atherosclerosis Risk in Communities (ARIC) Study. J Electrocardiol. 2014;47:342–50.

[31] Okin PM, et al. Heart rate adjustment of the time-voltage ST segment integral: identification of coronary disease and relation to standard and heart rate-adjusted ST segment depression criteria. J Am Coll Cardiol. 1991;18:1487–92.

[32] Hänninen H, et al. ST-T integral and T-wave amplitude in detection of exercise-induced myocardial ischemia evaluated with body surface potential mapping. J Electrocardiol. 2003;36:89–98.

[33] de Simone G, et al. Gender differences in left ventricular growth. Hypertension. 1995;26:979–83.

[34] Kenigsberg DN, et al. Prolongation of the QTc interval is seen uniformly during early transmural ischemia. J Am Coll Cardiol. 2007;49:1299–305.

[35] Nowinski K, et al. Changes in ventricular repolarization during percutaneous transluminal coronary angioplasty in humans assessed by QT interval, QT dispersion and T vector loop morphology. J Intern Med. 2000;248:126–36.

[36] Maeda T, et al. QT interval shortening and ST elevation in intracoronary ECG during PTCA. Clin Cardiol. 1992;15:525–8.

[37] Kataoka H, et al. How epicardial U-wave changes are reflected in body surface precordial electrocardiograms in anterior or inferoposterior myocardial ischaemia during coronary angioplasty. Heart. 1996;76:397–405.

[38] Lepeschkin E, Surawicz B. The measurement of the Q-T interval of the electrocardiogram. Circulation. 1952;6:378–88.

3.2.1 Supplemental material

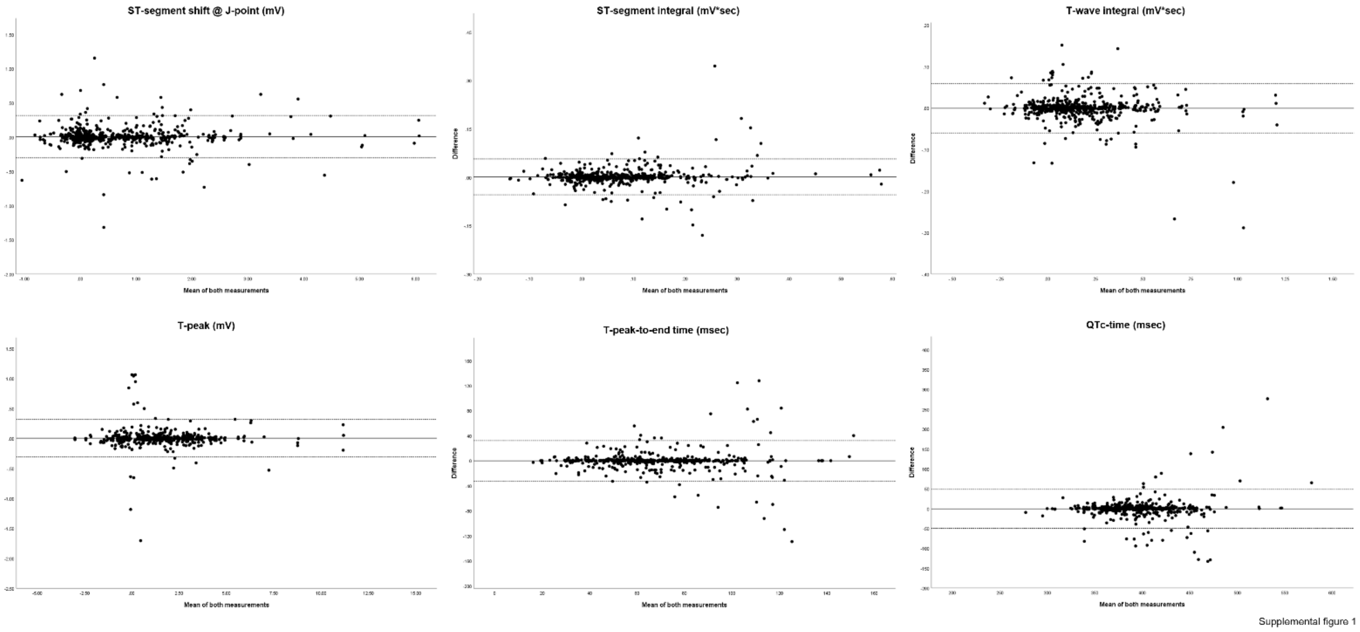

Supplemental figure 1: Bland and Altman plots for intra-rater variability. *Difference = measurement 1 minus measurement 2; Solid black lines = mean difference; dashed grey lines = 95% limits of agreement. Y-axis is scaled 1,5-fold minimum respectively maximum value. Please see table 2 for the detailed Bland and Altman analysis*

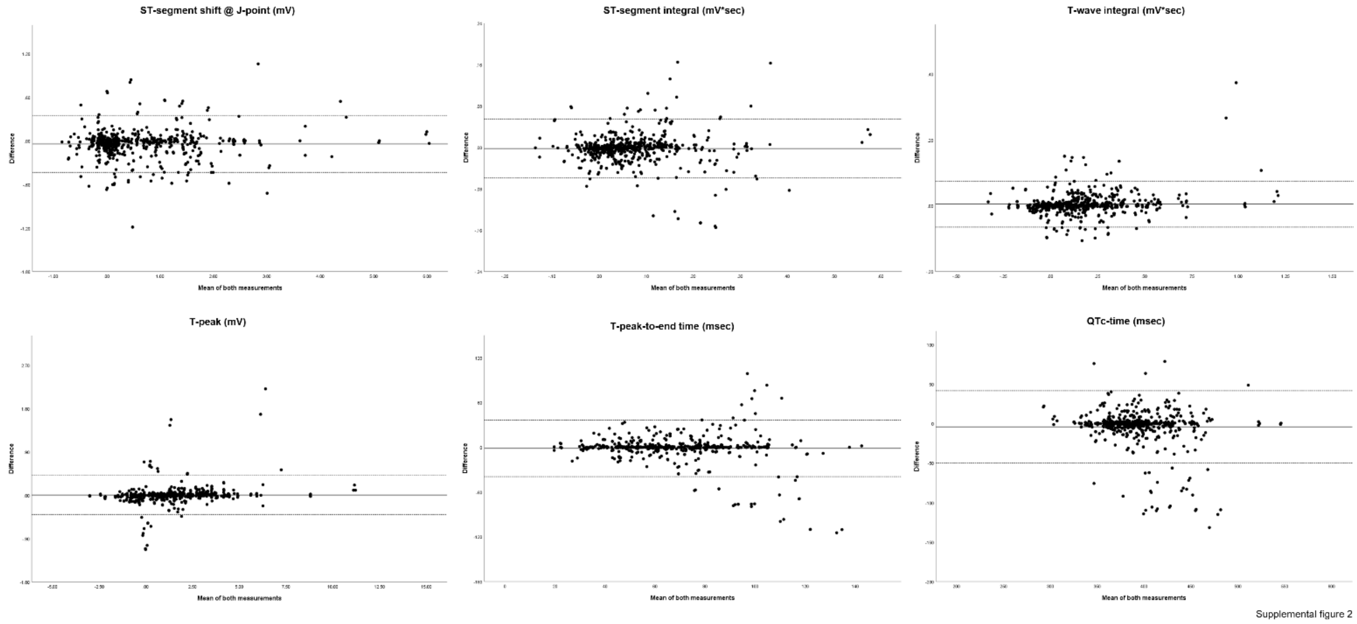

Supplemental figure 2: Bland and Altman plots for inter-rater variability. *Difference = rater 1 minus rater 2 with the following pairing: MB-PZ, MB-AP, PZ-AP; Solid black lines = mean difference; dashed grey lines = 95% limits of agreement. Y-axis is scaled 1,5-fold minimum respectively maximum value. Please see table 2 for the detailed Bland and Altman analysis.*

Supplemental table 1: ANOVA table of results for intra-rater and inter-rater variability

	Intra-rater			**Inter-rater**		
	Degrees of freedom	**Mean Square**	**F-Value**	**Degrees of freedom**	**Mean Square**	**F-Value**
ST-segment shift at J-point (mV)						
Between groups	1	0.014	0.014 p=0.905	2	0.245	0.255 p=0.775
Within groups	1198	0.959		597	0.960	
ST-segment integral (mV*sec)						
Between groups	1	0.001	0.062 p=0.804	2	0.001	0.134 p=0.875
Within groups	1198	0.009		597	0.008	
T-wave integral (mV*sec)						
Between groups	1	0.000	0.002 p=0.965	2	0.003	0.069 p=0.934
Within groups	1198	0.047		597	0.048	
T-peak (mV)						
Between groups	1	0.010	0.003 p=0.958	2	0.006	0.002 p=0.998
Within groups	1198	3.620		597	3.639	
T-peak to end-time (msec)						
Between groups	1	15.73	0.028 p=0.868	2	630.39	1.105 p=0.332
Within groups	1198	566.90		597	570.64	
QTc-time (msec)						
Between groups	1	127.56	0.085 p=0.771	2	2403.09	1.714 p=0.181
Within groups	1198	1500.21		597	1402.42	

3.3 Project III

Detection of Myocardial Ischemia by Intracoronary ECG Using Convolutional Neural Networks

The third project aimed at determining the optimal icECG ischemic parameter using a deep learning approach. In comparison to the second project, where different icECG parameters were selected based on a literature search and analyzed in a setting with artificially induced absolute myocardial, this project used the same (extended) data to train convolutional neural networks (CNN) to differentiate between non-ischemic and ischemic 2D-images of icECG as good as possible. In a second step, visualization of the activation patterns of the CNN were used to detect the morphology responsible for the network prediction. These activation patterns were evaluated with regard to pathophysiologic plausibility.

My contributions were the conception and design of this retrospective study as well as data analysis and interpretation, writing the first draft with production of all figures and revision of the manuscript.

The results of this project have been accepted for publication in *PLOS ONE* in May 2021. In the year of publication, *PLOS ONE* had an impact factor of 3.04 and was ranked Q1 according to SCImago Journal Rank in the subject area “Multidisciplinary”.

For a better understanding of the used methodology, the project starts with a brief introduction to deep learning and CNN with an explanation of the most important terms and the general principles. However, in depth explanation of deep learning is beyond the scope of this thesis[105].

3.3.1 Preamble: Convolutional neural networks

Machine learning and deep learning

Machine learning is a field of expertise in computational sciences, where applied statistics are used to estimate complex functions assumed behind data patterns. The algorithm tries to find natural patterns in the data without relying on a predetermined model. Machine learning is used to solve problems in a wide variety of applications such as classification (e.g., object/face recognition), regression (e.g., temperature development) or transcription (e.g., speech recognition).

Generally, machine learning uses two types of learn mechanisms: supervised and unsupervised learning. The first involves observing numerous examples of data X (e.g., images) and associating it with data Y (e.g., classification labels) to predict Y from X. In other words, supervised learning imitates (“learns”) the pattern of a (training) data set to later apply the gained evidence on a new and uncertain (test) data set to predict the required output. Unsupervised learning observes examples of a data set to find hidden patterns in the distribution without available labels/output classes resulting in the formation of clusters within the data set[105,106].

Deep learning is a subset of machine learning with the basic principle that data are generated by a probability distribution called the data-generating process. For clinical data, pathophysiologic mechanisms are the basis for this probability distribution, e.g., the different distribution of icECG ST-segment shifts before or at the end of a coronary balloon occlusion as shown in figure 4 of Project II. Assuming that the test data to be analyzed share the underlying data-generating distribution, deep learning applies the basics of machine learning to approximate the function of this underlying probability distribution. In this process, deep learning uses a composite of functions called networks[105]. The most common architecture of this central structure in deep learning is a chain of layers (figure IX). In simple terms, assuming a network with three functions f_1, f_2, and f_3, the functions are in succession so that they form $f(x) = f_3(f_2(f_1(x)))$[105]. f_1 is called the first layer of the network, f_2 the second layer and so on. Layers, where the network does not show the output (i.e., layer 1 and 2 in our example) are called hidden layers.

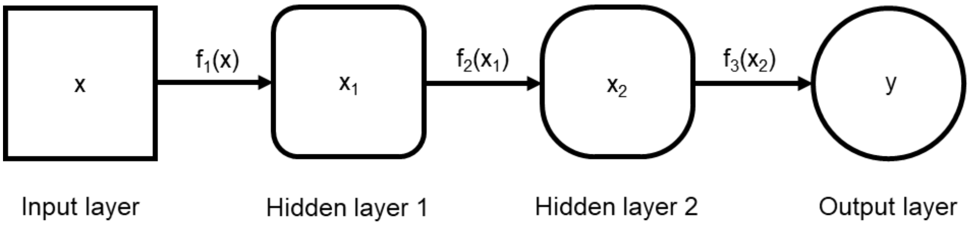

Figure IX: Illustration of a simplified network *with three functions in a chain structure.*

The length of this chain-function defines the depth of the model and is responsible for the term “deep learning”. In addition, these networks are called neural networks because they were inspired by the organization of the animal visual cortex[105]. Similar to the natural model, a neural network adaptively learns spatial hierarchies of features from low (i.e., edges) to high-level patterns[107-109]. In deep learning, each neuron represents a unit that receives an input and computes its own activation value (output).

Feedforward networks are models where the information is processed form the input x through all functions to the output y. There is no feedback mechanism in such models between the layers. Networks with feedback connections are called recurrent neural networks. However, most of the networks used for classification are feedforward networks. Consequently, I will restrict the introduction to these networks.

Operating principle of neural networks

For a brief explanation of the operating principle, it is straightforward to start with a linear model and subsequently provide solutions for its limitation. This linear model is given by y = x*w, where x represents the input data, w the weight of the function and y the known output. During supervised learning, the algorithm adapts the weight of the function until the predicted value y* corresponds to the true value y as good as possible with respect to the squared error (see figure X)[105,106].

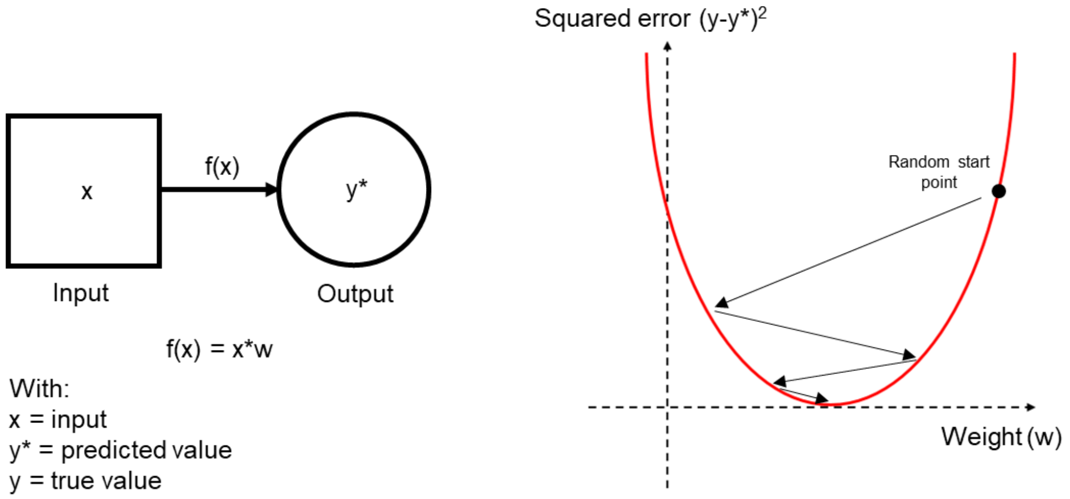

Figure X: Linear network and its corresponding cost function with squared error. *Using squared, rather than direct error causes a weighting of the error (i.e., small error cause less correction than big errors).Note that this cost function is solely for illustrative purposes. Commonly used cost functions are more complicated and have multiple local minima, complicating the search of the optimal configuration (see below).*

This procedure is conducted by a three-tier principle:

1. Prediction
2. Comparison
3. Adaptation

After initialization with random weights, y^* is calculated by the underlying function of the network. In the next step, this prediction is compared with the known output and an error (y-y*) is calculated. According to this error, the weight is adapted, and the procedure starts with a second prediction iteration. This sequence is repeated until the prediction has reached optimality (that is a minimal squared error) or time has run out.

This starter example shows a linear relation between inputs and expected output. However, most of the problems to which neural networks are applied are non-linear. Therefore, multiple functions have to be stacked to achieve a reasonable prediction[106] (figure IX). This concept is explained by the schematic of a heart and its binary representation (figure XI).

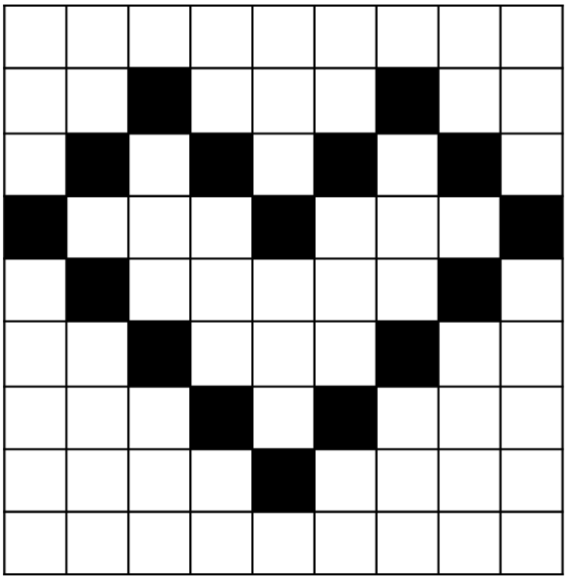

0	0	0	0	0	0	0	0	0
0	0	1	0	0	0	1	0	0
0	1	0	1	0	1	0	1	0
1	0	0	0	1	0	0	0	1
0	1	0	0	0	0	0	1	0
0	0	1	0	0	0	1	0	0
0	0	0	1	0	1	0	0	0
0	0	0	0	1	0	0	0	0
0	0	0	0	0	0	0	0	0

Figure XI: Schematic picture of a heart and its binary representation in a matrix

While it is not possible to recognize the heart by a single pixel, the combination of several pixels form the characteristic structure. Hence, several pixels have to be jointly analyzed for an optimal prediction. This is, however, not possible in a linear network and in general also not with a single function in a single layer and requires more sophisticated structures. In these structures, the prediction of the first layer serves as the input to the second layer, i.e., it produces intermediate measures, serving as inputs to the next layer. Such intermediate layers are denoted as *hidden layers*, since their output is not visible from outside of the neural network. However, in a linear model, every network with two functions ($y=(x*w_1)*w_2$) can be replaced by a simpler function with a combination of the weights (i.e., $y = x*w_{comb;}$ with $w_{comb}.=w_1*w_2$)[106]. Hence, there is no benefit of a deeper structure in this situation. Differently, implementation of non-linear functions, for example functions that are linear for values meeting the condition and return the value “0” otherwise, enable the network to deal with different inputs and increase the efficacy of deeper structures. This characteristic is also called conditional correlation, and the corresponding function is called activation function. The default activation function of most neural networks is the rectified linear unit (ReLU)[110-112], which is linear for x>0 and returns 0 otherwise (figure XII).

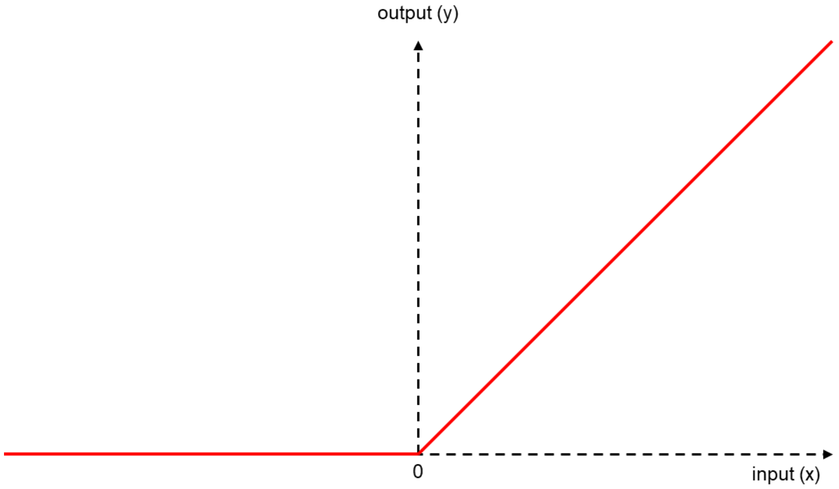

***Figure XII: Illustration of a rectified linear unit**. This activation function is linear for all input values x>0 and 0 for all other input values.*

The last layer of the network serves as the output function. Its purpose is to receive the results of the previous layers and merge them into one prediction. If the network is used for a classification task, the output function produces a probability measure for every class, i.e., a value between 0 and 1. Obviously, the probabilities of all classes should sum up to 1. This is achieved by the application of a so-called softmax function. This function represents the probability distribution over C different classes and is given by the formula:

$$softmax(x_i) = \frac{e^{Inputvalue\ x_i}}{\sum_{j=1}^{C} e^{Inputvalue\ x_j}}$$

The application of this function leads to the result, that the more probable one option is rated, the less probable are all other options (i.e., a form of “the winner takes it-all”[105]). Hence, it enhances the effect of a strong prediction, independent of its correctness. This characteristic will be important for the next steps.

After calculation of the probability measure of each class, the result is compared with the actual value (1 for the correct class, 0 for all others) during supervised learning. The error can be determined by computing the mean squared error over all classes. In practice, however, the error is commonly determined by calculation of the cross entropy loss, i.e., the difference between two probability distributions for a set of events. Cross entropy is derived from the information theory, where lower probability events have more information (as they are rarer), and the term entropy is used for "the number of bits required to transmit a randomly selected event from a probability distribution"[113]. Pursuing this information theory, cross-entropy calculates the number of additional bits to represent an event using the distribution Y (network prediction) instead of P (data generating distribution). Cross entropy loss for multi-label classification is given by the following formula[114]:

$$loss = -\sum_{i=1}^{N}\sum_{j=1}^{C}(P_{i,j} * \ln(Y_{i,j}))$$

$$\begin{aligned} with\text{:}\quad Y_{i,j} &= softmax\ output\ for\ a\ given\ category \\ P_{i,j} &= target\ value\ of\ that\ category \\ C &= total\ number\ of\ categories \\ N &= total\ number\ of\ examples \end{aligned}$$

In short, "that is, the probability that the network associates the ith input with class j."[115]. Application of this negative log-likelihood cost function leads to a strong penalization of the most active incorrect prediction, while correct answers contributes little to the overall training adaptation[105].

This adaptation is performed according to the calculated error and causes a change in every weight of each function, which has contributed to the results. Hence, functional paths which has been set to 0 by the ReLU-function are not updated. The process of weight updating is called backpropagation and is performed by an optimizer algorithm. This algorithm searches the optimal configuration of weights, which produces a minimal error. Hence, from a mathematical point of view, optimizer algorithms search minima in the cost function. One of the simplest algorithms fulfilling this requirement is called gradient descent. This algorithm computes the gradient of the loss function, i.e., its first derivative in respect to the current weight. Then, to find a minimum, the algorithm has to move into the opposite direction of the gradient (see figure XIII).

Figure XIII: Simplified cost function with illustration of the gradient at a randomly chosen point. *On the right side of the minimum, the gradient will be positive, while it is negative on the left side of the minimum. Hence, for the correct adaptation of the weight (on the x-axis), we have to move into the opposite direction of the gradient (e.g., decrease of the weight by a <u>negative value</u> at the current position).*

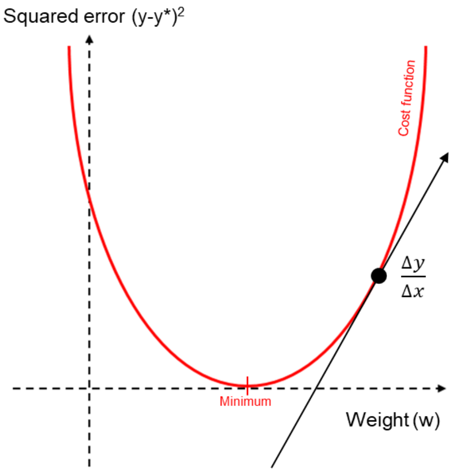

While moving into the opposite direction, it is important to avoid an exaggeration of the correction. For this purpose, optimizer algorithms multiply the intended step with a value between 1 and 0, called the learning rate. Thus, it moves only a fraction of the initially intended step into the right direction and starts with the three-tier principle from this new point. Correct choice of the learning rate is the most crucial factor for a successful learning process.

Algorithms that use the entire data set for one adaptation of the weights are called deterministic gradient methods. However, currently, most of the programmers use a stochastic method where the data set is divided into *n* training sets (called minibatch) and the weights are updated after each minibatch. This method is called stochastic gradient descent (SGD)[116,117]. SGD can be enhanced by applying an additional momentum algorithm[118], which introduces inertia to the SGD by calculating an exponentially decaying moving average of past gradients[119]. In short, SGD with momentum (SGDM) gains speed (=takes bigger steps) when several calculated gradients showed into the same direction. Figure XIV illustrates the advantage of this approach[120].

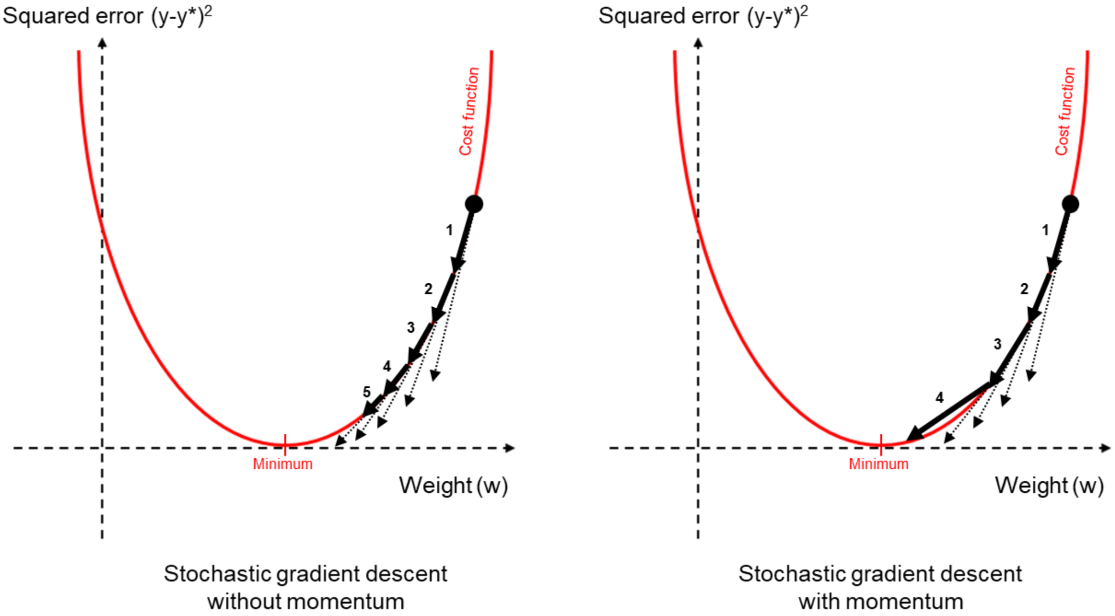

Figure XIV: Illustration of weight adaption with two different optimizer algorithms *Stochastic gradient descent without momentum calculates the gradient at each point and takes a step into the right direction (multiplied by the learning rate to prevent an exaggerated step). On the right side, additional momentum algorithm increases the step size after several steps showed into the same direction resulting into a higher speed.*

The second common optimizer algorithm is an adaptive moment estimation learning rate algorithm, short ADAM[121]. ADAM uses an exponentially decaying average of the past squared gradients to scale the learning rate and in addition a moving average of the gradient (similar to momentum)[105,122]. In this process, ADAM estimates the first and second moments (i.e., the mean and the uncentered variance of the cost function[123]) to adapt the learning rate for each weight of the neural network[122].

In general, ADAM reaches a minimum in fewer steps than SGD[123]. However, both optimizer algorithm perform fairly robust and there is no consensus on the choice of the right optimization algorithm as stated by Goodfellow et al.[105]. Thus, a practical recommendation is to spend more time on the optimal network model (see below), rather than on a more sophisticated optimizer algorithm.

Convolutional neural networks

The special algorithm behind convolutional neural networks was first introduced by LeCun et al.[124] in 1989 and most of the current classification networks are based on it[125-129]. Convolutional networks use a special kind of linear operation called convolution in at least one of their layers[105]. The idea behind the convolutional stages is to replace a large-scale linear layer through multiple small-scale linear layers which “search” for specific features[106]. Of note, convolution in deep learning does not precisely correspond to the mathematical definition used in engineering etc.[105].

In neural networks, convolution operation applies a special weight matrix called kernel to the input to extract features of it[124]. Figure XV illustrates this procedure in a simplified form with a 4x4 kernel reacting to diagonal lines from bottom left to upper right, which investigates a 9x9 input matrix. After calculating the output value at position 0 (upper left corner) by multiplying each input value with the corresponding kernel weight and reporting the sum of all multiplications, the kernel migrates one pixel to the right and repeats its operation. This results in a 6x6-output matrix that presents us the position of diagonal lines in the input value. Hence, convolutional layers in the neural network can be seen as a scan procedure with a template (i.e., kernel), where related structures causing a higher output value. Application of multiple different kernels with randomly chosen initial weights and weight adaptation during the training process allows a complex scan of the input data with extraction of various features necessary for pattern recognition[106].

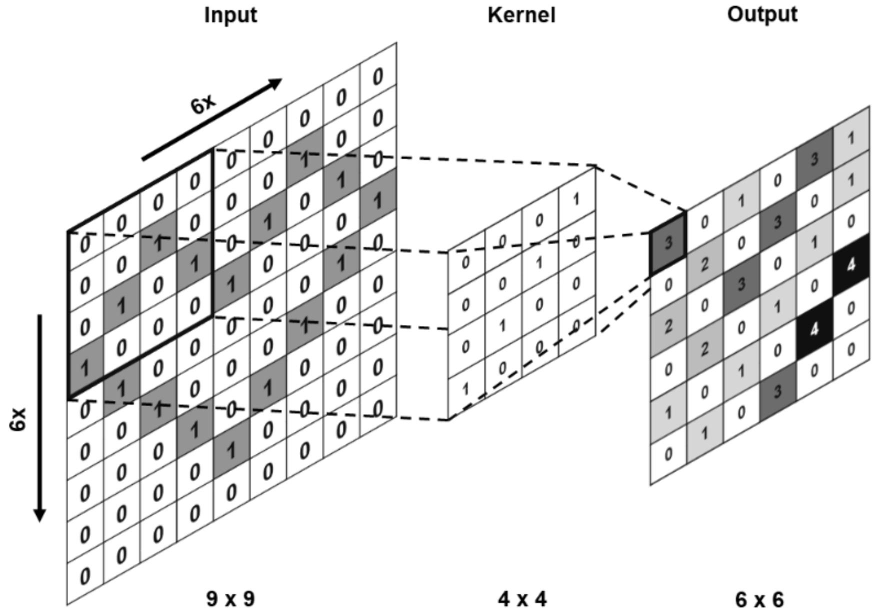

***Figure XV: Illustration of the convolution process**. Application of a single kernel to the input data with extraction of one feature. In this example, the 4x4 kernel reacts in the presence of diagonal lines from the bottom left corner to the upper right corner (all other elements are 0 in this kernel). The output of the kernel sums up all multiplication (in this example 16 per position) and then moves one position on the input matrix further. Of note, the dimension of the convolutional stage output depends on the input size, the kernel size, the steps of the kernel as well as the number of different kernels. In this example, it would be 6x6x1 (as only one kernel was used).*

Convolutional stages with parallel application of kernels are then followed by an activation function (e.g., ReLU) as well as a pooling function[105] (see figure XVI).

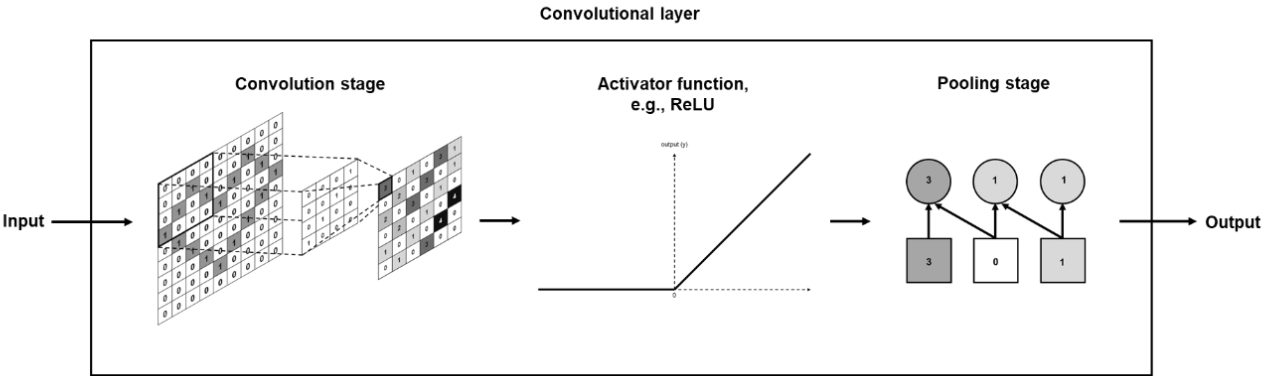

***Figure XVI: Illustration of the components of a common convolutional layer.** In a first step, the convolutional stage, multiple, parallel running kernel-operations enables the simultaneous extraction of various features. After this (linear) step, an activator function (normally a rectified linear unit (ReLU) is used to introduce non-linearity, followed by the pooling stage to merge the results of each kernel into a single matrix, necessary for the output.*

The latter merges the results of all the different kernel output matrixes together for the final output of the convolutional layer. There are different possibilities of this procedure with element-by-element addition, mean calculation of all output values or extraction of the highest value (called max-pooling[130]). As an advantages of this last step, pooling “helps to make the representation approximately invariant to small translation of the input”[105]. This is especially helpful if we are more interested in the presence (yes/no) than the exact location of a feature[105]. Notable, it is possible to illustrate the activation map of each layer (respectively each kernel) to understand the procedures on the different layers of the network (for the Matlab code see Appendix 8.6). However, with increasing depth, the activation map becomes more and more abstract.

Current convolutional neural networks consists of several convolutional layers with variable connection between the layers. The number of layers as well as the specific connection between the layers are defined by the architecture of the network. The general architecture includes an input layer, a variable number of convolutional layers as well as a fully connected layer. This fully connected layer receives his input from each unit of the previous layer (thus, fully connected) to merge all the previously performed calculation and returns an output vector with the size of the numbers of categories. After this step, an activation function (usually softmax in classification networks) as well as a classification layer complete the structure. Figure XVII illustrates a simple convolutional neural network with a depth of six layers.

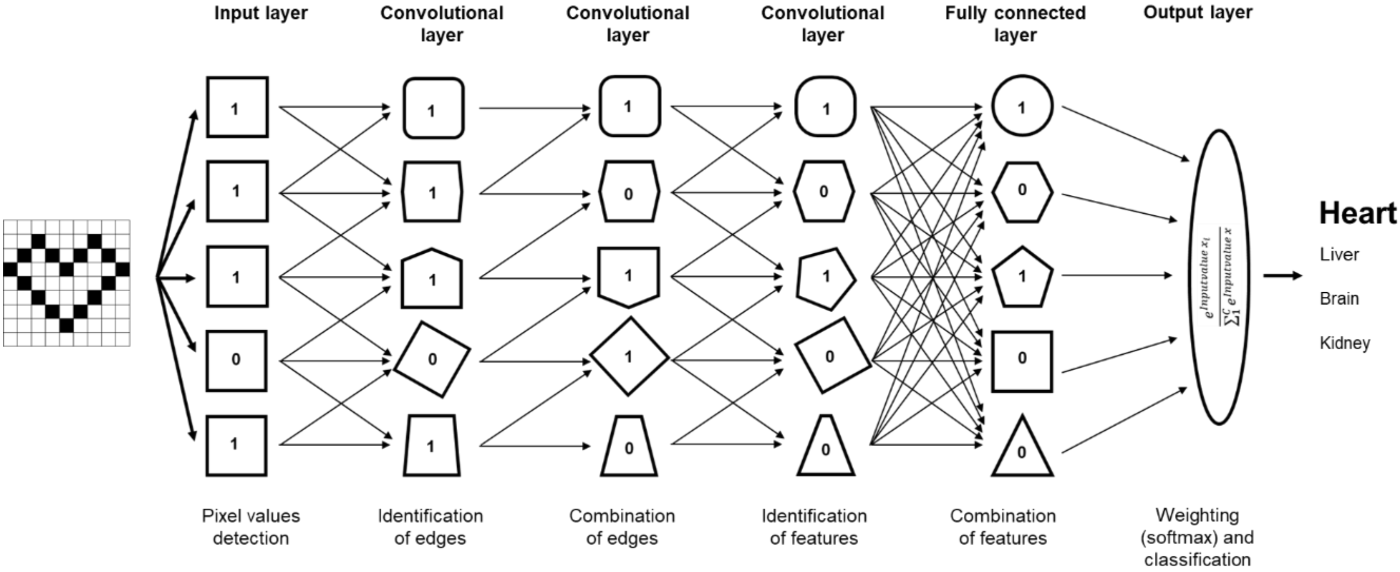

Figure XVII: Structure of a convolutional neural network with a depth of six layers *The connections between the layers as well as the different intended tasks vary for each layer. With increasing depth, the extracted features can hierarchically and progressively become more complex*[3].

This architecture, i.e., the number of convolutional layers is crucial for the performance of a neural network. As a rule of thumb, the capacity, i.e., “the ability to fit a wide variety of function”[105] grows with an increasing number of layers. However, with increasing capacity, a network is prone to overfit. This means that there are enough functions to remember each example of the training data resulting in an excellent classification accuracy in the training without extracting of the underlying data pattern. As a result, the network performs low in previously unseen inputs. This ability, i.e., to perform well on unseen inputs, is called generalization[105]. Achievement of an optimal generalization is the central challenge in the design and training of neural networks.

While a lower capacity does not have the problem of overfitting (also called overspecialization), it is often socialized with a high training error (i.e., underfitting). In this situation, the network is not able to extract the different underlying data pattern to calculate reasonable prediction because of the restricted possibilities. Hence, most up-to-date approaches use network architectures with a high capacity and introduce further restrictions to prevent overfitting. The best solution to prevent overfitting is to increase the number of training data.

This is, however, not always possible. Hence, another possibility is to augment the existing training data by random translocation, rotation and/or reflection of the images[105,106].

Further, most networks are trained with a restriction called dropout[131]. This function randomly samples a binary mask to all input and hidden units in the network, removing all units that received a “0” from the underlying network (see figure XVIII).

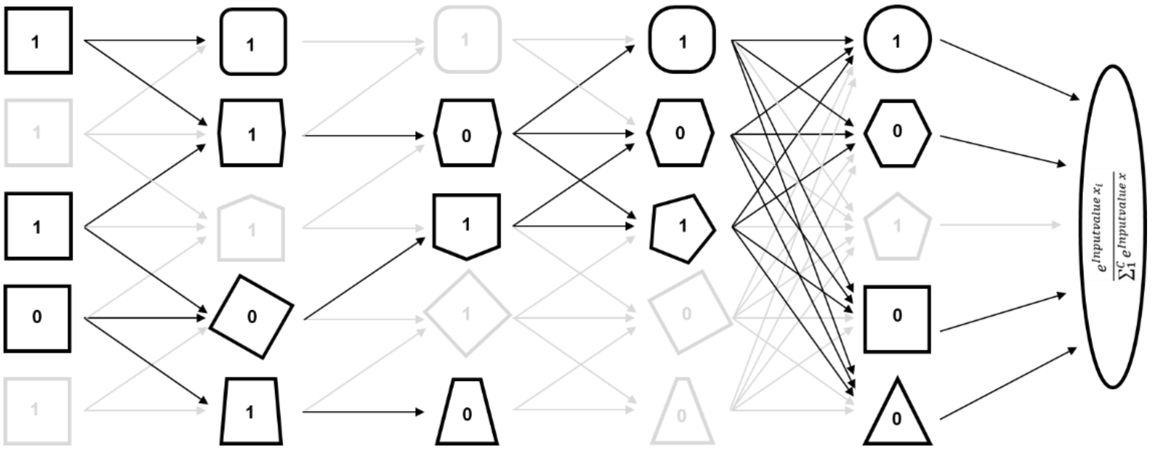

Figure XVIII: Illustration of the dropout regularization procedure. *The dropout function randomly deactivates units in the network and creates a subnetwork with a decreased capacity. This prevents overfitting. Weights of neurons, which do not participate in the current prediction, are not updated.*

This binary mask is removed after each minibatch and a newly configured mask is applied before the start of the next minibatch iteration. Application of this dropout function decreases the capacity of the network and “regularizes each unit to be not merely a good feature but a feature that is good in many context”[105]. From another point of view, dropout generates numerous subnetworks with lower capacity, which are not able to recognize all details of the images. Hence, every subnetwork will focus on the same strong signal, while considering randomly various small details (i.e., data noise). Thus, combination of all these subnetworks results in an augmentation of the strong signal and a deletion of the randomly small noise signals[106].

Last, a very simple but effective method to prevent overfitting is the manual early stopping of the training process[132,133] after the occurrence of first overfitting signs, i.e., the divergence of the training and validation performance. For this purpose, the training process is displayed in real-time showing the current performance on the training data as well as the preliminary performance on the validation data. Figure XIX shows an example of such a training process, where missing data augmentation caused overfitting at an early stages and where manual early stopping should have been performed.

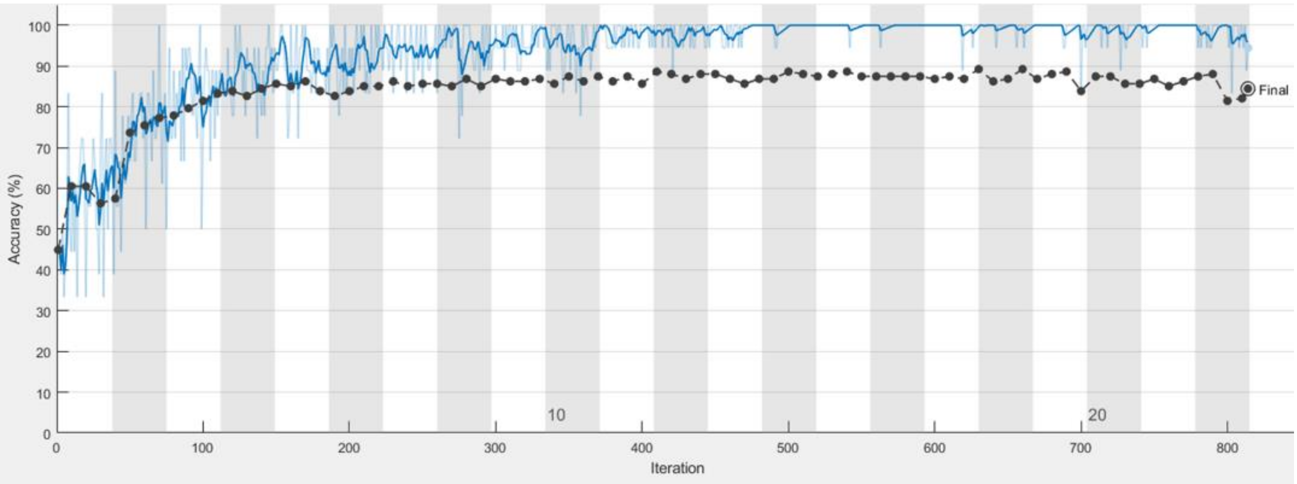

***Figure XIX: Overfitting due to missing data augmentation**. Overfitting is characterized by early divergence of the training performance (blue) and the validation performance (black, performed every 10 iterations). After 150 iterations, there is no improvement in the validation accuracy, while the training accuracy is close to 100%.*

Of note, it is rarely possible to achieve an accuracy of 100% on previously unseen data even for an utopian ideal model. This is because on the natural noise within the data-generating distribution (see also Project II, figure 4 for a frequency distribution of the icECG parameters grouped by the non-ischemic and the ischemic state). This error incurred by an utopian ideal model is called Bayes error[105].

Hyperparameter of a neural network

Adaptation of each weight during the training process occurs based on the underlying optimizer algorithm. However, there are parameters, called hyperparameters, which are not automatically adapted during the training process. Instead, adaptation is conducted according to the performance of the trained network on the validation data.

The most important hyperparameter is the learning rate. Hence, it is recommended to spend most time optimizing this parameter. The learning rate determines the size of each adaptation step towards a minimum. Setting the learning rate above a certain range causes overshooting corrections with consecutive oscillation of the network, while an inadequate low learning rate results in a prolongation of the training process[134] (see figure XX). In addition, choice of the learning rate depends on the optimizer algorithm. For example, training with SGDM requires an approximately 10-fold higher learn rate than training with ADAM[135]. In practice, the learning rate is normally adapted during the training progress, i.e., starting with a high learning rate, which gradually decreases after each x training iterations[105].

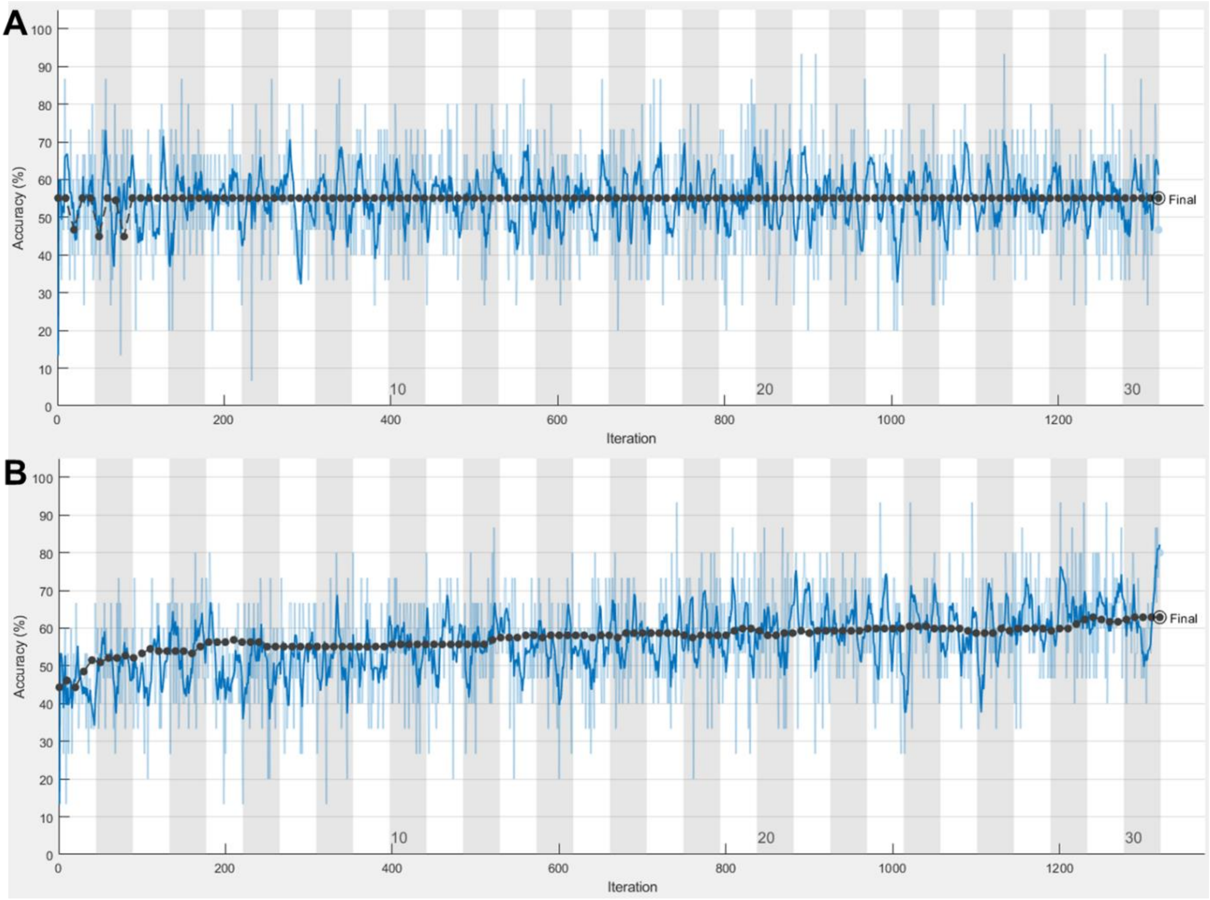

Figure XX: Effect of the learn rate on the training process A) *Training process with an inadequate high learning rate ($7*10^{-4}$) resulting in overshooting corrections with consecutive oscillation around a low level of prediction accuracy.* ***B)*** *Training process with an inadequate low learning rate ($1*10^{-6}$) results in a low performance increase within a reasonable amount of time. Both networks were trained using the ADAM optimizer algorithm with the same training data and hyperparameter settings except of the learning rate. Training duration was 75 minutes each.*

Another important hyperparameter is the probability for the binary mask in the dropout layer to randomly remove layers from the network. Those newly formed subnetworks should be big enough to have an adequate capacity to solve the task but small enough to prevent overfitting. As recommended by Goodfellow et al., hidden units should be excluded with approximately a probability of 50% (i.e., 0.5)[105]. Of note, if this number is too high, a significant proportion of the resulting subnetwork does not have input units and in the worst case, there exists no path connecting the input to the output resulting in a non-functional network.

A further hyperparameter is the minibatch size, i.e., the size of the subset of the training data that is used to evaluate the gradient of the loss function and to update the weights. The optimizer algorithm calculates the steps towards minimizing the loss function after completion of all images within a minibatch. In general, larger minibatches provide a more accurate estimation of the gradient. However, small batches have been shown to offer a regularizing effect on the training process, probably because of the noise they add since each training image has more direct impact on the weight adaptation[136]. Consequently, minibatch size affects the acceptable range of possible learning rates. In a recent study analyzing the effect of the minibatch size on the training process, the authors concluded that “smaller is better and the best performance is obtained by minibatch size between 2 and 32”[137].

Last, the number of iterations of all training data, called an epoch, affects the training process. Preliminary termination of the training process because of a limited number of epochs causes suboptimal network performance, while missing termination increases the risk for overfitting. Most training options includes a preliminary termination term, which terminates the training process when the validation and the training performance diverges several steps in a row[135].

Hyperparameter optimization

Unfortunately, the setting of these parameters is often more or less based on trial and error (within a certain range)[105]. The simplest option to find the best hyperparameter setting is a grid search[138]. This approach requires a small finite set of values to explore for each hyperparameter (i.e., 2-32 for the minibatch size) and then trains a model for every possible hyperparameter configuration within this finite set (see figure XXI A). Afterwards, the experiment with the best validation accuracy is chosen to be the optimal hyperparameter setting. Another more convenient approach is random search (figure XXI B)[138]. Here, hyperparameter configurations are randomly chosen within a range. The model is then trained x-times with a random configuration. In practice, random search provides faster good values[105]. However, neither approach does include the results of the preceding trainings into its evaluation and thus, does not guarantee a successful search of an optimal hyperparameter setting (i.e., tracing of a global minima as outlined in figure XXI). In addition, both approaches require numerous training runs and thus, time.

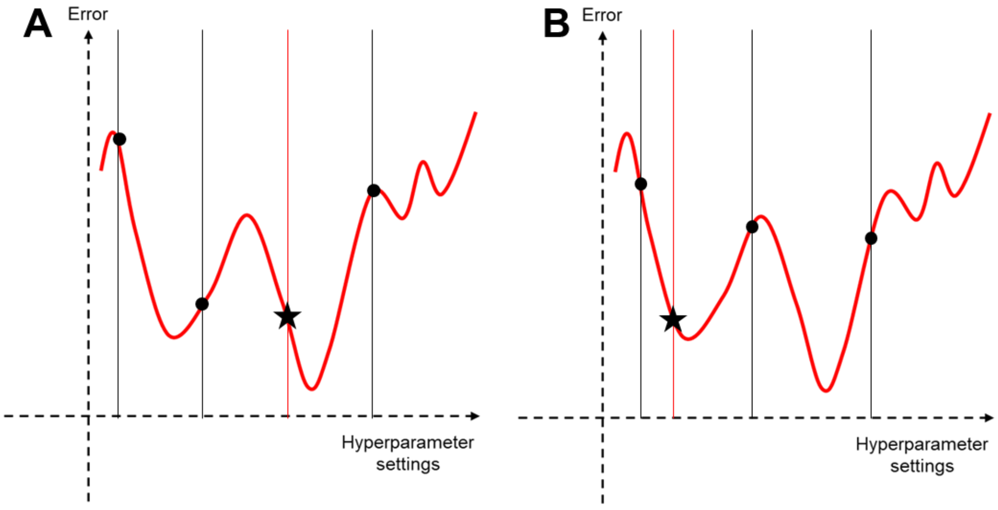

Figure XXI: Searching of optimal hyperparameter settings using grid and random search *on a complex cost function with several local minima and one global minimum.* ***A)*** *Grid search with organized testing of different hyperparameter settings within a finite set. There is a constant difference between the tested hyperparameters settings* ***B)*** *Random search of the optimal settings with varying differences between the tested hyperparameter settings. Black thin line = one tested hyperparameter setting; black point = achieved error rate with the corresponding settings; red thin line = best hyperparameter setting; black star = best achieved error rate*

Another, more systematic approach is based on the Bayes' theorem, i.e., "the updating of a previous belief in light of new information to produce an updated posterior belief"[139]. This Bayesian optimization approach[140] starts with few training runs with randomly chosen hyperparameter settings. After n-runs, a surrogate function of the cost-function is constructed, which is considerable simpler than the true cost function (see figure XXII for an illustration of this approach). In a second step, minima of this surrogate function are calculated and designated as promising regions. Hence, in the second round of n-runs, the algorithm tries different combination in these promising regions as well as on a different region to update the surrogate function (as it is possible that the first function missed an important region). Thus, after a certain number of iterations, the algorithm will find a good configuration of the hyperparameters.

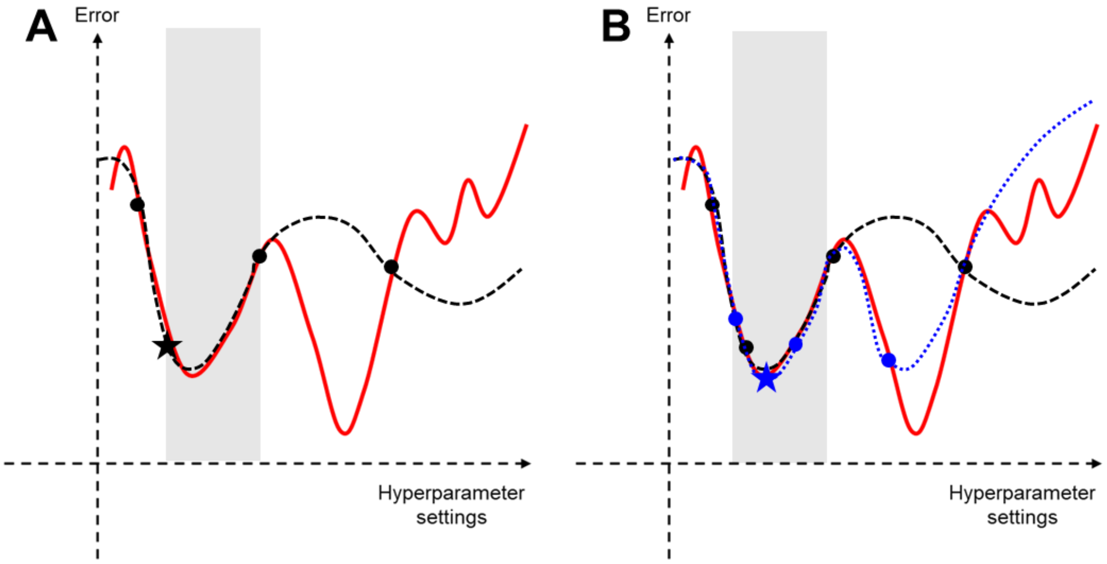

Figure XXII: Searching of optimal hyperparameter settings using Bayesian optimization A) *After initialization with random hyperparameter settings (black point = one training run), a surrogate function (dashed black line) of the cost function is calculated. Based on this surrogate function, a promising region is defined (grey; around the minimum of the surrogate function including the currently best configuration (black star)).* ***B)*** *In the second step, new configurations within the promising region are tried (blue circle) as well as few randomly chosen settings to update the surrogate function beyond the promising region (dashed blue line). After this iteration, a new promising region is defined based on the best configuration (blue star) as well as the newly calculated minima of the cost function.*

Nevertheless, Goodfellow et al.[105] does not unambiguously recommend Bayesian hyper-parameter optimization as it fails in very complex cost functions. However, they recommend to try it once to see if it works on that particular problem.

Transfer learning

Transfer learning generally refers to the situation, where a model trained on one task is used in some way on a second task, which is similar to the first one to some extent[141]. It has the benefit of decreasing the training time and further results in lower generalization error[142]. However, the most important reason to use transfer learning is that there are not enough data to adequately train a deep neural network. Hence, instead of provoking overfitting by numerous iterations on the smaller data set, usage of a deep neural network, which has been previously trained on a large data set, is preferable[143].

Of note, transfer learning is only possible if the features learned from the first tasks are general[142]. In image classification task, these features include recognition of characterizing structures as edges, lines and other geometrical patterns. As these features are essential in every classification task, it is common to use a neural network previously trained for weeks on a challenging image classification tasks as ImageNet[144]. ImageNet is a large image database, which offers millions of sorted images in 1000 categories to train networks. Further, its ImageNet Large Scale Visual Recognition Competition (ILSVRC[145]; http://www.image-net.org/challenges/LSVRC/) is a reputed platform to compare classification neural networks and most of the commonly used networks for transfer learning won this challenge once[125-127,129]. These networks are publicly available with the trained weights proven effective on extracting features from images and serve as the starting point for the new training process after a few adaptation.

Detection of Myocardial Ischemia by Intracoronary ECG Using Convolutional Neural Networks

Bigler et al. – CNN for icECG ischemia detection

Marius Reto Bigler, MD; Christian Seiler, MD

Department of Cardiology, Inselspital, Bern University Hospital, University of Bern, Switzerland

Correspondence:

Christian Seiler, MD

Inselspital, Bern University Hospital

Department of Cardiology

Freiburgstrasse 8, CH-3010 Bern, Switzerland

Phone: +41 31 632 36 93, Fax. +41 31 632 42 99

e-Mail: christian.seiler@insel.ch

Total word count: 5’000 words

3.3.2 Abstract

Introduction The electrocardiogram (ECG) is a valuable tool for the diagnosis of myocardial ischemia as it presents distinctive ischemic patterns. Deep learning methods such as convolutional neural networks (CNN) are employed to extract data-derived features and to recognize natural patterns. This study aimed to determine the optimal ischemic parameter as obtained from the highly susceptible intracoronary ECG (icECG) using pre-trained CNN.

Method This was a retrospective observational study in 228 patients with chronic coronary syndrome. Each patient had participated in clinical trials with icECG recording and ST-segment shift measurement at the beginning (i.e., non-ischemic) and the end (i.e., ischemic) of a one-minute proximal coronary artery balloon occlusion establishing the reference. Using these data (893 icECGs in total), two pre-trained, open-access CNN (GoogLeNet and ResNet101) were trained to recognize ischemia. The best performing CNN during training were compared with the icECG ST-segment shift for diagnostic accuracy in the detection of artificially induced myocardial ischemia.

Results Using coronary patency or occlusion as reference for absent or present myocardial ischemia, receiver-operating-characteristics(ROC)-analysis of manually obtained icECG ST-segment shift(mV) showed an area under the ROC-curve(AUC) of 0.903±0.043 ($p<0.0001$, sensitivity 80%, specificity 92% at a cut-off of 0.279mV). The best performing CNN showed an AUC of 0.924 (sensitivity 93%, specificity 92%).DeLong-Test of the ROC-curves showed no significant difference between the AUCs. The underlying morphology responsible for the network prediction differed between the trained networks but was focused on the ST-segment and the T-wave for myocardial ischemia detection.

Conclusions When tested in an experimental setting with artificially induced coronary artery occlusion, quantitative icECG ST-segment shift and CNN using pathophysiologic prediction criteria detect myocardial ischemia with similarly high accuracy.

Keywords: Intracoronary electrocardiogram, myocardial ischemia, ST-segment shift, convolutional neural networks, deep learning

3.3.3 Introduction

The electrocardiogram (ECG) is an easy available biomedical tool yielding diagnostic information on various cardiac pathologies, specifically acute myocardial ischemia, where the presence or absence of ECG ST-segment shift has therapeutic consequences[1].
However, as myocardial ischemia directly affects all energy-dependent cellular processes, several ECG parameters other than ST-segment shift also reflect myocardial ischemia. Recently, our research group employed an experimental setting with complete coronary artery balloon occlusion during 1 minute, thus creating a brief myocardial ischemia[2, 3]. Intracoronary ECG (icECG) was used to assess the diagnostic accuracy of various ECG parameters for ischemia detection[4], whereby the icECG ST-segment shift measured at the J-point at a threshold of 0.365mV was superior to other parameters for ischemia detection. In the mentioned study, selection of the analyzed parameters was based on a literature search for ECG ischemia parameters. Thus, it is likely that potentially well-performing parameters were overlooked based on missing literature.

In comparison, deep learning methods, such as convolutional neural networks (CNN) are not affected by a selection bias based on available literature. Instead, the algorithm tries to find patterns in a given dataset to solve a pre-defined task[5, 6]. Hence, CNN focuses on data-derived features rather than on pre-defined parameters, offering an interesting novel approach.

The present study aimed to determine the optimal icECG parameter for myocardial ischemia detection using a deep learning approach with transfer learning (i.e., retraining) of pre-trained CNN. In a first step, multiple CNN were trained to differentiate between non-ischemic and ischemic images of icECG. Then, parametric visualization of the CNN-derived activation patterns was used to find the ECG morphology responsible for the network prediction.

3.3.4 Methods

Study design and patients

This was a retrospective observational study in patients with chronic coronary syndrome who underwent coronary angiography due to chest pain, and participated in one of several clinical trials[7-9] our research group carried out between July 2016 and October 2020. As part of all those trials, coronary collateral flow index (CFI) was obtained, i.e., the quantitative measure of coronary collateral function during a brief, artificial coronary artery occlusion. A detailed description of CFI has been previously published[10]. In brief, CFI is a measure of collateral blood supply to a coronary artery proximally balloon-occluded for the duration of 1 minute, and it is defined as mean coronary occlusive pressure relative to mean aortic pressure, both subtracted by central venous pressure[11]. Hence, the present study employs the same temporal landmarks with non-ischemic (i.e., before coronary occlusion), and controlled ischemic (i.e., at the end of the occlusion) conditions as recently[4]. Of note, the experimental setting of a brief artificial coronary balloon occlusion creates an independent reference essential for the subsequent analysis.

Criteria for inclusion in the present analysis were previously conducted CFI measurements with simultaneous recording of icECG, and written informed consent for further use of the patient’s data. Exclusion criteria were the presence of ECG bundle branch blocks, and of non-sinus rhythm or paced rhythm. Application of these criteria resulted in 893 icECG tracings. A patient could thus provide more than two (one non-ischemic and one ischemic) icECG tracings to the data set. IcECGs did not have to be present in pairs of both conditions.

All original studies had been approved by the Ethics Committee of the Canton of Bern, Switzerland, and all patients gave written informed consent for further use of their data.

Acquisition and preparation of the intracoronary ECG

IcECG was acquired by attaching an alligator clamp to the 0.014-inch pressure monitoring angioplasty guidewire (PressureWire™ X Guidewire, Abbott, Chicago, Illinois, United States) positioned in the distal third of a major coronary artery, and connecting it to a precordial lead. The structure of this guidewire with non-conductive coating allows the generation of an icECG-lead between the Wilson Central Terminal and the conductive pressure sensor of the guidewire located near the tip without the need for additional isolation. IcECG recording was performed at a sampling frequency of 2’000 Hz, and with standard system filtering (corresponding to a bandpassfilter 0.05-100Hz). The same guidewire served as angioplasty guidewire for the balloon catheter used for proximal coronary balloon occlusion.

In a subsequent step, 12 to 15 consecutive cardiac cycles were manually chosen according to the intra-procedural tagging as “non-ischemic” or “ischemic” (i.e., recorded during coronary patency respectively coronary occlusion). The chosen cardiac cycles were then signal averaged, additionally plotted in Matlab and saved as jpg -images and stored in group-specific folders (491 non-ischemic, and 402 ischemic icECG images; figure 1).

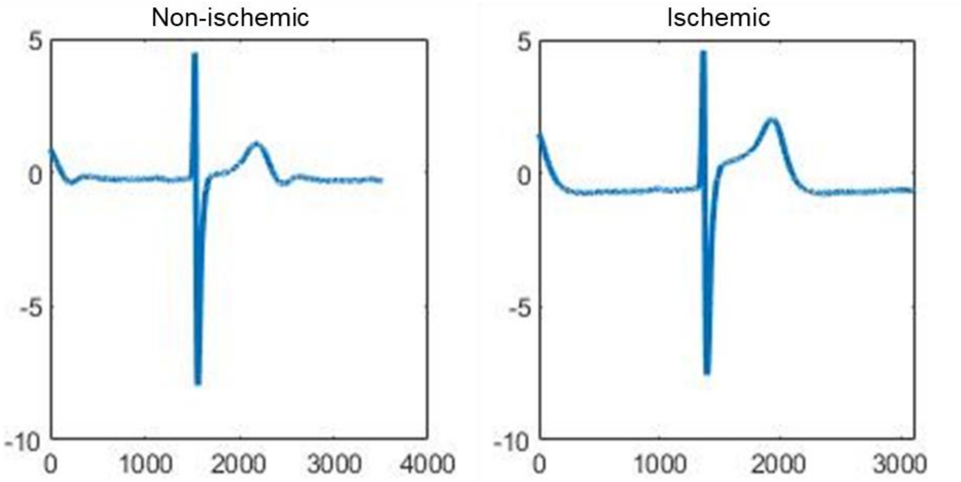

Figure 1: Input data for the neural networks *The input data were taken from the original study analysis and converted into jpgs with a predefined image size (224x224x3 pixels). Each image contained either the illustration of a non-ischemic (i.e., recorded directly before the coronary balloon occlusion) or an ischemic (i.e., recorded at the end of the balloon occlusion) intracoronary ECG as well as the corresponding label (non-ischemic respectively ischemic). In this example, both icECGs are from the same vessel (left anterior descending coronary artery) from the same patient. IcECG ST-segment shift was 0.056mV respectively 0.858mV.*

Image allocation and data augmentation

Of the 893 icECG images, 58 were randomly separated into an examination folder for final diagnostic accuracy assessment independent of the training and validation data. The remaining 835 icECG images were randomly allocated to training and validation data (80% respectively 20% as recommended by Goodfellow et al.[5]), the validation data being used to assess the performance of the trained networks during the training process. This resulted in 668 training and 167 validation images. Because of the strong spatial dependence of the icECG with relevant regional morphologic changes within each patient, the likelihood that the network performs overfitting on single patients was judged small. Thus, randomization was not made on a patient level and recordings from two different coronary arteries of the same patient were allowed in two different data sets.

Before the start of each training iteration, all training images were randomly shuffled and processed by adding data noise to prevent overfitting[5, 12]. That is, the images were randomly rotated in a range between ±45°, translocated ±10 pixels in every direction and/or reflected on the horizontal axis.

Selection and preparation of the pretrained convolutional neural networks

Pretrained CNN were trained on millions of images (for the ImageNet[13] Large Scale Visual Recognition Challenge (ILSVRC; http://www.image-net.org/challenges/LSVRC/), whereby general pattern recognition skills have been already previously developed, thus, allowing the application of a complex network architecture on a small data set. For this study, two CNN with different depth and network architecture were chosen. Both had an input size of 224x224x3 pixels for the images allowing a single data set preparation.

- GoogLeNet (GN) is a 22 convolutional layer deep CNN developed by Szegedy et al.[14] named in honor of the first CNN (LeNet by Yann LeCun[15]). GN has a special architecture with networks within networks (called inception modules). These modules contain multiple different filter sizes allowing simultaneous feature extraction on different levels of details[16].

- Resnet101 (RN) is a 101 convolutional layer deep CNN developed by Kaiming He et al.[17] using a special residual learning framework allowing the training of a deeper and thus more accurate network. As a trade-off, its prediction time is significantly longer as that of GN.

To prepare for the transfer learning process, the last three layers of the networks responsible for the network prediction had to be replaced for the new task, i.e., the classification of icECG images into non-ischemic respectively ischemic. In addition, a dropout layer was added to prevent the network from overfitting[18]. The remaining layers responsible for pattern recognition and feature extraction were not changed. General learning rate was chosen low while the new layers received a learning rate weight factor of 10 (i.e., 10-fold the normal learning rate) to improve and accelerate their training process.

Transfer learning (CNN training)

During transfer learning, the pretrained CNN were retrained on the new task. For this purpose, the network analysed each image in the training data set and classified it. After n-images (i.e., minibatch size), the network parameters were updated to reflect the new insights learned from the n-images, and the training continued until all images were analyzed once (i.e., one epoch). During this process, several parameters were involved, which had to be determined before training. In this study, GN was used for determining the range of the four hyperparameters, i.e., learning rate, dropout probability, minibatch size and number of epochs. For each hyperparameter, approximately ten training runs were conducted within a broad range of values (e.g. for the dropout probability 0-1 in 0.1 steps) using two optimizer algorithms (stochastic gradient descent with momentum, SGDM[19], and adaptive moment estimation learning rate algorithm, ADAM[20]).

After defining a range of working values for each hyperparameter, 111 training runs using the random search approach[21] were performed using the ADAM optimizer algorithm. A random search was performed only with ADAM because of the better performance in less time. Further, hyperparameter optimization for GN with five cycles of Bayesian optimization[22] (each with 30 training runs, three cycles with SGDM, two cycles with ADAM) was performed resulting in 150 trained networks.

Based on the experience with GN hyperparameter optimization and the concordance of working values for each hyperparameter with the literature, no grid or random search was performed for RN. Instead, optimal setting of the hyperparameter was directly assessed by Bayesian optimization. Because of the significantly longer training duration for RN compared to GN, only two cycles (each with 30 training runs using the ADAM optimizer algorithm) were performed.

Network performance analysis

Network performance analysis resulted in 321 trained networks (261 GN, 60 RN). Networks performing above the arbitrary threshold of 85% classification accuracy (i.e., (true positive + true negative)/(true positive + true negative + false positive + false negative)) on the validation data were stored for in-depth evaluation with determination of diagnostic accuracy on the validation data, the examination data as well as the combined data sets. Based on the results of this evaluation, the best ten networks (independent of the architecture) were further evaluated with class activation mapping (CAM)[23, 24], i.e., parametric visualization of their activation patterns to findthe morphology responsible for the network prediction using ten characteristic icECGs (supplemental figures 1-10).

Computational hardware

Network training was simultaneously performed on two computers (Intel® Core™ i7-7700 CPU@3.60GHz, 8GB RAM respectively Intel® Core™ i7-8550U CPU@1.80GHz, 8GB RAM) using customized software (written in Matlab R2019b and R2020a). Average training time during Bayesian optimization was 117 minutes for GN and 186 minutes for RN.

Statistical analysis

Two study groups based on the temporal landmarks for non-ischemic (i.e., before coronary occlusion) and controlled ischemic (i.e., at the end of the occlusion) conditions were formed.

Between-group comparison of continuous study parameters was performed by a paired student’s t-test.

Network performance was analyzed by determination of classification accuracy (i.e., correct classified images/all images) using a 4-field matrix and calculation of sensitivity, specificity and F1-score (harmonic mean of sensitivity and positive predictive value). Nonparametric receiver operating characteristics (ROC) analysis using the reference of coronary patency or occlusion for absent or present myocardial ischemia was performed for accuracy assessment of detecting myocardial ischemia by manually obtained icECG ST-segment shift (continuous) and the CNN prediction (dichotomous). Comparison of the area under the ROC curves was performed using the DeLong-Test.

Statistical significance was defined at a p-level of <0.05. Continuous variables are given as mean ± standard deviation. All analyses were performed using SPSS version 25 (IBM Statistics, Armonk, New York) or MedCalc for Windows, version 19.1 (MedCalc Software, Ostend, Belgium).

3.3.5 Results

Eight-hundred ninety three icECGs from 228 patients were included in the study. Six-hundred sixty eight were used for CNN training and two-hundred twenty five icECGs for the performance evaluation.

Patient characteristics

Patient characteristics are presented on table 1.

Descriptive statistics

Descriptive statistics of icECG ST-segment shift and the target vessel distribution grouped according to the non-ischemic vs. ischemic state are presented on table 2. Right coronary artery served most frequent as the study vessel. Manually determined IcECG ST-segment shift was different between the groups in each data set.

Figure 2 shows the distribution of icECG ST-segment shift grouped according to the state of absent or present coronary artery balloon occlusion for the combination of validation and examination data as well as the corresponding network prediction from a selected trained network (RN5).

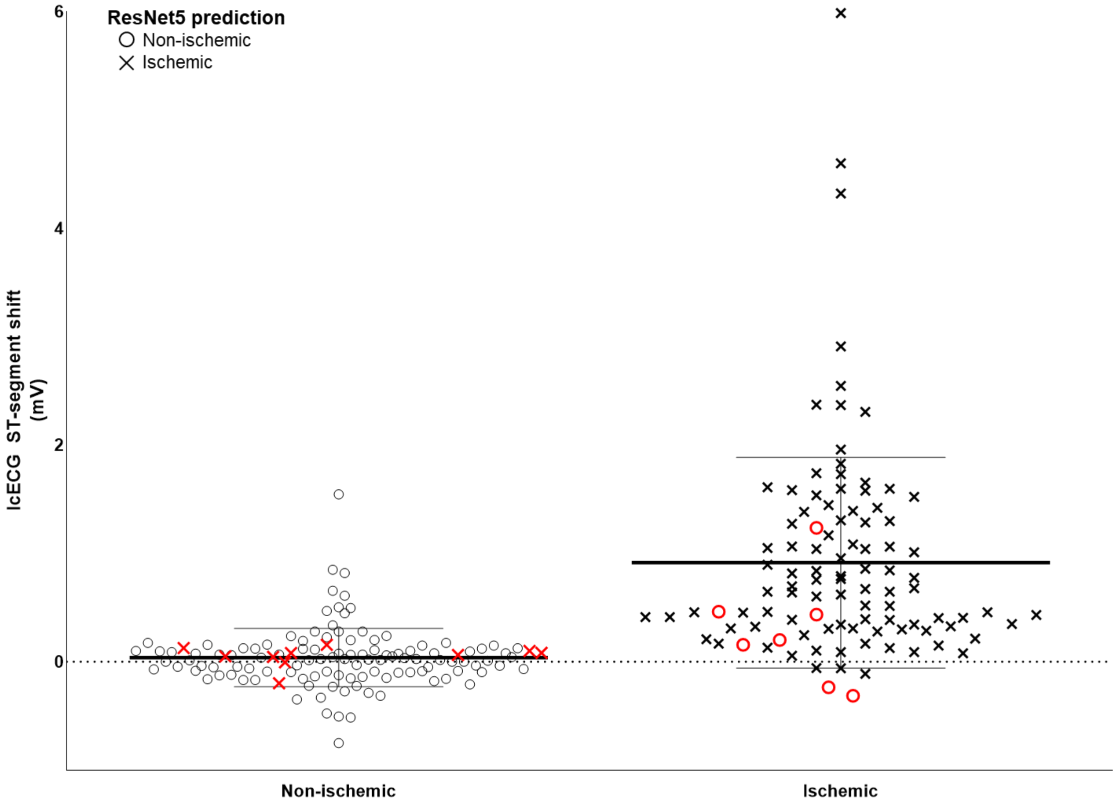

Figure 2: IcECG ST-segment shift grouped according to the state of absent or present coronary artery balloon occlusion *Combination of the validation and the examination data (n=225) was used for the performance analysis. Black circles: Non-ischemic prediction of RN5, black crosses: Ischemic prediction of RN5. Red signals: wrong predictions of RN5. Error bars indicate mean values and SD*

Receiver-operating characteristic curves

Using coronary artery patency or occlusion as dichotomic reference for absent or present myocardial ischemia, receiver-operating-characteristics (ROC) analysis of manually obtained icECG ST-segment shift in mV showed an area under the ROC-curve for the combined validation and examination data of 0.903±0.043 ($p<0.0001$; figure 3). AUC for the training data was 0.941±0.019 ($p<0.0001$), for validation data 0.897±0.051 ($p<0.0001$), for examination data 0.927±0.074 ($p<0.0001$) and for the complete data 0.932±0.018 ($p<0.0001$, supplemental table 1)

Regarding the optimum cut-off for ischemia detection, an icECG ST-segment shift of 0.279mV distinguished best between non-ischemic and ischemic myocardium, sensitivity 80%, specificity 92% for the combined validation and examination data

Figure 3: Nonparametric receiver-operating characteristic curve of the icECG ST-segment shift and the network predictions using coronary artery patency or occlusion as dichotomic reference for absent or present myocardial ischemia *Of note, network prediction provides a dichotomous output (non-ischemic respectively ischemic), resulting in a triangular ROC-curve. Hence, there is only one combination of sensitivity and specificity possible for each CNN. Dashed black line = reference line.*

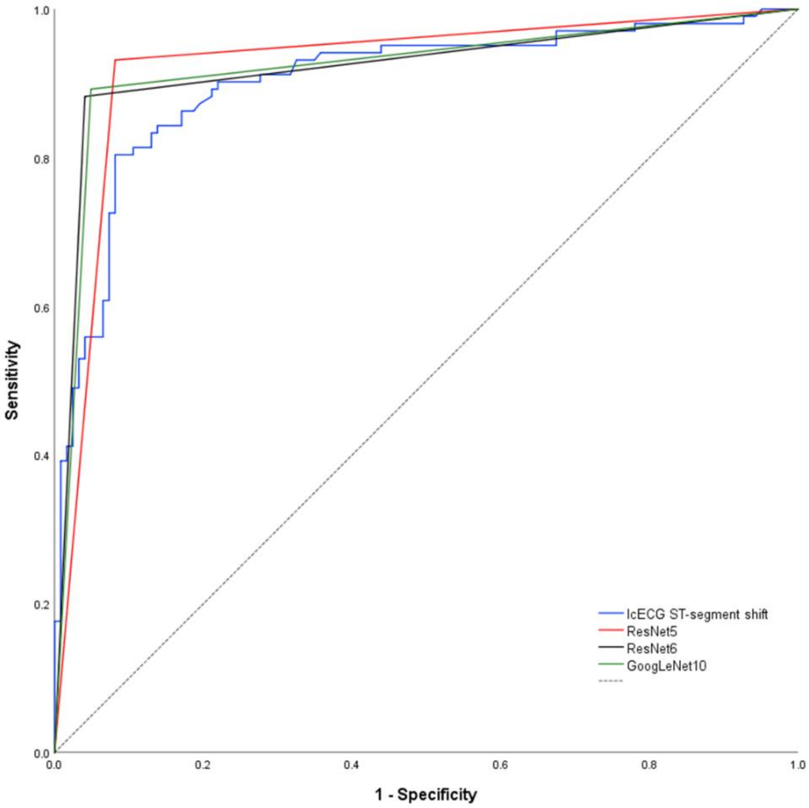

Network performance

Prediction of the ten best performing networks and their accuracy, sensitivity, specificity and network-activating icECG morphology are presented on table 3, and in detail on supplemental table 2. Using the reference (i.e., temporal landmarks before respectively at the end of a coronary balloon occlusion) for absent or present myocardial ischemia, the three best-performing networks showed a diagnostic accuracy of 92% (RN5: sensitivity 93%, specificity 92%; RN6: sensitivity 88%, specificity 96%; GN10: sensitivity 89%, specificity 95%; figure 3). Visualization of the network activation patterns are shown on figure 4, and in detail on supplemental figures 1-10.

Comparison of icECG ST-segment shift and network performance

DeLong-Test of the ROC-curves (figure 3) showed no significant difference of AUCs between manually obtained icECG ST-segment shift and the three networks (RN5: p=0.384; RN6: p=0.435; GN10: p=0.438). There was no significant difference either between the AUCs among the three networks.

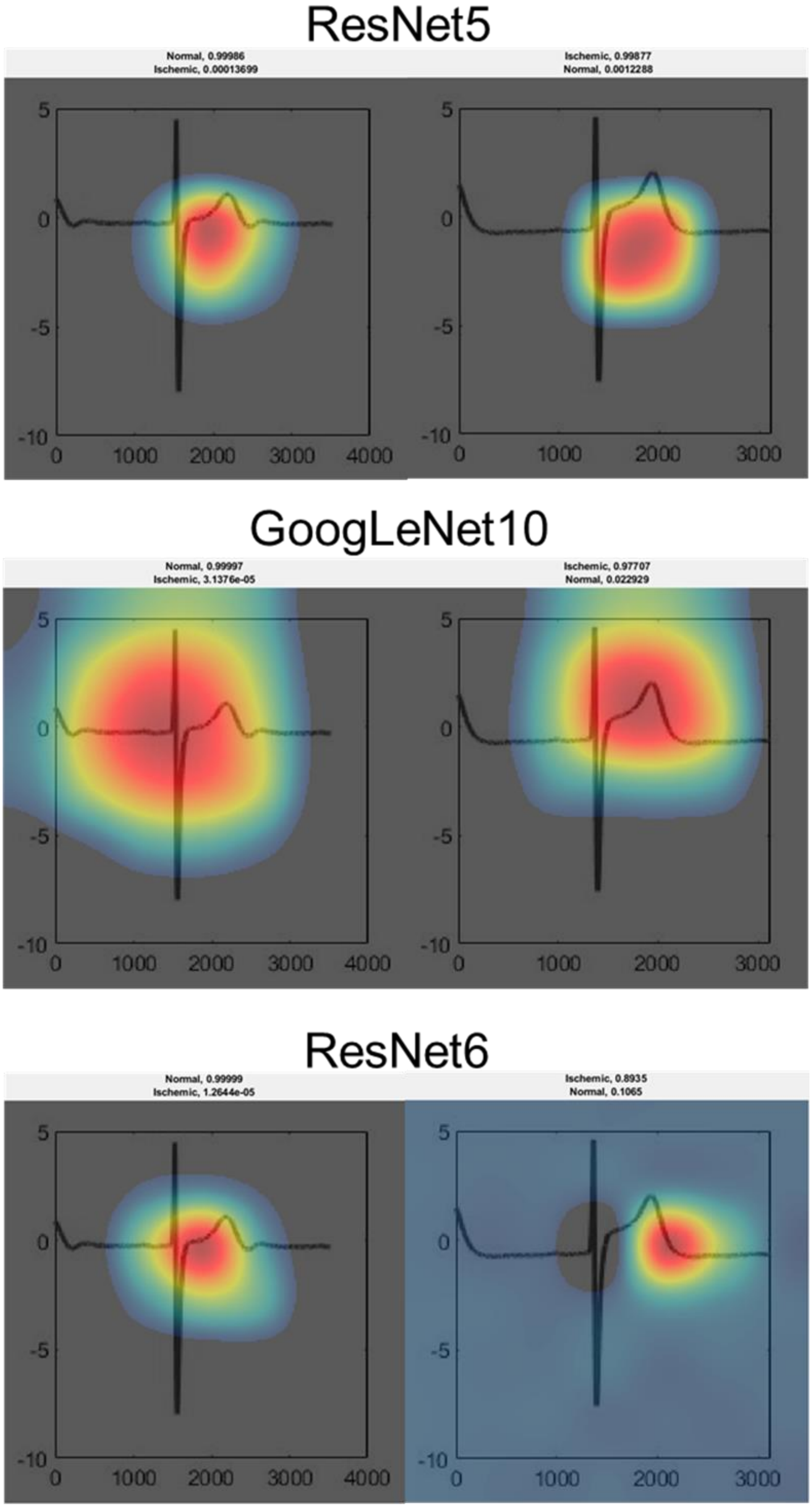

Figure 4: Visualization of network activation patterns of the three best performing CNN *Red regions contributed most to the network class prediction. Please note the rather uncertain prediction of ResNet6 on the ischemic ECG.*

3.3.6 Discussion

When tested in an experimental setting with systematically induced, complete coronary balloon occlusion, thus establishing the reference of non-ischemic and ischemic myocardium, these conditions are distinguishable by icECG with equal accuracy using manually determined icECG ST-segment shift and convolutional network analysis. The underlying morphology responsible for the network prediction differs between the trained networks, but for myocardial ischemia detection focuses mainly on the icECG ST-segment and the T-wave.

Assessment of myocardial ischemia by intracoronary ECG

Slightly different from previously published results, icECG ST-segment shift showed a lower diagnostic accuracy (0.903±0.043 for the evaluation data versus 0.963±0.029[4]), and was less pronounced during myocardial ischemia in the current analysis (0.915±0.972mV vs. 1.272±0.998mV). This resulted in a lower optimal cut-off level for ischemia detection at 0.279mV (compared to 0.365mV). This difference is related to biological and not statistical variance between the recent and the actual investigation. The extent of myocardial ischemia, i.e., the cause of icECG ST-segment shift, depends on multiple factors, namely duration of coronary occlusion, ischemic area at risk for infarction, myocardial oxygen consumption and coronary collateral blood supply[25]:

$$\text{Extent of icECG ST-segment shift} \triangleq \frac{\text{Duration of occlusion} * \text{Area at risk} * \text{Myocardial oxygen consumption}}{\text{Coronary collateral blood supply}}$$

$$\triangleq: being\ related\ to$$

While the duration of coronary artery occlusion was identical in the recent and the present study (i.e., 60 seconds), the other determinants of myocardial ischemia differed. Compared to the previous analysis[4], where left anterior descending coronary artery was the most frequent study vessel, the right coronary artery currently served as the most frequent study vessel, causing a relevant decrease in the myocardial area at risk.

In addition, considering the higher heart rate during myocardial ischemia in the previous study (95±25 vs 72±14 beats per minute), it can be assumed that myocardial oxygen consumption (resulting from ventricular wall stress, heart rate and contractility) was increased as well. Last, coronary collateral function presently did not serve as an exclusion criterion. Accordingly, CFI was significantly higher in the present than the former analysis: 0.123±0.081 vs. 0.084±0.055 ($p<0.001$).

Application of CNN on icECG

Based on the ubiquitous availability of the ECG in clinical practice, and together with the rise of wearable devices, an increasing amount of ECG data is available. Effective processing of these data by physicians is not feasible even if it could provide valuable information. Thus, several studies used CNN to process ECGs, primarily with the intention of classifying them according to their rhythm[26-29]. Further, one study has demonstrated that CNN trained on a per-patient level may be an interesting, low-computational possibility to automatically monitor long-term continuous ECG data (e.g., output of implantable devices)[30].

Aside from arrhythmia detection, CNN has also been used to distinguish between other cardiac pathologies. Van de Leur et al. used a huge data set with >300’000 ECG recordings to train a CNN to perform a triage into four categories (normal, not acutely abnormal, subacutely abnormal and acutely abnormal)[31]. A panel of five cardiologist served as the reference. Deep neural network in that study demonstrated an excellent overall discrimination with an AUC of 0.93. So called class activation mapping has shown that the network based its predictions on the same regions in the ECG as would physicians[31].

Makimoto et al. trained a small 6-layered CNN on 289 images of a 12-lead ECG resulting in a comparable capability as physicians in recognizing myocardial ischemia on ECG[32]. Visualization of the activation patterns revealed that the CNN was triggered by elevated ST-T-segments. However and as stated by the authors, conclusions of this visualization have to be drawn carefully, as it has been shown that class activation mapping can fail to properly localize objects in an image if the image contains multiple occurrences of the same classification (as it is the case in a 12-lead ECG)[32].

Comparison of CNN and manual icECG ST-segment shift measurement

This study demonstrated that transfer learning of a pretrained CNN is highly accurate for detecting myocardial ischemia as reflected by icECG. CNN focuses on distinctive features in the icECG ST-segment and the T-wave. The pathophysiologic basis of these characteristic patterns is the reduced resting potential of the ischemic myocardial cells, caused by a pathologic ion current across the injured cell membrane with subsequent distortion of the normally isoelectric ST-segment[4, 36]. In addition, inadequate energy supply during ischemia directly affects the ventricular repolarization and thus, the morphology and duration of the T-wave[36]. As shown by our previous study, icECG ST-segment shift measured at the J-point outperformed all other icECG parameters in differentiating between non-ischemic and ischemic icECG tracings (area under the ROC curve of 0.963±0.029 vs 0.811±0.057 for amplitude of the T-wave[4]). Hence, it is remarkable that CNN, which focused on the same ECG morphologies revealed a trend to even higher diagnostic accuracy than manually obtained icECG ST-segment shift for ischemia detection.

As compared to icECG ST-segment shift, CNN were not limited to a single, “hand-picked” but to all icECG parameters. Hence, combination of two characteristics, e.g., ST-segment and T-wave integral, enabled the numerically higher diagnostic accuracy. Most CNN used one morphology for the non-ischemic (e.g., QRS-complex), and another one for the ischemic images. Thus, they were also able to differentiate between the physiologic and pathophysiologic state of ischemia on a larger scale.

IcECGs recorded in the RCA are especially challenging as they often show a large atrial signal (P-wave), unstable isoelectric lines and negative T-waves (supplemental figures 1-10, middle image in both rows). Further, recording of the icECG in the proximal and mid RCA assesses myocardial ischemia in the low-mass right ventricle (i.e., small ischemic signal) further complicating ischemia detection. Thus, it is not astonishing that 14 out of the 17 (82%) falsely classified images of RN5 were recorded in the RCA, the latter of which represented 60% of the data (see supplemental figure 11 for all falsely classified icECGs of RN5). Nevertheless, and despite the high proportion of RCA icECG recordings, CNN were able to distinguish between non-ischemic and ischemic images with high accuracy demonstrating the robustness of the method.

Limitations

The biggest limitation of the application of CNN on various problems lies in the very nature of neural networks, i.e., “its complicated interconnected hierarchical representations of the training data to produce its predictions”[34] on unseen data. Thus, interpretation of these predictions is challenging and often referred to as a “black box” problem[34]. While class activation mapping offers a visualization of the activation patterns and enables conclusions on the general distinction procedure, prediction can remain unexplainable. Supplemental figure 11 demonstrates all falsely predicted icECG images of RN5. Most of them are understandable, e.g., ischemic morphology of a non-ischemic icECG recorded in the RCA. However, some predictions are incomprehensible. Track-down of the activation pattern in each convolutional layer would possibly enlighten the erroneous predictions. However, such a process within a network architecture with numerous convolutional layers is extremely complex and time-consuming.

Further, the used networks were exceeding the complexity of the presented task by far. This was, however, on purpose, as the objective of our study was to demonstrate the feasibility of a hypothesis-generating process. Thus, to ensure generalizability to other, future tasks, highly capable pretrained networks were used in combination with excessive data augmentation to prevent overfitting. Hence, this method does not provide the most appropriate and efficient CNN, but rather a well-performing CNN to allow generating hypotheses, which need further verification. In addition, the presented task (i.e.,to distinguish between non-ischemic and ischemic icECG tracings), would have been possible with raw icECG signal data without the conversion into jpg-images associated with an increase of data points and a loss of details. In this case, pretraining would have been feasible with open source ECG databases. However, this approach would limit the generalizability of the proposed, deep learning approach, as the requirements are not ubiquitous applicable.

While transfer learning of pretrained CNN enabled the application of networks with a high capacity on a small data set, this approach determines also the format of the input data. Thus, data has to be images with restricted input size, which limits the resolution. A requirement, which could cause the missing of subtle patterns. In addition, quantitative assessment is not possible using this deep learning approach and it requires a certain accordance between the original task and the problem to be addressed. As this requirement is not always given, it is possible that the presented approach does not provide accurate network predictions. However, taken into account the relatively low effort and the potentially valuable information, we recommend to try this approach at least once on a particular problem.

Finally, ROC-analysis with binary predictors (i.e., the dichotomous classification by the CNN) is a potential misleading metric[35]. However, the ROC-analysis was not the only statistical assessment of the network performance and all (consistent) results were shown.

Implications

This study demonstrates the feasibility of a hypothesis generating process using transfer learning of pretrained CNN on a small (n<1000) data set. Contrary to previously conducted ECG studies using deep learning, the goal of this study was not to develop a diagnostic aid for physicians in daily clinical practice, but rather to enable an unbiased view on a well-known clinical phenomenon, i.e., myocardial ischemia. Implementation of this view did not require big data or specialized computational hardware. Instead, a small but well-defined data set was used to perform transfer learning on pretrained CNN using single CPU computers. Hence, the proposed approach is feasible without extensive computational hardware and for a wide variety of clinical problems. Conditions are the presence of a well-defined, independent reference (absent vs present ischemia), and the possibility to transform the data into images (as most of the high capacity, open-available CNN were trained on the ImageNet[13] database).

In the present study, data-derived features used by the CNN to distinguish between absent or present myocardial ischemia were similar to the common practices and focused mainly on the icECG ST-segment and the T-wave. Hence, the hypothesis-generating process did not provide unknown ischemic patterns but rather confirmed the common parameters used to quantify myocardial ischemia in the icECG.

Conclusion

When tested in an experimental setting with artificially induced coronary artery occlusion, quantitative icECG ST-segment shift and CNN using pathophysiologic prediction criteria detect myocardial ischemia with similarly high accuracy.

Funding

None.

Disclosures

None.

3.3.7 Tables

Table 1: Patient characteristics

	Overall
Number of patients	228
Patient characteristics	
Age (years)	68±10
Female gender (%)	17
Body mass index (kg/m^2)	28±5
Angina pectoris before intervention (%)	50
Duration of angina pectoris (months)	8±17
Canadian cardiovascular society class of angina pectoris	2.13±0.97
Diabetes mellitus (%)	34
Arterial hypertension (%)	75
Current smoking (%)	17
Cumulative pack years of cigarettes	38±25
Dyslipidemia (%)	80
Family history for coronary artery disease, CAD (%)	29
Prior myocardial infarction (%)	44
Medical treatment	
Aspirin (%)	85
Platelet inhibitor (%)	40
Calcium channel-blocker (%)	28
Beta-blocker (%)	61
Nitrate (%)	14
Oral anticoagulation (%)	18
Statin (%)	78
ACE inhibitor or ARB (%)	70
Diuretics (%)	38

Table 2: ST-segment shift and target vessel distribution

	Overall	Non-ischemic	Ischemic	p-value
Overall, n	**893**	**491**	**402**	**-**
ST-segment shift at J-point (mV)	-	0.004±0.300	1.015±0.956	p<0.001
Left anterior descending (LAD), n	278	147	131	p=0.630
Left circumflex coronary artery (LCX), n	196	107	89	
Right coronary artery (RCA), n	419	237	182	
Training data	**668**	**368**	**300**	**-**
ST-segment shift at J-point (mV)	-	-0.007±0.309	1.050±0.950	p<0.001
Left anterior descending (LAD), n	229	119	110	p=0.456
Left circumflex coronary artery (LCX), n	154	85	69	
Right coronary artery (RCA), n	285	164	121	
Validation data	**167**	**92**	**75**	**-**
ST-segment shift at J-point (mV)	-	0.042±0.290	0.931±0.820	p<0.001
Left anterior descending (LAD), n	46	26	20	p=0.978
Left circumflex coronary artery (LCX), n	35	19	16	
Right coronary artery (RCA), n	86	47	39	
Examination data	**58**	**31**	**27**	**-**
ST-segment shift at J-point (mV)		0.026±0.197	0.870±1.326	p=0.003
Left anterior descending (LAD), n	3	2	1	p=0.876
Left circumflex coronary artery (LCX), n	7	3	4	
Right coronary artery (RCA), n	48	26	22	
Validation + Examination data	**225**	**123**	**102**	**-**
ST-segment shift at J-point (mV)	-	-0.038.±0.269	0.915±0.972	p<0.001
Left anterior descending (LAD), n	49	28	21	p=0.897
Left circumflex coronary artery (LCX), n	42	22	20	
Right coronary artery (RCA), n	134	73	61	

Table 3: Prediction and performance of the best ten trained networks

Convolutional neural network	*True* *Predicted*	**Non-ischemic**	**Ischemic**	**Accuracy**	**Sensitivity**	**Specificity**	**F1-score**	**Activating Morphology**
ResNet5: L1e-4_D0.80_M14_E60	Non-ischemic	113	7	92.44	93	92	0.918	Area under the ST-segment and the T-wave
	Ischemic	10	95					
GoogLeNet10: L1e-4_D0.26_M18_E28	Non-ischemic	117	11	92.44	89	95	0.915	QRS + J-point
	Ischemic	6	91					ST-segment + T-wave
ResNet6: L2e-4_D0.52_M25_E60	Non-ischemic	118	12	92.44	88	96	0.914	ST-segment
	Ischemic	5	90					End of T-wave
GoogLeNet2: L1e-4_D0.25_M18_E20	Non-ischemic	114	9	92.00	91	93	0.912	QRS + J-point
	Ischemic	9	93					Mainly J-Point
ResNet7: L1e-4_D0.60_M14_E60	Non-ischemic	116	11	92.00	89	94	0.910	Mainly T-wave
	Ischemic	7	91					
GoogLeNet8: L1e-4_D0.45_M18_E25	Non-ischemic	119	14	92.00	86	97	0.907	QRS + J-point
	Ischemic	4	88					Mainly J-Point
GoogLeNet12: L1e-4_D0.6_M15_E20	Non-ischemic	120	15	92.00	85	98	0.906	Small QRS
	Ischemic	3	87					J-Point
ResNet10: L1e-4_D0.63_M12_E60	Non-ischemic	113	9	91.56	91	92	0.907	ST-segment
	Ischemic	10	93					T-wave
ResNet8: L1e-4_D0.64_M22_E60	Non-ischemic	121	17	91.56	83	98	0.899	J-point/ST-segment
	Ischemic	2	85					T-wave
GoogLeNet13: L1e-4_D0.3_M20_E30	Non-ischemic	121	17	91.56	83	98	0.899	QRS
	Ischemic	2	85					Mainly T-wave

Order according to accuracy. L = learning rate, D = dropout rate, M = minibatch size, E = number of epochs.
Please note that all ResNet-networks were trained with a preliminary termination term (thus, all had E60 but were automatically stopped by the training algorithm).

3.3.8 References

1. Ibanez B, James S, Agewall S, Antunes MJ, Bucciarelli-Ducci C, Bueno H, et al. 2017 ESC Guidelines for the management of acute myocardial infarction in patients presenting with ST-segment elevation: The Task Force for the management of acute myocardial infarction in patients presenting with ST-segment elevation of the European Society of Cardiology (ESC). European heart journal. 2018;39(2):119-77.
2. Meier B, Rutishauser W. Coronary pacing during percutaneous transluminal coronary angioplasty. Circulation. 1985;71(3):557-61.
3. Pande AK, Meier B, Urban P, Moles V, Dorsaz PA, Favre J. Intracoronary electrocardiogram during coronary angioplasty. American heart journal. 1992;124(2):337-41.
4. Bigler MR, Zimmermann P, Papadis A, Seiler C. Accuracy of intracoronary ECG parameters for myocardial ischemia detection. Journal of electrocardiology. 2020;64:50-7.
5. Goodfellow I, Bengio Y, Courville A. Deep Learning: MIT Press; 2016.
6. LeCun Y, Bengio Y, Hinton G. Deep learning. Nature. 2015;521(7553):436-44.
7. Bigler MR, Stoller M, Tschannen C, Grossenbacher R, Seiler C. Effect of permanent right internal mammary artery occlusion on right coronary artery supply: A randomized placebo-controlled clinical trial. American heart journal. 2020.
8. Bigler MR, Grossenbacher R, Stoller M, Tschannen C, Seiler C, cardiology I. Functional assessment of myocardial ischemia by intracoronary electrocardiogram. accepted for publication.
9. Stoller M, Seiler C. Effect of Permanent Right Internal Mammary Artery Closure on Coronary Collateral Function and Myocardial Ischemia. Circulation Cardiovascular interventions. 2017;10(6).
10. Vogel R, Zbinden R, Indermuhle A, Windecker S, Meier B, Seiler C. Collateral-flow measurements in humans by myocardial contrast echocardiography: validation of coronary pressure-derived collateral-flow assessment. European heart journal. 2006;27(2):157-65.
11. Seiler C, Fleisch M, Garachemani A, Meier B. Coronary collateral quantitation in patients with coronary artery disease using intravascular flow velocity or pressure measurements. Journal of the American College of Cardiology. 1998;32(5):1272-9.
12. Trask AW. Neuronale Netze und Deep Learning kapieren: mitp; 2020.
13. Deng J, Dong W, Socher R, Li L, Kai L, Li F-F, editors. ImageNet: A large-scale hierarchical image database. 2009 IEEE Conference on Computer Vision and Pattern Recognition; 2009 20-25 June 2009.
14. Szegedy C, Liu W, Jia Y, Sermanet P, Reed S, Anguelov D, et al. Going Deeper with Convolutions. CoRR. 2014;abs/1409.4842.
15. LeCun Y, Bottou L, Bengio Y, Haffner P. Gradient-Based Learning Applied to Document Recognition. Proceedings of the IEEE1998.
16. Lundervold AS, Lundervold A. An overview of deep learning in medical imaging focusing on MRI. Z Med Phys. 2019;29(2):102-27.
17. He K, Zhang X, Ren S, Sun J. Deep Residual Learning for Image Recognition. CoRR. 2015;abs/1512.03385.
18. Srivastava N, Hinton G, Krizhevsky A, Sutskever I, Salakhutdinov R. J Mach Learn Res. 2014;15:1929–58.
19. Polyak BT. Some methods of speeding up the convergence of iteration methods. USSR Computational Mathematics and Mathematical Physics. 1964;4(5):1-17.
20. Diederik P Kingma, Ba J. Adam: A Method for Stochastic Optimization. CoRR. 2014;arXiv:1412.6980.
21. Bergstra J, Bengio Y. Random search for hyper-parameter optimization. Journal of Machine Learning Research 2012;13:281-305.
22. Bengio Y. Gradient-Based Optimization of Hyperparameters. Neural Computation. 2000;12(8):1889-900.
23. Zhou B, Khosla A, Lapedriza A, Oliva A, Torralba A. Learning Deep Features for Discriminative Localization. CoRR. 2015;abs/1512.04150.

24. Selvaraju RR, Cogswell M, Das A, Vedantam R, Parikh D, Batra D, editors. Grad-CAM: Visual Explanations from Deep Networks via Gradient-Based Localization. 2017 IEEE International Conference on Computer Vision (ICCV); 2017 22-29 Oct. 2017.
25. Seiler C, Engler R, Berner L, Stoller M, Meier P, Steck H, et al. Prognostic relevance of coronary collateral function: confounded or causal relationship? Heart (British Cardiac Society). 2013;99(19):1408-14.
26. Attia ZI, Noseworthy PA, Lopez-Jimenez F, Asirvatham SJ, Deshmukh AJ, Gersh BJ, et al. An artificial intelligence-enabled ECG algorithm for the identification of patients with atrial fibrillation during sinus rhythm: a retrospective analysis of outcome prediction. Lancet (London, England). 2019;394(10201):861-7.
27. Acharya UR, Fujita H, Lih OS, Hagiwara Y, Tan JH, Adam M. Automated detection of arrhythmias using different intervals of tachycardia ECG segments with convolutional neural network. Information Sciences. 2017;405:81-90.
28. Hannun AY, Rajpurkar P, Haghpanahi M, Tison GH, Bourn C, Turakhia MP, et al. Cardiologist-level arrhythmia detection and classification in ambulatory electrocardiograms using a deep neural network. Nature medicine. 2019;25(1):65-9.
29. Ribeiro AH, Ribeiro MH, Paixão GMM, Oliveira DM, Gomes PR, Canazart JA, et al. Automatic diagnosis of the 12-lead ECG using a deep neural network. Nature Communications. 2020;11(1):1760.
30. Kiranyaz S, Ince T, Gabbouj M. Real-Time Patient-Specific ECG Classification by 1-D Convolutional Neural Networks. IEEE Transactions on Biomedical Engineering. 2016;63(3):664-75.
31. van de Leur RR, Blom LJ, Gavves E, Hof IE, van der Heijden JF, Clappers NC, et al. Automatic Triage of 12-Lead ECGs Using Deep Convolutional Neural Networks. Journal of the American Heart Association. 2020;9(10):e015138.
32. Makimoto H, Höckmann M, Lin T, Glöckner D, Gerguri S, Clasen L, et al. Performance of a convolutional neural network derived from an ECG database in recognizing myocardial infarction. Scientific reports. 2020;10(1):8445.
33. Yan GX, Lankipalli RS, Burke JF, Musco S, Kowey PR. Ventricular repolarization components on the electrocardiogram: cellular basis and clinical significance. Journal of the American College of Cardiology. 2003;42(3):401-9.
34. Lundervold AS, Lundervold A. An overview of deep learning in medical imaging focusing on MRI. Zeitschrift für Medizinische Physik. 2019;29(2):102-27.
35. Muschelli J. ROC and AUC with a Binary Predictor: a Potentially Misleading Metric. Journal of Classification. 2020;37(3):696-708.

3.3.9 Supplemental material

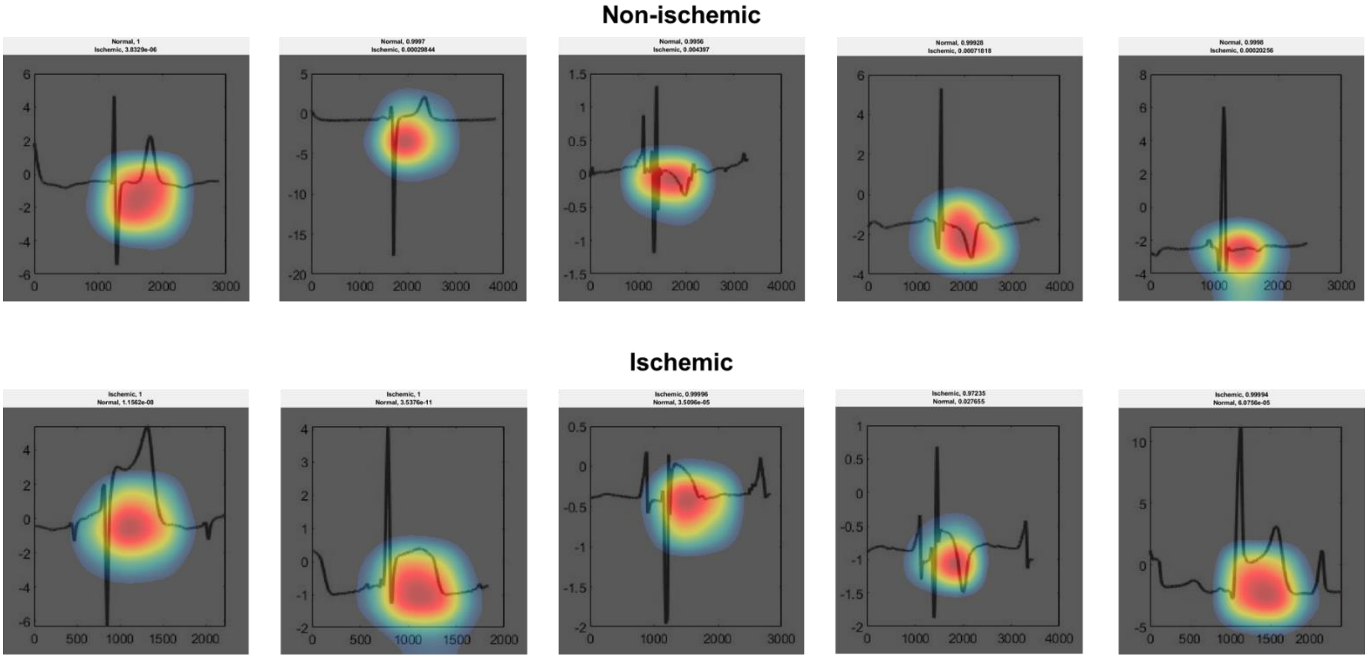

Supplemental figure 1: Visualization of network activation patterns of ResNet5 *Red regions contributed most to the network class prediction.*

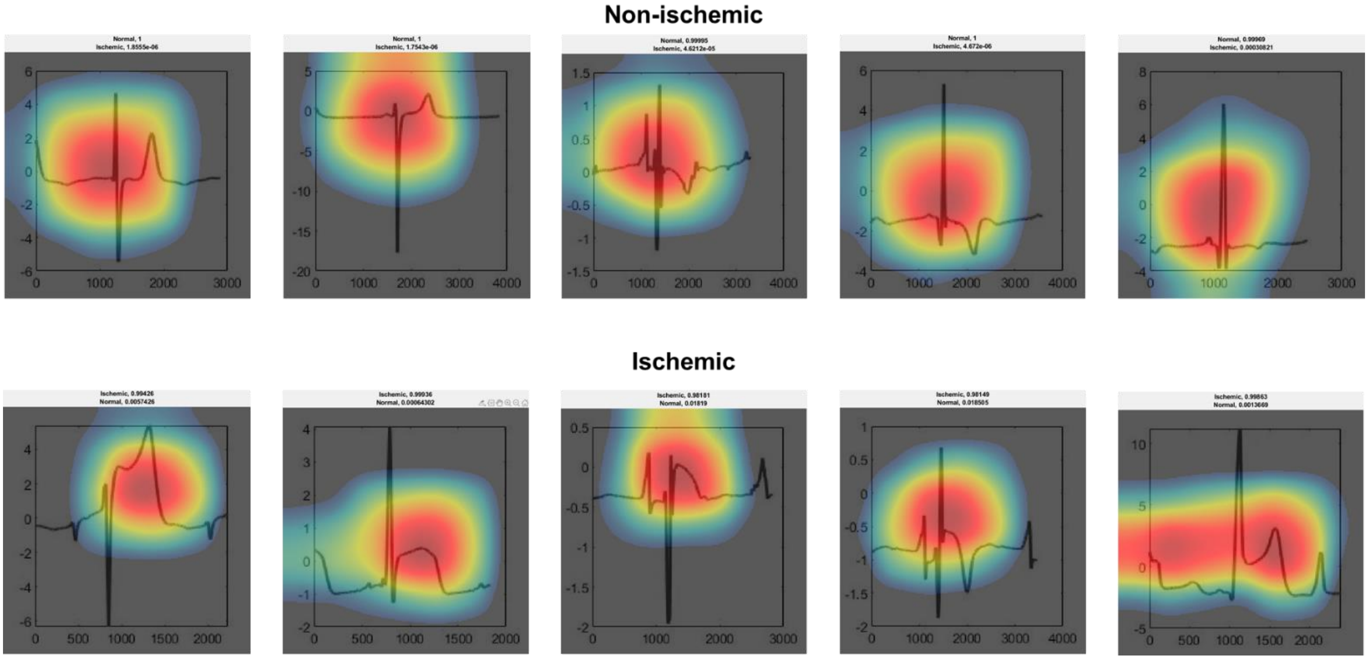

Supplemental figure 2: Visualization of network activation patterns of GoogLeNet10 *Red regions contributed most to the network class prediction.*

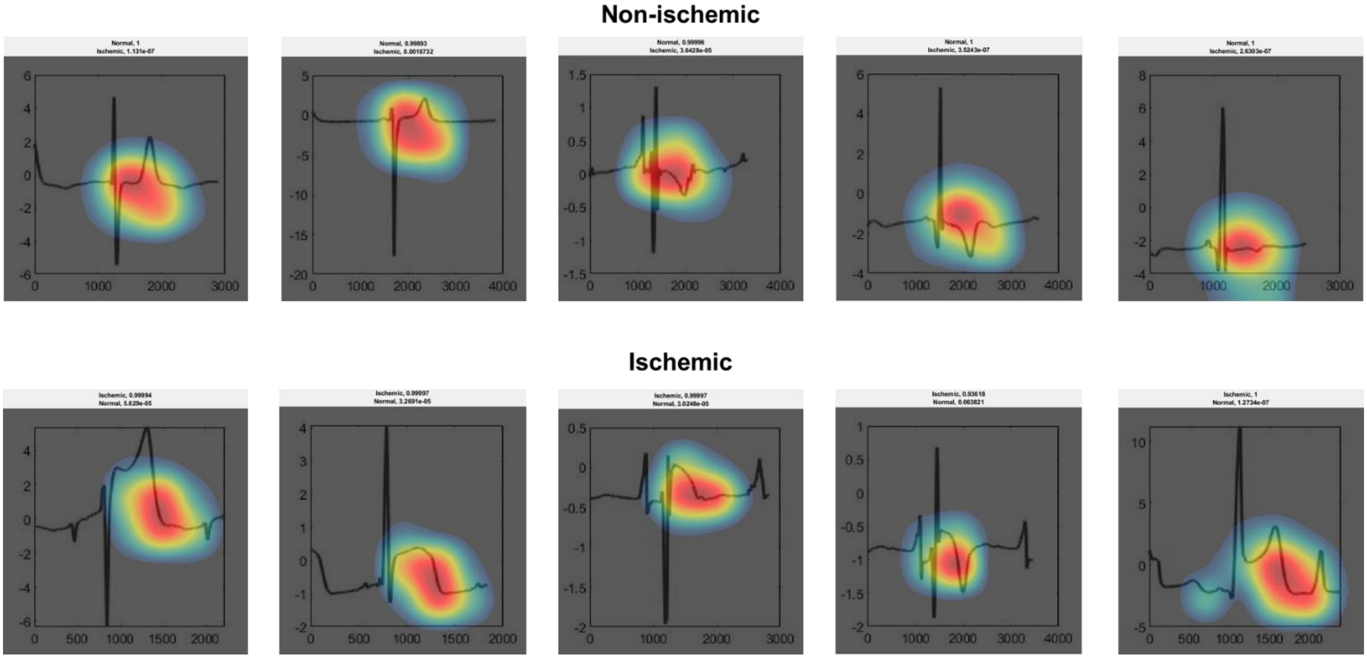

Supplemental figure 3: Visualization of network activation patterns of ResNet6 *Red regions contributed most to the network class prediction.*

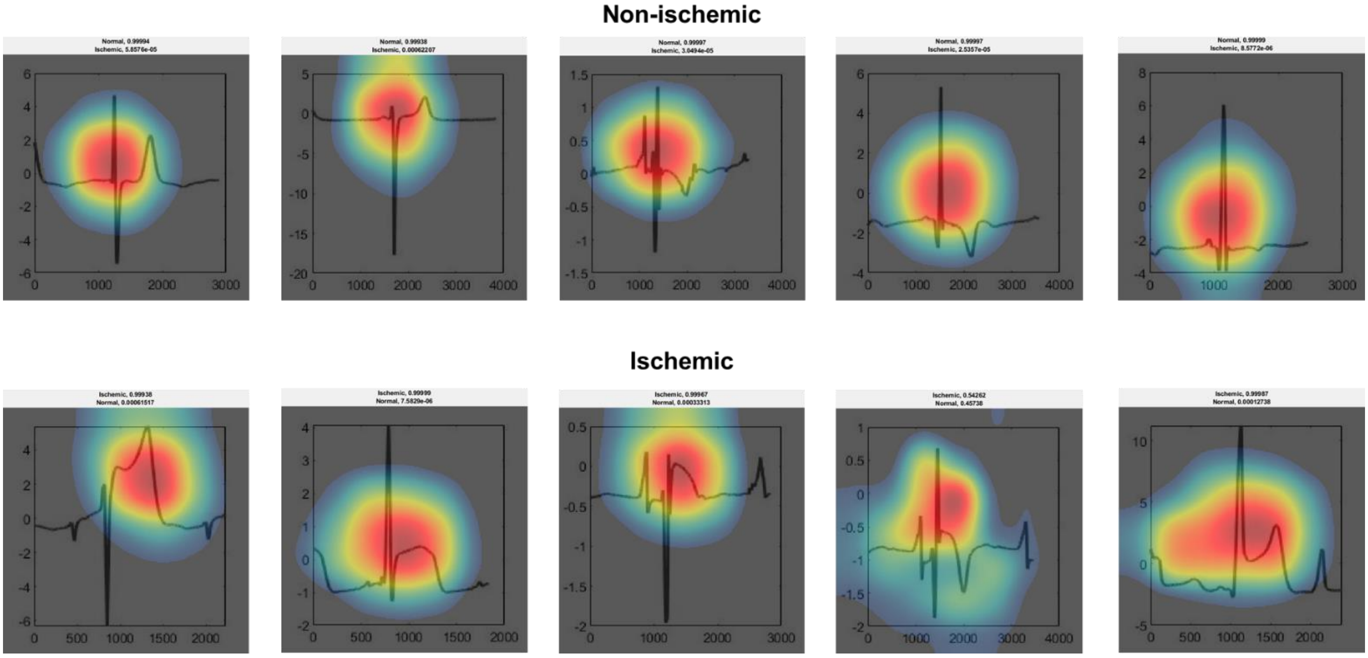

Supplemental figure 4: Visualization of network activation patterns of GoogLeNet2 *Red regions contributed most to the network class prediction.*

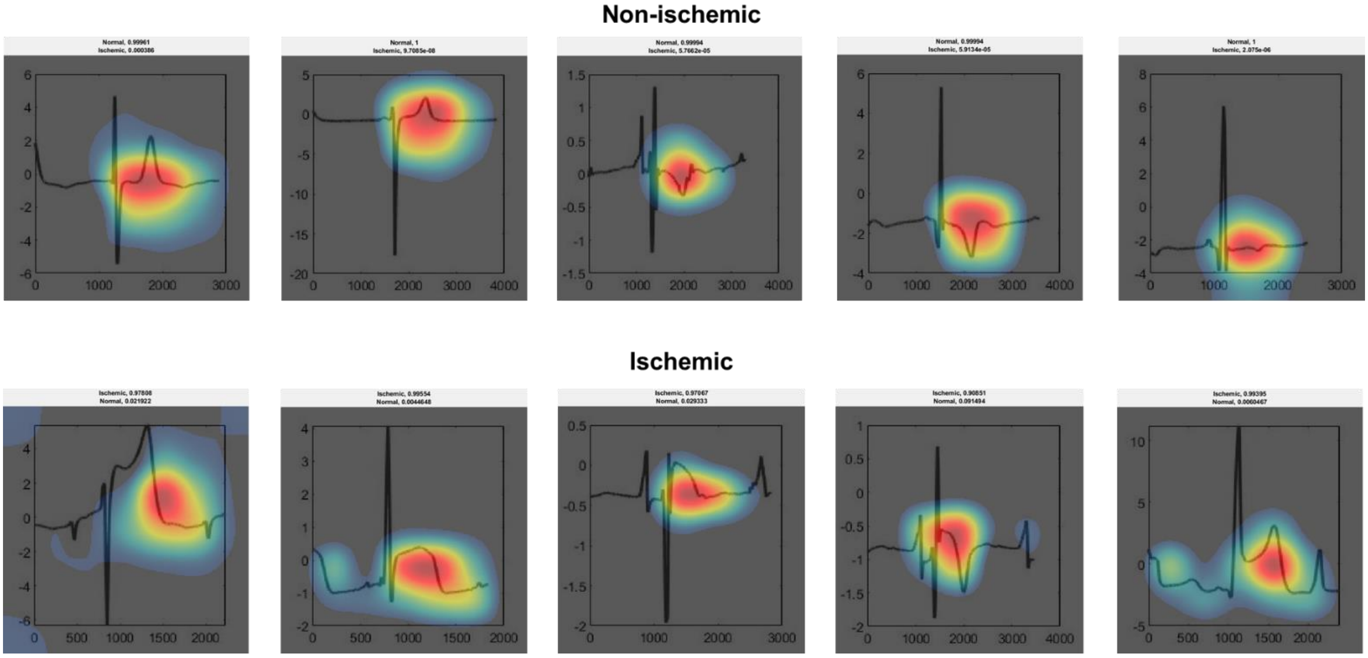

Supplemental figure 5: Visualization of network activation patterns of ResNet7 *Red regions contributed most to the network class prediction.*

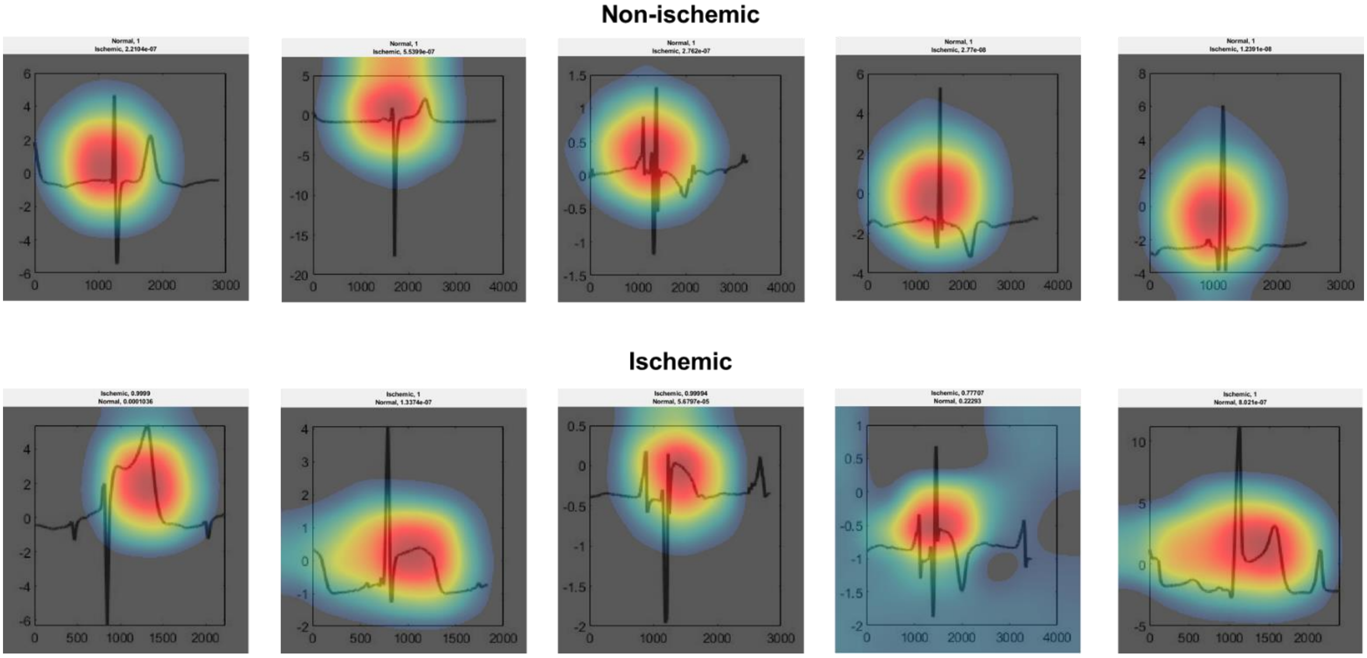

Supplemental figure 6: Visualization of network activation patterns of GoogLeNet8 *Red regions contributed most to the network class prediction.*

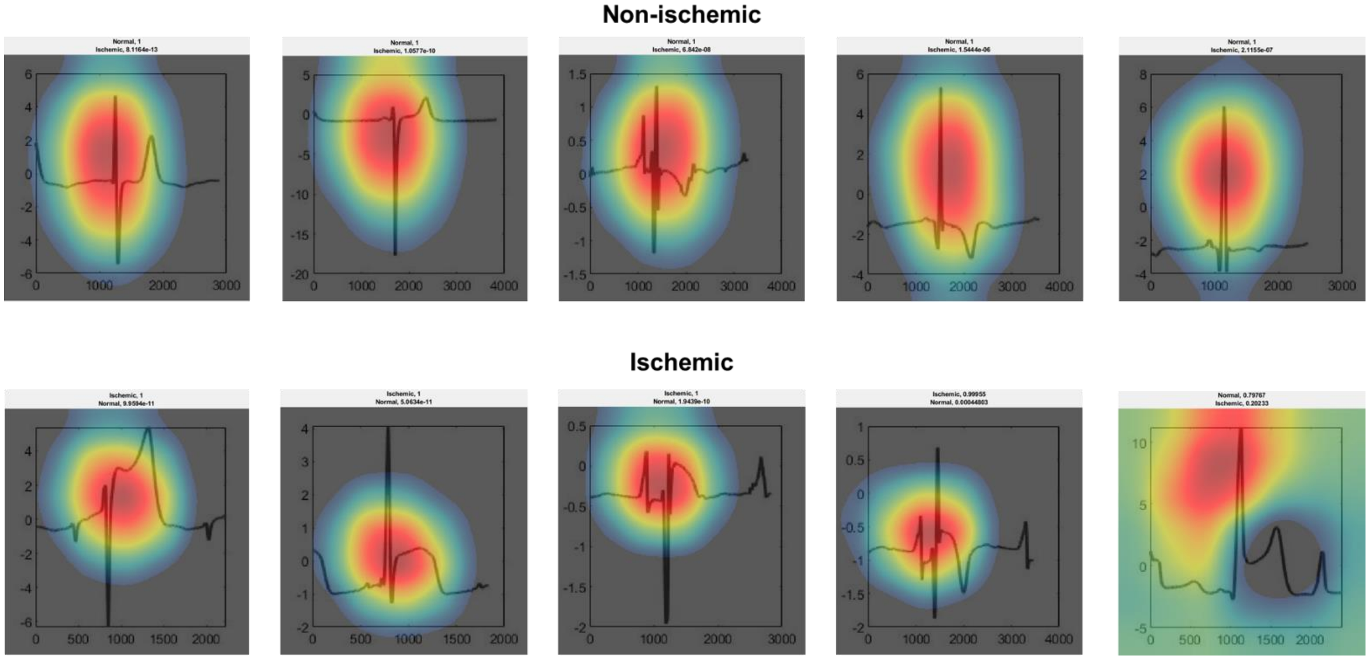

***Supplemental figure 7: Visualization of network activation patterns of GoogLeNet12** Red regions contributed most to the network class prediction.*

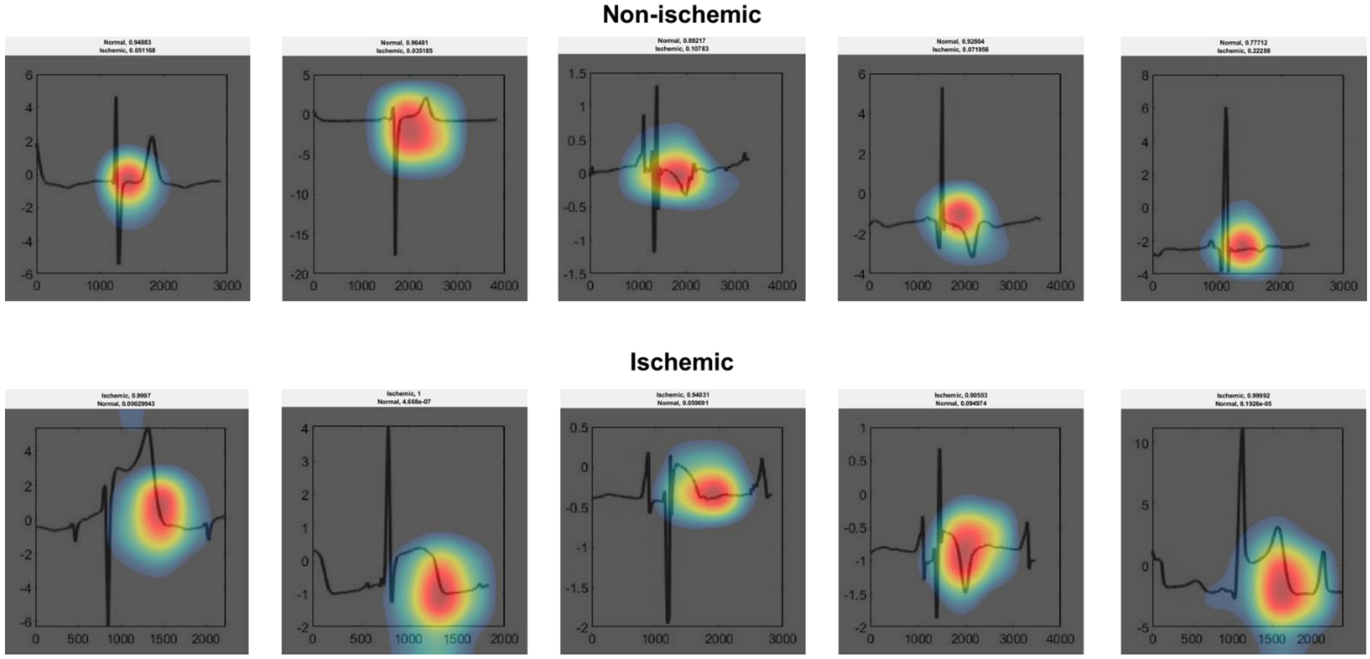

***Supplemental figure 8: Visualization of network activation patterns of ResNet10** Red regions contributed most to the network class prediction.*

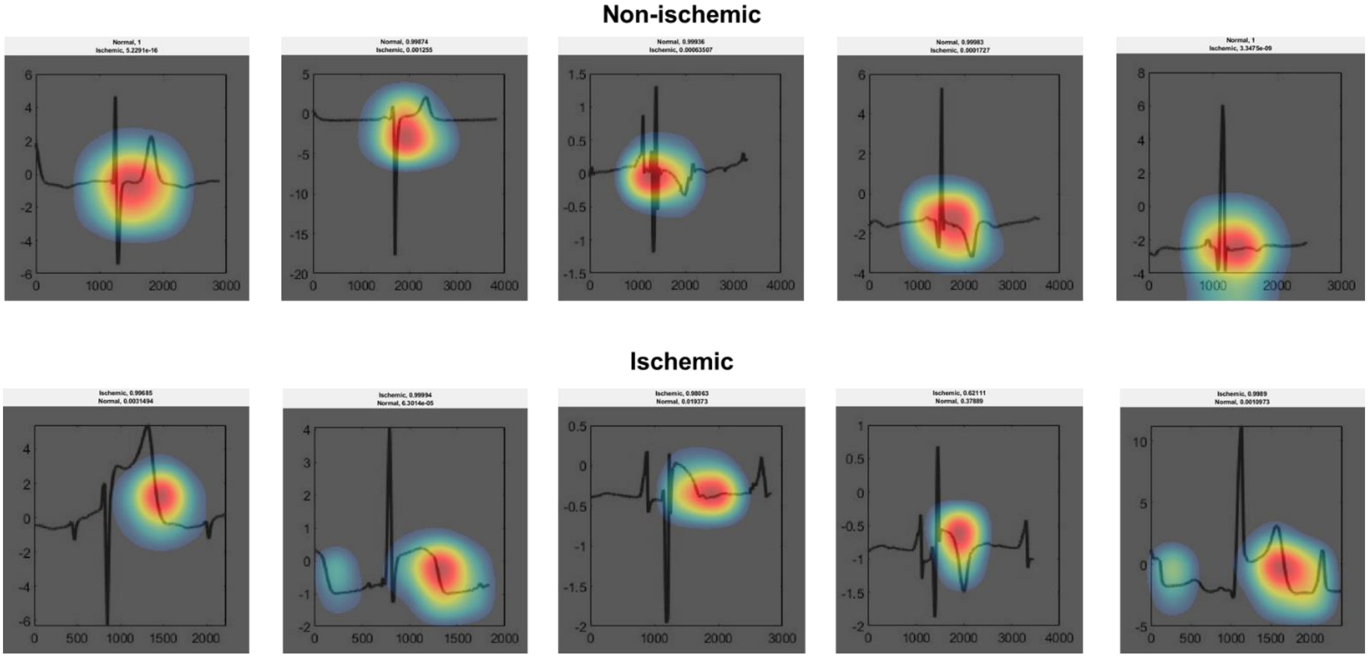

Supplemental figure 9: Visualization of network activation patterns of ResNet8 *Red regions contributed most to the network class prediction.*

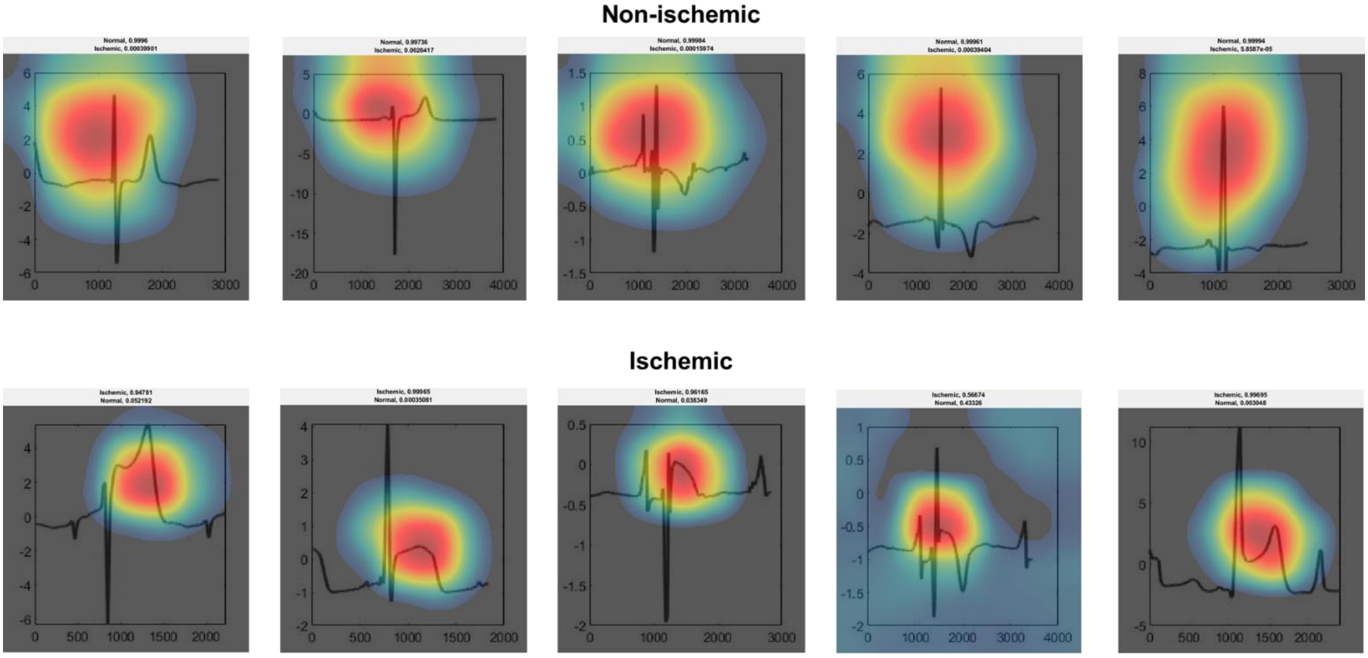

Supplemental figure 10: Visualization of network activation patterns of GoogLeNet13 *Red regions contributed most to the network class prediction.*

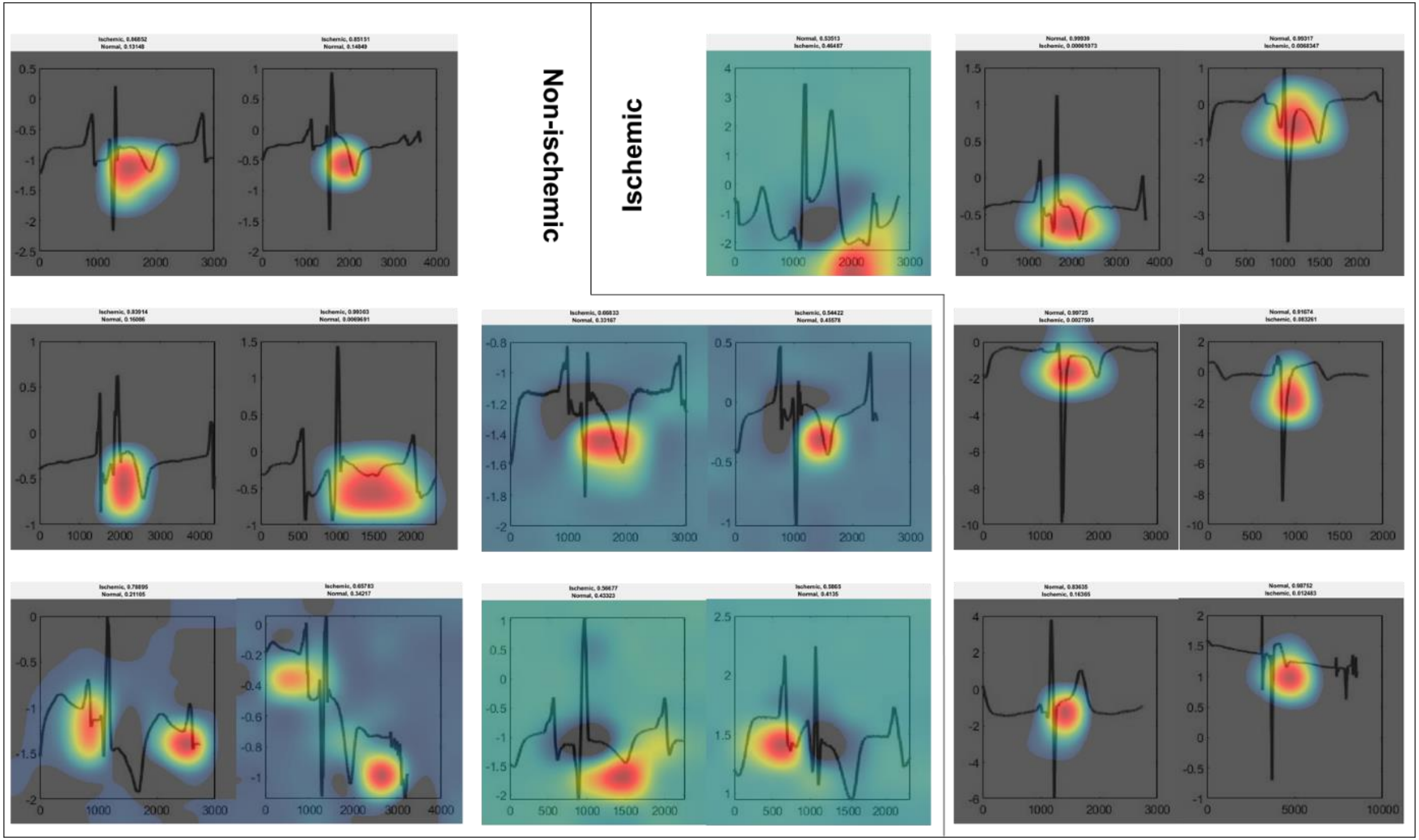

Supplemental figure 11: Visualization of network activation patterns of all false prediction of ResNet5 *Red regions contributed most to the network class prediction. While some predictions are understandable (left and right column), others are incomprehensible (middle column).*

Supplemental tables

Supplemental table 1: Nonparametric receiver-operating characteristic curves of manually determined icECG ST-segment shift and corresponding collateral flow index and heart rate

	Overall
Overall, n	**893**
AUC	0.932±0.018
CFI (mmHg/mmHg)	0.116±0.085
Heart rate (bpm)	73±14
Training data, n	**668**
AUC	0.941±0.019
CFI (mmHg/mmHg)	0.114±0.086
Heart rate (bpm)	74±14
Validation data, n	**167**
AUC	0.897±0.051
CFI (mmHg/mmHg)	0.122±0.080
Heart rate (bpm)	72±14
Examination data, n	**58**
AUC	0.927±0.074
CFI (mmHg/mmHg)	0.126±0.084
Heart rate (bpm)	74±16
Validation + Examination data, n	**225**
AUC	0.903±0.043
CFI (mmHg/mmHg)	0.123±0.081
Heart rate (bpm)	72±14
AUC = Area under the ROC-curve; CFI = Collateral flow index	

Supplemental table 2: In-detail performance of the ten best performing networks

	Validation Data				Examination Data				Validation + Examination Data			
Convolutional neural network	True Predicted	**Non-Ischemic**	**Ischemic**	**Accuracy**	True Predicted	**Non-Ischemic**	**Ischemic**	**Accuracy**	True Predicted	**Non-Ischemic**	**Ischemic**	**Accuracy**
Resnet5: L1e-4_D0.80_M14_E60	Non-Ischemic	88	6	94.01	Non-Ischemic	25	1	87.93	Non-Ischemic	113	7	92.44
	Ischemic	4	69		Ischemic	6	26		Ischemic	10	95	
GoogleNet10: L1e-4_D0.26_M18_E28	Non-Ischemic	88	5	94.61	Non-Ischemic	29	6	86.21	Non-Ischemic	117	11	92.44
	Ischemic	4	70		Ischemic	2	21		Ischemic	6	91	
Resnet6: L2e-4_D0.52_M25_E60	Non-Ischemic	90	10	92.81	Non-Ischemic	28	2	91.38	Non-Ischemic	118	12	92.44
	Ischemic	2	65		Ischemic	3	25		Ischemic	5	90	
GoogleNet2: L1e-4_D0.25_M18_E20	Non-Ischemic	85	7	91.62	Non-Ischemic	29	2	93.10	Non-Ischemic	114	9	92.00
	Ischemic	7	68		Ischemic	2	25		Ischemic	9	93	
Resnet7: L1e-4_D0.60_M14_E60	Non-Ischemic	87	8	92.22	Non-Ischemic	29	3	91.38	Non-Ischemic	116	11	92.00
	Ischemic	5	67		Ischemic	2	24		Ischemic	7	91	
GoogleNet8: L1e-4_D0.45_M18_E25	Non-Ischemic	89	9	92.81	Non-Ischemic	30	5	89.66	Non-Ischemic	119	14	92.00
	Ischemic	3	66		Ischemic	1	22		Ischemic	4	88	
GoogleNet12: L1e-4_D0.6_M15_E20	Non-Ischemic	90	11	92.22	Non-Ischemic	30	4	91.38	Non-Ischemic	120	15	92.00
	Ischemic	2	64		Ischemic	1	23		Ischemic	3	87	
Resnet10: L1e-4_D0.63_M12_E60	Non-Ischemic	84	8	90.42	Non-Ischemic	29	1	94.83	Non-Ischemic	113	9	91.56
	Ischemic	8	67		Ischemic	2	26		Ischemic	10	93	
Resnet8: L1e-4_D0.64_M22_E60	Non-Ischemic	90	12	91.62	Non-Ischemic	31	5	91.38	Non-Ischemic	121	17	91.56
	Ischemic	2	63		Ischemic	0	22		Ischemic	2	85	
GoogleNet13: L1e-4_D0.3_M20_E30	Non-Ischemic	91	10	93.41	Non-Ischemic	30	7	86.21	Non-Ischemic	121	17	91.56
	Ischemic	1	65		Ischemic	1	20		Ischemic	2	85	

Order according to accuracy. L = learning rate, D = dropout rate, M = minibatch size, E = number of epochs.
Please note that all ResNet-networks were trained with a preliminary termination term (thus, all had E60 but were automatically stopped by the training algorithm).

3.4 Project IV

The fourth project aimed at combining the methods of Project II and III with the data of Project I. More specifically, diagnostic accuracy of the six icECG parameters was assessed for determining a hemodynamic relevant stenotic lesion according to the structural parameter of percent diameter coronary narrowing during induced myocardial ischemia. Further, the same icECGs at maximal heart rate were classified by three CNN.

Please note that there is no intention to publish these results taken into account the missing clinical relevance of this analysis. All analysis were primary conducted to complete this thesis. The following sections summarizes the methods and results used, while the discussion of the results is integrated in the general discussion of the thesis.

3.4.1 Methods

Study design and patients

This was a retrospective analysis of the icECGs with maximal ST-segment shift obtained within 1 minute after reaching maximal heart rate (i.e., icECG data from Project I). Primary endpoint was the diagnostic accuracy of the icECG parameters from Project II to detect a hemodynamic relevant coronary lesion according to percent diameter stenosis. Further, the icECG tracings were classified into non-ischemic and ischemic by the three best performing CNN from Project III.

Assessment of icECG

In the original study, primary study endpoint, i.e., the maximal change in icECG ST-segment shift obtained within 1 minute after reaching maximal heart rate, was measured 60ms after the J-point on 10-15 consecutive and signal-averaged QRS-complexes. The identical signal-averaged icECGs were used for assessment of the icECG parameters as described in Project II. In brief, quantitative processing of icECG parameters was performed with customized software (written in Matlab, R2017b) by manually determine six cornerstones (isoelectric line, Q-point, J-point as well as start, peak and end of the T-wave). Further, the icECGs were converted in jpg-images without labels for the CNN.

For illustration, figure XXIII shows the development of each icECG parameter and the corresponding network prediction of ResNet5 during the pharmacologic inotropic stress test (i.e., analogous to figure 2 of Project I).

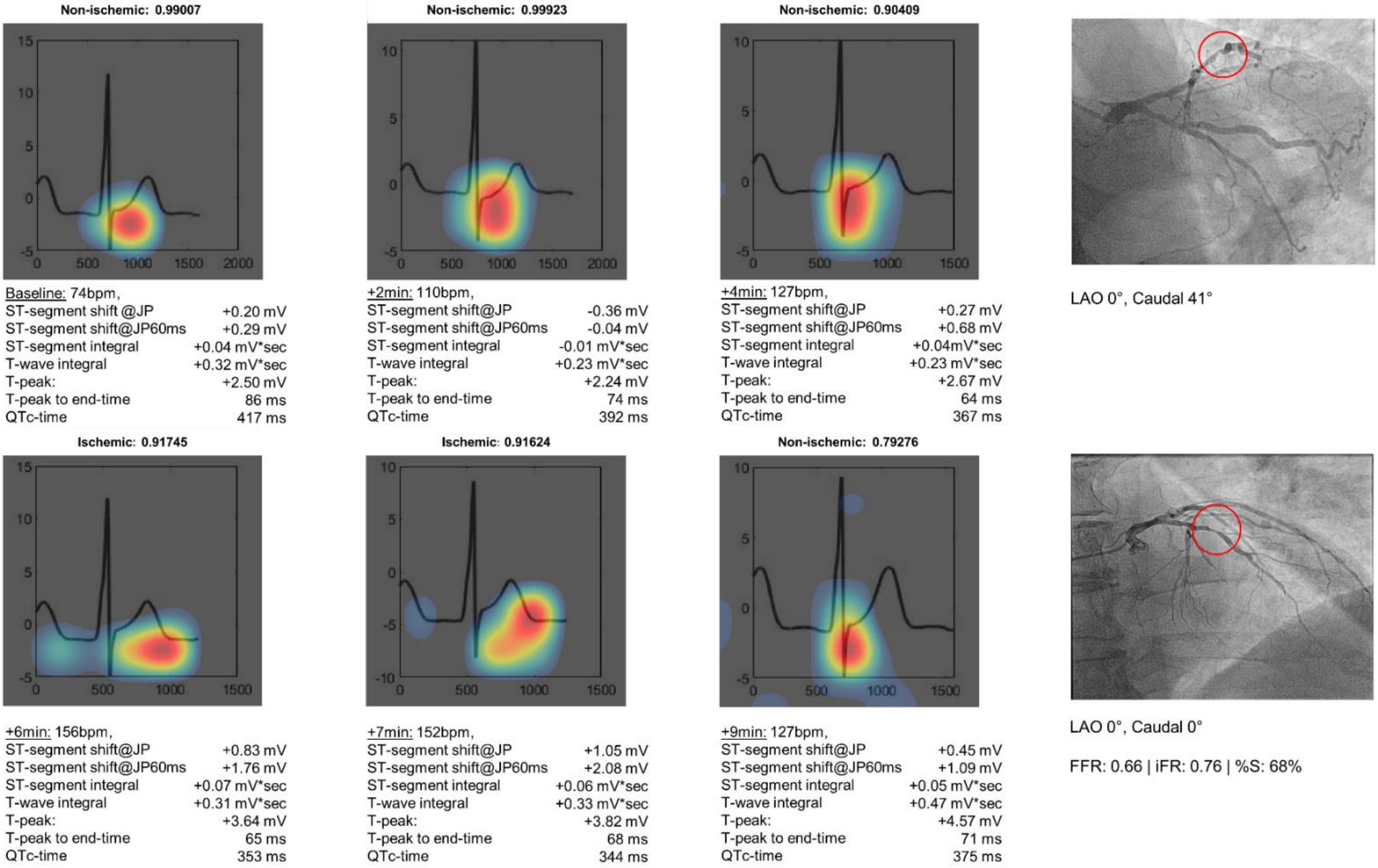

Baseline: 74bpm,	
ST-segment shift @JP	+0.20 mV
ST-segment shift@JP60ms	+0.29 mV
ST-segment integral	+0.04 mV*sec
T-wave integral	+0.32 mV*sec
T-peak:	+2.50 mV
T-peak to end-time	86 ms
QTc-time	417 ms

+2min: 110bpm,	
ST-segment shift@JP	-0.36 mV
ST-segment shift@JP60ms	-0.04 mV
ST-segment integral	-0.01 mV*sec
T-wave integral	+0.23 mV*sec
T-peak:	+2.24 mV
T-peak to end-time	74 ms
QTc-time	392 ms

+4min: 127bpm,	
ST-segment shift@JP	+0.27 mV
ST-segment shift@JP60ms	+0.68 mV
ST-segment integral	+0.04mV*sec
T-wave integral	+0.23 mV*sec
T-peak:	+2.67 mV
T-peak to end-time	64 ms
QTc-time	367 ms

LAO 0°, Caudal 41°

+6min: 156bpm,	
ST-segment shift@JP	+0.83 mV
ST-segment shift@JP60ms	+1.76 mV
ST-segment integral	+0.07 mV*sec
T-wave integral	+0.31 mV*sec
T-peak:	+3.64 mV
T-peak to end-time	65 ms
QTc-time	353 ms

+7min: 152bpm,	
ST-segment shift@JP	+1.05 mV
ST-segment shift@JP60ms	+2.08 mV
ST-segment integral	+0.06 mV*sec
T-wave integral	+0.33 mV*sec
T-peak:	+3.82 mV
T-peak to end-time	68 ms
QTc-time	344 ms

+9min: 127bpm,	
ST-segment shift@JP	+0.45 mV
ST-segment shift@JP60ms	+1.09 mV
ST-segment integral	+0.05 mV*sec
T-wave integral	+0.47 mV*sec
T-peak:	+4.57 mV
T-peak to end-time	71 ms
QTc-time	375 ms

LAO 0°, Caudal 0°

FFR: 0.66 | iFR: 0.76 | %S: 68%

Figure XXIII: Pharmacological inotropic stress test with recording of intracoronary ECG (icECG, analog to figure 2 of project I). *With increasing heart rate and myocardial oxygen consumption, flow impairment of the coronary lesion causes first subendocaridal and later transmural myocardial ischemia with an icECG ST-segment elevation. Each icECG represents at least 12 consecutive, signal-averaged QRS-complexes. Probability measure and corresponding network predictions are above the visualization of the network prediction. Red regions contributed most to the network class prediction. %S, percent diameter stenosis; FFR, fractional flow reserve; iFR, instantaneous wave-free ratio; LAO, left anterior oblique projection*

Statistical analysis

For the purpose of data presentation, two study groups were formed based on %S (< or ≥50%). Between-group comparison was performed by χ^2 for nominal parameters and by an unpaired student's t-test for continuous study parameters.

Linear regression analysis was performed for univariate association testing between icECG parameters and % diameter stenosis. One-way analysis of variance (ANOVA) was performed to analyse continuous study parameters as a function of the network predictions.

Nonparametric receiver operating characteristics (ROC) curve analysis was used for accuracy assessment of detecting a %S of ≥50% defining coronary structural stenosis significance by icECG parameters respectively the CNN. Optimal cut-off points for each parameter were determined by the Youden-Index. Comparison of the area under the ROC curves was performed using the DeLong-Test.

Statistical significance was defined at a p-level of <0.05. Continuous variables are given as mean ± standard deviation. All analyses were performed using SPSS version 25 (IBM Statistics, Armonk, New York) or MedCalc for Windows, version 19.1 (MedCalc Software, Ostend, Belgium).

3.4.2 Results

One hundred patients were included in the study. Using the %S threshold of ≥50% as definition for structural significance, 52 patients were in the group with a significant coronary stenosis. Patient characteristics and coronary angiography data were described in the original study (Project I). Of note, patients with a %S≥50% showed a higher number of structurally relevant stenosis on coronary angiogram. Further left anterior descending artery served more often as the study vessel than other coronary arteries.

Descriptive statistics

Descriptive statistics are presented on table 1, grouped according to %S (< or ≥50%). Overall, four icECG parameters (ST-segment shift measured at the J-point, ST-segment integral, T-wave integral and T-peak) showed significant differences between the groups, while TPE and QTc-time were not statistically different. From the three CNN, only predictions from GoogLeNet showed a significant difference between the groups.

Table 1: Angiographic data and study parameters grouped according to % diameter stenosis

<table>
<tr><th colspan="2"></th><th>Overall</th><th>%S<50%</th><th>S≥50%</th><th>p-value</th></tr>
<tr><td colspan="2">Number of patients</td><td>100</td><td>48</td><td>52</td><td>-</td></tr>
<tr><td colspan="6">Coronary angiographic parameters</td></tr>
<tr><td colspan="2">Number of diseased vessels</td><td>1.81±0.94</td><td>1.50±0.99</td><td>2.10±0.84</td><td>0.001</td></tr>
<tr><td colspan="2">Number of coronary lesions (visually relevant)</td><td>1.83±1.60</td><td>1.21±1.21</td><td>2.38±1.68</td><td><0.001</td></tr>
<tr><td colspan="6">Target vessel distribution</td></tr>
<tr><td colspan="2">Left anterior descending (LAD), n</td><td>55</td><td>23</td><td>32</td><td rowspan="3">0.362</td></tr>
<tr><td colspan="2">Left circumflex coronary artery (LCX), n</td><td>24</td><td>14</td><td>10</td></tr>
<tr><td colspan="2">Right coronary artery (RCA), n</td><td>21</td><td>11</td><td>10</td></tr>
<tr><td colspan="6">Original study parameters</td></tr>
<tr><td colspan="2">Maximum heart rate achieved (beats per minute)</td><td>150±16</td><td>149±18</td><td>151±13</td><td>0.508</td></tr>
<tr><td colspan="2">Maximal heart rate in % of theoretical maximal heart rate (220-age)</td><td>98±11</td><td>98±12</td><td>98±10</td><td>0.705</td></tr>
<tr><td colspan="2">Quantitative coronary angiography of the lesion of interest (%)</td><td>53±17</td><td>39±6</td><td>66±12</td><td>-</td></tr>
<tr><td colspan="2">Fractional flow reserve</td><td>0.798±0.143</td><td>0.887±0.073</td><td>0.716±0.143</td><td><0.001</td></tr>
<tr><td colspan="2">Instantaneous wave-free ratio</td><td>0.812±0.209</td><td>0.922±0.052</td><td>0.710±0.245</td><td><0.001</td></tr>
<tr><td colspan="2">Intracoronary electrocardiogram ST-segment shift measured @ J-point+60ms (mV) within 1 minute after maximal heart rate</td><td>0.965±1.324</td><td>0.545±0.892</td><td>1.352±1.533</td><td>0.002</td></tr>
<tr><td colspan="2">Collateral flow index</td><td>0.118±0.100</td><td>0.083±0.070</td><td>0.148±0.113</td><td>0.001</td></tr>
<tr><td colspan="6">IcECG study parameters</td></tr>
<tr><td colspan="2">ST-segment shift @ J-point (mV)</td><td>0.367±0.806</td><td>0.151±0.559</td><td>0.565±0.944</td><td>0.010</td></tr>
<tr><td colspan="2">ST-segment integral (mV*sec)</td><td>0.026±0.045</td><td>0.016±0.038</td><td>0.036±0.048</td><td>0.022</td></tr>
<tr><td colspan="2">T-wave integral (mV*sec)</td><td>0.167±0.184</td><td>0.117±0.159</td><td>0.214±0.194</td><td>0.007</td></tr>
<tr><td colspan="2">T-peak (mV)</td><td>1.767±1.949</td><td>1.160±1.717</td><td>2.328±2.072</td><td>0.003</td></tr>
<tr><td colspan="2">T-peak to end-time (msec)</td><td>62.47±16.32</td><td>59.84±18.62</td><td>64.91±13.59</td><td>0.121</td></tr>
<tr><td colspan="2">QTc-time (msec)</td><td>351.62±28.70</td><td>356.59±32.44</td><td>347.03±24.17</td><td>0.096</td></tr>
<tr><td colspan="6">Network predictions</td></tr>
<tr><td rowspan="2">ResNet5</td><td>Non-ischemic</td><td>52</td><td>28</td><td>24</td><td rowspan="2">0.237</td></tr>
<tr><td>Ischemic</td><td>48</td><td>20</td><td>28</td></tr>
<tr><td rowspan="2">GoogLeNet10</td><td>Non-Ischemic</td><td>52</td><td>30</td><td>22</td><td rowspan="2">0.048</td></tr>
<tr><td>Ischemic</td><td>48</td><td>18</td><td>30</td></tr>
<tr><td rowspan="2">ResNet6</td><td>Non-Ischemic</td><td>47</td><td>26</td><td>21</td><td rowspan="2">0.229</td></tr>
<tr><td>Ischemic</td><td>53</td><td>22</td><td>31</td></tr>
</table>

Linear regression

There was a direct linear relation between icECG ST-segment shift at J-point and %S: ST-segment shift@JP = -0.8 + 0.02*%S (r^2=0.183; $p<0.001$, figure XXIV), between ST-segment integral and %S: STI = $-3*10^{-2} + 1*10^{-3}$*%S (r^2=0.143; $p<0.001$), between T-wave integral and %S: TI = $-4*10^{-2} + 3.9*10^{-3}$*%S (r^2=0.123; $p<0.001$) and between T-peak and %S: T-peak = -0.7 + $4.6*10^{-2}$*%S (r^2=0.147; $p<0.001$). There was an inverse linear correlation between QTc-time and %S: QTc-time = 371 – 0.37*%S (r^2=0.045; $p=0.035$). Linear correlation between TPE and %S was not significant.

Correlation coefficients respectively χ^2 or Eta and the corresponding significance are shown in table 2.

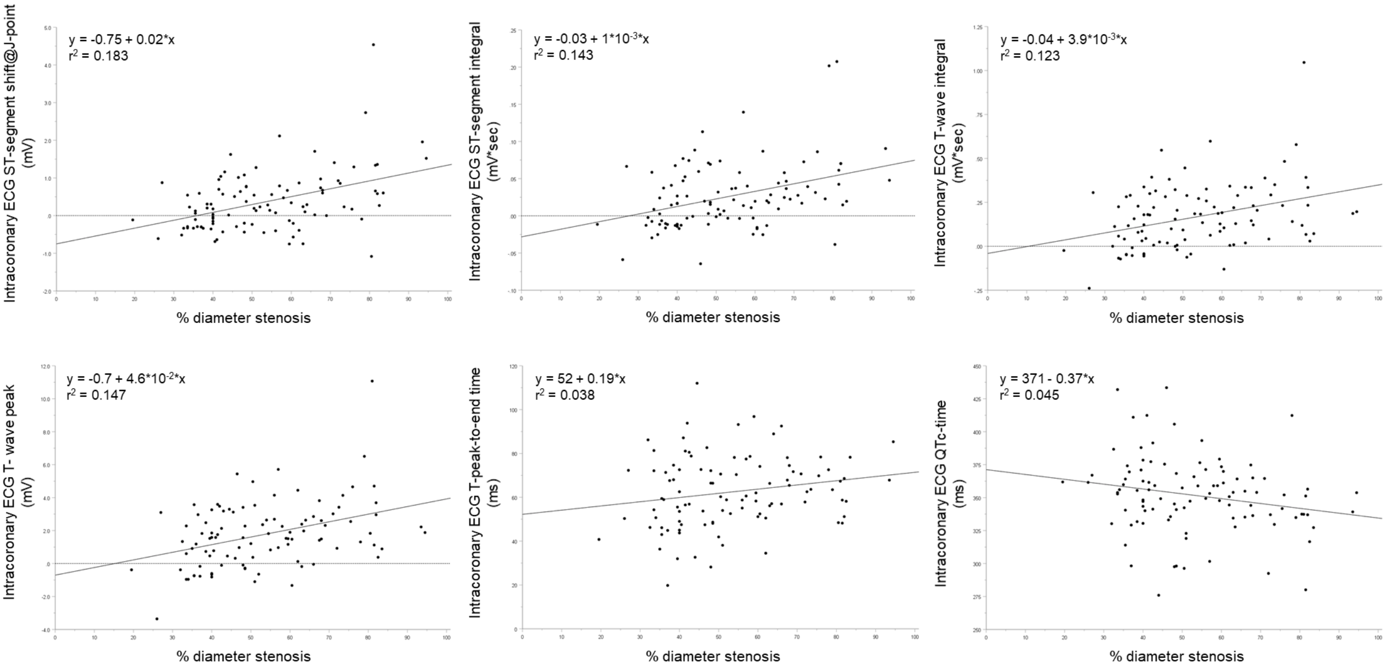

Figure XXIV: Linear regression between intracoronary ECG parameters and percent diameter coronary stenosis. *Solid line=regression line; dashed line=marker for 0 (if the parameters showed negative and positive values)*

Table 2: Correlation coefficient and DeLong-Test

		FFR	**iFR**	**ST-segment shift@ JP60ms**	**ST-segment shift@JP**	**ST-segment integral**	**T-wave integral**	**T-peak**	**TPE time**	**QTc-time**	**ResNet5**	**GoogLe Net10**	**ResNet6**
% diameter stenosis	Correlation/ ETA/ χ^2	-0.703	-0.679	0.406	0.428	0.378	0.350	0.384	0.194	-0.211	0.157	0.341	0.203
	Sig. (2-tailed)	p<0.001	p<0.001	p<0.001	p<0.001	p<0.001	p<0.001	p<0.001	p=0.053	p=0.035	p=0.119	p=0.001	p=0.043
FFR	Correlation/ ETA/ χ^2		0.858	-0.505	-0.476	-0.450	-0.435	-0.452	-0.251	0.206	0.275	0.413	0.322
	Sig. (2-tailed)		p<0.001	p<0.001	p<0.001	p<0.001	p<0.001	p<0.001	p=0.012	p=0.040	p=0.006	p<0.001	p=0.001
	DeLong-Test:		p=0.315	**p=0.002**	**p<0.001**	**p<0.001**	**p<0.001**	**p<0.001**	**p<0.001**	**p<0.001**	**p<0.001**	**p<0.001**	**p<0.001**
iFR	Correlation/ ETA/ χ^2			-0.491	-0.526	-0.461	-0.393	-0.419	-2.15	0.226	0.295	0.437	0.305
	Sig. (2-tailed)			p<0.001	p<0.001	p<0.001	p<0.001	p<0.001	p=0.032	p=0.024	p=0.003	p<0.001	p=0.002
	DeLong-Test:			**p=0.024**	**p=0.008**	**p=0.005**	**p=0.010**	**p=0.009**	**p<0.001**	**p=0.001**	**p<0.001**	**p<0.001**	**p<0.001**
ST-segment shift@ JP60ms	Correlation/ ETA/ χ^2				0.858	0.869	0.912	0.895	0.403	-0.084	0.357	0.520	0.400
	Sig. (2-tailed)				p<0.001	p<0.001	p<0.001	p<0.001	p<0.001	p=0.406	p<0.001	p<0.001	p<0.001
	DeLong-Test:				p=0.360	p=0.084	p=0.466	p=0.547	p=0.118	p=0.304	p=0.054	p=0.113	p=0.056
ST-segment shift@ JP	Correlation/ ETA/ χ^2					0.882	0.717	0.678	0.348	-0.208	0.576	0.600	0.533
	Sig. (2-tailed)					p<0.001	p<0.001	p<0.001	p<0.001	p=0.038	p<0.001	p<0.001	p<0.001
	DeLong-Test:					p=0.660	p=0.768	p=0.746	p=0.449	p=0.513	p=0.072	p=0.335	p=0.128
ST-segment integral	Correlation/ ETA/ χ^2						0.820	0.821	0.308	-0.133	0.365	0.489	0.396
	Sig. (2-tailed)						p<0.001	p<0.001	p=0.002	p=0.188	p<0.001	p<0.001	p<0.001
	DeLong-Test:						p=0.474	p=0.443	p=0.563	p=0.653	p=0.238	p=0.554	p=0.274
T-wave integral	Correlation/ ETA/ χ^2							0.974	0.464	0.101	0.169	0.403	0.237
	Sig. (2-tailed)							p<0.001	p<0.001	p=0.319	p=0.092	p<0.001	p=0.017
	DeLong-Test:							p=0.858	p=0.239	p=0.471	p=0.161	p=0.313	p=0.145
T-peak	Correlation/ ETA/ χ^2								0.347	0.062	0.105	0.385	0.205
	Sig. (2-tailed)								p<0.001	p=0.538	p=0.300	p<0.001	p=0.040
	DeLong-Test:								p=0.271	p=0.448	p=0.160	p=0.297	p=0.162
TPE	Correlation/ ETA/ χ^2									0.343	0.203	0.261	0.148
	Sig. (2-tailed)									p<0.001	p=0.043	p=0.009	p=0.142
	DeLong-Test:									p=0.997	p=0.638	p=0.928	p=0.722
QTC	Correlation/ ETA/ χ^2										0.241	0.275	0.216
	Sig. (2-tailed)										p=0.016	p=0.006	p=0.031
	DeLong-Test:										p=0.626	p=0.935	p=0.711
ResNet5	Correlation/ ETA/ χ^2											0.639	0.784
	Sig. (2-tailed)											p<0.001	p<0.001
	DeLong-Test:											p=0.351	p=0.810
GoogLe Net10	Correlation/ ETA/ χ^2												0.704
	Sig. (2-tailed)												p<0.001
	DeLong-Test:												p=0.414

FFR = Fractional flow reserve; iFR = instantaneous wave-free ratio; JP = J-point; TPE = T-peak-to-end time; QTc = corrected QT time
Sig. = significance; Non-significant (i.e., p≥0.05) correlations are marked by a grey background, significant differences in the area under the curves by a bold p-value.

One-way ANOVA

There was a significant difference in %S in the predicted groups of GoogLeNet10 and ResNet6 (p=0.001 respectively p=0.043, figure XXV), but not in the groups according to ResNet5 (p=0.119).

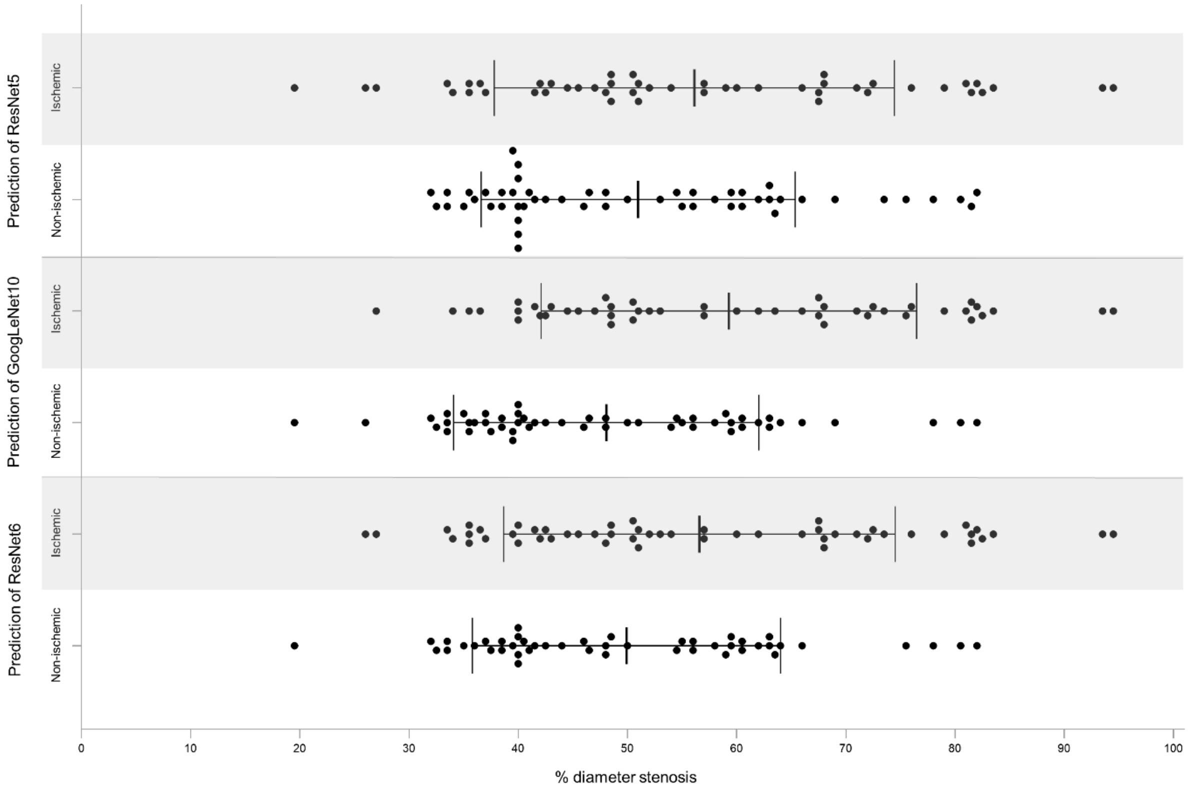

Figure XXV: ***Individual values of percent diameter stenosis grouped according to the network prediction***
Error bars indicate mean values and SD.

Receiver-operating characteristic curves

Using a %S threshold of ≥50% as the reference for structural stenosis relevance, ROC-analysis of absolute icECG ST-segment shift at the J-point showed an area under the curve (AUC) of 0.604±0.057 (p=0.073). AUC for ST-integral was 0.588±0.058 (p=0.129), for T-wave integral 0.642±0.055 (p=0.015), for T-peak amplitude 0.642±0.056 (p=0.014), for TPE 0.595±0.059 (p=0.102), and for QTc-time 0.595±0.057 (p=0.101, figure XXVI).

Using the same reference for assessment of the network predictions, AUC for ResNet 5 was 0.560 (p=0.294), for GoogLeNet10 0.600 (p=0.082), and for ResNet6 0.570 (p=0.235, figure XXVI)

AUC of the original study parameters was 0.678±0.054 (p=0.002) for icECG ST-segment shift measured 60ms after the J-point, 0.854±0.037 (p<0.001) for FFR, and 0.816±0.043 (p<0.001) for iFR.

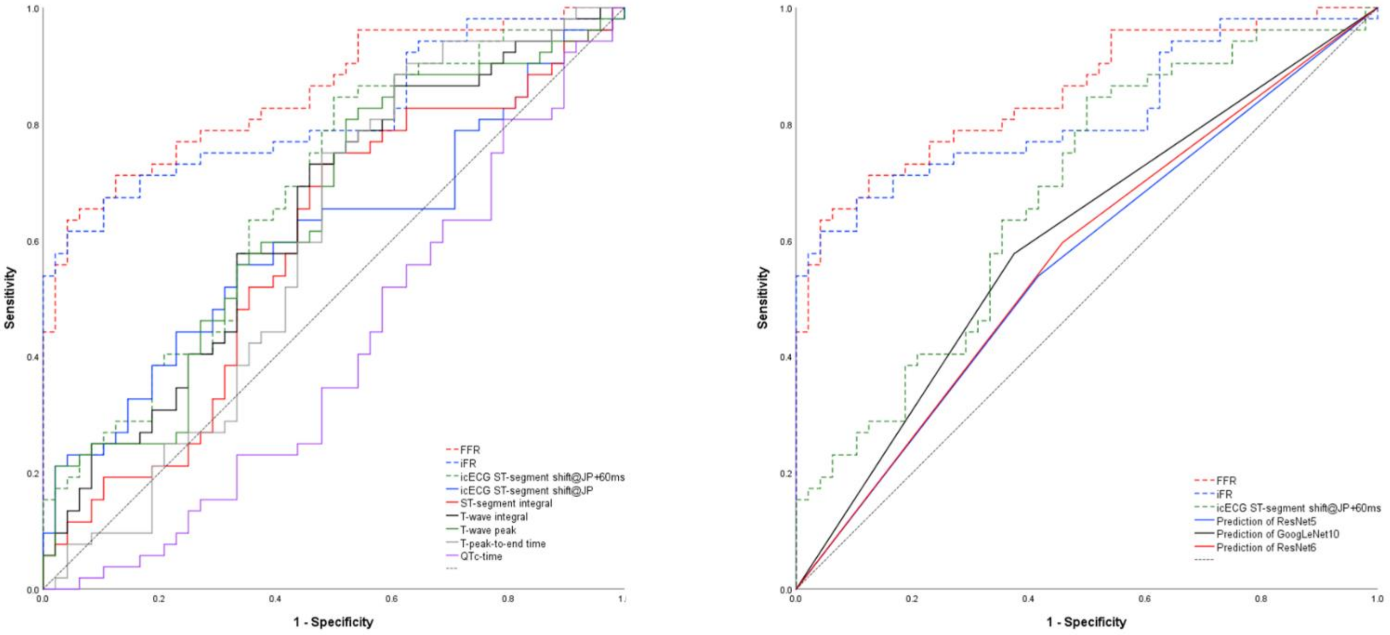

Figure XXVI: Non-parametric receiver-operating characteristic curve of intracoronary ECG (icECG) parameters (left) and CNN predictions (right) using a %S threshold of ≥50% as structural significance definition. *Original study parameters (FFR, iFR and icECG ST-segment shift measured 60ms after the J-point) are presented with a dashed ROC-curve. Of note, all parameters but QTc-time increased with increasing %S. Thus, QTc-time is below the reference line (dotted black line). %S, percent diameter stenosis; FFR, fractional flow reserve; iFR instantaneous wave-free ratio.*

The DeLong-Test of the ROC-curves showed a significant difference for FFR and iFR as compared with all icECG parameters. There was no relevant difference in AUC between the icECG parameters and/or the CNNs. All results of the DeLong-Test are shown in table 2.

Regarding the optimum cut-off of the parameters for detection of a structurally relevant coronary lesion, a ST-segment shift measured at the J-point of 0.543mV distinguished best between non-ischemic and ischemic ECG, sensitivity 55%, specificity 67%. The best cut-off point for ST-integral was 0.017mV*sec (sensitivity 73%, specificity 52%), for T-integral 0.118mV*sec (sensitivity 73%, specificity 47%), for T-peak 1.03mV (sensitivity 81%, specificity 48%), for TPE 51msec (sensitivity 88%, specificity 40%) and for QTc-time 359msec (sensitivity 75%, specificity 48%). Of note, all parameters but QTc-time increased with increasing %S.

Thus, the optimum cut-off point for QTc-time is inverse (i.e., structurally relevant coronary lesion below 359msec).

There is no optimum cut-off point for the CNNs, but the other statistical measures of performance (ResNet 5 sensitivity 54%, specificity 58%; GoogLeNet10 sensitivity 58%, specificity 63%; ResNet 6 sensitivity 60%, specificity 54%).

3.4.3 Conclusion

Of the icECG parameters during pharmacologic inotropic stress, ST-segment shift measured 60ms after the J-point distinguished most accurately between non-relevant and relevant stenotic lesions as defined by the structural parameter of percent diameter coronary narrowing. However, differences were not statistical significant between the icECG parameters or CNN predictions and overall detection is less accurate by icECG than by hemodynamic indices.

4. Discussion

The main aims of this PhD project were to investigate the diagnostic accuracy of icECG ST-segment shift during pharmacologic inotropic stress to assess the hemodynamic relevance of coronary artery stenotic lesions (Project I), and the determination of the optimal parameter for myocardial ischemia detection in the icECG (Project II and III). The studies demonstrate that icECG is a sensitive instrument qualitatively and quantitatively in the sense of accuracy measurement for the assessment of myocardial ischemia. It provides information about the adequacy of coronary blood flow to the regional mass of viable myocardium independent of structural or hemodynamic parameters. The icECG does, however, not distinguish between the causes of myocardial ischemia.

4.1 Intracoronary ECG as a direct measure of myocardial ischemia

The objective of Project I was to determine the diagnostic accuracy of icECG ST-segment shift during pharmacologic inotropic stress in comparison to established hemodynamic indices for coronary lesion severity assessment using percent diameter stenosis as reference value. The underlying idea is based on the relation of coronary blood flow and coronary stenosis severity as illustrated by figure VI. The concept was that by induction of maximal coronary blood flow, coronary lesions inducing flow restrictions beyond the compensatory autoregulation of the myocardial microcirculation would be unravelled by icECG recording myocardial ischemia. However, the study showed that though icECG during pharmacologic inotropic stress is highly sensitive it is not specific for a hemodynamically relevant stenosis. Hence, presence of myocardial ischemia requires further specification of coronary lesion severity, while the absence of ischaemia allows abstaining from further tests.

As outlined in chapter 1.4, myocardial ischemia has multiple causes and is not always related to epicardial coronary lesions (i.e., CAD). Instead, CMD (most often within the course of a hypertensive cardiomyopathy) can cause myocardial ischemia in the absence of relevant coronary stenosis providing an explanation for the low specificity of the icECG. Hence, in the situation of a hemodynamic index clearly above the threshold of myocardial ischemia on icECG, CMD can be assumed (as it is the most likely cause in this situation). As shown in the original paper using a combination of icECG and iFR, 23% of the study participants belonged in this subgroup (figure XXVII, upper right corner). Fifteen (65%) of the patients in this group showed signs of hypertensive cardiomyopathy in the ventriculography and/or the typical corkscrew pattern on coronary angiography. This pattern is caused by undirected growth (both in coronary artery calibre and length) during structural arterial remodelling (a process called arteriogenesis) to comply with an increase in myocardial mass[41,146].

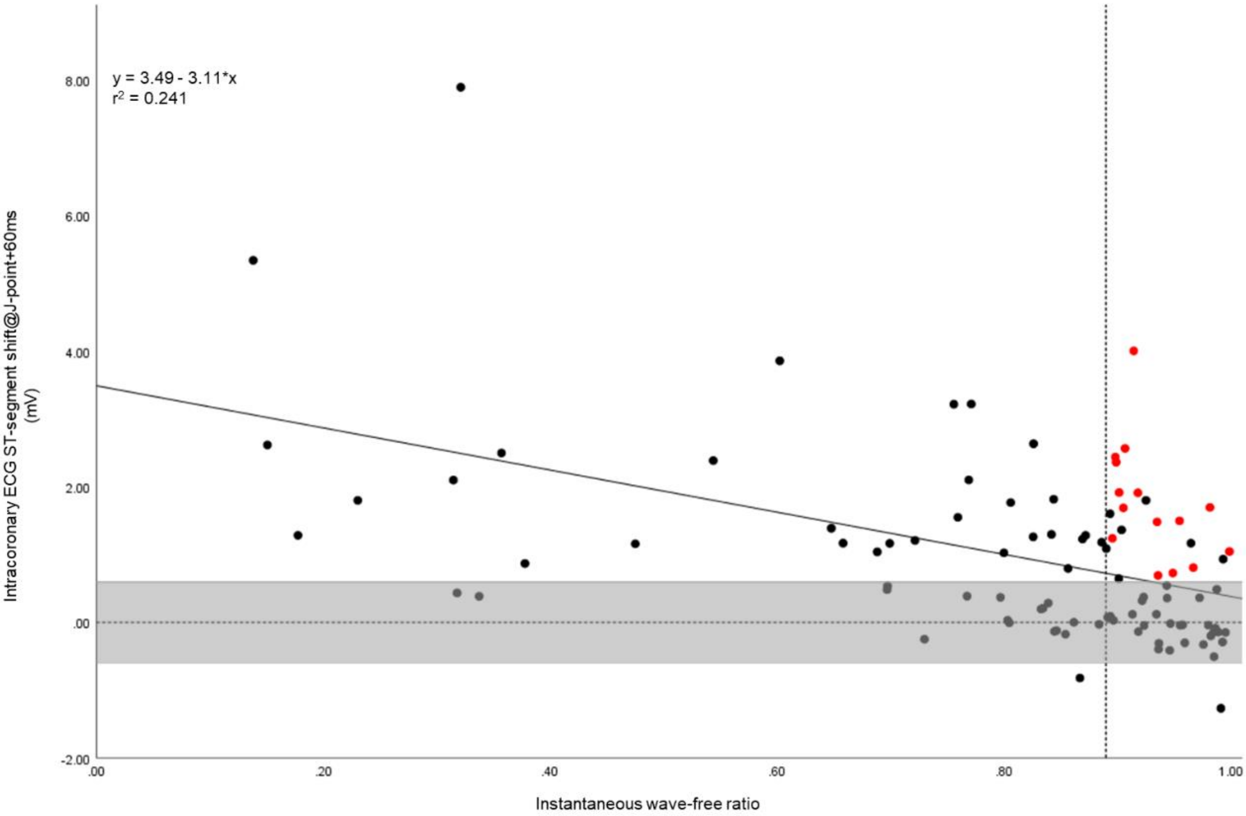

Figure XXVII: Linear regression between intracoronary ECG (icECG) ST-segment shift measured 60ms after the J-point and instantaneous wave-free ratio (iFR) *solid line=regression line; dashed horizontal line=marker for 0 mV icECG ST-segment shift; dashed vertical line = threshold for iFR (0.89); grey box = absence of myocardial ischemia according to the icECG; red dots = angiographic signs of hypertensive cardiomyopathy (only assessed for the 23 patients with a relevant icECG ST-segment shift but an iFR above the threshold.*

However, diagnosis of hypertensive cardiomyopathy requires the determination of myocardial mass[147] and thus, the statement above remains speculative. Apart from arterial hypertension, diabetes mellitus has been associated with CMD[95,96]. In the respective subgroup of our study, eight out of the twenty-three (35%) patients had diabetes mellitus (overall prevalence in the study population was 23%).

Differentiation between CAD and CMD can be difficult because of the significant overlap of these pathologies[98]. Coronary flow measurements could help to distinguish the different contribution of CAD and CMD to the recorded myocardial ischemia[148,149]. However, invasive measurement of coronary flow is practically not feasible in the clinical setting[73]. Instead, surrogates of coronary flow are used and obtained either by Doppler-derived coronary flow velocity or by thermodilution, i.e., “the transit time of an intracoronary bolus of saline at room temperature over a defined distance”[73]. Together with simultaneous pressure measurement and during hyperemia, coronary hemodynamic indices (e.g., CFR or the index of microvascular resistance (IMR)) can be calculated. While CFR estimates both, macro- and microcirculatory function, IMR provides an estimate of microcirculatory function. Hence, combination of these two hemodynamic indices would provide the required information. However, both methods for coronary blood flow estimates are prone to inaccurate measurements, technically demanding and time consuming. The reason why they were replaced by the more robust coronary pressure measurement in daily clinical practice.

To conclude, myocardial ischemia relies on the interplay between macro- and microcirculation as well as additional factors (e.g., perfusion pressure, ventricular filling pressure, blood oxygenation) and thus, explains icECG ST-segment shift inferior diagnostic specificity to diagnose structurally significant coronary lesions when compared to hemodynamic indices. While the latter are capable of specifying epicardial coronary lesions, icECG reflects the supply-demand (mis-)match of regional myocardial perfusion and thus, CAD, CMD *and* additional factors. Accordingly, other icECG parameters or re-trained CNN do -obviously- not significantly change its diagnostic accuracy as this discrepancy is related to pathophysiologic mechanisms.

4.2 Time point of icECG ST-segment shift determination

The retrospective analysis of Project IV demonstrated that during pharmacologic inotropic stress (i.e., simulation of physical exercise) with coronary artery patency, icECG ST-segment shift measured 60ms after the J-point provided the highest diagnostic accuracy (AUC = 0.678±0.054) followed by T-wave integral and T-wave peak (0.642±0.055 respectively 0.642±0.056). IcECG ST-segment shift measured at the J-point had a numerically lower AUC of 0.604±0.057. Conversely in Project II, that is a setting with artificially induced coronary occlusion, i.e., *absolute* myocardial ischemia, ST-segment shift measured at the J-point distinguished best between absence and presence of ischemia (AUC = 0.963±0.029 versus 0.956±0.031 for ST-segment shift measured 60ms after the J-point with a best cut-off value of 0.579mV, sensitivity 84%, specificity 97%). The icECG ST-segment shift data at the J-point are, however, not statistically significant different from those obtained 60ms after the J-point (DeLong-Test 0.360 and 0.578 for pharmacological stress, respectively absolute myocardial ischemia).

Nevertheless, the numerically higher diagnostic accuracy is in accordance with common practice, i.e., determination of ST-segment shift directly at the J-point in the acute setting[14], and assessment of ST-segment shifts 60ms after the J-point during (physical) stress test[16,17]. The latter has been evidenced by multiple studies assessing the diagnostic accuracy of exercise electrocardiogram to detect CAD[17,150-153]. In the setting of physical stress testing, especially subendocardial myocardial ischemia is encountered resulting in ST-segment depression on surface ECG. While quantifying ST-segment deviation, the authors observed a relationship between ST-segment shift and the slope of the ST-segment[150-152]. Okin et al.[17] showed that clinically normal subjects with a J-point depression presented with rapidly upsloping ST-segments, while patients with CAD did not exhibit this behaviour of the ST-segment. The concluded that this behaviour can be captured by measurement of the ST-segment deviation 60ms after the J-point. In the study by Okin et al.[17], application of this consideration resulted in a higher diagnostic accuracy for the ST-segment measurement 60ms after the J-point when compared to the measurement at the J-point (AUC of 0.88 versus 0.82, p=0.001).

On icECG, ST-segment depression is rarely seen during maximal hyperemia (figure XXVII). Instead, most patients developed elevated and upsloping ST-segment because of simultaneously altered ST-segment and T-wave morphology. Hence, ST-segment shift measured 60ms after the J-point increases faster than ST-segment shift measured at the J-point. As a result, the measurement 60ms after the J-point enables differentiation between non-relevant and relevant ST-segment shift at an earlier stage of myocardial ischemia than measurement at the J-point. This behaviour is shown by figure XXIII, where ST-segment shift measured 60ms after the J-point exceeds the threshold of transmural ischemia (i.e., 0.579 mV for this parameter) at a time point during the pharmacologic stress test, where ST-segment shift measured at the J-point is still below its threshold (i.e., 0.365mV).

This advantage is, however, only present at the beginning of myocardial ischemia and mitigates with the formation of transmural ischemia as outlined by figure XXVIII. Considering the population of Project I with a broad range of coronary lesion severity (20-95% diameter stenosis) and thus, varying degree of myocardial ischemia during exercise stress test, the advantage of earlier discrimination of present or absent myocardial ischemia for ST-segment shift measured 60ms after the J-point versus at the J-point diminishes. Hence and conversely to the results by Okin et al.[17], the results of Project IV did not show a statistical significant difference between the two parameters. On the other hand, the simplicity of the measurement directly at the J-point provides an explanation for the application of this parameter during acute transmural myocardial ischemia in daily clinical practice.

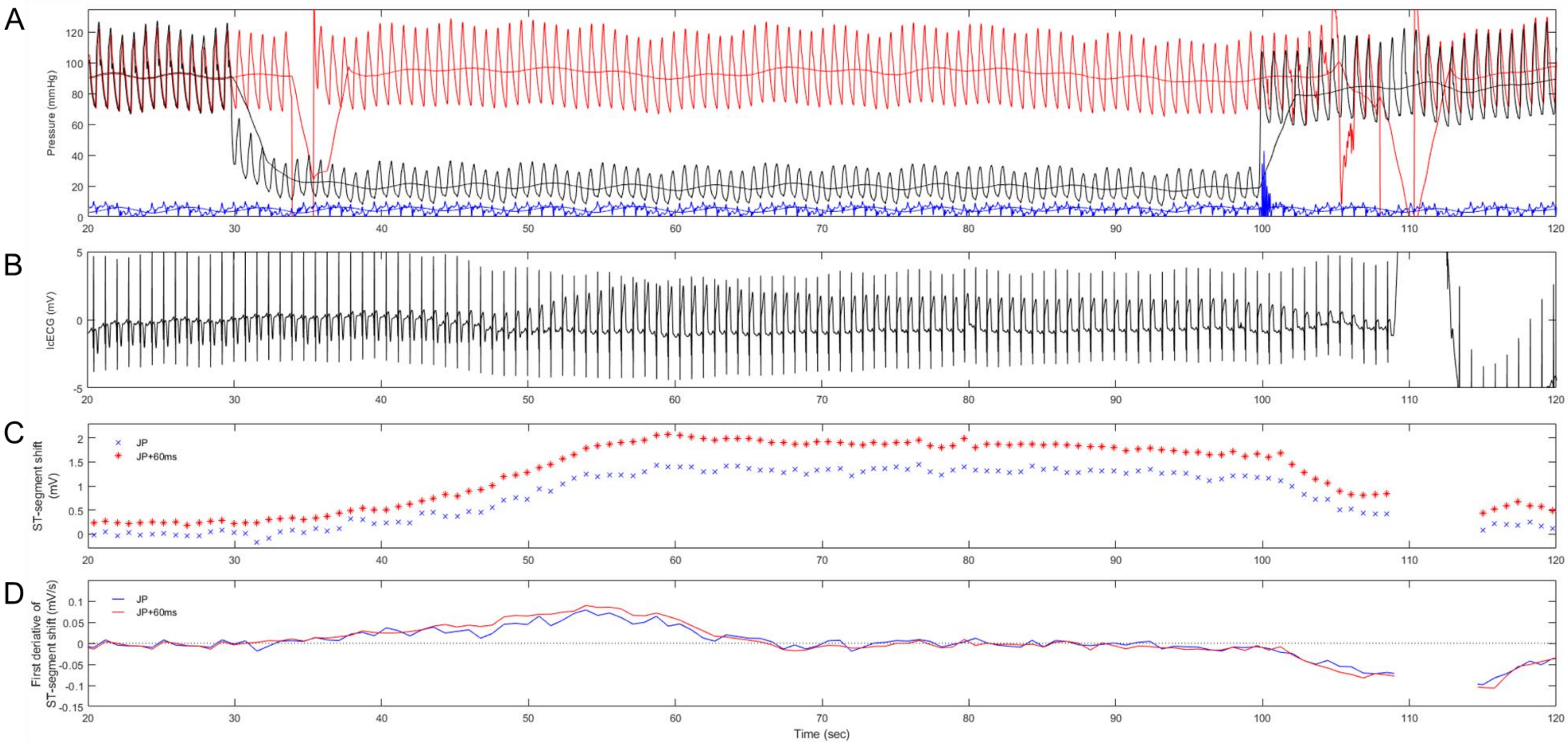

Figure XXVIII: Collateral flow index (CFI) measurement (identical to figure VI). A) *Simultaneous recordings of mean and phasic aortic (red signals), coronary occlusive (black signals), central venous pressure (blue signals) and intracoronary ECG (**B**) immediately before (left side) and during coronary artery occlusion in a patient with poorly functional collaterals.* **C)** *Quantitative measurement at the ST-segment shift for every single heartbeat; blue cross = measurement at the J-point, red star = measurement 60ms after the J-point.* **D)** *First derivative of the ST-segment shift filtered with a moving-average filter (window-size = 10).*

4.3 Limitation

The results of this thesis were obtained in a selected population without arrhythmia or bundle branch blocks as these disorders are known to distort the ST-segment and to impede myocardial ischemia detection on ECG[154,155]. Hence, diagnostic accuracy and cut-off threshold values may be not generally representative.

The low percentage of female patients in the different projects did not allow gender specific statistical analysis. However, such an analysis would have been beneficial taken into account the gender specific difference in myocardial mass with consecutive difference in the amplitude of ischemic signals[156].

All icECG analysis were performed offline. Thus, direct quantitative feedback to the interventional cardiologist was not possible restricting the application of the icECG to a scientific context.

4.4 Conclusion

The intracoronary electrocardiogram is an easy available diagnostic method providing highly accurate information on the amount of myocardial ischemia in real-time. Quantitative assessment of acute, transmural myocardial ischemia by icECG is most accurately performed by measuring ST-segment shift at the J-point, while the quantitative assessment during physical exercise, respectively its pharmacologic simulation, is most accurately performed by measuring ST-segment shift 60ms after the J-point.

5. Outlook

As stated by Yong et al.[23], “the current lack of commercially available systems to obtain and quantify icECG discourages routine use” despite ample evidence for its diagnostic value as outlined by this thesis. Hence, we started an interdisciplinary research project in collaboration with Prof. R. Wildhaber (Institute for Human Centered Engineering, Bern University of Applied Sciences) to develop and validate an autonomous icECG analysing device. The project aims to enable quantitative assessment of the icECG ST-segment shift in real-time during coronary interventions.

For the development a fully autonomous icECG analysing algorithm, R. Wildhaber applies an existing ECG software, denoted as EsoLive, currently developed at University of Applied Science, Biel. The algorithm starts with a baseline wander extraction method akin to Kalman filtering[157] (i.e., an algorithm that uses a series of measurements with noise to produce estimates of unknown variables with higher accuracy than those based on a single measurement alone). Then, a common QRS-complex detection sets the initial points for a sophisticated “edge”, i.e., J-point, search using model-based and machine-learning related approaches[158]. In the next step, the algorithm processes in a similar way to identify the isoelectric line level. Temporal as well as quantitative (in mV) determination of those two points allows the calculation of the icECG ST-segment shift for each single QRS-complex. Figure XXIX shows the approach of the algorithm on the known CFI measurement from figure VI.

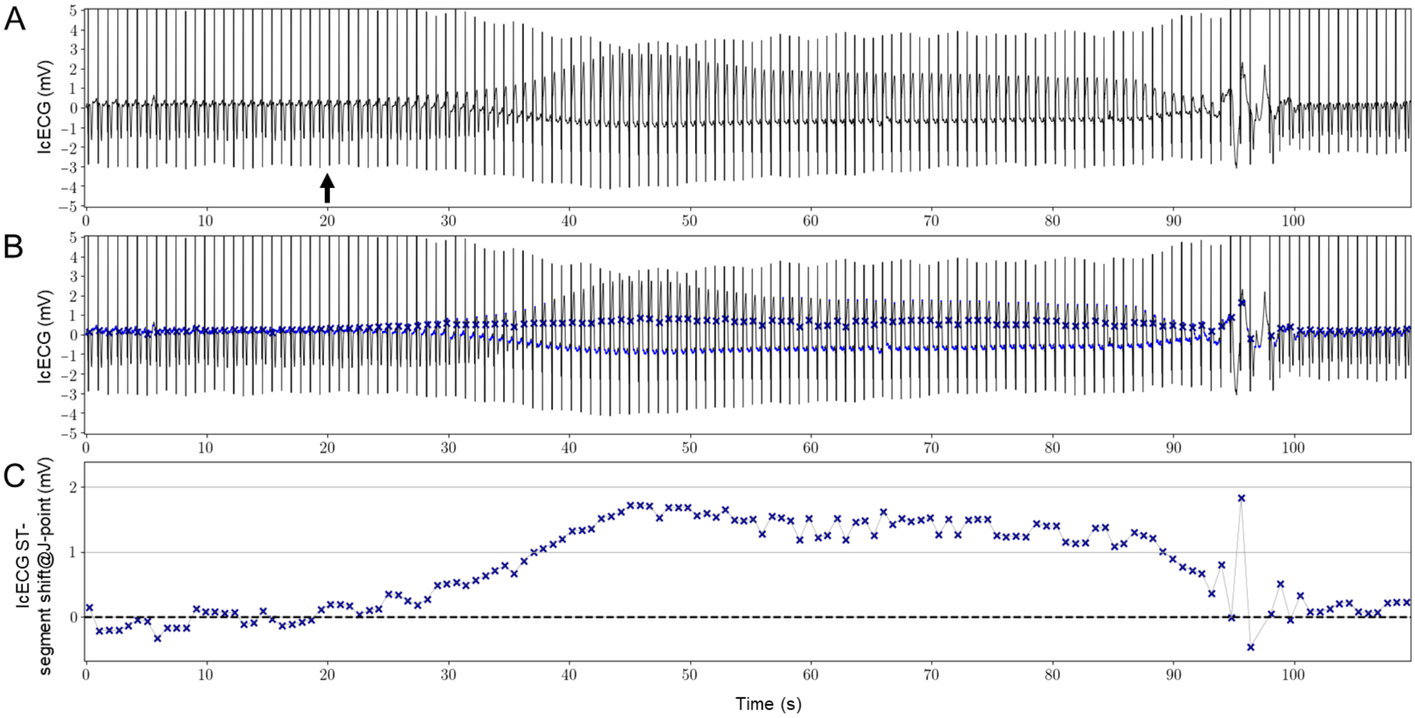

Figure XXIX: Preliminary software-algorithm based quantitative assessment of icECG ST-segment shift during a 60-second proximal coronary balloon occlusion (known from figure VI) A) *Native icECG with development of electrical alterations directly after the balloon occlusion (black arrow). Conversely to the icECG in figure VI, this icECG was additional filtered by the algorithm to remove the baseline wander.* ***B)*** *Autonomous detection of the isoelectric line (blue marks) as well as well as the J-point (blue cross) for every single heartbeat.* ***C)*** *Quantitative determination of the icECG ST-segment shift in mV for each heartbeat. Dashed black line = 0mV.*

Preliminary validation analysis demonstrated already an excellent correlation of the algorithm with the manual analysis by M. Bigler ($r^2 = 0.945$; ST-segment $\text{shift}_{\text{Algorithm}} = -7.5*10^{-3} + 1.06*$ST-segment $\text{shift}_{\text{M.Bigler}}$; $p<0.001$). Using the icECG recording during coronary patency or occlusion as criterion for absent or present myocardial ischemia (similar to Project II and III), ROC-analysis of icECG ST-segment shift measured by M.Bigler showed an AUC of 0.968±0.021, while AUC for the algorithm was 0.967±0.026. DeLong-Test of the ROC-curves showed no significant difference (p=0.925).

The current, preliminary algorithm (currently set-up for off-line processing) demonstrates feasibility of a fully software-based beat-per-beat detection with good agreement to manual analysis results. However, there exist remaining inaccuracies (especially in the analysis of icECG recorded in the RCA) and the implementation into a device has to be solved to overcome the barriers, which discourages routine use of icECG.

6. Acknowledgments

I would like to thank Christian Seiler for offering me the possibility to gain a comprehensive impression of clinical research. During this MD PhD-program, I had the opportunity to start clinical trials from the initial submission to the Ethics Committee, raising financial funding, enrolling patients as well as performing comprehensive data analysis, manuscript drafting and finally publication and presentation of the data at national and international congresses.

Further, I would like to thank Christine Tschannen and Raphael Grossenbacher for their excellent work in patient enrolment and study organisation, without whom this thesis would not have been finished yet.

Then, I thank Michael Stoller for preparing me this excellent work place with up-to-date data analysis based on self-written Matlab codes. In the same topic, I would like to appreciate the collaboration with my co-advisor, Josef Götte, which taught me the basics of biomedical signal processing and analyzing as well as showing me the engineering point of view on various topics. Thanks to him, we established a valuable cooperation with Reto Wildhaber for ongoing projects (see above).

Last, I would like to thank the Department of Cardiology, Bern University Hospital and especially Eric Buffle, Fabien Praz, Georgios Siontis, Christoph Gräni, Lorenz Räber and Stephan Windecker, for being always open-minded and helpful in the realization of research projects.

7. Bibliography

1. Galvani L. An Account of the Experiments and Discoveries of Lewis Galvani, Professor of Anatomy at Bologna, Relative to the Powers of Electricity in Muscular Motion: Vide Aloysii Galvani de Viribus Electricitatis in Motu Musculari Commentarium. 4to. Bologna, 1791. Medical facts and observations 1792;3:180-90.
2. Waller AD. A Demonstration on Man of Electromotive Changes accompanying the Heart's Beat. The Journal of physiology 1887;8:229-34.
3. Rivera-Ruiz M, Cajavilca C, Varon J. Einthoven's string galvanometer: the first electrocardiograph. Texas Heart Institute journal 2008;35:174-8.
4. Mathewson FA, Jackh H. The telecardiogram. American heart journal 1955;49:77-82.
5. Einthoven W, Jaffe A, Venge P, Lindahl B. Galvanometrische registratie van het menschelijk electrocardiogram. Herinneringsbundel Professor SS Rosenstein 1902:101-7.
6. Einthoven W. Le Telecardiogramme. Arch Internat Physiol 1906;4:132.
7. Goldberger E. A simple, indifferent, electrocardiographic electrode of zero potential and a technique of obtaining augmented, unipolar, extremity leads. American heart journal 1942;23:483-92.
8. Knowles JR. Enzyme-Catalyzed Phosphoryl Transfer Reactions. Annual Review of Biochemistry 1980;49:877-919.
9. Santana LF, Cheng EP, Lederer WJ. How does the shape of the cardiac action potential control calcium signaling and contraction in the heart? Journal of molecular and cellular cardiology 2010;49:901-3.
10. Yan GX, Lankipalli RS, Burke JF, Musco S, Kowey PR. Ventricular repolarization components on the electrocardiogram: cellular basis and clinical significance. Journal of the American College of Cardiology 2003;42:401-9.
11. Bigler MR, Zimmermann P, Papadis A, Seiler C. Accuracy of intracoronary ECG parameters for myocardial ischemia detection. Journal of electrocardiology 2020;64:50-7.
12. Safi AM, Kwan T, Feit A, Gonzalez J, Stein RA. Use of intracoronary electrocardiography for detecting ST-T, QTc, and U wave changes during coronary balloon angioplasty. Heart disease (Hagerstown, Md) 2001;3:73-6.
13. Pardee HEB. An Electrocardiographic Sign of Coronary Artery Obstruction. Archives of Internal Medicine 1920;26:244-57.
14. Ibanez B, James S, Agewall S, et al. 2017 ESC Guidelines for the management of acute myocardial infarction in patients presenting with ST-segment elevation: The Task Force for the management of acute myocardial infarction in patients presenting with ST-segment elevation of the European Society of Cardiology (ESC). European heart journal 2018;39:119-77.
15. Antman EM, Anbe DT, Armstrong PW, et al. ACC/AHA guidelines for the management of patients with ST-elevation myocardial infarction--executive summary: a report of the American College of Cardiology/American Heart Association Task Force on Practice Guidelines (Writing Committee to Revise the 1999 Guidelines for the Management of Patients With Acute Myocardial Infarction). Circulation 2004;110:588-636.
16. Fletcher GF, Ades PA, Kligfield P, et al. Exercise standards for testing and training: a scientific statement from the American Heart Association. Circulation 2013;128:873-934.
17. Okin PM, Bergman G, Kligfield P. Effect of ST segment measurement point on performance of standard and heart rate-adjusted ST segment criteria for the identification of coronary artery disease. Circulation 1991;84:57-66.
18. Birnbaum Y, Alam M. LVH and the diagnosis of STEMI - how should we apply the current guidelines? Journal of electrocardiology 2014;47:655-60.
19. Hashimoto K, Corday E, Lang TW, et al. Significance of S-T segment elevations in acute myocardial ischemia. Evaluation with intracoronary electrode technique. The American journal of cardiology 1976;37:493-500.

20. Meier B, Rutishauser W. Coronary pacing during percutaneous transluminal coronary angioplasty. Circulation 1985;71:557-61.
21. Friedman PL, Shook TL, Kirshenbaum JM, Selwyn AP, Ganz P. Value of the intracoronary electrocardiogram to monitor myocardial ischemia during percutaneous transluminal coronary angioplasty. Circulation 1986;74:330-9.
22. Pande AK, Meier B, Urban P, Moles V, Dorsaz PA, Favre J. Intracoronary electrocardiogram during coronary angioplasty. American heart journal 1992;124:337-41.
23. Yong AS, Lowe HC, Ng MK, Kritharides L. The intracoronary electrocardiogram in percutaneous coronary intervention. Journal of interventional cardiology 2009;22:68-76.
24. Piessens J, Vrolix M, Sionis D, Glazier JJ, De Geest H, Willems J. The value of the intracoronary electrogram for the early detection of myocardial ischaemia during coronary angioplasty. European heart journal 1991;12:1176-82.
25. Abboud S, Cohen RJ, Selwyn A, Ganz P, Sadeh D, Friedman PL. Detection of transient myocardial ischemia by computer analysis of standard and signal-averaged high-frequency electrocardiograms in patients undergoing percutaneous transluminal coronary angioplasty. Circulation 1987;76:585-96.
26. Goette J. Review of Various Biomedical Signals. Biomedical Signal Processing and Analysis. Bern University of Applied Sciences: Institute of Human Centered Engineering; 2018.
27. Hishikari K, Yonetsu T, Lee T, et al. Intracoronary electrocardiogram ST-segment elevation in patients with non-ST-segment elevation myocardial infarction and its association with culprit lesion location and myocardial injury. EuroIntervention : journal of EuroPCR in collaboration with the Working Group on Interventional Cardiology of the European Society of Cardiology 2014;10:105-12.
28. Hishikari K, Kakuta T, Lee T, Murai T, Yonetsu T, Isobe M. ST-segment elevation on intracoronary electrocardiogram after percutaneous coronary intervention is associated with worse outcome in patients with non-ST-segment elevation myocardial infarction. Catheterization and cardiovascular interventions : official journal of the Society for Cardiac Angiography & Interventions 2016;87:E113-21.
29. Uetani T, Amano T, Kumagai S, et al. Intracoronary electrocardiogram recording with a bare-wire system: perioperative ST-segment elevation in the intracoronary electrocardiogram is associated with myocardial injury after elective coronary stent implantation. JACC Cardiovascular interventions 2009;2:127-35.
30. Balian V, Galli M, Marcassa C, et al. Intracoronary ST-segment shift soon after elective percutaneous coronary intervention accurately predicts periprocedural myocardial injury. Circulation 2006;114:1948-54.
31. Sato T, Yuasa S, Ohta Y, Goto S, Aizawa Y. Small lipid core burden index in patients with stable angina pectoris is also associated with microvascular dysfunction: Insights from intracoronary electrocardiogram. Journal of thrombosis and thrombolysis 2021.
32. Balian V, Marcassa C, Galli M, et al. Intracoronary electrocardiogram ST segment shift evaluation during intravenous adenosine infusion: a comparison with fractional flow reserve. Cardiology journal 2011;18:662-7.
33. Ferrari E, Vidal R, Migneco O, Thiry M, Baudouy M. Usefulness of endocoronary electrocardiogram in the detection of myocardial viability and comparison with single-photon emission computed tomography Tl-201. The American journal of cardiology 1998;82:1279-81, a9.
34. Yajima J, Saito S, Honye J, Takayama T, Ozawa Y, Kanmatsuse K. Intracoronary electrocardiogram for early detection of myocardial viability during coronary angioplasty in acute myocardial infarction. International journal of cardiology 2001;79:293-9.
35. Abaci A, Oguzhan A, Topsakal R, et al. Intracoronary electrocardiogram and angina pectoris during percutaneous coronary interventions as an assessment of myocardial viability: comparison with low-dose dobutamine echocardiography. Catheterization and cardiovascular interventions : official journal of the Society for Cardiac Angiography & Interventions 2003;60:469-76.

36. Petrucci E, Balian V, Bocchieri A. Real-time assessment of myocardial viability in the catheterization laboratory using the intracoronary electrograms recorded by the PTCA guidewire in patients with left ventricular dysfunction: comparison with delayed-enhancement magnetic resonance imaging. JACC Cardiovascular interventions 2014;7:988-96.
37. Bigler MR, Seiler C. The Human Coronary Collateral Circulation, Its Extracardiac Anastomoses and Their Therapeutic Promotion. Int J Mol Sci 2019;20:3726.
38. Bloor CM, Keefe JF, Browne MJ. Intercoronary anastomoses in congenital heart disease. Circulation 1966;33:227-31.
39. Reiner L, Molnar J, Jimenez FA, Freudenthal RR. Interarterial coronary anastomoses in neonates. Archives of pathology 1961;71:103-12.
40. Zoll PM, Wessler S, Schlesinger MJ. Interarterial coronary anastomoses in the human heart, with particular reference to anemia and relative cardiac anoxia. Circulation 1951;4:797-815.
41. Bigler MR, Seiler C. The Human Coronary Collateral Circulation, Its Extracardiac Anastomoses and Their Therapeutic Promotion. International journal of molecular sciences 2019;20.
42. Seiler C, Stoller M, Pitt B, Meier P. The human coronary collateral circulation: development and clinical importance. European heart journal 2013;34:2674-82.
43. Seiler C, Fleisch M, Garachemani A, Meier B. Coronary collateral quantitation in patients with coronary artery disease using intravascular flow velocity or pressure measurements. Journal of the American College of Cardiology 1998;32:1272-9.
44. Pijls NH, van Son JA, Kirkeeide RL, De Bruyne B, Gould KL. Experimental basis of determining maximum coronary, myocardial, and collateral blood flow by pressure measurements for assessing functional stenosis severity before and after percutaneous transluminal coronary angioplasty. Circulation 1993;87:1354-67.
45. Wustmann K, Zbinden S, Windecker S, Meier B, Seiler C. Is there functional collateral flow during vascular occlusion in angiographically normal coronary arteries? Circulation 2003;107:2213-20.
46. de Marchi SF, Streuli S, Haefeli P, et al. Determinants of prognostically relevant intracoronary electrocardiogram ST-segment shift during coronary balloon occlusion. The American journal of cardiology 2012;110:1234-9.
47. Seiler C, Engler R, Berner L, et al. Prognostic relevance of coronary collateral function: confounded or causal relationship? Heart (British Cardiac Society) 2013;99:1408-14.
48. Billinger M, Fleisch M, Eberli FR, Garachemani A, Meier B, Seiler C. Is the development of myocardial tolerance to repeated ischemia in humans due to preconditioning or to collateral recruitment? Journal of the American College of Cardiology 1999;33:1027-35.
49. Koning R, Cribier A, Korsatz L, et al. Progressive decrease in myocardial ischemia assessed by intracoronary electrocardiogram during successive and prolonged coronary occlusions in angioplasty. American heart journal 1993;125:56-61.
50. Tomai F, Crea F, Gaspardone A, et al. Effects of A1 adenosine receptor blockade by bamiphylline on ischaemic preconditioning during coronary angioplasty. European heart journal 1996;17:846-53.
51. Tomai F, Crea F, Gaspardone A, et al. Phentolamine prevents adaptation to ischemia during coronary angioplasty: role of alpha-adrenergic receptors in ischemic preconditioning. Circulation 1997;96:2171-7.
52. Tomai F, Crea F, Gaspardone A, et al. Effects of naloxone on myocardial ischemic preconditioning in humans. Journal of the American College of Cardiology 1999;33:1863-9.
53. Tomai F, Crea F, Gaspardone A, et al. Ischemic preconditioning during coronary angioplasty is prevented by glibenclamide, a selective ATP-sensitive K+ channel blocker. Circulation 1994;90:700-5.
54. Tomai F, Crea F, Ghini AS, et al. Ischemic preconditioning during coronary angioplasty is preserved in elderly patients. Italian heart journal : official journal of the Italian Federation of Cardiology 2000;1:562-8.

55. Bigler MR, Stoller M, Tschannen C, Grossenbacher R, Seiler C. Effect of permanent right internal mammary artery occlusion on right coronary artery supply: A randomized placebo-controlled clinical trial. American heart journal 2020;230:1-12.
56. Gloekler S, Meier P, de Marchi SF, et al. Coronary collateral growth by external counterpulsation: a randomised controlled trial. Heart (British Cardiac Society) 2010;96:202-7.
57. Gloekler S, Traupe T, Stoller M, et al. The effect of heart rate reduction by ivabradine on collateral function in patients with chronic stable coronary artery disease. Heart (British Cardiac Society) 2014;100:160-6.
58. Meier P, Gloekler S, de Marchi SF, et al. Myocardial salvage through coronary collateral growth by granulocyte colony-stimulating factor in chronic coronary artery disease: a controlled randomized trial. Circulation 2009;120:1355-63.
59. Pohl T, Wustmann K, Zbinden S, et al. Exercise-induced human coronary collateral function: quantitative assessment during acute coronary occlusions. Cardiology 2003;100:53-60.
60. Seiler C, Fleisch M, Meier B. Direct intracoronary evidence of collateral steal in humans. Circulation 1997;96:4261-7.
61. Seiler C, Pohl T, Wustmann K, et al. Promotion of collateral growth by granulocyte-macrophage colony-stimulating factor in patients with coronary artery disease: a randomized, double-blind, placebo-controlled study. Circulation 2001;104:2012-7.
62. Senti S, Fleisch M, Billinger M, Meier B, Seiler C. Long-term physical exercise and quantitatively assessed human coronary collateral circulation. Journal of the American College of Cardiology 1998;32:49-56.
63. Stoller M, de Marchi SF, Seiler C. Function of natural internal mammary-to-coronary artery bypasses and its effect on myocardial ischemia. Circulation 2014;129:2645-52.
64. Stoller M, Seiler C. Effect of Permanent Right Internal Mammary Artery Closure on Coronary Collateral Function and Myocardial Ischemia. Circulation Cardiovascular interventions 2017;10.
65. Stoller M, Traupe T, Khattab AA, de Marchi SF, Steck H, Seiler C. Effects of coronary sinus occlusion on myocardial ischaemia in humans: role of coronary collateral function. Heart (British Cardiac Society) 2013;99:548-55.
66. Togni M, Gloekler S, Meier P, et al. Instantaneous coronary collateral function during supine bicycle exercise. European heart journal 2010;31:2148-55.
67. Zbinden R, Zbinden S, Meier P, et al. Coronary collateral flow in response to endurance exercise training. European journal of cardiovascular prevention and rehabilitation : official journal of the European Society of Cardiology, Working Groups on Epidemiology & Prevention and Cardiac Rehabilitation and Exercise Physiology 2007;14:250-7.
68. Zbinden S, Zbinden R, Meier P, Windecker S, Seiler C. Safety and efficacy of subcutaneous-only granulocyte-macrophage colony-stimulating factor for collateral growth promotion in patients with coronary artery disease. Journal of the American College of Cardiology 2005;46:1636-42.
69. Westerhof N, Boer C, Lamberts RR, Sipkema P. Cross-Talk Between Cardiac Muscle and Coronary Vasculature. Physiological Reviews 2006;86:1263-308.
70. Sanders M, White FC, Peterson TM, Bloor CM. Characteristics of coronary blood flow and transmural distribution in miniature pigs. The American journal of physiology 1978;235:H601-9.
71. Feigl EO. Coronary physiology. Physiological Reviews 1983;63:1-205.
72. Duncker DJ, Bache RJ, Merkus D, Laughlin MH. Chapter 22 - Exercise and the Coronary Circulation. In: Zoladz JA, ed. Muscle and Exercise Physiology: Academic Press; 2019:467-503.
73. Seiler C. (F)Utility of invasive haemodynamic measurements to guide percutaneous intervention in chronic coronary artery disease. Swiss medical weekly 2015;145:w14143.
74. de Marchi SF, Gloekler S, Rimoldi SF, Rölli P, Steck H, Seiler C. Microvascular response to metabolic and pressure challenge in the human coronary circulation. American journal of physiology Heart and circulatory physiology 2011;301:H434-41.

75. Pschyrembel W, Walter de Gruyter Gmb H, Co KG. Pschyrembel Klinisches Wörterbuch2017.
76. Lilly LS, School HM. Pathophysiology of Heart Disease: A Collaborative Project of Medical Students and Faculty: Wolters Kluwer/Lippincott Williams & Wilkins; 2011.
77. Hachamovitch R, Rozanski A, Shaw LJ, et al. Impact of ischaemia and scar on the therapeutic benefit derived from myocardial revascularization vs. medical therapy among patients undergoing stress-rest myocardial perfusion scintigraphy. European heart journal 2011;32:1012-24.
78. Pathophysiology of Heart Disease. Fith Edition ed: Wolters Kluwer; 2011.
79. Benjamin EJ, Muntner P, Alonso A, et al. Heart Disease and Stroke Statistics-2019 Update: A Report From the American Heart Association. Circulation 2019;139:e56-e528.
80. Timmis A, Townsend N, Gale C, et al. European Society of Cardiology: Cardiovascular Disease Statistics 2017. European heart journal 2018;39:508-79.
81. Hibbert B, Nathan HJ, Simard T, O'Brien ER. Chapter 5 - Coronary Physiology and Atherosclerosis. In: Kaplan JA, ed. Kaplan's Essentials of Cardiac Anesthesia (Second Edition). Philadelphia: Elsevier; 2018:80-93.
82. Jones DP, True HD, Patel J. Leukocyte Trafficking in Cardiovascular Disease: Insights from Experimental Models. Mediators of inflammation 2017;2017:9746169.
83. Falk E. Pathogenesis of atherosclerosis. Journal of the American College of Cardiology 2006;47:C7-12.
84. Lusis AJ. Atherosclerosis. Nature 2000;407:233-41.
85. Newby DE. Computed Tomography or Functional Stress Testing for the Prediction of Risk: Can I Have My Cake and Eat It? Circulation 2017;136:2006-8.
86. Gould KL, Lipscomb K. Effects of coronary stenoses on coronary flow reserve and resistance. The American journal of cardiology 1974;34:48-55.
87. Zhang H, Mu L, Hu S, et al. Comparison of Physician Visual Assessment With Quantitative Coronary Angiography in Assessment of Stenosis Severity in China. JAMA internal medicine 2018;178:239-47.
88. Gould KL, Lipscomb K, Hamilton GW. Physiologic basis for assessing critical coronary stenosis. Instantaneous flow response and regional distribution during coronary hyperemia as measures of coronary flow reserve. The American journal of cardiology 1974;33:87-94.
89. van Nunen LX, Zimmermann FM, Tonino PA, et al. Fractional flow reserve versus angiography for guidance of PCI in patients with multivessel coronary artery disease (FAME): 5-year follow-up of a randomised controlled trial. Lancet (London, England) 2015;386:1853-60.
90. Stegehuis VE, Wijntjens GW, Piek JJ, van de Hoef TP. Fractional Flow Reserve or Coronary Flow Reserve for the Assessment of Myocardial Perfusion. Current cardiology reports 2018;20:77.
91. Pijls NH, De Bruyne B, Peels K, et al. Measurement of fractional flow reserve to assess the functional severity of coronary-artery stenoses. The New England journal of medicine 1996;334:1703-8.
92. Sen S, Escaned J, Malik IS, et al. Development and validation of a new adenosine-independent index of stenosis severity from coronary wave-intensity analysis: results of the ADVISE (ADenosine Vasodilator Independent Stenosis Evaluation) study. Journal of the American College of Cardiology 2012;59:1392-402.
93. Davies JE, Sen S, Dehbi HM, et al. Use of the Instantaneous Wave-free Ratio or Fractional Flow Reserve in PCI. The New England journal of medicine 2017;376:1824-34.
94. Knuuti J, Wijns W, Saraste A, et al. 2019 ESC Guidelines for the diagnosis and management of chronic coronary syndromes: The Task Force for the diagnosis and management of chronic coronary syndromes of the European Society of Cardiology (ESC). European heart journal 2019;41:407-77.
95. Bove KB, Michelsen MM, Schroder J, et al. Impaired coronary flow velocity reserve is associated with cardiovascular risk factors but not with angina symptoms. Open Heart 2021;8:e001486.

96. Sharaf B, Wood T, Shaw L, et al. Adverse outcomes among women presenting with signs and symptoms of ischemia and no obstructive coronary artery disease: findings from the National Heart, Lung, and Blood Institute-sponsored Women's Ischemia Syndrome Evaluation (WISE) angiographic core laboratory. American heart journal 2013;166:134-41.
97. Jespersen L, Hvelplund A, Abildstrøm SZ, et al. Stable angina pectoris with no obstructive coronary artery disease is associated with increased risks of major adverse cardiovascular events. European heart journal 2012;33:734-44.
98. Kunadian V, Chieffo A, Camici PG, et al. An EAPCI Expert Consensus Document on Ischaemia with Non-Obstructive Coronary Arteries in Collaboration with European Society of Cardiology Working Group on Coronary Pathophysiology & Microcirculation Endorsed by Coronary Vasomotor Disorders International Study Group. European heart journal 2020;41:3504-20.
99. Corban MT, Prasad A, Gulati R, Lerman LO, Lerman A. Sex-specific differences in coronary blood flow and flow velocity reserve in symptomatic patients with non-obstructive disease. EuroIntervention : journal of EuroPCR in collaboration with the Working Group on Interventional Cardiology of the European Society of Cardiology 2021;16:1079-84.
100. Mejía-Rentería H, van der Hoeven N, van de Hoef TP, et al. Targeting the dominant mechanism of coronary microvascular dysfunction with intracoronary physiology tests. The international journal of cardiovascular imaging 2017;33:1041-59.
101. Pries AR, Badimon L, Bugiardini R, et al. Coronary vascular regulation, remodelling, and collateralization: mechanisms and clinical implications on behalf of the working group on coronary pathophysiology and microcirculation. European heart journal 2015;36:3134-46.
102. Escaned J, Flores A, García-Pavía P, et al. Assessment of microcirculatory remodeling with intracoronary flow velocity and pressure measurements: validation with endomyocardial sampling in cardiac allografts. Circulation 2009;120:1561-8.
103. Rezkalla SH, Kloner RA. Cocaine-induced acute myocardial infarction. Clinical medicine & research 2007;5:172-6.
104. Almaddah N, Ajayi TO. Cocaine-Induced Coronary-Artery Vasospasm. New England Journal of Medicine 2016;374:e5.
105. Goodfellow I, Bengio Y, Courville A. Deep Learning: MIT Press; 2016.
106. Trask AW. Neuronale Netze und Deep Learning kapieren: mitp; 2020.
107. Yamashita R, Nishio M, Do RKG, Togashi K. Convolutional neural networks: an overview and application in radiology. Insights into imaging 2018;9:611-29.
108. Hubel DH, Wiesel TN. Receptive fields and functional architecture of monkey striate cortex. The Journal of physiology 1968;195:215-43.
109. Fukushima K. Neocognitron: a self organizing neural network model for a mechanism of pattern recognition unaffected by shift in position. Biological cybernetics 1980;36:193-202.
110. Jarrett K, Kavukcuoglu K, Ranzato MA, LeCun Y. What is the best multi-stage architecture for object recognition? 2009 IEEE 12th International Conference on Computer Vision, ICCV 20092009:2146--53.
111. Nair V, Hinton GE. Rectified linear units improve restricted boltzmann machines. Proceedings of the 27th International Conference on International Conference on Machine Learning2010:807–14.
112. Glorot X, Bordes A, Bengio Y. Deep Sparse Rectifier Neural Networks. Proceedings of the 14th International Conference on Artificial Intelligence and Statistics 2011:315-23.
113. Brownlee J. A Gentle Introduction to Cross-Entropy for Machine Learning. https://machinelearningmastery.com/2019.
114. Bishop CM. Pattern Recognition and Machine Learning. New York: Springer; 2006.
115. MathWorks. classificationLayer. MathWorks Help Center2016.
116. Bushaev V. How do we "train" neural networks? : https://towardsdatascience.com/; 2017.
117. Bottou L. Online algorithms and stochastic approximations. In: Saad D, ed. Online Learning in Neural Networks. Cambridge, UK: Cambridge University Press; 1998.
118. Polyak BT. Some methods of speeding up the convergence of iteration methods. USSR Computational Mathematics and Mathematical Physics 1964;4:1-17.

119. Murphy KP. Machine Learning: A Probabilistic Perspective. Cambridge, Massachusetts, USA: MIT Press; 2012.
120. Bushaev V. Stochastic Gradient Descent with momentum. https://towardsdatascience.com/2017.
121. Diederik P Kingma, Ba J. Adam: A Method for Stochastic Optimization. CoRR 2014.
122. Bushaev V. Adam - latest trends in deep learning optimization. towardsdatascience.com2018.
123. Ruder S. An overview of gradient descent optimization algorithms. CoRR 2016;abs/1609.04747.
124. LeCun Y. Generalization and network design strategies. In: Pfeifer R, Schreter Z, Fogelman F, Steels L, eds. Connectionism in perspective. Zurich, Switzerland: Elsevier; 1989.
125. LeCun Y, Bottou L, Bengio Y, Haffner P. Gradient-Based Learning Applied to Document Recognition. Proceedings of the IEEE1998.
126. Szegedy C, Liu W, Jia Y, et al. Going Deeper with Convolutions. CoRR 2014;abs/1409.4842.
127. Krizhevsky A, Sutskever I, Hinton GE. ImageNet Classification with Deep Convolutional Neural Networks. In: Pereira F, Burges CJC, Bottou L, Weinberger KQ, eds. Neural Information Prcoessing Systems2012.
128. Szegedy C, Ioffe S, Vanhoucke V. Inception-v4, Inception-ResNet and the Impact of Residual Connections on Learning. CoRR 2016;abs/1602.07261.
129. He K, Zhang X, Ren S, Sun J. Deep Residual Learning for Image Recognition. CoRR 2015;abs/1512.03385.
130. Zhou Y, Chellappa R. Computation of optical flow using a neural network. IEEE 1988 International Conference on Neural Networks. San Diego, CA, USA1988:71-8.
131. Srivastava N, Hinton G, Krizhevsky A, Sutskever I, Salakhutdinov R. J Mach Learn Res 2014;15:1929–58.
132. Bishop CM. Regularization and complexity control in feed-forward networks. International Conference on Artificial Neural Networks ICANN'95: EC2 et Cie; 1995:141-8.
133. Sjöberg J, Ljung L. Overtraining, Regularization, and Searching for Minimum in Neural Networks. IFAC Proceedings Volumes 1992;25:73-8.
134. Brownlee J. How to Configure the Learning Rate When Training Deep Learning Neural Networks. https://machinelearningmastery.com/2019.
135. MathWorks. trainingOptions. MathWorks Help Center2016.
136. Wilson DR, Martinez TR. The general inefficiency of batch training for gradient descent learning. Neural Networks 2003;16:1429-51.
137. Masters D, Luschi C. Revisiting Small Batch Training for Deep Neural Networks. CoRR 2018;abs/1804.07612.
138. Bergstra J, Bengio Y. Random search for hyper-parameter optimization. Journal of Machine Learning Research 2012;13:281-305.
139. Ye A. The Beauty of Bayesian Optimization, Explained in Simple Terms. https://towardsdatascience.com; 2020.
140. Bengio Y. Gradient-Based Optimization of Hyperparameters. Neural Computation 2000;12:1889-900.
141. Yosinski J, Clune J, Bengio Y, Lipson H. How transferable are features in deep neural networks? In: Ghahramani Z, Welling M, Cortes C, Lawrence N, Weinberger KQ, eds. Advances in Neural Information Processing Systems 27 (NIPS 2014): Red Hook; 2014.
142. Brownlee J. How to Improve Performance With Transfer Learning for Deep Learning Neural Networks. https://machinelearningmastery.com/2019.
143. Seif G. 7 Practical Deep Learning Tips. https://towardsdatascience.com2018.
144. Deng J, Dong W, Socher R, Li L, Kai L, Li F-F. ImageNet: A large-scale hierarchical image database. 2009 IEEE Conference on Computer Vision and Pattern Recognition; 2009 20-25 June 2009. p. 248-55.
145. Russakovsky O, Deng J, Su H, et al. ImageNet Large Scale Visual Recognition Challenge. International Journal of Computer Vision 2015;115:211-52.

146. Seiler C, Kirkeeide RL, Gould KL. Basic structure-function relations of the epicardial coronary vascular tree. Basis of quantitative coronary arteriography for diffuse coronary artery disease. Circulation 1992;85:1987-2003.
147. Williams B, Mancia G, Spiering W, et al. 2018 ESC/ESH Guidelines for the management of arterial hypertension: The Task Force for the management of arterial hypertension of the European Society of Cardiology (ESC) and the European Society of Hypertension (ESH). European heart journal 2018;39:3021-104.
148. de Bruyne B, Bartunek J, Sys SU, Pijls NH, Heyndrickx GR, Wijns W. Simultaneous coronary pressure and flow velocity measurements in humans. Feasibility, reproducibility, and hemodynamic dependence of coronary flow velocity reserve, hyperemic flow versus pressure slope index, and fractional flow reserve. Circulation 1996;94:1842-9.
149. Fearon WF, Balsam LB, Farouque HM, et al. Novel index for invasively assessing the coronary microcirculation. Circulation 2003;107:3129-32.
150. Bruce RA, Mazzarella JA, Jordan JW, Jr., Green E. Quantitation of QRS and ST segment responses to exercise. American heart journal 1966;71:455-66.
151. Simoons ML, Hugenholtz PG. Gradual changes of ECG waveform during and after exercise in normal subjects. Circulation 1975;52:570-7.
152. Kurita A, Chaitman BR, Bourassa MG. Significance of exercise-induced junctional S-T depression in evaluation of coronary artery disease. The American journal of cardiology 1977;40:492-7.
153. Simoons ML. Optimal measurements for detection of coronary artery disease by exercise electrocardiography. Computers and biomedical research, an international journal 1977;10:483-99.
154. Sgarbossa EB, Pinski SL, Barbagelata A, et al. Electrocardiographic diagnosis of evolving acute myocardial infarction in the presence of left bundle-branch block. GUSTO-1 (Global Utilization of Streptokinase and Tissue Plasminogen Activator for Occluded Coronary Arteries) Investigators. The New England journal of medicine 1996;334:481-7.
155. Tabas JA, Rodriguez RM, Seligman HK, Goldschlager NF. Electrocardiographic criteria for detecting acute myocardial infarction in patients with left bundle branch block: a meta-analysis. Annals of emergency medicine 2008;52:329-36.e1.
156. de Simone G, Devereux RB, Daniels SR, Meyer RA. Gender differences in left ventricular growth. Hypertension (Dallas, Tex : 1979) 1995;26:979-83.
157. Kalman RE. A New Approach to Linear Filtering and Prediction Problems. Journal of Basic Engineering 1960;82:35-45.
158. Wildhaber RA. Localized State Space and Polynomial Filters with Applications in Electrocardiography: ETH Zurich; 2019.

8. Appendix

The following sections include the code used on Matlab R2019b. Since the Matlab version R2020b, Matlab provides the application “Experiment Manager”, allowing the creation of a “deep learning experiment to train networks under various initial conditions and to compare the results” (Cited from: https://ch.mathworks.com/help/deeplearning/ ref/experimentmanager-app.html). Usage of this application requires less programming work.

8.1 Available pretrained neural networks on Matlab

Matlab provides multiple pretrained neural networks for classification tasks. Each network has different characteristics like network accuracy, speed and required size on the disc. It is recommended to start with a simple and fast network (e.g., AlexNet/GoogLeNet) and later try the tested settings on a network with a more sophisticated architecture (e.g., ResNet). For more detailed information, please see https://ch.mathworks.com/help/deeplearning/ug/pretrained-convolutional-neural-networks.html .

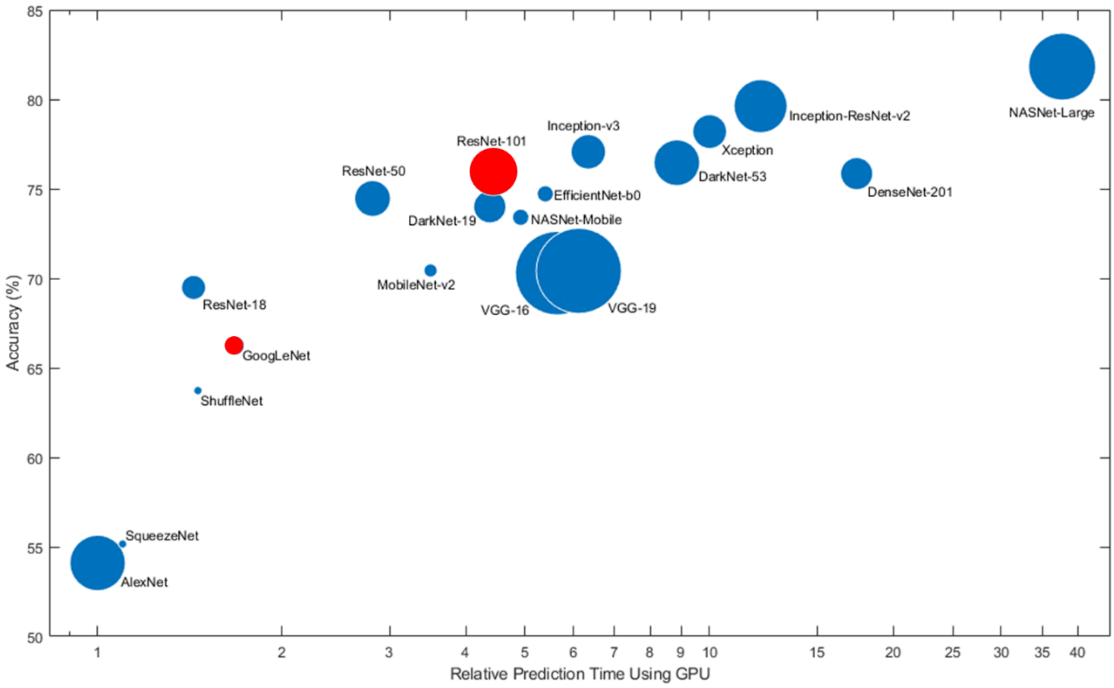

Appendix figure I: Overview of the available pretrained classification networks on Matlab. *As illustrated, choice of the network is socialized with a tradeoff between accuracy and relative prediction time. Of note, the prediction time is directly dependent on the used computational power (i.e., CPU vs GPU). The area of each marker is proportional to the size of the network on disk. The used networks for Project III are highlighted in red. This image was taken from: https://ch.mathworks.com/help/deeplearning/ug/pretrained-convolutional-neural-networks.html and slightly adapted for my purpose.*

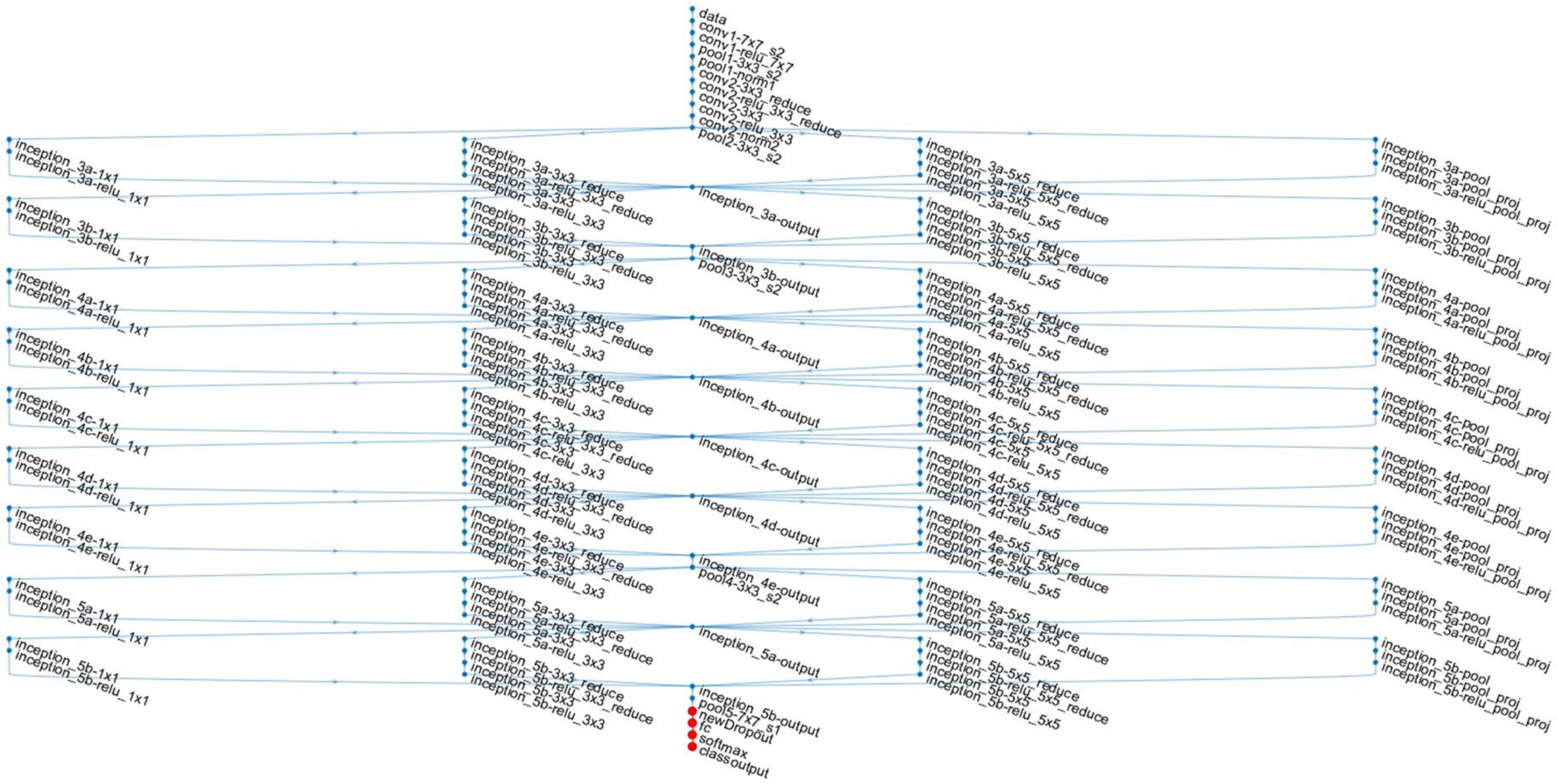

Appendix figure II: Network architecture of GoogLeNet. *GoogLeNet is a 22 convolutional layer deep convolutional neural network with a special architecture containing networks within the network architecture (called inception modules). These modules contains multiple different filter sizes (1x1, 3x3, 5x5) allowing simultaneous feature extraction on different levels of details. For transfer learning, the last four layers (marked red) were adapted to the new task.*

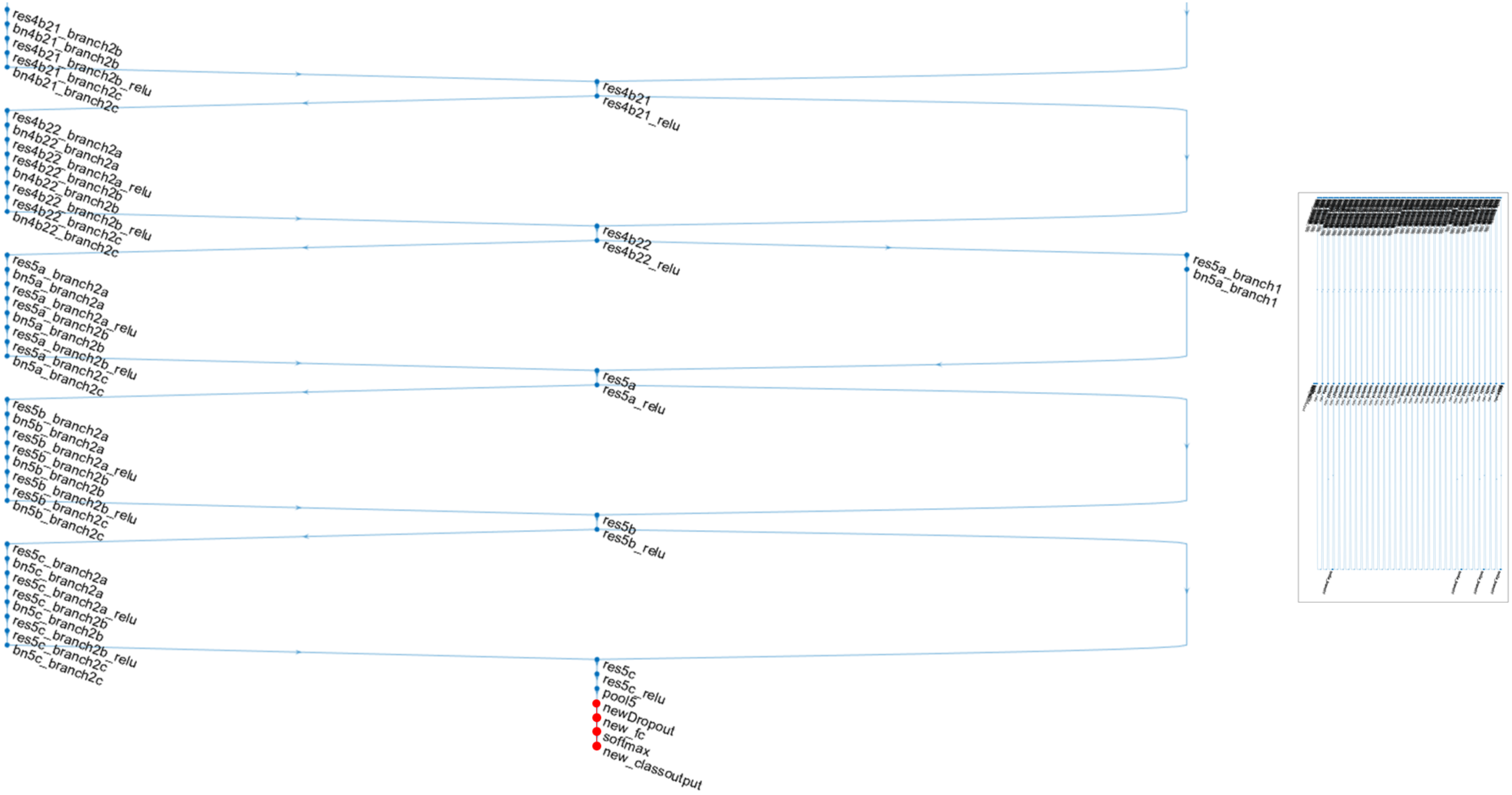

Appendix figure III: Network architecture of ResNet101. *ResNet101 is a 101 convolutional layer deep convolutional neural network with a special residual learning framework allowing the training of substantially deeper networks with subsequent improved accuracy without relevant increasing training difficulties. This learning framework is depicted on the right side, while the convolutional layers are listed on the left side of this figure. Please note that it was not possible to illustrate the whole network architecture on one page. The small figure presents an overview of the whole network architecture without readable layers, while the big figure illustrates the last layers including the four output layers (marked red), which were adapted to the new task.*

8.2 Image randomization, allocation and augmentation

```
% This is a MATLAB m-file
% ------------------------------------------------------------------------
% File          : Imagerandomisation_and_allocation.m
% Author        : Marius Reto Bigler, adapted from an example from
%                 Mathworks
% Date adapted  : 15.10.2020
% Last Change   : 20.10.2020
% Institute     : Department of Cardiology
% ------------------------------------------------------------------------
% Description:
%
% This function randomly allocates all available data into a virtual
% training and a validation datastore necessary for the transfer learning
% process.
% Further, it uses data augmentation to prevent overfitting.
%
% The code is based from an MathWork example and adapted to this task. Link
% to the original example:
https://ch.mathworks.com/help/deeplearning/ref/trainnetwork.html#mw_d13a492
2-1dd5-4409-a0fd-fc489c353a9f

% File path
parentDir =  'C:\Users\Marius\Documents\Googlenet';

% Folder name
dataDir = 'Data2';

% Create a data store of all images. Of note, the ECG images have to be
% already sorted to "normal" and "ischemic" according to the time point of
% ECG recording (i.e. before or at the end of a 1-minute coronary
% occlusion)in two subfolders named accordingly.
allImages = imageDatastore(fullfile(parentDir,dataDir),...
'IncludeSubfolders',true,...
'LabelSource','foldernames');

% rng default => "controlled" randomization, repeatable so that each
% network is trained with the same training data, which was once randomly
% selected
rng default

% randomly allocate the images to training and validation with a ratio of
% 80% training and 20% validation images
[imgsTrain,imgsValidation] = splitEachLabel(allImages,0.8,'randomized');

% display the number of image in each group
disp(['Number of training images: ',num2str(numel(imgsTrain.Files))]);
disp(['Number of validation images:
',num2str(numel(imgsValidation.Files))]);

% define the inputSize (for both CNNs the same)
inputSize = [224,224,3];

%% Data augmentation
% Data augmentation (i.e., an augmented data store), transforms batches of
% training sets with optional preprocessing such as resizing, rotation etc.
% This helps to prevent the network from overfitting and memorizing the
% exact details of the training image => in particular recommended with
% limited data.
```

```
% Define the preprocessing, here with a random rotation, a shift in both
% directions and reflection along the x-axis
imageAugmenter = imageDataAugmenter('RandRotation',[-45,45],...
    'RandYReflection',1,...
    'RandXTranslation',[-10,10],...
    'RandYTranslation',[-10,10]);

% create the augmented data store
augimgsTrain = augmentedImageDatastore(inputSize,imgsTrain,...
'DataAugmentation',imageAugmenter);
```

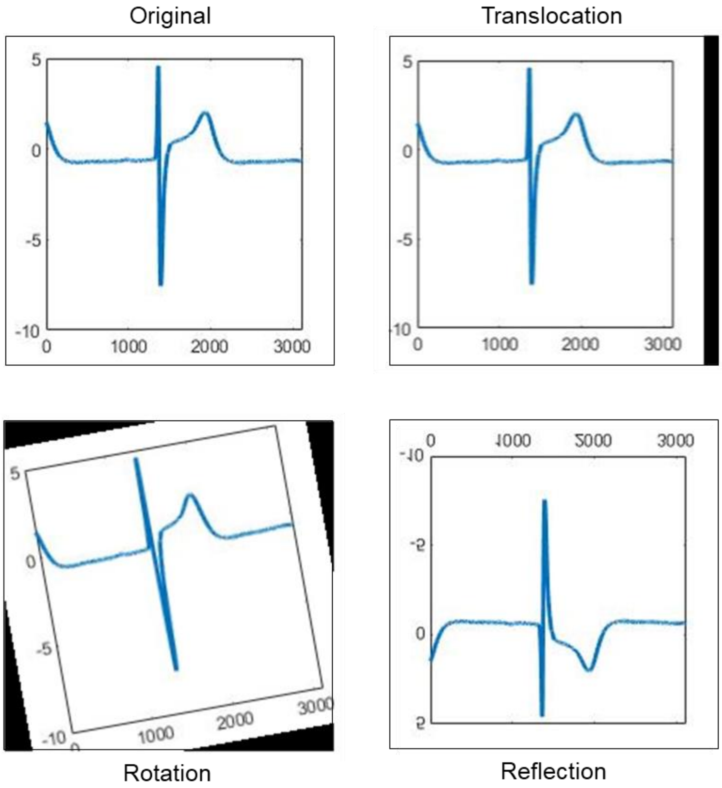
Original
Translocation
Rotation
Reflection

Appendix figure IV: Visualization of the data augmentation effect. *The original icECG image (the same as figure 1 in Project III) is depicted on the upper left corner. Three different data augmentation effects were used: 1. Translocation up to 10 pixels in every direction (x and y-axis). 2. Rotation up to 45° in every direction (in the bottom left corner, the image is rotated 10°) 3. Reflection along the x-axis (bottom right corner). Data augmentation was performed to prevent overfitting and to make the network invariant to translation of the input.*

8.3 Transfer learning using Bayesian optimization

```
% This is a MATLAB m-file
% -------------------------------------------------------------------------
% File          : deeplearningusingbayesianoptimization.m
% Author        : Marius Reto Bigler, adapted from an example from
%                 Mathworks
% Date adapted  : 15.10.2020
% Last Change   : 19.10.2020
% Institute     : Department of Cardiology
% -------------------------------------------------------------------------
% Description:
%
% Hyperparameter optimization using Bayesian optimization. After few
% training runs with randomly chosen hyperparameter settings within the
% predefined range, a surrogate function of the cost-function is
% constructed and further hyperparameter settings are tried according to
% the presumed minima.
%
% Please note, explanations are directly copied from the Mathworks example:
% https://ch.mathworks.com/help/deeplearning/ug/deep-learning-using-
bayesian-optimization.html

%% Deep Learning Using Bayesian Optimization
%
% Choose hyperparameter to optimize
optVars = [
    optimizableVariable('InitialLearnRate',[1e-5 2e-4],'Type','real',
    'Transform','log')
    optimizableVariable('MiniBatchSize',[8 32],'Type','integer',
    'Transform','none')
    optimizableVariable('Dropout',[0.3 0.8],'Type','real',
    'Transform','none')];

% Create the objective function for the Bayesian optimizer, using the
% training and validation data as inputs. The objective function trains a
% convolutional neural network and returns the classification error on the
% validation set. This function is defined at the end of this script.
%
% Because bayesopt uses the error rate on the validation set to choose the
% best model, it is possible that the final network overfits on the
% validation set. The final chosen model is then tested on the independent
% test set to estimate the generalization error.
ObjFcn = makeObjFcn(XTrain,YTrain,XValidation,YValidation);

% Perform Bayesian optimization by minimizing the classification error on
% the validation set. After each network finishes training, bayesopt
% prints the results to the command window.
BayesObject = bayesopt(ObjFcn,optVars);

%% Evaluation
% Load the best network found in the optimization and its validation
accuracy.
bestIdx = BayesObject.IndexOfMinimumTrace(end);
fileName = BayesObject.UserDataTrace{bestIdx};
savedStruct = load(fileName);
valError = savedStruct.valError

% Predict the labels of the test set
[YPredicted,probs] = classify(savedStruct.trainedNet,imgsExam);
```

```
% Compare it to the true values (i.e., the image labels). Further,
% calculate the test error.
testError = 1 - mean(YPredicted == imgsExam.Labels)

% Plot the confusion matrix for the test data. Display the precision and
% recall for each class by using column and row summaries.
figure('Units','normalized','Position',[0.2 0.2 0.4 0.4]);
cm = confusionchart(imgsExam.Labels,YPredicted);
cm.Title = 'Confusion Matrix for Test Data';
cm.ColumnSummary = 'column-normalized';
cm.RowSummary = 'row-normalized';

%% Objective Function for Optimization
% Define the objective function for optimization. This function performs
% the following steps:
%
% 1) Takes the values of the optimization variables as inputs. bayesopt
% calls the objective function with the current values of the optimization
% variables in a table with each column name equal to the variable name.
% For example, the current value of the network section depth is
% optVars.SectionDepth.
%
% 2. Defines the network architecture and training options.
%
% 3. Trains and validates the network.
%
% 4. Saves the trained network, the validation error, and the training
% options to disk.
%
% 5. Returns the validation error and the file name of the saved network.
function ObjFcn = makeObjFcn(XTrain,YTrain,XValidation,YValidation)
    ObjFcn = @valErrorFun;

    function [valError,cons,fileName] = valErrorFun(optVars)

%% load the pretrained neural network
net = resnet101; %or alternatively GoogLeNet

% display the structure of the network including some information
numClasses = numel(categories(YTrain));
lgraph = layerGraph(net);

% remove the previous output layers
lgraph =
removeLayers(lgraph,{'fc1000','prob','ClassificationLayer_predictions'});

% define new layers for this specific task including a new classification
% layer with normal and ischemic classes
newLayers = [dropoutLayer(optVars.Dropout,'Name','newDropout')
     fullyConnectedLayer(numClasses,'Name','new_fc','WeightLearnRateFactor'
     ,10,'BiasLearnRateFactor',10)
     softmaxLayer('Name','softmax')
     classificationLayer('Name','new_classoutput')];

% add the layers at the end of the CNN and connect them
lgraph = addLayers(lgraph,newLayers);
lgraph = connectLayers(lgraph,'pool5','newDropout');
inputSize = net.Layers(1).InputSize;
```

```
numberOfLayers = numel(lgraph.Layers);

% To check that the new layers are connected correctly, plot the new layer
% graph and zoom in on the last layers of the network. (Please note, this
% was only done once and not for each network)
figure('Units','normalized','Position',[0.3 0.3 0.4 0.4]);
plot(lgraph)
ylim([0,10])

% define the training options for the transfer learning. Please note, this
% example was coded with ValidationPatience = “number of times that the
% loss on the validation set can be larger than or equal to the previously
% smallest loss before network training stops.” Thus, number of epochs was
% chosen large as the training stopped automatically.
options = trainingOptions('adam',...
    'MiniBatchSize',optVars.MiniBatchSize,...
    'MaxEpochs',60,...
    'InitialLearnRate',optVars.InitialLearnRate,...
    'ValidationData',XValidation,...
    'ValidationFrequency',10,...
    'ValidationPatience',15,...
    'Verbose',1,...
    'Shuffle','every-epoch',...
    'ExecutionEnvironment','auto',...
    'Plots','training-progress');

% start with the training process
trainedNet = trainNetwork(datasource,lgraph,options);

% Evaluate the trained network on the validation set, calculate the
% predicted image labels, and calculate the error rate on the validation
% data.
YPredicted = classify(trainedNet,XValidation);
valError = 1 - mean(YPredicted == YValidation);

% save the network using the calculated error rate as name
fileName = num2str(valError) + ".mat";
save(fileName,'trainedNet','valError','options')
cons = [];

    end

end
```

8.4 Network performance analysis

```
% This is a MATLAB m-file
% --------------------------------------------------------------------------
% File          : NetworkPerformanceAnalysis.m
% Author        : Marius Reto Bigler, adapted from an example from
%                 Mathworks
% Date adapted  : 15.10.2020
% Last Change   : 19.10.2020
% Institute     : Department of Cardiology
% --------------------------------------------------------------------------
% Description:
%
% This function was used to assess the performance of the trained neural
% network. First, it loads the images into a data store (exactly the same
% code as in Appendix 1.2) and allocates them into the training group and
% the validation group. Further, it loads the examination data from a
% separate folder. Parts of the code are directly copied from
https://ch.mathworks.com/help/deeplearning/ug/deep-learning-using-bayesian-
optimization.html

% File path
parentDir =  '\\filer300\users3006\i0316914\Documents\Aktuelle Studien\MD-
PhD Thesis\Neural Network\ResNet101';

% Folder name
dataDir = 'NewData';

% create a data store of all images. Of note, the ECG images in data 2 are
% already sorted to normal and ischemic according to the time point of
% ECG recording (i.e. before or at the end of a 1-minute coronary
% occlusion)
allImages = imageDatastore(fullfile(parentDir,dataDir),...
'IncludeSubfolders',true,...
'LabelSource','foldernames');

%rng default => "controlled" randomization, repeatable
rng default

% randomly allocate the images to training and validation
[imgsTrain,imgsValidation] = splitEachLabel(allImages,0.8,'randomized');

% delete the training images and the first data store with all images as
% they are not further required in the workspace
clear allImages
clear imgsTrain

% Further, the examination images as well as the combination of the
% examination and the validation images were stored separately to simplify
% the performance analysis.
% Examination images
imgsExam = imageDatastore(fullfile(parentDir,'NewExam'),...
'IncludeSubfolders',true,...
'LabelSource','foldernames');

% Combination of examination and validation images
imgsValExam =
imageDatastore(fullfile(parentDir,'ValidationExaminationData'),...
'IncludeSubfolders',true,...
'LabelSource','foldernames');
```

```
%% Predictions
% Predict the labels of the Validation Data Set.
[YPredicted1,probs] = classify(net,imgsValidation);

% Compare it with the true labels and calculate the accuracy.
ValAccuracy = mean(YPredicted1 == imgsValidation.Labels)

% Visualize the results in a confusion matrix
figure(1);
cm1 = confusionchart(imgsValidation.Labels,YPredicted1);
cm1.Title = 'Confusion Matrix for Validation Data';
cm1.ColumnSummary = 'column-normalized';
cm1.RowSummary = 'row-normalized';

% Predict the labels of the Examination Data Set.
[YPredicted,probs] = classify(net,imgsExam);

% Compare it with the true labels and calculate the accuracy.
ExamAccuracy = mean(YPredicted == imgsExam.Labels)

% Visualize the results in a confusion matrix
figure(2);
cm = confusionchart(imgsExam.Labels,YPredicted);
cm.Title = 'Confusion Matrix for Examination Data';
cm.ColumnSummary = 'column-normalized';
cm.RowSummary = 'row-normalized';

% Predict the labels of the ValidationExamination Data Set.
[YPredicted2,probs] = classify(net,imgsValExam);

% Compare it with the true labels and calculate the accuracy.
ValExamAccuracy = mean(YPredicted2 == imgsValExam.Labels)

% Visualize the results in a confusion matrix
figure(3);
cm1 = confusionchart(imgsValExam.Labels,YPredicted2);
cm1.Title = 'Confusion Matrix for ValidationExaminationData';
cm1.ColumnSummary = 'column-normalized';
cm1.RowSummary = 'row-normalized';
```

Appendix figure V: Confusion matrix for the combination of validation and examination data for ResNet 5. *As outlined above (Appendix 8.1), choice of the network is a tradeoff between accuracy and prediction time. With increasing numbers of convolutional layers, the prediction time rises. Upload into the datastore, network prediction, calculation of the accuracy and plotting of the three confusion matrixes (code above) took 55sec for ResNet5 and for 19sec GoogLeNet10.*

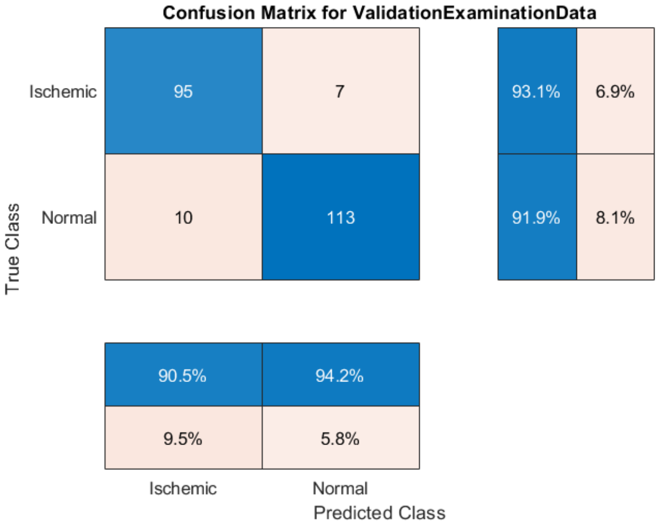

8.5 Visualization of network predictions

```
% This is a MATLAB m-file
% -------------------------------------------------------------------------
% File          : InvestigateNetworkPredictions.m
% Author        : Marius Reto Bigler, adapted from an example from
%                 Mathworks
% Date adapted  : 15.10.2020
% Last Change   : 19.10.2020
% Institute     : Department of Cardiology
% -------------------------------------------------------------------------
% Description:
%
% This function gives us a visual explanation what triggered the prediction
% of the neural network based on the code from the Mathworks example on
% Investigate Network Predictions Using Class Activation Mapping
% (https://ch.mathworks.com/help/deeplearning/ug/investigate-network-
predictions-using-class-activation-mapping.html )
%
% The class activation map shows which regions of the input image
% contributed the most to the predicted class (red = the most).

% Load a pretrained convolutional neural network for image classification.
load('\\filer300\users3006\i0316914\Documents\Aktuelle Studien\MD-PhD
Thesis\Neural Network\ResNet101\BestResnet101\Resnet5_D0.80_M14_E60_L1e-
4.mat')

% Provide the general network architecture (necessary to know the name of
% the correct output layer required for the class activation mapping
netName = "resnet101";

% Extract the image input size and the output classes of the network.
% The activationLayerName helper function, defined at the end of this
% example, returns the name of the layer to extract the activations from.
% This layer is the ReLU layer that follows the last convolutional layer of
% the network.
inputSize = net.Layers(1).InputSize(1:2);
classes = net.Layers(end).Classes;
layerName = activationLayerName(netName);

%% Display Class Activation Maps
% Create a figure and perform class activation mapping in a loop.
% To terminate execution of the loop, close the figure.
h = figure('Units','normalized','Position',[0.05 0.05 0.9
0.8],'Visible','on');

while ishandle(h)

% File paths of the ten images used to discover the underlying morphology
% responsible for the network prediction (i.e., Project III, supplemental
% figures). Please note, for reasons of space, only one file path is shown.
im = imread('\'\\filer300\users3006\i0316914\Documents\Aktuelle Studien\MD-
PhD Thesis\Neural
Network\VisualisierungsData\38002_vessel1_arm_1_cfi60_ECGavg.mat.jpg');

% The class activation map for a specific class is the activation map of
% the ReLU layer that follows the final convolutional layer, weighted by
% how much each activation contributes to the final score of that class.
%
```

```
% Those weights equal the weights of the final fully connected layer of the
% network for that class. Please note, you can generate a class activation
% map for any output class. For example, if the network makes an incorrect
% classification, you can compare the class activation maps for the true
% and predicted classes.
%
% However, here, we are interested in the class activation map for the
% predicted class with the highest score.
    scores = squeeze(mean(imageActivations,[1 2]));

    if netName ~= "squeezenet"
        fcWeights = net.Layers(end-2).Weights;
        fcBias = net.Layers(end-2).Bias;
        scores =  fcWeights*scores + fcBias;

        [~,classIds] = maxk(scores,3);

        weightVector = shiftdim(fcWeights(classIds(1),:),-1);
        classActivationMap = sum(imageActivations.*weightVector,3);

    else
        [~,classIds] = maxk(scores,3);
        classActivationMap = imageActivations(:,:,classIds(1));

    end

% Calculate the top class labels and the final normalized class scores.
    scores = exp(scores)/sum(exp(scores));
    maxScores = scores(classIds);
    labels = classes(classIds);

% Plot the class activation map. Display the original image in the first
% subplot. In the second subplot, use the CAMshow helper function, defined
% at the end of this example, to display the class activation map on top of
% a darkened grayscale version of the original image. Display the top three
% predicted labels with their predicted scores.
    subplot(1,2,1)
    imshow(im)

    subplot(1,2,2)
    CAMshow(im,classActivationMap)
    title(string(labels) + ", " + string(maxScores));

    drawnow

end


%% ActivationLayerName function

% provides the correct layer name, i.e., the name of the ReLU layer that

% follows the final convolutional layer

function layerName = activationLayerName(netName)

     if netName == "squeezenet"
         layerName = 'relu_conv10';

     elseif netName == "googlenet"
         layerName = 'inception_5b-output';

     elseif netName == "resnet18"
```

```
         layerName = 'res5b_relu';

     elseif netName == "resnet101"
          layerName = 'res5c_relu';

     elseif netName == "mobilenetv2"
         layerName = 'out_relu';
     end

end

%% CAMshow function
% Please note, this function was provided by the Mathworks example
function CAMshow(im,CAM)
imSize = size(im);
CAM = imresize(CAM,imSize(1:2));
CAM = normalizeImage(CAM);
CAM(CAM<0.2) = 0;
cmap = jet(255).*linspace(0,1,255)';
CAM = ind2rgb(uint8(CAM*255),cmap)*255;

combinedImage = double(rgb2gray(im))/2 + CAM;
combinedImage = normalizeImage(combinedImage)*255;
imshow(uint8(combinedImage));
end
```

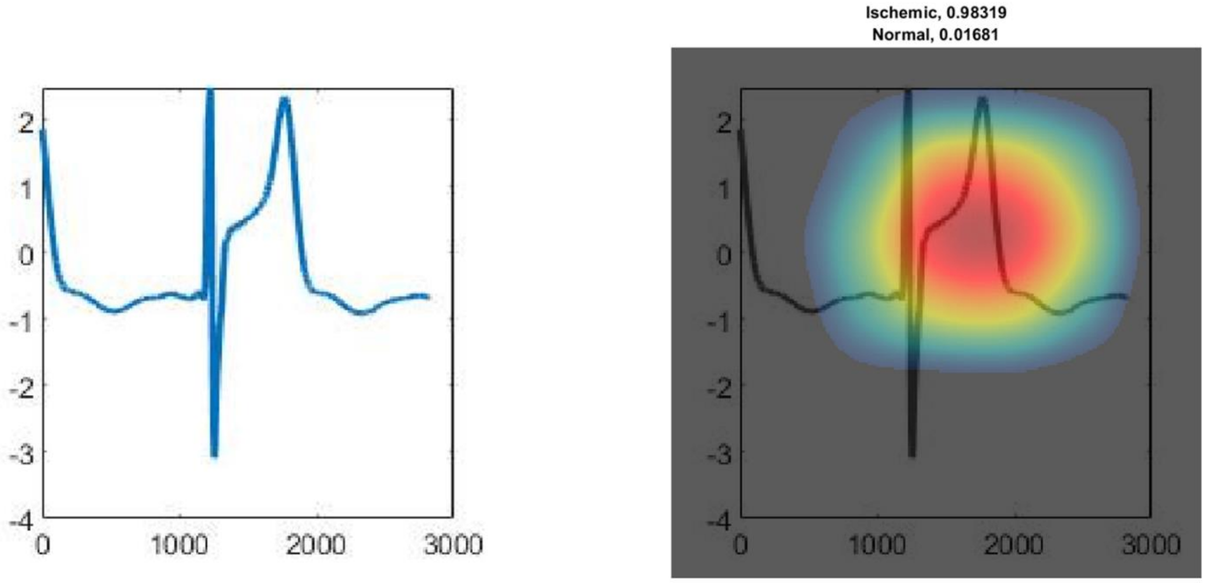

Appendix figure VI: Visualization of network activation patterns of GoogLeNet10 as it is shown by running the code above. *Red regions contribute most to the network prediction, while grey region do not contribute to the prediction.*

8.6 Visualization of hidden layers

```
% This is a MATLAB m-file
% -------------------------------------------------------------------------
% File          : VisualizationofHiddenLayers.m
% Author        : Marius Reto Bigler, adapted from an example from
%                 Mathworks
% Date adapted  : 01.12.2020
% Last Change   : -
% Institute     : Department of Cardiology
% -------------------------------------------------------------------------
% Description:
%
% This function gives us a visual explanation of the activation in each
% convolutional layer of the network. The code is based on the Mathworks
% example on Visualize Activations of a Convolutional Neural Network
% https://ch.mathworks.com/help/deeplearning/ug/visualize-activations-of-a-
convolutional-neural-network.html
% and further adapted for the application on a trained GoogleNet-CNN.
% Descriptions are directly copied from the example.
%
% The function returns 24 figures, 2 of each central convolutional layer of
% GoogleNet. One with an overview and one with the strongest channel. All
% figures are grayscaled with white = strongest activations.

%% Visualization of hidden layer activations
% load a pretrained network
net = savedStruct.trainedNet;

% load an image
im = imread('\\filer300\users3006\i0316914\Documents\Aktuelle Studien\MD-
PhD Thesis\Neural Network\Beispiel Ischämieentwicklung\Bsp1jpgs\
35068_FU_vessel2_arm_1_maxhf_dobu_ECGavg.mat.jpg');

% and show it
figure(1)
imshow(im)

% Save its size for future use.
imgSize = size(im);
imgSize = imgSize(1:2);

%% Investigate features by observing which areas in the convolutional
% layers activate on an image and comparing with the corresponding areas in
% the original images. Each layer of a convolutional neural network
% consists of many 2-D arrays called channels. Pass the image through the
% network and examine the output activations of the conv1 layer. Please
% note that we have to adjust the number of subplots (i.e., actsize)
% according to the number of kernels of this convolutional layer (e.g., 64
% for the first example)

for i=1:12 % since we want to get figures from each central convolutional
layer (e.g., “conv1-7x7_s2”)
     if i==1
    act1 = activations(net,im,'conv1-7x7_s2');
    actsize = [8 8];
    filtername = 'conv1-7x7_s2';

    elseif i==2
    act1 = activations(net,im,'conv2-3x3_reduce');
    actsize = [8 8];
```

```
    filtername = 'conv2-3x3_reduce';
    elseif i==3
    act1 = activations(net,im,'conv2-3x3');
    actsize = [12 16];
    filtername = 'conv2-3x3';

    elseif i==4
    act1 = activations(net,im,'conv2-norm2');
    actsize = [12 16];
    filtername = 'conv2-norm2';

    elseif i==5
    act1 = activations(net,im,'inception_3a-output');
    actsize = [16 16];
    filtername = 'inception_3a-output';

    elseif i==6
    act1 = activations(net,im,'inception_3b-3x3');
    actsize = [12 16];
    filtername = 'inception_3b-3x3';

    elseif i==7
    act1 = activations(net,im,'inception_3b-output');
    actsize = [20 24];
    filtername = 'inception_3b-output';

    elseif i==8
    act1 = activations(net,im,'inception_4a-output');
    actsize = [16 32];
    filtername = 'inception_4a-output';

    elseif i==9
    act1 = activations(net,im,'inception_4b-output');
    actsize = [16 32];
    filtername = 'inception_4b-output';

    elseif i==10
    act1 = activations(net,im,'inception_4c-output');
    actsize = [16 32];
    filtername = 'inception_4c-output';

    elseif i==11
    act1 = activations(net,im,'inception_4d-output');
    actsize = [22 24];
    filtername = 'inception_4d-output';

    elseif i==12
    act1 = activations(net,im,'inception_4e-output');
    actsize = [26 32];
    filtername = 'inception_4e-output';

    end
% The activations are returned as a 3-D array, with the third dimension
% indexing the channel on the conv1 layer. To show these activations using
% the imtile function, reshape the array to 4-D. The third dimension in the
% input to imtile represents the image color. Set the third dimension to
% have size 1 because the activations do not have color. The fourth
% dimension indexes the channel.
sz = size(act1);
act1 = reshape(act1,[sz(1) sz(2) 1 sz(3)]);
```

```
% Now you can show the activations. Each activation can take any value,
% so normalize the output using mat2gray. All activations are scaled so
% that the minimum activation is 0 and the maximum is 1. Display the 64
% images on an 8-by-8 grid, one for each channel in the layer.
I = imtile(mat2gray(act1),'GridSize',actsize);

figure(i)
txt = ['Overview Activation pattern of ',filtername];
imshow(I, 'Parent', gca );
title(gca, txt );

% Each tile in the grid of activations is the output of a channel in the
% conv1 layer. White pixels represent strong positive activations and
% black pixels represent strong negative activations. A channel that is
% mostly gray does not activate as strongly on the input image. The
% position of a pixel in the activation of a channel corresponds to the
% same position in the original image. A white pixel at some location in
% a channel indicates that the channel is strongly activated at that
% position

%% Find the strongest activation
[maxValue,maxValueIndex] = max(max(max(act1)));
act1chMax = act1(:,:,:,maxValueIndex);
act1chMax = mat2gray(act1chMax);
act1chMax = imresize(act1chMax,imgSize);

I = imtile({im,act1chMax});
figure(i+12)
txt = ['Strongest Activation pattern of ',filtername];
hImage = imshow(I, 'Parent', gca );
title(gca, txt );

end
```

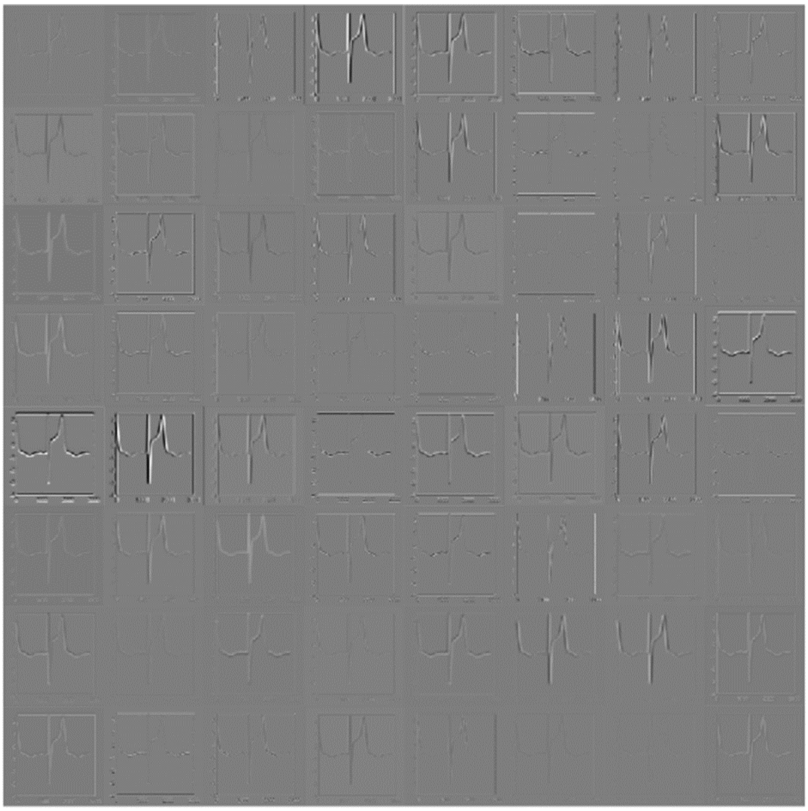

***Appendix figure VII: Overview of the activation pattern of the first convolutional layer of GoogLeNet (conv1-7x7_s2)**: As outlined in figure XVII, the first convolutional layer is responsible for the detection of simple geometric structures (e.g., edges). The first convolutional layer of GoogLeNet uses 64 different kernels for this purpose. "White pixels represent strong positive activations and black pixels represent strong negative activations. A channel that is mostly gray does not activate as strongly on the input image." Cited from https://ch.mathworks.com/help/deeplearning/ug/visualize-activations-of-a-convolutional-neural-network.html*

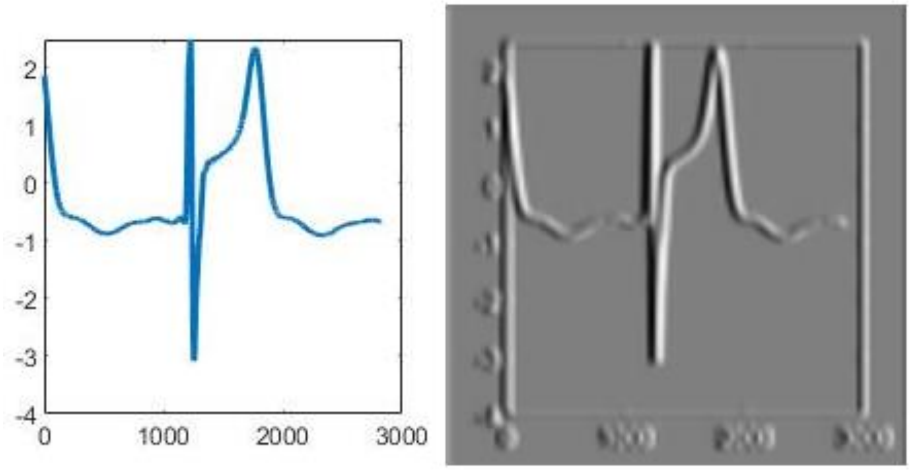

Appendix figure VIII: Strongest activation pattern of the first convolutional layer of GoogLeNet (conv1-7x7_s2)*: The first convolutional layer is responsible for edge detection. Hence, the strongest activation was provided by a kernel which activates positively (i.e., white signal) on dark left /light right edges and negatively (i.e., black signal) on light left/dark right edges. Consequently, the activation is strongest on the QRS-complex, the up- and downslope of the T-wave as well as on the frame of the image. The underlying kernel operation is a simple subtraction of the value from one pixel and its neighboring pixel.*

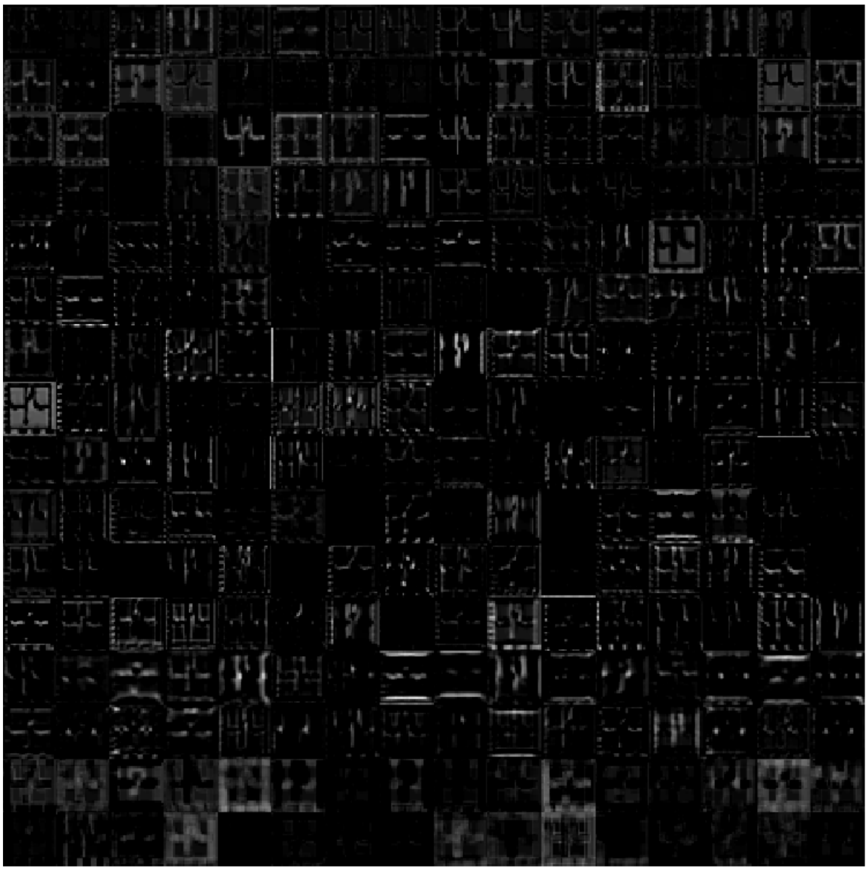

Appendix figure IX: Overview of the activation pattern of the first inception convolutional layer of GoogLeNet (inception_3a_output)*: This layer is notable deeper in the network architecture. Thus, illustration of the activation patterns shows more abstract patterns as the purpose of these layers is to extract features, rather than geometrical structures. Of note, inception_3a_output is a layer that uses 256 different kernels, resulting in the illustration of 256 different activation pattern.*

9. Curriculum vitae and list of publications

Marius Reto Bigler

Date of birth: 08.09.1991
Address: Schänzlihalde 30
3013 Bern, CH
+41 79 697 60 92
e-mail: mariusreto.bigler@insel.ch
mariusbigler@hotmail.com
Citizen of: Worb, Canton of Bern, Switzerland
Marital status: unmarried

Formation

10/17 –	University of Bern MD-PhD at the Graduate School for Cellular and Biomedical Sciences Research project: “Functional assessment of myocardial ischemia by intracoronary electrocardiogram”
09/11 – 06/17	University of Bern Bachelor and Master of Medicine MD thesis: “Morphometry of skeletal muscle capillaries: The relationship between capillary ultrastructure and aging in humans.”

Professional activities

10/17 -	Research fellow Department of Cardiology Inselspital, University Hospital of Bern 20% clinical work cardiac catheter laboratory
05/15 – 11/16	Practical training during the Master of Medicine at the University of Bern with focus on cardiology, heart surgery and neurology

03/15 – 05/15	Research internship at the Charité Cross Over (CCO) in Berlin Research group: Wall shear stress and vascular biology
07/10 – 04/11	Military service in the Swiss Army

Academic awards/ Grants

Winner of the Otto Hess Trainee Award 2021 of the Swiss Society of Cardiology for young trainees in cardiology with active involvement in research

”Best Abstract 2019 – ACS, PCI, CABG” from the Swiss Society of Cardiology: “Effect of permanent right internal mammary artery occlusion on right coronary artery collateral function. A randomized controlled trial”

Grant from the Bangerter-Rhyner Foundation (#0418/2019): CHF 60’000.00 for the research project: “Myocardial Viability Assessment by Intracoronary Electrocardiogram”

Grant from the Swiss National Science Foundation as collaborator (#320030_200871/1; Main applicant Prof. Dr. med. C. Gräni, PhD): CHF 323’461.00 for the research project: “Noninvasive anatomical assessment for ruling out hemodynamically relevant coronary artery anomalies – A comparison of coronary-CT to invasive coronary angiography (NARCO)”

Presentations

Swiss Society of Cardiology - Joint Annual Meeting

- 2018 (Basel) Rapid Fire Oral Presentation - “Functional assessment of myocardial ischemia by intracoronary electrocardiogram”
- 2019 (Interlaken) Rapid Fire Oral Presentation - “Effect of permanent right internal mammary artery occlusion on right coronary artery collateral function. A randomized controlled trial”
- 2019 (Interlaken) Poster presentation - “Invasive assessment of the human palmar arch collateral function during transradial catheterisation”
- 2020 (digital) Video Abstract Presentation - “Functional assessment of myocardial ischemia by intracoronary electrocardiogram” (Video available here: https://youtu.be/0nFLMT0QVXk)

European Society of Cardiology (ESC) Congress

- 2018 (Munich) Poster presentation - "Functional assessment of myocardial ischemia by intracoronary electrocardiogram"
- 2019 (Paris) Poster presentation - "Effect of permanent right internal mammary artery occlusion on right coronary artery collateral function. A randomized controlled trial"
- 2020 (digital) ePoster presentation - "Functional assessment of myocardial ischemia by intracoronary electrocardiogram"

Internal presentations:

- 3 presentation at the GCB Symposium in Bern (2019 poster flash presentation, 2020 poster presentation, 2021 oral presentation)
- 3 poster presentations at the "Day of BioMedical Research", University Hospital of Bern, Inselspital (2018-20)

Publications

Bigler MR., Stoller M., Praz F., Siontis G.C.M., Grossenbacher R., Tschannen C., Seiler C.: **Functional Assessment of Myocardial Ischemia by Intracoronary Electrocardiogram**
Open Heart 2021:e001447
DOI: 10.1136/openhrt-2020-001447
Original article: Impact factor: 2.130

Bigler MR., Zimmermann P., Papadis A., Seiler C.: **Accuracy of intracoronary ECG parameters for myocardial ischemia detection**
J Electrocard 2020 Dec 05
DOI:10.1016/j.jelectrocard.2020.11.018
Original article: Impact factor: 0.944

Bigler MR., Stoller M., Tschannen C., Grossenbacher R., Seiler C.: Effect of permanent right internal mammary artery occlusion on right coronary artery supply: A randomized placebo-controlled clinical trial
Am Heart J. 2020 Sep 16;S0002-8703(20)30259-3.
DOI:10.1016/j.ahj.2020.09.006.
Original article: Impact factor: 4.153

Bigler MR., Buffle E., Siontis G.C.M., Stoller M., Grossenbacher R., Tschannen C., Seiler C.: Invasive Assessment of the Human Arterial Palmar Arch and Forearm Collateral Function During Transradial Access.
Circ Cardiovasc Interv. 2019 Jul;12(7): e007744.
DOI: 10.1161/CIRCINTERVENTIONS.118.007744.
Original article: Impact factor: 6.060

Bigler MR., Koutsantonis D., Odriozola A., Halm S., Tschanz S. A., Zakrzewicz A., Weichert A., Baum O.: Morphometry of skeletal muscle capillaries: The relationship between capillary ultrastructure and aging in humans.
Acta Physiol, Volume 218, Issue 2, October 2016, Pages 98–111,
DOI: 10.1111/apha.12709
Original article: Impact factor: 4.867

Bigler MR., Ashraf A., Seiler C., Praz F., Ueki Y., Windecker S., Kadner A., Räber L., Gräni C.: Hemodynamic relevance of anomalous coronary arteries originating from the opposite sinus of Valsalva - in search of the evidence
Front. Cardiovasc. Med.
DOI:10.3389/fcvm.2020.591326
Review: Impact factor: 3.915

Bigler MR, Seiler C: The Human Coronary Collateral Circulation, Its Extracardiac Anastomoses and Their Therapeutic Promotion.
Int J Mol Sci. 2019 Jul 30;20(15). pii: E3726.
DOI: 10.3390/ijms20153726.
Review: Impact factor: 4.183

Baum O., **Bigler MR**.: Pericapillary basement membrane thickening in human skeletal muscles.
Am J Physiol Heart Circ Physiol., Vol. 311 no. 3, H654-H666,
DOI: 10.1152/ajpheart.00048.2016
Review: Impact factor: 3.348

Bigler MR., Huber, AT., Räber L., Gräni C.: A case report of a symptomatic right anomalous coronary artery with concomitant atherosclerotic disease: the benefit of a sequential comprehensive noninvasive and invasive diagnostic approach
EHJ – Case Reports
DOI: 10.1093/ehjcr/ytab081
Case report: Impact factor: -

Bigler MR., Ueki Y., Otsuka T., Huber A.T., Kadner A., Räber L., Gräni C.: Discrepancy between SPECT and dobutamine FFR in right anomalous coronary artery undergoing unroofing.
Ann Thorac Surg. 2020 Jul 21;S0003-4975(20)31183-8.
DOI: 10.1016/j.athoracsur.2020.05.128
Case report: Impact factor: 3.919

Bigler MR., Hunziker L., de Marchi S.F., Pilgrim T., Windecker S., Seiler C.: Pulmonary Artery Pressure Ventricularization in a Patient With Carcinoid Heart Disease
JACC: Case Reports, Volume 2, Issue 8, July 2020
DOI: 10.1016/j.jaccas.2020.05.057
Case report: Impact factor: -

Bigler MR., Gräni C.: The power of zero calcium score: Is there a need for improvement?
J Nucl Cardiol. 2020 Aug 27.
DOI: 10.1007/s12350-020-02326-7
Editorial: Impact factor: 3.847

Declaration of Originality

Last name, first name: Bigler, Marius Reto

Matriculation number: 11-115-342

I hereby declare that this thesis represents my original work and that I have used no other sources except as noted by citations.
All data, tables, figures and text citations which have been reproduced from any other source, including the internet, have been explicitly acknowledged as such.
I am aware that in case of non-compliance, the Senate is entitled to withdraw the doctorate degree awarded to me on the basis of the present thesis, in accordance with the "Statut der Universität Bern (Universitätsstatut; UniSt)", Art. 69, of 7 June 2011.

Place, date

Bern, 10.06.2021

Signature